UNIVERSITY OF SOUTHAMPTON
FACULTY OF ENGINEERING AND THE ENVIRONMENT
Aerodynamics and Flight Mechanics Research Group

Receptivity and transition to turbulence of supersonic boundary layers with surface roughness

by
Nicola De Tullio

Thesis for the degree of Doctor of Philosophy

February 2013

UNIVERSITY OF SOUTHAMPTON

ABSTRACT

FACULTY OF ENGINEERING AND THE ENVIRONMENT

Doctor of Philosophy

RECEPTIVITY AND TRANSITION TO TURBULENCE OF SUPERSONIC BOUNDARY LAYERS WITH SURFACE ROUGHNESS

by Nicola De Tullio

A deeper understanding of the different factors that influence the laminar-turbulent transition in supersonic boundary layers will help the design of efficient high-speed vehicles. In this work we study the effects of surface roughness on the stability and transition to turbulence of supersonic boundary layers. The investigation is carried out by direct numerical simulations (DNS) of the compressible Navier-Stokes equations and focuses on the modifications introduced in the transition process by localised roughness elements, for Mach numbers $M_\infty = 6.0$ and $M_\infty = 2.5$, and distributed slender pores at $M_\infty = 6.0$. The first part of the investigation into the effects of localised roughness deals with the receptivity and initial exponential amplification of disturbances in boundary layers subjected to small external perturbations. Different transition scenarios are investigated by considering different free-stream disturbances and roughness elements with different heights. The results show that, for roughness heights approaching the local displacement thickness, transition is dominated by the growth of a number of instability modes in the roughness wake. These modes are damped by wall cooling and their receptivity is found to be more efficient in the case of free-stream disturbances dominated by sound. At $M_\infty = 6$ the growth of Mack modes in the boundary layer is found to play a crucial role in the excitation of the most unstable wake modes. An investigation into the nonlinear stages of transition shows that the breakdown to turbulence starts with nonlinear interactions of the wake instability modes. This leads to the formation of a turbulent wedge behind the roughness element, which spreads laterally following mechanisms similar to those observed for the evolution of compressible turbulent spots. An oblique shock impinging on the transitional boundary layer significantly accelerates the breakdown process and leads to a wider turbulent wedge. The study ends with an analysis of porous walls as a passive method for transition control, which is carried out using a temporal DNS approach. The results show damping of both the primary, of second or Mack mode type, and secondary instabilities and indicate that, despite the high Mack number, first mode waves regain importance in this modified transition scenario.

Contents

Nomenclature **xi**

Declaration of Authorship **xvii**

Acknowledgements **xix**

1 Introduction **1**
1.1 Motivation 1
1.2 Transition due to small external disturbances 3
1.3 Receptivity mechanisms 6
1.4 Transient growth and bypass transition 8
1.5 Roughness-induced transition 10
1.6 Transition over porous surfaces 13
1.7 Objectives and thesis outline 14

2 Equations and methods **17**
2.1 The Navier-Stokes equations 17
2.2 Numerical strategy 19
2.2.1 The core of the *SBLI* code 19
2.2.2 Computational geometry for the roughness cases 20
2.2.3 Boundary conditions for the roughness cases 22
2.2.4 Disturbance generation 22
2.2.5 Multi-block grid configuration and sharp corner treatment . 23
2.2.6 Grid generation 27
2.2.7 Validation of the multi-block strategy 28

3 Small disturbance receptivity due to roughness **31**
3.1 The parametric study 32
3.2 Characterisation of the disturbances in the free-stream 35
3.3 Receptivity and stability of the clean flat plate boundary layer . . . 39
3.4 Grid convergence study and influence of filtering 46
3.5 Analysis of the basic flow in the presence of roughness 48
3.6 Roughness receptivity at $M_\infty = 6.0$ 51
3.6.1 Effect of roughness height 52
3.6.2 Effect of disturbance type and position 56
3.6.3 Wall temperature effects 60

3.7 Roughness receptivity at $M_\infty = 2.5$ 61
3.7.1 Effect of roughness height 62
3.7.2 Effect of disturbance type and position 67
3.7.3 Wall temperature effects 70
3.8 Synthesis and discussion of receptivity results 71

4 Nonlinear stages in supersonic roughness-induced transition 75
4.1 Numerical simulations 77
4.2 Roughness-induced breakdown to turbulence at $M_\infty = 6.0$ 79
4.2.1 Main features of the laminar-turbulent transition process . . 79
4.2.2 Mechanisms responsible for the breakdown to turbulence . . 82
4.2.3 Turbulent wedge development 89
4.2.4 Effects of a shock wake impinging on the transitional boundary layer 95
4.3 Roughness-induced breakdown to turbulence at $M_\infty = 2.5$ 102
4.3.1 Mean flow features 103
4.3.2 Mechanisms responsible for the breakdown to turbulence . . 106
4.3.3 Turbulent wedge development 109
4.3.4 Effects of a shock wave impinging on the transitional boundary layer 115
4.4 Synthesis and discussion of key findings 122

5 Transition control using surface porosity 127
5.1 Introduction 127
5.2 Numerical simulations 129
5.3 Transition to turbulence due to second mode waves 132
5.3.1 Evolution and interactions of boundary layer modes 132
5.3.2 Dissipation of disturbance energy inside the pores 142
5.3.3 Evolution of the averaged boundary layer quantities 143
5.4 The role of the fundamental secondary waves 149
5.5 The importance of first mode waves 150
5.6 Validity of the forcing term 152
5.7 Conclusions 154

6 Conclusions and future work 157

Bibliography 163

List of Figures

1.1 Morkovin's roadmap to transition. The letters indicate the different paths to transition. Taken from Morkovin *et al.* (1994). 2

2.1 Computational domain and boundary conditions. Domain A is used for simulations of the complete transition process while Domain B is used for the study of roughness receptivity. 20
2.2 Multi-block strategy. Side view in top figure, top view in bottom figure. 24
2.3 Description of the corner problem. 25
2.4 Grid stretching using polynomials of high degree. 27
2.5 Validation of the multi-block strategy employed. (a) Mack mode growth rate comparison (Navier-Stokes against LST), (b) comparison between Navier-Stokes amplitude function and LST eigenfunction for the Mack mode primary instability (u_f is the u-velocity Fourier mode amplitude function for the Navier-Stokes result and the u-velocity eigenfunction for the LST result). 29

3.1 Position of non-zero inflow disturbances relative to the boundary layer for internal and external disturbances. 34
3.2 Streamwise averaged disturbance amplitudes for $|\boldsymbol{\omega}|$, $|\nabla \cdot \mathbf{u}|$ and $|\nabla\sqrt{e}|$ in the free-stream. (a), (c), (e) $M_\infty = 6.0$ and (b), (d), (f) $M_\infty = 2.5$. . . 36
3.3 Streamwise $\phi(x)/\omega$ evolution for a selection of free-stream $\nabla \cdot u$ disturbances, showing the phase speed of the dominant free-stream acoustic waves. (a) type A disturbances, $M_\infty = 6.0$, (b) type A disturbances, $M_\infty = 2.5$. 37
3.4 Amplitude of pressure disturbances in the free-stream. (a) $F = 0.32$ and $k = 0.314$ at Mach 6.0, (a) $F = 0.14$ and $k = 0.314$ at $M_\infty = 2.5$. 37
3.5 Temporal LST stability diagrams. (a) $M_\infty = 6.0$ ($k_z = 0$), the dashed contourlines indicate $-\alpha_i = 0.010$ to 0.025 with steps of 3×10^{-3}, (b) $M_\infty = 2.5$ ($k_z = 0.314$), the dashed contourlines show $-\alpha_i = 0.0010$ to 0.005 with steps of 8×10^{-4}. 39
3.6 Spatial LST growth rates as a function of frequency. (a) $M_\infty = 6.0$ ($k_z = 0$), (b) $M_\infty = 2.5$ ($k_z = 0.314$). 40
3.7 Transient growth of u' disturbances in the case of internal type V disturbances, sowing the boundary layer response for all the frequencies contained in the forcing signal ($0.02 \leq F \leq 0.32$). (a) $M_\infty = 6.0$, (b) $M_\infty = 2.5$. 42

3.8 Comparison of DNS and LST eigenfunctions. (a) mode $F = 0.06$ and $k = 0.314$ at $M_\infty = 6.0$, (b) mode $F = 0.18$ and $k_z = 0.314$ at $M_\infty = 6.0$, (c) mode $F = 0.02$ and $k_z = 0.314$ at $M_\infty = 2.5$. 43
3.9 Contours of the real part of $\hat{p}_w$ for $F = 0.18$ showing the development of a Mack mode instability. (a) case $HSAI_a$ (contour limits $\Re\{\hat{p}_w\} = \pm 9.5 \times 10^{-5}$), (b) case $HSVI_a$ (contour limits $\Re\{\hat{p}_w\} = \pm 2.2 \times 10^{-5}$). 44
3.10 Streamwise $\phi(x)/\omega$ evolution for p' disturbances at the wall, showing that fast acoustic waves dominate the near wall disturbance field for certain frequencies. (a) $F = 0.28$ at $M_\infty = 6.0$, (b) $F = 0.12$ at $M_\infty = 2.5$. 44
3.11 Maximum total amplitude of boundary-layer disturbances for the different forcing frequencies. (a) $M_\infty = 6.0$, (b) $M_\infty = 2.5$. 45
3.12 Contribution of single spanwise modes to the total amplitude of disturbances inside the boundary-layer for the different forcing frequencies. (a) $M_\infty = 6.0$, (b) $M_\infty = 2.5$. 45
3.13 Effect of grid resolution on the streamwise evolution of disturbances downstream of the roughness element. (a) $HR1.0AI_a$, (b) $HR1.0AI_b$ . . 47
3.14 Effect of grid resolution on the overall boundary layer response to the incoming disturbances. (a) $HR1.0AI_a$, (b) $HR1.0AI_b$ 47
3.15 Effect of filtering parameter on the overall boundary layer response to the incoming disturbances. (a) $HR1.0AI_a$, (b) $HR1.0AI_b$ 48
3.16 Flow topology around the roughness element: (a) $HR1.0_a$, (b) $HR1.0_b$. Isosurfaces of small negative u show the separated flow regions in blue. Grey isosurfaces of ω_x, positive on the right and negative on the left part of the computational domain looking downstream, show the roughness-induced vortices. 49
3.17 Contours of $u_S := \sqrt{(\partial u/\partial y)^2 + (\partial u/\partial z)^2}$ showing the localised shear generated by the roughness-induced counter-rotating vortices. (a) $M_\infty = 6.0$, $h = 1.0$ at $x = 120$, (b) $M_\infty = 6.0$, $h = 0.5$ at $x = 120$, (c) $M_\infty = 2.5$, $h = 1.0$ at $x = 80$, (d) $M_\infty = 2.5$, $h = 0.5$ at $x = 80$. 50
3.18 Contours of u. Separated flow regions and reattachment shock shown as $u = 0$ (red line) and negative $\nabla \cdot \mathbf{u}$ (black line) respectively. (a) case $HR1.0_a$, (b) case $CR1.0_b$. 51
3.19 Streamwise evolution of u' disturbances inside the boundary-layer for cases $HSAI_a$, $HR0.5AI_a$ and $HR1.0AI_a$. (a) $F = 0.02$, (b) $F = 0.06$, (c) $F = 0.14$, (d) $F = 0.18$. 52
3.20 Contours of $|\hat{u}|$ in a crossflow plane at $x = 140$ showing the shape of the instability modes developing in the roughness wake for case $HR1.0AI_a$. The red dashed line indicates the roughness position. (a) $F = 0.02$, (b) $F = 0.06$, (c) $F = 0.12$, (d) $F = 0.14$. 53
3.21 Isosurfaces of $\Re\{\hat{v}\}$ showing the three-dimensional structure of the wake modes for case $HR1.0AI_a$. (a) $F = 0.02$, (b) $F = 0.06$, (c) $F = 0.12$, (d) $F = 0.14$. 54
3.22 Streamwise evolution of v' disturbances inside the boundary-layer for cases $HR1.0VI_a$, $HR1.0AI_a$ and $HR1.0ÆI_a$. (a) $F = 0.06$, (b) $F = 0.14$. 56

3.23 Streamwise evolution of v' disturbances inside the boundary-layer for cases *HR1.0VE*$_a$, *HR1.0AE*$_a$ and *HR1.0ÆE*$_a$. (a) $F = 0.06$, (b) $F = 0.14$. 56
3.24 Contours of $|\hat{u}|$ in a crossflow plane at $x = 140$ showing the shape of the instability modes developing in the roughness wake for different inflow disturbances. The red dashed line indicates the roughness position. (a) $F = 0.06$ for case *HR1.0VE*$_a$, (b) $F = 0.06$ for case *HR1.0AE*$_a$, (c) $F = 0.14$ for case *HR1.0VE*$_a$, (d) $F = 0.14$ for case *HR1.0AE*$_a$. 57
3.25 Contours of the real part of $\hat{u}$ showing the excitation of wake instability modes. The white squares indicate the roughness location. (a) $F = 0.06$ for case *HR1.0VI*$_a$ at $y = 0.88$, (b) $F = 0.06$ for case *HR1.0AI*$_a$ at $y = 0.88$, (c) $F = 0.14$ for case *HR1.0VE*$_a$ at $y = 1.2$, (d) $F = 0.14$ for case *HR1.0AE*$_a$ at $y = 1.2$. 59
3.26 Streamwise evolution of v' disturbances inside the boundary-layer for cases *HR1.0AI*$_a$ and *CR1.0AI*$_a$. (a) $F = 0.02$, (b) $F = 0.06$, (c) $F = 0.14$ for case *HR1.0AI*$_a$ and $F = 0.10$ for case *CR1.0AI*$_a$, (d) $F = 0.18$ for case *HR1.0AI*$_a$ and $F = 0.14$ for case *CR1.0AI*$_a$. 61
3.27 Streamwise evolution of u' disturbance amplitude for cases *HSAI*$_b$, *HR0.5AI*$_b$ and *HR1.0AI*$_b$. 62
3.28 Growth of u' disturbances inside the boundary layer as a function of frequency for case *HR1.0AI*$_b$. (a) amplitude of boundary layer disturbances at different streamwise positions, (b) maximum disturbance growth rate in the region $73 < x < 75$, calculated from $\mathcal{I}_\eta^u(x)$. 63
3.29 Contours of $\Re\{\hat{u}\}$ showing the excitation of instabilities downstream of the roughness. The white squares indicate the roughness position. (a) case *HR0.5AI*$_b$ for $F = 0.04$ at $y = 0.75$, (b) case *HR1.0AI*$_b$ for $F = 0.1$ at $y = 1.1$. The two horizontal planes show the region of maximum disturbance amplitude in the two cases. 64
3.30 Shear layer instability amplitude functions for $F = 0.08$ and $F = 0.26$ in a crossflow plane at $x = 70$ (case *HR1.0AI*$_b$). The red dashed line indicates the roughness position. (a) $|\hat{u}|$ for $F = 0.08$, (b) $|\hat{u}|$ for $F = 0.26$, (c) $|\hat{v}|$ for $F = 0.08$, (d) $|\hat{v}|$ for $F = 0.26$, (e) $|\hat{w}|$ for $F = 0.08$, (f) $|\hat{w}|$ for $F = 0.26$ 65
3.31 Showing the nature of the shear layer and the streak modes. Contours of $\Re\hat{w}$ at $y = 1.4$. (a) $F = 0.08$, where the shear layer mode is dominant, (b) $F = 0.26$, dominated by the streak instability, shows the sinuous nature of the mode. 66
3.32 Streamwise evolution of disturbance amplitude for cases *HR1.0VI*$_b$, *HR1.0AI*$_b$ and *HR1.0EI*$_b$. (a) $F = 0.08$, (b) $F = 0.1$, (c) $F = 0.12$, (d) $F = 0.14$, (e) $F = 0.18$, (f) $F = 0.24$. 68
3.33 Comparing the growth rates of mode VT and mode SL. The plot gives growth rate as a function of streamwise distance, calculated at the roughness centreline plane. 69
3.34 Oscillations in the upstream separation bubble, shown by v-velocity contours at $y = 0.4$. 71

3.35 Position of the numerical simulations carried out for the receptivity study relative to the transition criteria proposed by Redford *et al.* (2010) (a) and Bernardini *et al.* (2012) (b). Circles indicate hot wall cases with $h = 1.0$, triangles indicate cooled wall cases with $h = 1.0$ and squares indicate hot wall cases with $h = 0.5$. Red symbols are for the $M_\infty = 6.0$ cases and blue symbols for the $M_\infty = 2.5$ cases. 74

4.1 Contours of streamwise vorticity (ω_x) in a crossflow plane placed 40 displacement thicknesses downstream of the roughness (shaded contours), showing the modifications introduced on the roughness wake by the Reynolds number increase. Contours of u_S (white lines) show regions of high detached shear. (a) case *NL6.0* ($Re_h = 726$, $u_S = 0.38, 0.74, 1.1$), (b) case *HR1.0$_b$* ($Re_h = 331$, $u_S = 0.65, 1.025, 1.4$). Different u_S levels were used to highlight the structure of the high shear layers in the two cases. 80

4.2 Contours of instantaneous temperature. The red squares indicate the roughness position. (a) side view at the roughness mid-plane ($z = 25$), (b) top view in a horizontal plane at $y = 1.2$. 81

4.3 Streamwise evolution of time-averaged skin friction at three positions across the span. 81

4.4 Contours of time averaged v-velocity (green for negative and red for positive) in a crossflow plane at $x = 292$ showing how the upwash generated by the roughness induced streamwise vortices near the roughness mid-plane ($z = 25$) persists after breakdown to turbulence. The white line indicates the local boundary layer thickness ($\overline{u} = 0.99$) and the dashed yelow square shows the roughness position. 82

4.5 Effect of the isolated roughness, and the induced transition to turbulence, on the wall heat transfer and wall pressure fluctuations. (a) contours of wall-normal mean velocity gradient, (b) contours of wall-normal mean temperature gradient, (c) contours of the rms of the fluctuating wall-pressure normalised by free-stream pressure. 83

4.6 Linear and nonlinear evolution of disturbances in the roughness wake. The grey rectangle indicates the roughness position. (a) maximum u'_{rms} inside the boundary layer, (b) maximum v'_{rms} inside the boundary layer, (c) maximum w'_{rms} inside the boundary layer, (d) maximum (over y and z) rms velocity fluctuations inside the roughness wake. 85

4.7 Visualisation of the downstream development of roughness wake instabilities. (a), (c), (e), (g), (i) contours of u'_{rms} (shaded), superimposed by $u_S = 0.65, 1.025, 1.4$ contours and (b), (d), (f), (h), (j) contours of u'. . . 86

4.8 Streamwise evolution of the asymmetry parameter $\mathcal{S}_\phi$, giving an indication of the onset of considerable nonlinear interactions. The blue line shows the streamwise variations of maximum v'_{rms} inside the roughness wake and is plotted for reference. The grey rectangle shows the roughness position. 88

4.9 Development of two-dimensional waves inside the boundary layer. Contours of fluctuating v'-velocity in a horizontal plane at $y = 0.3$. 88

4.10 Isosurfaces of $Q = 0.0055$, coloured by streamwise velocity, showing the flow structures appearing during breakdown to turbulence. 88
4.11 Visualisation of the turbulent wedge developing downstream of the roughness. The solid and dashed contourlines in (b) and (c) indicate, respectively, $TKE = 0.08$ and $TKE = 0.007$. (a) Isosurfaces of $Q = 0.02$, coloured by streamwise velocity, (b) TKE contours in the horizontal plane at $y = 1.1$, (c) crossflow TKE contours at $x = 281$. 90
4.12 Measuring the lateral spreading half angle of the turbulent wedge. The solid blue, dashed black and solid red lines are inclined at $\alpha = 2.8°$, $\alpha = 3.0°$ and $\alpha = 3.2°$ to the horizontal, respectively. (a) contours of $TKE \geq 0.07$ at $y = 1.1$, (b) contours of $0.06 \leq |\omega_y| \leq 0.08$ at $y = 1.1$. . . 91
4.13 Contours of $\overline{w} = \pm 5 \times 10^{-3}$ (red for positive and blue for negative), superimposed by mean crossflow velocity vectors. (a) $x = 241$, (b) $x = 277$, (c) $x = 289$. 93
4.14 Isosurfaces of mean $Q = 0.001$, coloured by wall-normal distance. The light grey lines are inclined at $\alpha = 3.0°$ to the streamwise direction. . . . 94
4.15 Flow features induced by the SBLI. (a) contours of $\sqrt{(\partial\rho/\partial x)^2 + (\partial\rho/\partial y)^2}$ at the roughness mid-plane, (b)contours of instantaneous temperature in a horizontal plane at $y = 1.2$. The red squares indicate the roughness position and the blue line shows regions of separated flow ($\overline{u} = 0$ at the first grid point above the wall). 95
4.16 Streamwise evolution of time-averaged skin friction at the roughness mid-plane, showing the effect of the SBLI on the breakdown to turbulence. . 96
4.17 Effects of SBLI on heat transfer and unsteady pressure loads at the wall. Blue lines show regions of separated flow ($\overline{u} = 0$ at the first grid point above the wall). (a) $\partial\overline{T}/\partial y$ for case *NL6.0*, (b) $\partial\overline{T}/\partial y$ for case *NL6.0S*, (c) p'_{rms}/p_∞ for case *NL6.0*, (d) p'_{rms}/p_∞ for case *NL6.0S*. 97
4.18 Effect of the SBLI on the growth of disturbances inside the roughness wake. White lines in (a) and (b) show $u_S = 0.65, 1.025, 1.4$. (a), (c), (e) case *NL6.0S* and (b), (d), (f) case *NL6.0*. 98
4.19 Pressure probe at $x = 210$ and $z = 25$ showing the amplification of low frequencies by the shock system. (a) *NL6.0*, (b) case *NL60S*. 99
4.20 Comparison of the turbulent wedge structure for cases *NL6.0* and *NL6.0S*. The solid and dashed contourlines in (c) and (d) indicate, respectively, $TKE = 0.07$ and $TKE = 0.008$. (a) TKE contours in the horizontal plane at $y = 1.1$ for case *NL6.0*, (b) TKE contours in the horizontal plane at $y = 1.1$ for case *NL6.0S*, (c) crossflow TKE contours at $x = 281$ for case *NL6.0*, (c) crossflow TKE contours at $x = 281$ for case *NL6.0S*. . 100
4.21 Crossflow contours of mean lateral velocity. Red and green contourlines show respectively $\overline{w} = +5 \times 10^{-3}$ and $\overline{w} = -5 \times 10^{-3}$. The dashed white line indicates the roughness position. (a) $x = 250$, (b) $x = 280$. 101
4.22 Contours of instantaneous temperature. The red squares indicate the roughness position. (a) side view at the roughness mid-plane, (b) top view in a horizontal plane at $y = 1.2$. 103
4.23 Streamwise evolution of time-averaged skin friction at the different positions across the span. 104

4.24 Effect of the isolated roughness, and the induced transition to turbulence, on the wall heat transfer and wall pressure fluctuations. (a) contours of wall-normal mean velocity gradient, (b) contours of wall-normal mean temperature gradient, (c) contours of the rms of the fluctuating wall-pressure normalised by free-stream pressure. 105
4.25 Visualisation of the downstream development of roughness wake instabilities. (a), (c), (e), (g), (i) contours of u'_{rms} (shaded), superimposed by $u_S = 0.65, 1.025, 1.4$ contours and (b), (d), (f), (h), (j) contours of u'. . . 107
4.26 Linear and nonlinear evolution of disturbances in the roughness wake, shown by the streamwise evolution of maximum disturbance amplitude inside the wake of the roughness. (a) logarithmic scale, (b) linear scale. . 108
4.27 Isosurfaces of $Q = 0.01$, coloured by wall-normal distance, showing the flow structures appearing during breakdown to turbulence. 108
4.28 Visualisation of the turbulent wedge developing downstream of the roughness. The solid and dashed contourlines in (b) and (c) indicate, respectively, $TKE = 0.07$ and $TKE = 0.008$: (a) Isosurfaces of $Q = 0.02$, coloured by wall-normal distance, (b) TKE contours in the horizontal plane at $y = 1.2$, (c) crossflow TKE contours at $x = 230$. 110
4.29 Measuring the lateral spreading half angle of the turbulent wedge. The solid blue, dashed black and solid red lines are inclined at $\alpha = 5.3°$, $\alpha = 5.5°$ and $\alpha = 5.7°$ to the horizontal, respectively. (a) contours of $TKE \geq 0.07$ at $y = 1.2$, (b) contours of $0.06 < |\omega_y| < 0.08$ at $y = 1.2$. . . 111
4.30 Crossflow contours of mean lateral velocity. Red and green contourlines show respectively $\overline{w} = +3 \times 10^{-3}$ and $\overline{w} = -3 \times 10^{-3}$. The dashed white line indicates the roughness position. (a) $x = 148$, (b) $x = 172$, (c) 220. . 112
4.31 Crossflow contours of instantaneous lateral velocity. Red and green contourlines show respectively $\overline{w} = +5 \times 10^{-3}$ and $\overline{w} = -5 \times 10^{-3}$. The dashed white line indicates the roughness position. (a) $x = 148$, (b) $x = 172$, (c) 220. 113
4.32 Generation of new vortices by destabilisation of surrounding laminar flow. Crossflow velocity vectors superimposed streamwise vorticity contours $\omega_x = \pm 0.05$, red for positive and blue for negative. (a) $x = 180$ and $t = 2852$, (b) $x = 200$ and $t = 2880$, (c) $x = 220$ and $t = 2904$, (d) $x = 240$ and $t = 2924$. 114
4.33 Flow features induced by the SBLI. (a) contours of $\sqrt{(\partial\rho/\partial x)^2 + (\partial\rho/\partial y)^2}$ at the roughness mid-plane, (b)contours of instantaneous temperature in a horizontal plane at $y = 1.2$. The red squares indicate the roughness position and the blue line shows regions of separated flow ($\overline{u} = 0$ at the first grid point above the wall). 115
4.34 Streamwise evolution of time-averaged skin friction at the roughness mid-plane, showing the effect of the SBLI on the breakdown to turbulence. . 116
4.35 Effects of SBLI on heat transfer and unsteady pressure loads at the wall. Blue lines show regions of separated flow ($\overline{u} = 0$ at the first grid point above the wall). (a) $\partial\overline{T}/\partial y$ for case *NL2.5*, (b) $\partial\overline{T}/\partial y$ for case *NL2.5S*, (c) p'_{rms}/p_∞ for case *NL2.5*, (d) p'_{rms}/p_∞ for case *NL2.5S*. 117

4.36 Effect of the SBLI on the growth of disturbances inside the roughness wake. White lines in (a) and (b) show $u_S = 0.70, 1.05, 1.4$. (a), (c), (e), (g) case *NL6.0S* and (b), (d), (f), (h) case *NL6.0*. 118
4.37 Pressure probe at $x = 110$ and $z = 28$ showing the amplification of low frequencies by the shock system. (a) *NL2.5*, (b) case *NL2.5S*. 119
4.38 Comparison of the turbulent wedge structure for cases *NL2.5* and *NL2.5S*. The solid and dashed contourlines in (c) and (d) indicate, respectively, $TKE = 0.08$ and $TKE = 0.007$. (a) TKE contours in the horizontal plane at $y = 1.2$ for case *NL2.5*, (b) TKE contours in the horizontal plane at $y = 1.2$ for case *NL2.5S*, (c) crossflow TKE contours at $x = 230$ for case *NL2.5*, (c) crossflow TKE contours at $x = 230$ for case *NL2.5S*. . 120
4.39 Crossflow contours of mean lateral velocity at $x = 230$. Red and green contourlines show respectively $\overline{w} = +5 \times 10^{-3}$ and $\overline{w} = -5 \times 10^{-3}$. The dashed white line indicates the roughness position. (a) case *NL2.5*, (b) case *NL2.5S*. 121
4.40 Cases *NL6.0* (red circles) and *NL2.5* (blue squares) in the context of the transition criteria proposed by Redford *et al.* (2010) (a) and Bernardini *et al.* (2012) (b). The dashed black lines are straight lines going through the two markers and are plotted to highlight the distance of each case from the critical line (solid black line). 123

5.1 Computational domain. (a) smooth wall, (b) porous wall. 129
5.2 Time history of selected v' Fourier modes. (a) case R2S, (b) case R2P . 133
5.3 Coherent structures during transition for case R2S (Q-criterion), colored by streamwise velocity increasing from blue to red. (a) $t = 350$, (b) $t = 360$, (c) $t = 368$. 134
5.4 Scattering of sound waves for case R2P (contours of pressure: increasing from dark to light). (a) $x - y$ plane, (b) $y - z$ plane 136
5.5 Time history of selected u' Fourier modes. (a) case R2S, (b) case R2P . 137
5.6 Streaks in the u-velocity profile due to transient growth, isosurfaces of u' (cyan: low speed streaks; magenta: high speed streaks). (a) case R2S, (b) case R2P 138
5.7 Comparison of secondary instability mode (1,1) growth rates: — , Smooth wall; – – – , Porous wall. Note that the curves where moved along the temporal axis to help the comparison. 138
5.8 Secondary mode energy profiles: — , Smooth wall; – – – , Porous wall. . 139
5.9 Coherent structures during transition for case R2P (Q-criterion), colored by streamwise velocity increasing from blue to red. (a) $t = 712$, (b) $t = 730$. 140
5.10 Time history of selected v' Fourier modes. (a) case R6S, (b) case R6P. . 141
5.11 Time history of selected v' Fourier modes (Case R6S-6×9). 142
5.12 Contours of v for case R2P during the primary instability stage (increasing from dark to light). 143
5.13 Contours of v during the secondary instability stage (increasing from dark to light). (a) case R2P, (b) case R2S. 144

5.14 Time history of drag coefficient for the $Re^*_\delta = 20000$ cases: — , total drag C_D (case R2S); – – – , skin friction drag C_{Df} (case R2P); – · – pressure drag C_{Dp} (case R2P). 144
5.15 Time history of averaged displacement thickness: — , case R2S; – – – , case R2P. 145
5.16 Time history of averaged momentum thickness: — , case R2S; – – – , case R2P. 146
5.17 Time history of averaged shape factor: — , case R2S; – – – , case R2P. . 146
5.18 Boundary layer averaged u-velocity profiles during transition. (a) case R2S, (b) case R2P. 147
5.19 Variation of Stanton number during transition: — , case R2S; – – – , case R2P. 148
5.20 Time history of selected v' Fourier modes (Case R6S-6×3). 149
5.21 Time history of selected v' Fourier modes. (a) case R2S-9×6, (b) case R2P-9×6. 151
5.22 The effect of the forcing term on the disturbance kinetic energy, a) case R2S, b) case R6S: — , net production of K; – – – , production term; – · – contribution of the forcing term. 153

List of Tables

2.1 Wall temperatures used for the isothermal wall boundary condition used in the different cases analysed. 21
2.2 Filter coefficients. 25
2.3 Filter coefficients. 26

3.1 Cases included in the parametric study. Note that the wall temperature in the hot-wall cases ($T_w = 2.055$ and $T_w = 7.022$) is equal to the adiabatic wall temperature. 32
3.2 Computational grids. N_x, N_y and N_z are the number of points in the streamwise, wall-normal and spanwise directions per block, while n_y^r is the number of points for $0 \leq y \leq h$. The values of Δx for the cases with roughness indicate the grid spacing at the beginning and at the end of the block. The multiple values of Δz indicate spanwise grid spacings at the beginning, at the centre and at the end of the domain. 33
3.3 Coarse computational grids used to to quantify the effects of different grid resolutions. 46
3.4 Separation bubble lengths for the three different configurations considered. 50

4.1 Flow conditions, simulation parameters, grid resolution and sampling information. Note that the wall temperature is equal to the laminar adiabatic wall temperature in all cases. The asterisk in Re_h^* indicates that the kinematic viscosity is taken at the wall. 76
4.2 Computational grids. N_x, N_y and N_z are the number of points in the streamwise, wall-normal and spanwise directions per block, while n_y^r is the number of points for $0 \leq y \leq h$. The values of Δx indicate the grid spacing at the beginning and at the end of the block. The multiple values of Δz indicate spanwise grid spacings at the beginning, at the centre and at the end of the domain respectively. 78

5.1 Simulation parameters. 130

Nomenclature

Roman symbols

a	amplitude in equation 2.12
a_0, a_1, a_2, a_3	filter coefficients (see section 2.2.5)
$a_{n,i}, a_{N_x-n,i}$	filter coefficients (see section 2.2.5)
b_y	wall-normal stretching factor
C	parameter in modified Ducros sensor (see eq. 2.9)
c_f	skin friction coefficient
c_{ph}	phase speed
C_p	specific heat at constant pressure
C_v	specific heat at constant volume
d	pore depth
e	internal energy
E	total energy, $E = e + \frac{1}{2}u_i u_i$
E_ϕ	total energy of Fourier modes in chapter 5
F	non-dimensional frequency, $F = f^* \delta_0^* / U_\infty^*$
f_d	damping function for inflow disturbances (section 2.2.4)
f_s	sampling frequency
g	parameter in $f_d := 1 - \exp\left(-y^p/g^l\right)$ in section 2.2.4
h	roughness height
H	shape factor
i	imaginary unit
J	total time sample in Fourier analysis (eq. 3.1)
k_z	spanwise wavenumber
K	total velocity disturbance energy (see section 5.6)
J	total space sample in Fourier analysis (eq. 3.1)
L_x, L_y, L_z	x, y and z domain lengths respectively
L_f	radius of forcing region in equation 2.13
l	coeffifient in $f_d := 1 - \exp\left(-y^p/g^l\right)$ in section 2.2.4

M	Mach number, or total number of spanwise wavenumbers
N_x, N_y, N_z	number of grid points in x-, y- and z-directions
N	total number of frequencies
n	porosity
n_x^r, n_y^r, n_z^r	number of grid points used to resolve the roughness element in x-, y- and z-directions respectively in x-, y- and z-directions respectively
p	pressure, or coeffifient in f_d function (section 2.2.4)
Pr	Prandtl number
Q	Q-criterion
q_j	heat flux vector
Re	Reynolds number
Re_h	roughness Reynolds number, $Re_h = u_h h/\nu_h$
Re_h^*	modified roughness Reynolds number, $Re_h = u_h h/\nu_w$
Re_{δ^*}	Reynolds number based on the displacement thickness
$Re_{\delta_0^*}$	Reynolds number based on the displacement thickness at the inlet of domain A (see figure 2.1)
$Re_{\tilde{x}^*}$	Reynolds number based on the distance from the flat plate leading edge
S	Sutherland constant
St	Stanton number
T	temperature
T_s	observation period
t	time
u, v, w	cartesian velocities
$\mathbf{U}$	array of conservative variables
$\mathbf{U}_f$	array of filtered conservative variables
u_S	$u_S := \sqrt{(\partial u/\partial y)^2 + (\partial u/\partial z)^2}$
$\tilde{x}^*$	dimensional streamwise distance from the flat plate leading edge
x, y, z	cartesian coordinates

Greek symbols

α	complex streamwise wavenumber, or turbulent wedge half angle in chapter 4
α_i	immaginary part of streamwise wavenumber

	(spatial amplification rate)
β_f	filter parameter (see section 2.2.5)
γ	ratio of specific heats
Δ	similarity scaling factor
δ_{ij}	Kronecker delta
δ^*	displacement thickness
δ_{99}	99% boundary layer thickness
Δt	time-step
$\Delta x, \Delta y, \Delta z$	local grid spacing (streamwise, wall-normal, spanwise directions)
Δx	oscillation period in section 3.2
ϵ	small number in modified Ducros sensor (see eq. 2.9)
η	wall-normal computational grid coordinate, or discretised Fourier frequency
θ	momentum thickness, or shock generator angle
Λ	parameter, see eq. 3.8
λ_z	spanwise wavelength
μ	dynamic viscosity
ν	kinematic viscosity
ξ	streamwise computational grid coordinate, or discretised Fourier spanwise wavenumber
π	ratio of a circle's circumference to its diameter, or phase in eq. 2.12
Π	modified Ducros sensor (see eq. 2.9)
ρ	density
σ	filter parameter
τ	sampling period in Fourier analisys (section 3.2)
ϕ	phase
ψ	inflow disturbances function (see equation 2.12)
ω	circular frequency, $\omega = 2\pi F$
$\boldsymbol{\omega}$	vorticity vector
ω_x, ω_y	streamwise and wall-normal vorticity components
ω_i	immaginary part of the circular frequency (temporal amplification rate)

Other symbols

$\widehat{S}_{\eta,\xi}$	discrete Fourier coefficients from an expansion into frequencies and spanwise wavenumbers (see eq. 3.1)
$\mathcal{A}_\eta$	spanwise wavenumber sum norm of $\lvert\widehat{S}_{\eta,\xi}(x,y)\rvert$ (eq. 3.2)
$\mathcal{I}_\eta$	integrated norm of $\mathcal{A}_\eta$ (see eq. 3.6)
$\mathcal{S}_\phi$	asymmetry parameter (see eq. 4.2)

Subscripts

a	reference to the $M_\infty = 6.0$ cases in chapter 3
ad	adiabatic wall
b	reference to the $M_\infty = 2.5$ cases in chapter 3, or basic flow variable
h	value taken at the edge of the roughness element
i, j, k	tensor indices
in	value at the domain inlet
o	value at the inlet of domain A (see section 2.2.2)
out	value at the domain outlet
r	reference (free-stream) value
rms	root mean square value
w	wall
∞	free-stream value

Superscripts

*	denotes a dimensional variable
$^+$	denotes a variable expressed in wall-units
$'$	denotes a disturbance, or a fluctuating quantity ($u' = \overline{u} - u$)
†	denotes complex conjugate variable

Operators

$\tilde{a}$	variable in a reference frame attached to the flat plate leading edge
$\overline{a}$	time-average of a

$\Re\{a\}$	real part of a

Acronyms

ACM	artificial compression method
DNS	direct numerical simulation
LST	linear stability theory
MPI	message passing interface
SBLI	shock/boundary layer interactions, code name
SL	sinuous lateral (roughness wake mode)
TS	Tollmien-Schlicting
TVD	total variation diminishing
TKE	turbulent kinetic energy
VC	varicose centred (roughness wake mode)
VL	varicose lateral (roughness wake mode)
VT	varicose top (roughness wake mode)

Declaration of Authorship

I, Nicola De Tullio declare that this thesis and the work presented in it are my own and has been generated by me as the result of my own original research. I confirm that:

- this work was done wholly or mainly while in candidature for a research degree at this University;
- where any part of this thesis has previously been submitted for a degree or any other qualification at this University or any other institution, this has been clearly stated;
- where I have consulted the published work of others, this is always clearly attributed;
- where I have quoted from the work of others, the source is always given. With the exception of such quotations, this thesis is entirely my own work;
- I have acknowledged all main sources of help;
- where the thesis is based on work done by myself jointly with others, I have made clear exactly what was done by others and what I have contributed myself;
- parts of this work have been published as:

  De Tullio, N., and Sandham, N. D., Direct Numerical Simulation of Breakdown to Turbulence in a Mach 6 Boundary Layer Over a Porous Surface, *Physics of Fluids*, Vol. 22, No. 9 (094105), 2010.

  De Tullio, N., and Sandham, N. D., Transitional shock-wave/boundary-layer interaction behind a roughness element, *Proceeding of the 28th International Symposium on Shock Waves*, 2011.

  De Tullio, N., and Sandham, N. D., Direct numerical simulations of roughness receptivity and transitional shock-wave/boundary-layer interactions, *NATO RTO-MP-AVT-200*, Paper No. 22, 2012.

Signed: .....

Date: .....

Acknowledgements

The author would like to acknowledge the financial support of the European Union through the Seventh Framework Program with the LAPCAT II and ATLLAS II projects. Computational time provided by the UK Turbulence Consortium (EPSRC Grant EP/G069581/1) on the UK Hector supercomputer is gratefully acknowledged. I am also grateful to the University of Southampton for access to the Iridis2 and Iridis3 supercomputers and I would like to thank Dr. Roderick Johnstone for his invaluable help in code-related issues. Most of all, I would like to acknowledge Prof. Neil D. Sandham for providing guidance, encouragement, support and inspiration.

This thesis would not have been possible without the encouragement and unconditional love of my family; my lovely parents Mercedes and Andrea, my inspirational sister Claudia, the most awesome brother Marco and Jenny, my love.

To Tia Nieves

Chapter 1

Introduction

This thesis is concerned with transition to turbulence in high-speed flows. We start with a general motivation for the study and then review the literature.

1.1 Motivation

In 1883 Osborne Reynolds (Reynolds, 1883) carried out the first detailed investigation into the circumstances that lead to laminar-turbulent transition, providing the basis for more than a century of research into the origins of turbulent motion in fluid flow. Since then, our knowledge on this subject has advanced considerably and, at the same time, we have also learned that transition to turbulence is a complex phenomenon which shows great sensitivity to a myriad of factors (e.g. Reynolds number, external disturbances, pressure gradient, wall roughness or curvature). Morkovin (1991) summarised the known transition scenarios in his transition roadmap, later updated by Morkovin *et al.* (1994) to include the effects of a newly discovered phenomenon called transient growth (see later), in order to obtain a general view of the different ways laminar boundary layers may become turbulent. Morkovin's roadmap, shown in figure 1.1, indicates that after the initial stage of receptivity, which is the process by which external disturbances enter the boundary layer, transition may take different paths depending on the amplitude of the external perturbations. Small disturbances may give rise to boundary layer eigenmodes of instability, which grow exponentially due to linear processes. The most unstable of these modes represents the primary instability and drives the initial stages of transition. These may then be followed by secondary instabilities and/or nonlinear interactions. At low speeds the primary instability is represented

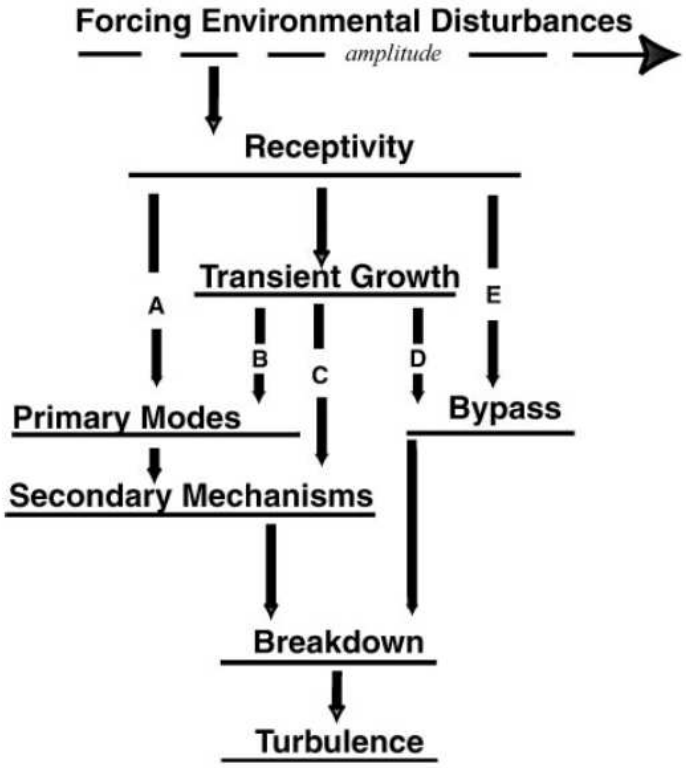

Figure 1.1: Morkovin's roadmap to transition. The letters indicate the different paths to transition. Taken from Morkovin *et al.* (1994).

by the well known Tollmien-Schlicting (TS) waves, whereas for high Mach numbers, typically $M_\infty > 4.0$, Mack modes (see Mack, 1984), i.e. two-dimensional inviscid instabilities of an acoustic nature, are the most unstable boundary layer linear eigenmodes. The initial transition stages may also be dominated by transient growth, which is an algebraic disturbance growth followed by an exponential decay, arising due to the non-normality of the linearised Navier-Stokes operator, and can be explained in physical terms by the so called *lift-up effect* (Landahl, 1980). Transient growth may contribute to the excitation of primary instabilities, or lead to secondary instabilities, or it may bypass the linear stages of transition and lead directly to breakdown to turbulence. A bypass nature of the transition process also appears in the presence of large amplitude external disturbances, in which case the dominant mechanisms seem to be inherently nonlinear and transition occurs following the appearance and growth of elongated streaky structures that give rise to turbulent spots (Emmons, 1951).

Experimental observations indicate that the dominant transition mechanisms in boundary layers can be greatly modified by the presence of localised or distributed

roughness, leading to a significant acceleration of the transition process both in noisy and in quiet environments (Schneider, 2008). Over the years, a number of possible scenarios have been postulated in order to explain these observations. Roughness may enhance the receptivity of boundary layer modes or generate highly unstable wakes thereby introducing new instabilities. Another possible mechanism is the onset of strong transient disturbance growth in the vicinity of the roughness, which might lead directly to nonlinear breakdown to turbulence. Despite numerous research efforts, however, the underlying physical mechanisms responsible for roughness-induced transition remain largely unknown. A deeper understanding of the effects of roughness on the stability of boundary layers is particularly important for high-speed applications, where transition leads to a significant increase in both the skin friction and wall heat transfer, with obvious implications for the design of high-speed vehicles.

Transition at high and low speeds present similarities but also numerous differences. The early experiments of Laufer & Vrebalovich (1960), Demetriades (1960) and Kendall (1975) and the numerical work of Mack (1984) demonstrated that transition mechanisms at high speeds are more complex than at low speeds. The present contribution deals with transition to turbulence in supersonic boundary layers under the effect of small external disturbances, focusing both on the physical mechanisms leading to early transition in the presence of roughness and on the processes responsible for the stabilisation of high-speed boundary layers by the use of porous coatings. An overview of the available literature on the subject of transition in supersonic and hypersonic flows is presented in the following sections. Some important results obtained in the framework of low speed transition will also be considered in order to help the discussion.

1.2 Transition due to small external disturbances

Following the receptivity process, the early stages of boundary layer transition to turbulence are dominated by the linear growth of unstable eigenmodes. The existence of sinusoidal disturbances in the boundary layer prior to transition was first postulated by Rayleigh (1878, 1880) and demonstrated experimentally by Schubauer & Skramstad (1948). Meanwhile, the research efforts of Tollmien and Schlichting led to the development of the viscous theory of boundary layer instability, so that, as already mentioned, the waves of the first unstable mode are often referred to as Tollmien-Schlichting waves (see Schlichting & Gersten, 2000).

In the framework of compressible flows the existence of instability modes was experimentally demonstrated by Laufer & Vrebalovich (1960). On this subject, the theoretical investigations carried out by Lees & Lin (1946) are considered one of the most important early advances. They developed a two-dimensional asymptotic theory and, through inviscid calculations, discovered the importance of the generalised inflection point, defined as the point where $\partial/\partial y\,(\rho\partial u/\partial y) = 0$. Inviscid instability increases with Mach number as the generalised inflection point moves away from the wall, while viscous instability decreases and eventually disappears for two-dimensional waves at $M_\infty > 3$, so that viscosity has a stabilising effect in high speed flows (Mack, 1984). Mack (see Mack (1984) and references therein) discovered the existence of higher acoustic modes appearing in supersonic boundary layers. He showed that the first of the additional modes, a two-dimensional wave known as the second (or Mack) mode, is the most unstable boundary layer mode for $M_\infty > 4$. For lower supersonic Mach numbers linear stability theory (LST) predicts that three-dimensional (oblique) first-mode waves are more unstable than two-dimensional waves, whereas for subsonic compressible and incompressible flows two-dimensional waves are the most unstable. Mack also analysed the effect of wall temperature, showing that cooling damps the first mode growth, in agreement with what was previously found by Lees (1947), while destabilising the higher modes. Therefore cooling, in fact, destabilises the boundary layer at high speeds. A complete review of the main results obtained by the compressible LST along with its mathematical formulation can be found in Mack (1984).

The results obtained by analysis and computation of the linearised stability equations were validated through experiments and direct numerical simulations (DNS) of the Navier-Stokes equations. For example, the higher modes of Mack were found experimentally by Kendall (1975) and the theoretical prediction that the second mode constitutes the primary instability for $M_\infty > 4$ was corroborated by experiments and DNS (Lysenko & Maslov, 1984; Erlebacher & Hussaini, 1990). Lysenko & Maslov (1984) also verified the effect of wall cooling on the first and second modes.

The use of experiments and accurate numerical simulations, however, is not limited to the assessment of LST predictions. A number of important discoveries on transition in high-speed boundary layers came from temporal and spatial DNS studies as well as from experiments. This is especially true for those stages of the transition process dominated by nonlinear interactions, where linear theories are no longer applicable. In a series of experiments in Mach 6 quiet wind tunnels Chokani and co-workers (Chokani, 1999, 2005; Wilkinson, 1997) investigated the

nonlinear evolution of Mach modes over flared cones using bispectral analysis. All the measurements were carried out in the layer of the maximum r.m.s. voltage. It was found that the Mack mode self interaction is the first nonlinearity arising, which enables energy exchange between the Mack mode and the mean flow and leads to the first harmonic. However, the experiments of Bountin *et al.* (2008) showed that low frequency nonlinear interactions at the edge of the boundary layer are the first nonlinear processes taking place. These interactions are present before any sign of nonlinearity appears in the layer of maximum r.m.s. voltage fluctuation. Moreover, when nonlinear processes disappear from this layer nonlinear interactions are still active above and below it.

At low supersonic Mach numbers nonlinear interactions of three-dimensional primary instability modes can be responsible for breakdown to turbulence without resorting to a secondary instability. Kosinov *et al.* (1990); Fasel *et al.* (1993); Sandham & Adams (1993), found that the most unstable eigenmode in a $M_\infty = 2.0$ laminar boundary layer is three-dimensional, in agreement with what was predicted by the linear theory. This particular behaviour was further studied by Chang & Malik (1994) and Sandham *et al.* (1995). It was found that the nonlinear interaction of oblique primary instability waves sustains the growth of quasi-streamwise vortices. These vortices generate high shear layers which roll-up into additional vortices leading to breakdown to turbulence.

At higher Mach numbers nonlinear interactions of the two-dimensional primary instability modes clearly cannot lead to a three-dimensional phenomenon like turbulence, so that growth of less unstable oblique eigenmodes or excitation of additional three-dimensional waves is needed. The question is whether the evolution of three-dimensionality in high speed and incompressible flows follows similar paths, given that both types of flow have two-dimensional primary instabilities. The late stages of breakdown to turbulence in incompressible flows are now fairly well understood. The secondary instability theory says that once the TS waves reach high amplitudes the boundary layer becomes unstable to three-dimensional waves (Herbert, 1988). This stage of the transition process is characterised by the appearance of Λ-shaped vortices located near the boundary layer edge. At this point, breakdown to turbulence can occur in three possible scenarios, the fundamental or K-type, the subharmonic or H-type and the detuned breakdown (Herbert, 1988). In the fundamental breakdown the secondary instability waves have the same streamwise wavenumber as the primary waves and the Λ-shaped vortices are aligned. In the subharmonic breakdown the streamwise wavenumber of the secondary instability doubles that of the primary wave and the Λ-shaped vortices are staggered. Finally,

in the detuned breakdown the secondary instability is detuned from the primary wave and presents streamwise wavelengths in between those of the fundamental and subharmonic waves.

The secondary instability of supersonic and hypersonic laminar boundary layers was first investigated by El-Hady (1992), Masad & Nayfeh (1990, 1991), Erlebacher & Hussaini (1990) and Ng & Erlebacher (1992). Erlebacher & Hussaini (1990) carried out temporal direct numerical simulations of the fundamental secondary instability of the $M_\infty = 4.5$ flow over a flat-plate. The results suggest that the K-type breakdown to turbulence is possible in compressible boundary layers and presents similarities with its incompressible counterpart. Overall, the effect of Mach number is to reduce the subharmonic growth rate (Masad & Nayfeh, 1990, 1991; Ng & Erlebacher, 1992). The secondary instability growth rates increase with an increasing amplitude of the primary instability and, at high Mach numbers ($M_\infty = 4.5$), secondary instabilities growing from the second (Mack) mode primary instability dominate those originating from the first mode primary instability (Ng & Erlebacher, 1992). At low supersonic Mach numbers the secondary instability shifts from subharmonic to fundamental as the amplitude of the primary waves increases (Chang & Malik, 1994), following the same trend found for incompressible flows.

A thorough numerical investigation on boundary layer transition at $M_\infty = 4.5$ was carried out by Adams & Kleiser (1996) using the temporal DNS approach. They considered the secondary instability generated by a Mack mode primary wave with streamwise wavenumber $\alpha = 2.52$ together with white noise. In agreement with Ng & Erlebacher (1992) no evidence of the fundamental type of transition was found, so that the attention was focused on the subharmonic secondary instability. Flow visualisations revealed the formation of Λ-shaped vortices close to the boundary layer edge. The Λ-vortices generate Y-shaped shear layers, *"located below and between two neighbouring vortices"* (Adams & Kleiser, 1996), which break up to give additional vortices above and below the critical layer, thereby being responsible for the first stages of breakdown. A second type of shear layers is created by the Λ-vortices at their symmetry plane and close to the boundary layer edge. The break up of this shear layers is responsible for the last stages of breakdown.

1.3 Receptivity mechanisms

Transition to turbulence starts when disturbances interact with the boundary layer causing the appearance of eigenmodes of instability, a process called receptivity which was first proposed by Morkovin in 1958 (see Morkovin, 1991). Sources of disturbance can be found in the free-stream as entropy, vorticity or acoustic waves (Kovasznay, 1953; Chu & Kovasznay, 1958), and on the wall as, for instance, localised roughness or curvature. In this section attention will be focused on the interaction of free-stream disturbances with the boundary layer. Over the past few decades, numerous fruitful investigations have been carried out into receptivity mechanisms and transition in general at low speeds (Kachanov, 1994; Saric *et al.*, 2002). In contrast, investigations carried out in the field of high speed flows have been much less productive and the problem of receptivity and transition is still open. This is mainly due to the level of complexity shown by the transition mechanisms at high speeds. Moreover, the high background noise level of most wind tunnels tends to promote bypass transition and makes the study of the linear receptivity mechanisms and the evolution of small internal disturbances, which would take place during flight, difficult. Nevertheless, successful experiments have been carried out which have helped in understanding some features of the receptivity at high speeds. Kendall (1975) performed experiments on the stability of supersonic and hypersonic boundary layers revealing the importance of sound radiation as a source of disturbances at high speeds and found evidence of the higher modes of instability discovered by Mack (see Mack, 1984), which were also found experimentally by Kosinov *et al.* (1990) and Stetson & Kimmel (1992) among others. Kendall (1975) and Demetriades (1989) reported that fluctuations of all frequencies were found to grow in a region where no growth was expected, between the leading edge and the predicted location of instability. More recently, Maslov *et al.* (2001) studied the receptivity of a flat plate boundary layer at $M_\infty = 5.92$ and found that acoustic waves interact with the leading edge and give rise to boundary layer eigenmodes. The receptivity was found to be dependent on the inclination angles of the acoustic radiation. Graziosi & Brown (2002) analysed the stability and transition of an $M_\infty = 3.0$ flat plate boundary layer and noted a substantial similarity between the wavelengths of the free-stream acoustic waves and the first unstable boundary layer mode. This feature may help the conversion from forced disturbances to instability eigenmodes and is in contrast with what is observed in low speed flows, where the wavelength of any TS wave is much shorter than that of free-stream sound waves. Measurements in the region close to the leading edge of the plate indicated that the amplitude of the excited eigenmodes

in that region were from 6 to 10 times larger than the corresponding free-stream disturbances.

Receptivity problems have also been approached theoretically and numerically. In connection with the experiments of Kendall (1975) and Demetriades (1989), Fedorov & Khokhlov (2001) analysed the growth of eigenmodes in the vicinity of the leading edge of a flat plate in a hypersonic boundary layer using an asymptotic method. They found that there exist two discrete modes, mode F and mode S as later denoted by Fedorov (2003), with phase speeds close to those of the external fast and slow acoustic waves respectively, near the leading edge. This synchronisation is considered to be responsible for the strong excitation of the boundary layer instabilities in the leading edge region. Downstream of the leading edge these two modes are synchronised with external entropy and vorticity waves, which, therefore, can be responsible for the continued excitation of boundary layer instabilities. Further downstream, a synchronisation between mode F and mode S leads to the growth of either of these two modes, as one loses energy to the other (inter-modal exchange). This growth was found to be associated with the Mack mode instability. Leading edge receptivity mechanisms were found by Fedorov (2003) to be influenced by the angle of incidence of the acoustic waves, in accordance with Maslov *et al.* (2001).

The receptivity of high-speed boundary layers to free-stream acoustic waves was also studied by Ma & Zhong (2003*a*,*b*) and Zhong & Ma (2006) using DNS and LST. Their work suggests the existence of a number of stable modes (denoted as mode I, mode II, etc) and a single unstable mode which comprises regions of first, second and higher modes of instability. The stable modes can grow substantially by resonating with the free-stream fast acoustic waves and, in particular, mode I was found to play a crucial role in the Mack mode excitation, either by transferring energy from the fast acoustic weaves to the Mack mode or by providing a link between first and second instability modes, in a mechanism similar to the inter-modal exchange proposed by Fedorov & Khokhlov (2001). A clear indication of the importance of mode I in the receptivity process was provided by the results obtained by Zhong & Ma (2006), which show that Mack modes do not grow until becoming synchronised with mode I, despite being in a region of instability according to LST. As pointed out by Forgoston & Tumin (2005), who showed that Fedorov's mode S also contains regions of the first, second and higher instability modes, the unstable mode reported by Ma & Zhong (2003*a*,*b*) is equivalent to mode S and modes I is equivalent to mode F.

Boundary layer modes can also be excited by free-stream vortical disturbances. This problem was analysed Ricco & Wu (2007), who concentrated on small amplitude convected-gust type perturbations. The results show that the interaction of free-stream turbulence with the boundary layer gives rise to Klebanoff modes and can lead to the excitation of TS waves.

1.4 Transient growth and bypass transition

In his roadmap to turbulence, Morkovin (1991) labelled as bypass transition all the transition phenomena that do not show the slow linear amplification of disturbances described in Section 1.2. Initially bypass transition was thought to be an exclusively nonlinear process, caused by the excitation of high amplitude disturbances, which grow nonlinearly having bypassed the linear stages (Reshotko, 2001). This point of view was abandoned when a number of studies demonstrated that small disturbances can be substantially amplified by the transient growth mechanism, leading directly to the nonlinear stages of transition, see for example Butler & Farrel (1991). Transient growth arises from the so called *lift-up effect* caused by slightly damped, highly oblique modes. This mechanism leads to algebraic disturbance growth followed by viscous exponential decay (Reshotko, 2001) and is mathematically explained by the non-normal character of the incompressible and compressible linearised Navier-Stokes operator. The *lift-up effect* was first recognised by Landahl (1975, 1980) when studying the algebraic growth of streamwise disturbances in incompressible inviscid flows in the absence of an inflection point, which was first discovered by Ellingsen & Palm (1975).

The literature on transient growth for compressible flows is very limited. The first temporal analysis of transient growth in compressible flows under the parallel flow approximation was carried out by Hanifi *et al.* (1995), who found that the physical mechanism behind transient growth in compressible flows is Landhal's *lift-up effect*. In agreement with the incompressible results they found that the maximum transient growth scales with Re^2 and the time at which this happens scales with Re, although the energy levels attained increase with increasing Mach number. Their results show that contribution to transient growth comes mostly from steady, slightly-damped streamwise vortices, in agreement with the result reported in almost all optimal transient growth studies, suggesting that streamwise vortices are the optimal initial disturbances for both incompressible and compressible flows. Hanifi & Henningson (1998) showed that there is a compressible

counterpart to the incompressible algebraic instability of streamwise disturbances discovered by Ellingsen & Palm (1975), which is also caused by the *lift-up effect*.

A spatial theory of optimal disturbances in compressible flows was developed by Tumin & Reshotko (2001), who then modified it to incorporate non-parallel effects (Tumin & Reshotko, 2003). They found that maximum transient growth is associated with steady streamwise vortices and that cooling decreases the overall amplification in parallel supersonic flows. When considering non-parallel effects the overall energy amplification was found to be almost insensitive to wall temperature. In subsonic flows cooling was found to destabilize parallel and non-parallel boundary layers. Farrel & Ioannou (2000) studied non-modal growth of disturbances in compressible constant shear and found that compressibility can increase transient growth in viscous flows. Recently, Zuccher *et al.* (2006) showed that the choice of the energy norm used to evaluate transient growth, and hence define the optimal disturbances, is critical in supersonic flows for Reynolds numbers (based on the flat plate length) of the order of 10^3. Wall cooling was found to destabilise the transient growth process in the flow over a sphere at $M_\infty = 6$.

As already mentioned, transient growth can lead to high amplitude disturbances, promoting the bypass transition scenario. One of the most notable characteristics of bypass transition is the formation of turbulent spots preceding the final breakdown to turbulence. Merging of these spots finally leads to a turbulent boundary layer, and hence it is important to understand how they evolve as they convect downstream in order to be able to predict the length of the transition region. Measurements of the propagation of turbulent spots in compressible boundary layers showed that the effect of compressibility is to decrease the lateral spreading angle (Clark *et al.*, 1994; Mee, 2002; Fiala *et al.*, 2006). The first numerical simulations of the evolution and merging of turbulent spots in compressible boundary layers were performed by Krishnan & Sandham (2006*a*,*b*). Their investigations provide a detailed representation of the three-dimensional structure of compressible turbulent spots, which are characterised by the presence of hairpin and streamwise vortices. They also showed that compressibility decreases the lateral spreading of the turbulent spot, thereby increasing the length of the transition region, in agreement with experiments. In a recent study Redford *et al.* (2012) showed that the main lateral turbulence spreading mechanisms in high speed spots are the lateral displacement of core structures due to the presence of spanwise jets at the sides of the spot and the destabilisation of the surrounding laminar fluid by the instability of these jets. They also reported a reduction of spreading half angle with increasing Mach number and decreasing wall temperature.

1.5 Roughness-induced transition

Experiments have shown that localised and distributed roughness can cause early transition to turbulence in both subsonic and supersonic boundary layers (Tani & Sato, 1956; Klebanoff & Tidstrom, 1972; Corke *et al.*, 1986; Fujii, 2006; Schneider, 2008). Recently, observations of boundary layer transition to turbulence occurring on the Space Shuttle Endeavour during re-entry (Horvath *et al.*, 2012) have provided evidence of the importance of roughness effects on transition in high speed applications. At $M_\infty = 5.8$, wall thermography revealed the occurrence of asymmetric transition on the windward side of the vehicle due to the presence of an isolated roughness element near the tip, while at higher Mach numbers the boundary layer was found to remain fully laminar, despite the high Reynolds numbers. The observations made over the observable part of the re-entry trajectory suggested that boundary layer transition to turbulence was mainly driven by roughness effects, highlighting the importance of roughness in transition at high speeds.

The influence of discrete two-dimensional roughness elements on incompressible boundary layers was investigated by Klebanoff & Tidstrom (1972) who provide an explanation for the early transition observed based on the modified stability of the tripped boundary layer. Experimental observations of transition induced by three-dimensional roughness, however, could not be explained by a similar argument (see Reshotko & A. (2004) and reference therein). Recently, it was recognised that the "bypass" nature of the transition to turbulence observed in the presence of surface roughness may be linked to the transient growth of stable boundary layer eigenmodes (Reshotko, 2001). The flow behind small three-dimensional localised roughness elements is characterised by the presence of counter-rotating streamwise vortices (Gaster *et al.*, 1994; Joslin & Grosch, 1995; Rizzetta & Visbal, 2007), which can be seen as roughness induced disturbances originating from a superposition of stable vorticity modes belonging to the continuous spectrum of the linearised Navier-Stokes operator (Tumin & Reshotko, 2005). The non-normality of these modes can potentially lead to strong algebraic growth and breakdown to turbulence. The transient growth route to turbulence in the context of roughness-induced transition has been investigated both numerically and experimentally mainly for incompressible flows. Experiments have shown that the disturbances introduced by roughness elements experience transient growth, although their evolution does not agree well with the optimal disturbance theory predictions (White, 2002; White, E. B. and Rice, J. M and Gökhan Ergin, F., 2005;

Downs *et al.*, 2008). Denissen & White (2009) showed that realisable roughness-induced disturbances are neither optimal nor properly described by linear receptivity theory. In the context of supersonic flows Wang & Zhong (2008) reported DNS results of an $M_\infty = 5.92$ flow over a flat plate with small three-dimensional surface roughness, showing only weak transient growth. The occurrence of transient growth is not limited to roughness-induced disturbances. In fact, near abrupt mean flow changes (i.e. near the roughness), the energy of boundary layer perturbations becomes redistributed into the modes of the new basic flow. These modes may then experience transient growth and lead to breakdown to turbulence.

Roughness can affect instability and transition by a number of different mechanisms. Balakumar (2008) has recently shown that the interaction of acoustic waves with roughness elements can excite disturbances "tuned" with boundary layer eigenmodes, following a mechanism originally proposed by Goldstein (1983, 1985) and studied theoretically by Crouch (1992) and Choudhari & Street (1992) for incompressible flows. The influence of small two-dimensional roughness elements on the stability of an $M_\infty = 3.5$ boundary layer subjected to acoustic disturbances was analysed by Balakumar (2009), who reported no amplification of boundary layer modes by the roughness. In supersonic flows additional sources of disturbances can also be the roughness induced shocks. Direct numerical simulations carried out by Marxen *et al.* (2010) for an $M_\infty = 4.8$ boundary layer flow over a two-dimensional isolated roughness element provide some evidence of the excitation of additional stable modes downstream of the roughness, believed by the authors to originate from the weak shock induced by the roughness. The results show that two-dimensional roughness can amplify disturbances for certain frequencies and make other frequencies stable. Examples of delayed transition due to small roughness can be found in the literature for both supersonic (Fujii, 2006; Saric *et al.*, 2004) and subsonic (Fransson *et al.*, 2005, 2006; Saric *et al.*, 2008) flows. Interest in the stabilising effect of roughness originated from the work of Cossu & Brandt (2002) who showed that TS waves can be stabilised by artificially generated finite amplitude optimal streaks.

As the height of the roughness increases different effects may become dominant. Highly unstable wakes might form behind the roughness elements, the instability of which can supersede the boundary layer instability. The importance of the roughness-induced shear layers in the transition to turbulence of tripped boundary layers was recognised both in experiments and DNS (Tani & Sato, 1956; Redford *et al.*, 2010). Redford *et al.* (2010) analysed the effects of smooth bumps on transition in supersonic boundary layers using DNS and found that transition is

promoted by localised roughness, provided the roughness Reynolds number $Re_h = u_h h/\nu_h$, where U_h and ν_h are the streamwise velocity and kinematic viscosity taken at $y = h$ in the corresponding clean flat plate boundary layer, exceeded a critical value which increases as the parameter $M_k T_\infty/T_w$ increases, where M_k is the Mach number calculated at the roughness edge. Their roughness-induced transition map suggests a critical value of $Re_h = 300$ for $M_k T_\infty/T_w = 0$. These findings were confirmed by Bernardini *et al.* (2012), who proposed a modified version of roughness Reynolds number $Re_h^* = u_h h/\nu_w$, with the kinematic viscosity taken at the wall. This new criterion incorporates compressibility effects in a single parameter and has a constant critical value of $Re_h^* = 460$.

Choundhari and co-workers (Choudhari *et al.*, 2009, 2010, 2012; Kegerise *et al.*, 2012) analysed the growth of instabilities in the wake of roughness elements with heights of the order of the local boundary layer thickness, both experimentally and through linear stability calculations. The results indicate the presence of different instability modes, even (or varicose) and odd (or sinuous), which can grow substantially and drive the transition process. Both sinuous and varicose modes can be dominating under different flow conditions. LST results and experimental data were found to be in good agreement.

For even larger roughness elements an absolute instability might take place introducing high amplitude flow unsteadiness. This possibility was investigated by Chang *et al.* (2010, 2011) who simulated the flow over large roughness elements and cavities. Roughness elements with heights approaching the local boundary layer thickness were found to introduce small oscillations in the wake region, while for bigger heights these oscillations led to early breakdown to turbulence. The results suggest that the origin of the wake oscillations might be an absolute instability developing in the separation bubble upstream of the roughness. Cavities, on the other hand, were found to be less effective in destabilising the boundary layer.

1.6 Transition over porous surfaces

Porous surfaces represent a new passive method for transition control (Fedorov, 2011). Porous materials have been found to stabilise the boundary layer, especially at supersonic and hypersonic speeds. The possibility of delaying transition in high-speed flows is very appealing to the hypersonic community since it would mean being able to design lighter thermal protection systems, with obvious advantages.

The first linear stability calculations for hypersonic boundary layers over porous surfaces were presented by Fedorov *et al.* (2001), using a model to account for the flow inside the pores. Considering thin pores (about 10 to 20 pores per wavelength of the Mack mode) and porosities up to $n = 0.6$ they were able to demonstrate the damping effect of porous coatings on the Mack mode. They reported that this effect decreases as the wall temperature increases and is enhanced by increasing the pore depth up to a value of $d/\delta^* \approx 0.3$, above which the growth rate of the Mack mode reached a limiting constant value. For $M_\infty = 6$, $T_w/T_{ad} = 0.2$, where T_{ad} is the adiabatic wall temperature, and $n \approx 0.2$ they found that the growth rate of the Mack mode reduces by about a factor of two. Boundary layer transition delay due to effects of porosity was also observed experimentally by Rasheed *et al.* (2002) for the $M_\infty = 5$ boundary layer flow over a cone. Additional experimental and theoretical studies were reported by Maslov (2003). These studies confirmed the stabilizing effect of pores and predicted that the damping effect increases for increasing Knudsen number. Fedorov *et al.* (2003) demonstrated that similar results can be achieved with a fibrous absorbent material. Nonlinear mode interactions were experimentally investigated by Chokani *et al.* (2005) for the $M_\infty = 6$ flow over a cone using bispectral analysis. The harmonic Mack mode resonance was found to be completely suppressed, while the subharmonic resonance was drastically reduced. The amount of experimental results available for transition over porous surfaces in high-speed flow is very limited. Theoretical models can help understand the flow physics but first need to be verified against reliable results. For this reason researchers have recently begun focusing on direct numerical simulations to study the effects of pores on boundary layer transition. Egorov *et al.* (2007) carried out 2D direct numerical simulations on hypersonic transition over a flat plate, a cone and a compression ramp, all with porous surfaces. The pores were modeled using the boundary conditions proposed by Fedorov *et al.* (2001). The results showed higher growth rates than those observed in experiments and predicted by LST. In the flat plate case it was observed that the pores reduce the amplitude of modes F and S, found by Fedorov and co-workers (Fedorov & Khokhlov, 2001; Fedorov, 2003) in their receptivity studies. Brés *et al.* (2008) investigated the interaction of acoustic disturbances with micro-cavities without the external boundary layer flow and reported the appearance of near wall resonant acoustic modes coming from the interaction of scattered waves. Sandham & Lüdeke (2009) and Wartemann *et al.* (2009) carried out 2D and 3D temporal direct numerical simulations of the $M_\infty = 6$ flat plate boundary layer over a porous surface, where the pores were resolved. They found that the calculated growth rates differ from the LST predictions by about 6%. In agreement with Fedorov

et al. (2001) they found that there is a limiting value of the pore depth, which depends on the pore diameter, above which the Mack mode growth rate remains unchanged.

1.7 Objectives and thesis outline

The effects of roughness on the laminar-turbulent transition at high speeds are currently not well understood. The main objective of this study is to gain some new insight into the mechanisms driving the different stages of small-disturbance transition to turbulence in the presence of roughness. The following are more detailed aims of the present work:

- To validate a high-order multi-block approach for the accurate numerical simulation of transition and turbulence in sharp-edge geometries
- To capture the instability modes growing in the wake of roughness elements using Navier-Stokes based simulations in connection with the use of Fourier analysis
- To investigate the receptivity of small disturbances in the presence of roughness in supersonic boundary layers
- To analyse numerically the structure of turbulent wedges developing downstream of the roughness element and to investigate the effect of an oblique shock impingement on their evolution
- To follow the temporal evolution of disturbances in a $M_\infty = 6.0$ porous wall boundary layer all the way until the onset of weakly nonlinear interactions

The present contribution provides the first thorough numerical investigation of roughness-induced receptivity, linear instability and breakdown to turbulence in supersonic boundary layers. Mechanisms responsible for the receptivity of small disturbances in the presence of roughness at $M_\infty = 6.0$ and $M_\infty = 2.5$ are clarified, showing that the receptivity process can modify substantially the linear instability of the wake behind the roughness element. Roughness wake modes are classified and the most dangerous under different conditions are identified. A detailed numerical investigation into the evolution of turbulent wedges downstream of a roughness element is given. Finally, the damping effect of porous surfaces

on the secondary instability growing from a Mack mode primary instability in an $M_\infty = 6.0$ boundary layer is shown for the first time.

The thesis is organised as follows. Chapter 2 deals with the mathematical formulation and the numerical considerations. In particular, the governing equations are introduced and the high-order multi-block strategy employed is explained and validated. Chapter 3 gives a discussion of the results obtained for the parametric study of the receptivity of small disturbances in the presence of roughness. It starts with the details of the numerical simulations carried out, followed by a description of the stability characteristics of $M_\infty = 6.0$ and $M_\infty = 2.5$ clean flat plate boundary layers. The $M_\infty = 6.0$ and $M_\infty = 2.5$ receptivity results are presented after an analysis of the influence of grid resolution and level of filtering. The nonlinear stages of the roughness-induced transition to turbulence are discussed in chapter 4, focusing on the breakdown mechanisms and the evolution of a turbulent wedge downstream of the roughness element. This chapter also deals with the effects of an oblique shock impingement onto the transitional boundary layer. Finally, chapter 5 focuses on a new passive method for transition control in high-speed boundary layers based on the use of porous materials to damp the growth of Mack mode instabilities. The thesis ends with the conclusions drawn from the results presented and with a list of suggestions for further study.

Chapter 2

Equations and methods

2.1 The Navier-Stokes equations

The Navier-Stokes equations for a Newtonian fluid with viscosity μ are obtained by imposing conservation of mass, momentum and energy. The result is a system of nonlinear partial differential equations which in dimensionless form can bewritten as

$$\begin{aligned} \frac{\partial \rho}{\partial t} + \frac{\partial \rho u_j}{\partial x_j} &= 0 \\ \frac{\partial \rho u_i}{\partial t} + \frac{\partial \rho u_i u_j}{\partial x_j} + \frac{\partial p}{\partial x_i} &= \frac{\partial \tau_{ij}}{\partial x_j} \\ \frac{\partial \rho E}{\partial t} + \frac{\partial \left(\rho E + p\right) u_i}{\partial x_i} &= -\frac{\partial q_i}{\partial x_i} + \frac{\partial u_i \tau_{ij}}{\partial x_j}. \end{aligned} \tag{2.1}$$

The symmetric viscous stress tensor, τ_{ij}, is defined as

$$\tau_{ij} = \frac{\mu}{Re}\left(\frac{\partial u_j}{\partial x_i} + \frac{\partial u_i}{\partial x_j} - \frac{2}{3}\frac{\partial u_k}{\partial x_k}\delta_{ij}\right), \tag{2.2}$$

where δ_{ij} is the Kronecker delta function defined as $\delta_{ij} = 1$ for $i = j$ and $\delta_{ij} = 0$ for $i \neq j$.

The properties of the fluid and the components of the heat flux vector (q_j) are calculated considering the equation of state and Fourier's law of heat conduction, given respectively by:

$$p = (\gamma - 1)\left(E - \frac{1}{2}\rho u_i u_i\right) = \frac{1}{\gamma M_r^2}\rho T \tag{2.3}$$

and

$$q_j = -\frac{\mu}{(\gamma-1)M_r^2 PrRe}\frac{\partial T}{\partial x_j}. \tag{2.4}$$

The non-dimensional parameters involved in the calculations are Reynolds number (Re), Prandtl number (Pr), Mach number (M_r) and ratio of specific heats (γ), defined as:

$$Re = \frac{\rho_r^* u_r^* l_r^*}{\mu_r^*}, \quad Pr = \frac{C_p^* \mu^*}{\lambda^*}, \quad M_r = \frac{u_r^*}{\sqrt{\gamma R^* T_r^*}} \quad and \quad \gamma = \frac{C_p^*}{C_v^*}, \tag{2.5}$$

where C_p^* and C_v^* are the specific heats at constant pressure and constant volume, R^* is the specific gas constant and λ^* is the thermal conductivity. Note that the subscript r refers to reference values whereas the asterisks (*) denote dimensional variables. The reference values for velocity (u_r^*), density (ρ_r^*), temperature (T_r^*) and dynamic viscosity (μ_r^*) are taken at the free stream. In the present work the reference length (l_r^*) is taken as the displacement thickness of the initial laminar similarity profile. The principal non-dimensional variables are defined as follows,

$$t = \frac{t^* u_r^*}{l_r^*}, \quad x_i = \frac{x_i^*}{l_r^*}, \quad \rho = \frac{\rho^*}{\rho_r^*}, \quad u_i = \frac{u_i^*}{u_r^*}, \tag{2.6}$$

$$p = \frac{p^*}{\rho_r^* u_r^{*2}}, \quad E = \frac{E^*}{u_r^{*2}}, \quad T = \frac{T^*}{T_r^*}, \quad \mu = \frac{\mu^*}{\mu_r^*}. \tag{2.7}$$

The molecular viscosity of a Newtonian fluid is, by definition, only dependent upon temperature and pressure. Here, only its variation with temperature is taken into account and is calculated by applying Sutherland's law,

$$\mu = T^{\frac{3}{2}} \frac{1 + S^*/T_r^*}{T + S^*/T_r^*}, \tag{2.8}$$

where, $S^* = 110.4$ K is the Sutherland constant for air. For all the numerical simulations carried out in this work $Pr = 0.72$ and $\gamma = 1.4$ have been considered, while $T_r^* = 273.15$ K for the roughness -induced transition cases and $T_r^* = 216.65$ K for the porous wall cases.

2.2 Numerical strategy

2.2.1 The core of the *SBLI* code

The calculations were carried out using the Southampton in-house *SBLI* code, a high order finite-difference code which solves the compressible Navier-Stokes equations. The code employs a fourth-order central difference scheme to calculate derivatives at internal points, while close to boundaries a stable boundary treatment by Carpenter *et al.* (1999) is applied, giving overall fourth-order accuracy. Time integration is based on a third-order compact Runge-Kutta method (Wray, 1986). An entropy splitting approach by Sandham *et al.* (2002) is used to split the inviscid flux derivatives into conservative and non-conservative parts, thereby improving stability. The code is made parallel using the *MPI* library. Details on the implementation of the numerical schemes can be found in Li (2003) and Jones (2008). A *TVD* shock capturing scheme and the artificial compression method (ACM) of Yee *et al.* (1999), coupled with the Ducros sensor (Ducros *et al.*, 1999), are implemented in the code to handle shocks and contact discontinuities. Here, we use a modified version of the Ducros sensor given by

$$\Pi = \frac{(\nabla \cdot \mathbf{u})^2}{(\nabla \cdot \mathbf{u})^2 + C(\boldsymbol{\omega})^2 + \epsilon}, \tag{2.9}$$

where $\epsilon = 10^{-10}$ is a small positive number used to avoid division by zero in regions where both $\nabla \cdot \mathbf{u}$ and $\boldsymbol{\omega}$ are zero. As the sensor proposed by Ducros *et al.* (1999) was not designed for boundary layers undergoing transition to turbulence, here we add a parameter C that controls how deep inside the boundary layer the shock capturing scheme is allowed to act. This modification is needed in order to capture contact discontinuities occurring in the region of breakdown to turbulence, where density gradients are high due to shear layer roll-up. A value of $C = 0.1$ was found to lead to a good resolution of contact discontinuities while not introducing noticeable numerical dissipation in regions of turbulent flow.

To model the sharp geometries considered, both roughnesses and pores, a multi-block version of the code was used, which was extensively validated by Yao *et al.* (2009). More details on the validation are provided at the end of this chapter.

2.2.2 Computational geometry for the roughness cases

The geometry of the problem under consideration consists of a flat plate with a sharp-edged rectangular isolated roughness element. The analysis of supersonic roughness-induced transition is divided into two complementary parts. In the first part, attention is focused on the receptivity and initial linear growth of disturbances, whereas in the second part we analyse the nonlinear stages of transition leading to the development of a turbulent wedge downstream of the roughness. Figure 2.1 shows a sketch of the configurations analysed. The difference in computational requirements between the two stages of the investigation dictates the use of two different numerical grids. Domain A was used for the simulations of the complete transition process while domain B was used for the receptivity study. Both computational domains are placed downstream of the flat plate leading edge and do not include the associated weak shock.

The roughness element is placed at a non-dimensional distance $x_h = x_h^*/\delta_0^* = 50$ from the inflow of domain A. Here, x_h^* is the dimensional streamwise position of the roughness leading edge in a reference frame positioned at the inflow of domain A and δ_0^* is the laminar displacement thickness at the same streamwise position. The laminar displacement thickness (δ^*) and the boundary-layer thickness (δ_{99}) grow in the streamwise direction according to the following

$$\begin{aligned} \frac{\delta^*(\tilde{x}^*)}{\delta_0^*} &= \Delta\frac{\sqrt{2Re_{\tilde{x}^*}}}{Re_{\delta_0^*}}, \\ \frac{\delta_{99}(\tilde{x}^*)}{\delta^*(\tilde{x}^*)} &= \frac{\Delta_{99}}{\Delta}, \end{aligned} \tag{2.10}$$

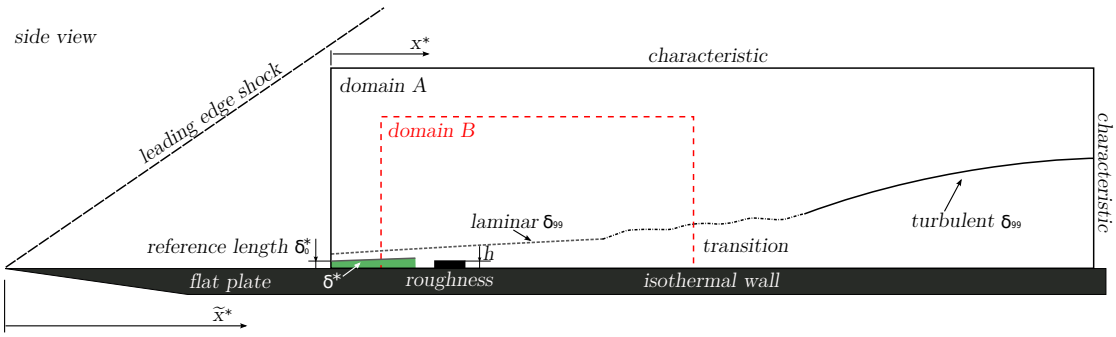

Figure 2.1: Computational domain and boundary conditions. Domain A is used for simulations of the complete transition process while Domain B is used for the study of roughness receptivity.

where

$$Re_{\tilde{x}^*} = \frac{1}{2}\left(\frac{Re_{\delta_0^*}}{\Delta}\right)^2 + Re_{\delta_0^*}\frac{x^*}{\delta_0^*}. \tag{2.11}$$

Equations 2.10 and 2.11 were derived from the similarity solution (see the section on the Illingworth transformation in White, 1991). Note that $\tilde{x}^*$ is the dimensional streamwise coordinate in a reference frame positioned at the flat plate leading edge. The scaling factors Δ and Δ_{99} vary with the Mach number and wall temperature. For the hot wall cases we have $\Delta = 9.071$ and $\Delta_{99} = 11.858$ for $M_\infty = 6.0$ and $\Delta = 2.897$ and $\Delta_{99} = 5.874$ for $M_\infty = 2.5$, while for the cooled-wall cases $\Delta = 6.183$ and $\Delta_{99} = 9.037$ for $M_\infty = 6.0$ and $\Delta = 2.286$ and $\Delta_{99} = 5.283$ for $M_\infty = 2.5$. All the lengths reported in the following are made non-dimensional using δ_0^*, so that domain B is considered as a subset of domain A.

Domain A was designed to accommodate the turbulent wedge evolution in all directions and has dimensions $L_x \times L_y \times L_z$=250×20×60 for $M_\infty = 2.5$ and 300×20×50 for $M_\infty = 6.0$. In particular, the wall normal domain size is about four and six times bigger than the turbulent boundary layer thickness at the outflow boundary, for $M_\infty = 2.5$ and $M_\infty = 6.0$ respectively. The dimensions of domain B are $L_x \times L_y \times L_z$=100×16×20 for $M_\infty = 2.5$ and 150×16×20 for $M_\infty = 6.0$. The streamwise extent was chosen to obtain a significant linear growth of the most unstable disturbances, while the wall normal domain size was designed so that any residual reflections coming from the top boundary would hit the outflow boundary without affecting the stability characteristics of the flow. The spanwise domain size for the $M_\infty = 2.5$ cases was chosen to include the most unstable smooth flat plate boundary layer mode, which has a spanwise wavelength of $\lambda_z \approx 20$. The same spanwise size was kept for the $M_\infty = 6.0$ cases, allowing for the presence of a number of unstable smooth flat plate first and second mode waves. Note that in this case the most linearly unstable mode is the two-dimensional second (Mack) mode.

Case	T_w/T_∞	T_w/T_{ad}
$M_\infty = 6.0$ (hot wall)	7.02	1.00
$M_\infty = 6.0$ (cooled wall)	3.50	0.50
$M_\infty = 2.5$ (hot wall)	2.05	1.00
$M_\infty = 2.5$ (cooled wall)	1.00	0.49

Table 2.1: Wall temperatures used for the isothermal wall boundary condition used in the different cases analysed.

2.2.3 Boundary conditions for the roughness cases

The spanwise domain boundaries are treated with periodic boundary conditions, while the walls are considered no-slip and isothermal. The wall temperatures considered for the hot and cooled wall conditions are provided in table 2.1. The reflection of waves from the domain external boundaries is minimised by using integrated and standard characteristic conditions for the top and outflow boundaries, respectively. The standard characteristic conditions used here are those originally derived by Thomson (1987, 1990), whereby incoming characteristics are set to zero at characteristic boundaries. The inflow is initialised with a compressible laminar similarity solution and a pressure extrapolation boundary condition is then applied, whereby in the subsonic region of the boundary-layer the inflow conservative variables are calculated by extrapolating the pressure from within the domain using a linear approximation. The boundary condition at the inflow changes to a prescribed time-varying condition when introducing inflow disturbances. To this end, the time-converged inlet flow field obtained with the extrapolation boundary condition is used as the base flow over which disturbances are superimposed. The methodology used to introduce disturbances in the flow field is the subject of the following section.

2.2.4 Disturbance generation

To analyse how different upstream perturbations influence the transition process we consider three different types of inflow disturbances, obtained as different variations of the following generic function

$$\psi(y,z,t) = a\left(1-\exp\left(-y^p/g^l\right)\right)\sum_{m=0}^{M}\sum_{n=1}^{N}\cos\left(\beta_m z+\phi_m\right)\cos\left(\omega_n t+\pi_n\right), \quad (2.12)$$

where $M = 6$ and $N = 16$ are the total number of spanwise wavenumbers and frequencies, respectively. It should be noted that for the $M_\infty = 2.5$ cases the zero wavenumber spanwise modes were not included in the forcing signal. Random phases ϕ and π are introduced to avoid spurious high amplitude peaks in the forcing signal which might trigger undesirable local nonlinearities. The damping function $f_d := 1-\exp\left(-y^p/g^l\right)$, where p and l are coefficients, was used to control the disturbance location with respect to the boundary-layer. An additional damping was employed to drive the forcing function to zero at the top domain

boundary to avoid the onset of numerical oscillations. The three types of disturbances considered are obtained by using the above function to perturb the fixed inflow boundary condition for different flow variables. The perturbations take the following form

$$\text{Type V: } v'(y,z,t) = -\partial\psi(y,z,t)/\partial z; w'(y,z,t) = \partial\psi(y,z,t)/\partial y; u' = \rho' = T' = 0$$

$$\text{Type A: } \rho'(y,z,t) = \psi(y,z,t); u' = v' = w' = T' = 0$$

$$\text{Type Æ: } T'(y,z,t) = \psi(y,z,t); u' = v' = w' = \rho' = 0$$

Note that, type V forcing introduces streamwise vorticity disturbances and results in a divergence free velocity disturbance field at the inflow boundary. This methodology was used to analyse the effects of different types of disturbances on the roughness-induced receptivity.

For the analysis of the turbulent wedge development downtream of the roughness an alternative acoustic broadband disturbance was placed in the free-stream, upstream of the roughness element, by adding the following forcing term to the continuity equation

$$\rho_f(\mathbf{x},t) = a\exp\left(-\tilde{r}^2\right)\sum_{m=0}^{M}\sum_{n=1}^{N}\cos\left(\beta_m z+\phi_m\right)\sin\left(\omega_n t+\phi_n\right), \tag{2.13}$$

with $M = 20$ and $N = 16$ for $M_\infty = 6.0$ and $M = 25$ and $N = 18$ for $M_\infty = 2.5$. The coordinate $\tilde{r}$ is defined as $\tilde{r}^2 = \left[(x-x_f)^2 + (y-y_f)^2\right]/L_f$, where $L_f = 1.0$ determines the radius of the forcing region and x_f and y_f its centre. Note that $x_f = 12.0$ and $y_f = 6.0$ for $M_\infty = 6.0$ and $x_f = 25.0$ and $y_f = 10.0$ for $M_\infty = 2.5$. This type of disturbance was included to mimic acoustic perturbations coming from turbulent boundary-layers developing in the wind tunnel walls upstream of the flat plate during experiments.

2.2.5 Multi-block grid configuration and sharp corner treatment

The sharp edges of the roughness elements analysed in this work are resolved by the grid by using the multi-block capabilities of the *SBLI* code, which allows the specification of interface and boundary points at different locations in the communication plane between two blocks. A sketch of the multi-block configuration used

is shown in figure 2.2. The grid is divided into six blocks, five of which are placed around the sharp-edged roughness element and one (block 2 in figure 2.2) placed on top of it. In the multi-block version of the code, boundary conditions are applied at each block boundary. At inter-block boundary points placed above the roughness element, interface boundary conditions are applied, which simply impose the use of the fourth-order central difference-scheme for the calculation of derivatives. On the other hand, for $0 \leq y \leq h$, wall boundary conditions (no-slip and isothermal wall) are imposed to construct the roughness geometry, with particular attention paid to blocks 4 and 6 which contain the roughness edges. Finally, periodicity is imposed by specifying interface conditions in the communication plane between two spanwise neighbouring blocks.

The inclusion of sharp geometries in the multi-block grid introduces a problem in the calculation of derivatives at the edges. In fact, the treatment of sharp corners in compressible flows represents a challenge when using standard high-order finite difference schemes. The problem is explained schematically in figure 2.3. At every instant t the time derivative of density at the corner point C is calculated from the continuity equation by using the mass fluxes obtained at the first six points on the fluid side, following the Carpenter one sided stencil. The flow topology

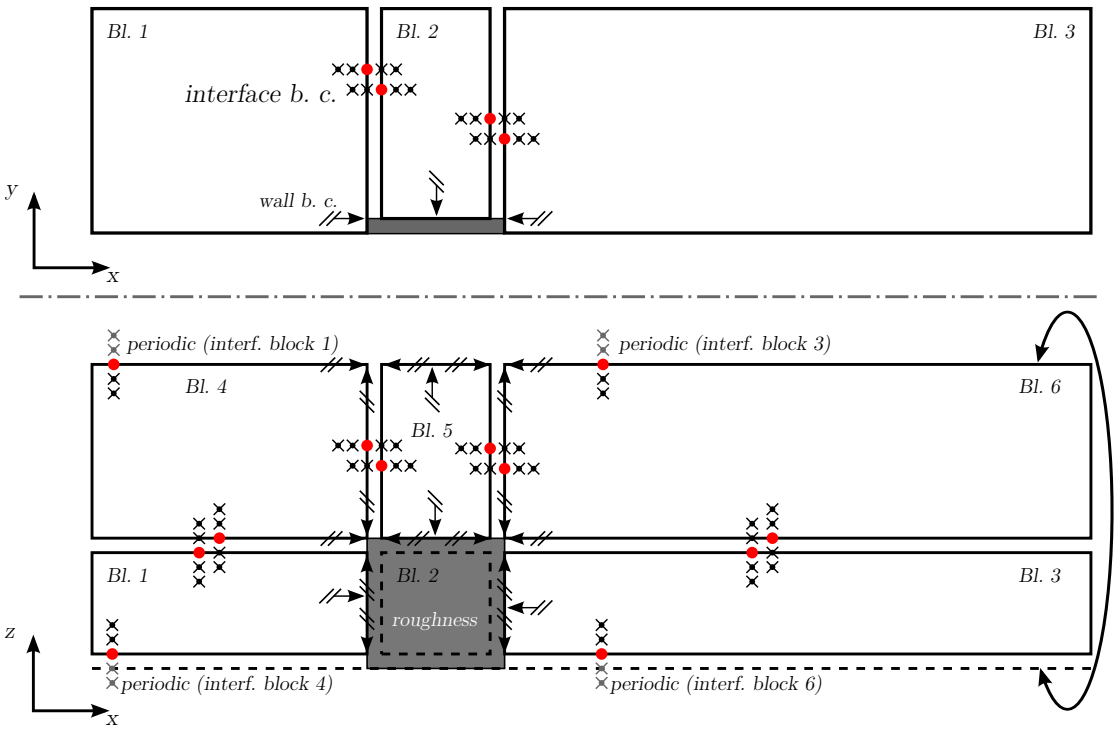

Figure 2.2: Multi-block strategy. Side view in top figure, top view in bottom figure.

is such that at point C a negative $\partial\rho u/\partial x$ combines with a positive $\partial\rho w/\partial z$ to determine the variation of density with time. For all the grids analysed here, this combination gives a continuously increasing density at the corner points. An additional problem appears at point P, where the $\partial\rho u/\partial x$ contribution to the density variation is zero, as the Carpenter stencil only uses wall points in this case. This implies that also the $\partial\rho w/\partial z$ term, which is the only non-zero term in the right-hand-side of the continuity equation during transients, will be zero in the final steady state solution. This seems to be prevented by the high density at point C and density at point P decreases monotonically.

Very fine grids might alleviate this problem but at a prohibitive cost, both in terms of number of grid points and time-step size, so that ultimately new high-order boundary schemes consistent with the conservation laws will have to be designed to resolve sharp corners in compressible flows. Here, the problem was mitigated by calculating the density at the corner points as an average of the neighbouring points belonging to the roughness surface, as depicted in figure 2.3, effectively rounding off the sharp edges at the grid scale.

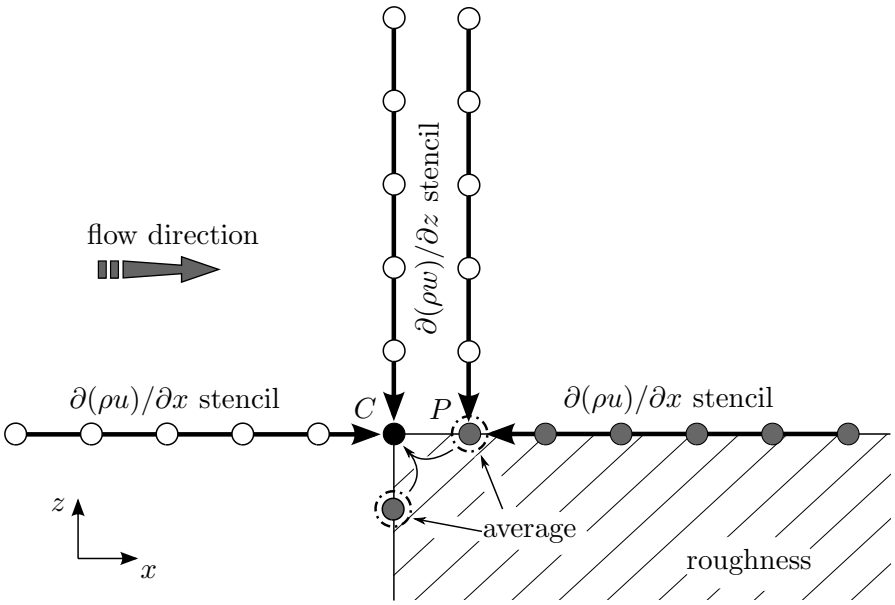

Figure 2.3: Description of the corner problem.

a_0	a_1	a_2	a_3
$\frac{11}{16}+\frac{5\beta_f}{8}$	$\frac{15}{32}+\frac{17\beta_f}{16}$	$\frac{-3}{16}+\frac{3\beta_f}{8}$	$\frac{1}{32}-\frac{\beta_f}{16}$

Table 2.2: Filter coefficients.

Point	$a_{1,i}$	$a_{2,i}$	$a_{3,i}$	$a_{4,i}$	$a_{5,i}$	$a_{6,i}$	$a_{7,i}$
i=2	$\frac{1}{64}+\frac{31\beta_f}{32}$	$\frac{29}{32}+\frac{3\beta_f}{16}$	$\frac{15}{64}+\frac{17\beta_f}{32}$	$\frac{-5}{16}+\frac{5\beta_f}{8}$	$\frac{15}{64}-\frac{15\beta_f}{32}$	$\frac{-3}{32}+\frac{3\beta_f}{16}$	$\frac{1}{64}-\frac{\beta_f}{32}$
i=3	$\frac{-1}{64}+\frac{\beta_f}{32}$	$\frac{3}{32}+\frac{13\beta_f}{16}$	$\frac{49}{64}+\frac{15\beta_f}{32}$	$\frac{5}{16}+\frac{3\beta_f}{8}$	$\frac{-15}{64}+\frac{15\beta_f}{32}$	$\frac{3}{32}-\frac{3\beta_f}{16}$	$\frac{-1}{64}+\frac{\beta_f}{32}$

Table 2.3: Filter coefficients.

This corner treatment prevents simulation blow-up, however the presence of a sharp-edged roughness element induces small spatial grid-to-grid-point oscillations in the density field due to an inherent discontinuity in the derivatives at the roughness edges. The computational grid was substantially refined near the roughness element and the residual spurious oscillations were treated using a sixth order filter by Visbal & Gaitonde (2002). The filter is applied at each time step and the conservative variables array ($\mathbf{U} = \{\rho, \rho u, \rho v, \rho w, \rho E\}^T$) is updated as follows

$$\mathbf{U} = \mathbf{U} - \sigma\left(\mathbf{U} - \mathbf{U}_f\right), \tag{2.14}$$

where $\sigma = 0.05$ for $M_\infty = 2.5$ and $\sigma = 0.14$ for $M_\infty = 6.0$, so that only 5% and 14% of the filtered field was used for the $M_\infty = 2.5$ and $M_\infty = 6.0$ cases respectively. Following Visbal & Gaitonde (2002) the array of filtered conservative variables ($\mathbf{U}_f$) is calculated at internal points by solving the tridiagonal system (for simplicity we consider a filter in the x-direction)

$$\beta_f \mathbf{U}_f^{i-1} + \mathbf{U}_f^i + \beta_f \mathbf{U}_f^{i+1} = \sum_{n=0}^{N_f} \frac{a_n}{2}\left(\mathbf{U}_f^{i+n} + \mathbf{U}_f^{i-n}\right), \tag{2.15}$$

with $i \in \{4 \ldots N_x - 3\}$. $2N_f$ gives the order of the filter (here $N_f = 3$), the $a_0, a_1, \ldots, a_n$ coefficients are given in table 2.2 and β_f is an adjustable (in the range $-0.5 < \beta_f \leq 0.5$) filter parameter. Higher values of β_f are associated with less dissipative filters, here $\beta_f = 0.45$. Boundary points are not filtered and at near boundary points the filter formula reads

$$\begin{aligned}
\beta_f \mathbf{U}_f^{i-1} + \mathbf{U}_f^i + \beta_f \mathbf{U}_f^{i+1} &= \sum_{n=1}^{7} a_{n,i} \mathbf{U}_f^n \quad i = 2, 3 \\
\beta_f \mathbf{U}_f^{i-1} + \mathbf{U}_f^i + \beta_f \mathbf{U}_f^{i+1} &= \sum_{n=0}^{6} a_{N_x-n,i} \mathbf{U}_f^{N_x-n} \quad i = N_x - 2, N_x - 1.
\end{aligned} \tag{2.16}$$

The left boundary coefficients ($a_{n,i}$) are given in table 2.3, while the right boundary coefficients can be obtained as $a_{N_s-n,i} = a_{n+1,N_x-i+1}$.

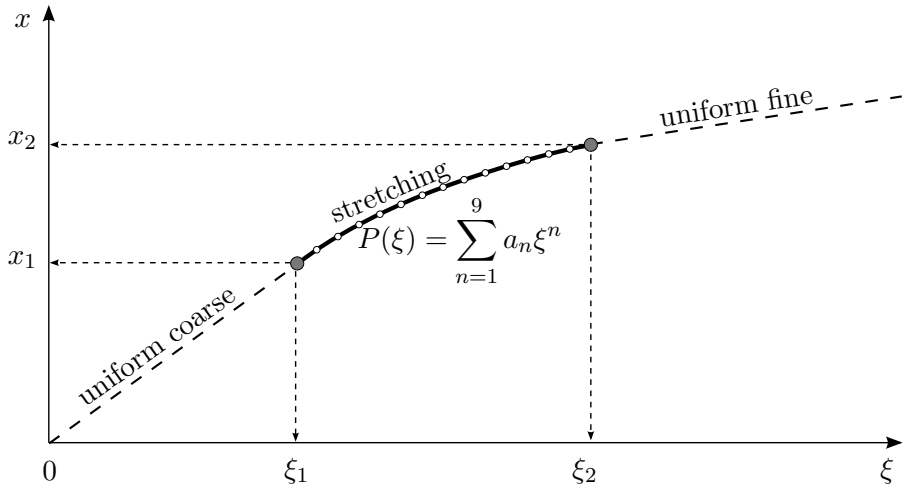

Figure 2.4: Grid stretching using polynomials of high degree.

2.2.6 Grid generation

All the numerical grids employed in this work were stretched in the wall normal direction using the following relation between the computational uniform grid ($0 < \eta < 1$) and the physical non-uniform grid ($0 < y < L_y$)

$$y = L_y \frac{\sinh(b_y \eta)}{\sinh b_y}, \tag{2.17}$$

where b_y is the stretching factor. In the cases including a roughness element the value of b_y was iteratively determined (close to a target) by imposing an integer number of grid points (n_{yr}) below the roughness and $y(n_{yr}) = h$, where h is the non-dimensional height of the roughness.

The distribution of grid points in the streamwise and spanwise directions is uniform in the cases involving clean flat plates, whereas for the roughness cases it was designed to adequately resolve the laminar flow near the roughness element and the turbulent flow downstream of it. The level of grid refinement necessary near the roughness, both for stability reasons and because of the high gradients induced by its sharp edges, requires the use of grid stretching in all directions in order to maintain a reasonable computational effort. Therefore, in the horizontal directions the computational grid presents regions of constant grid spacing with different levels of grid refinement, which are linked together by polynomials of the ninth degree. The procedure is sketched in figure 2.4, which shows an example of grid stretching in the streamwise direction. The objective is to link two uniform grids with different grid spacings using a polynomial function obtained by imposing C^4

continuity of the resulting stretching function at points x_1 and x_2. An important parameter in this procedure is the distance $\xi_2 - \xi_1$, which determines whether the polynomial is monotonic in the interval $[\xi_1, \xi_2]$. Here, for any given $x_2 - x_1$ the distance $\xi_2 - \xi_1$ was determined by considering that points x_1 and x_2 are joined by a straight line having a slope equal to the average between the coarse-grid and the fine-grid slopes in figure 2.4.

2.2.7 Validation of the multi-block strategy

As already mentioned, the multi-block version of the SBLI code was extensively validated in Yao *et al.* (2009). In this section we present results from a validation test case involving the numerical computation of the Mack mode instability temporal growth rate at $M_\infty = 6.0$. The results presented here validate the numerical implementation of the multi-block strategy, while cases involving more complex geometries can be found in Yao *et al.* (2009). The numerical simulation is carried out using the temporal DNS approach (see chapter 5 for details) and the results will be compared with LST predictions. This represents a very good validation case for any Navier-Stokes solver since instability growth rates and mode eigenfunctions are extremely sensitive to numerical errors. The case analysed here is case R2S in table 5.1.

A comparison of the Navier-Stokes and LST results is provided in figure 2.5. The calculated temporal Mack mode growth rate is $\omega_i = 0.03413$ against the LST growth rate of $\omega_i = 0.03414$. A comparison between the two growth rates is shown in figure 2.5(a), showing that the agreement is practically perfect. In addition, figure 2.5(b) shows a comparison between the Navier-Stokes amplitude functions and the LST eigenfunction. Again, the agreement is remarkable.

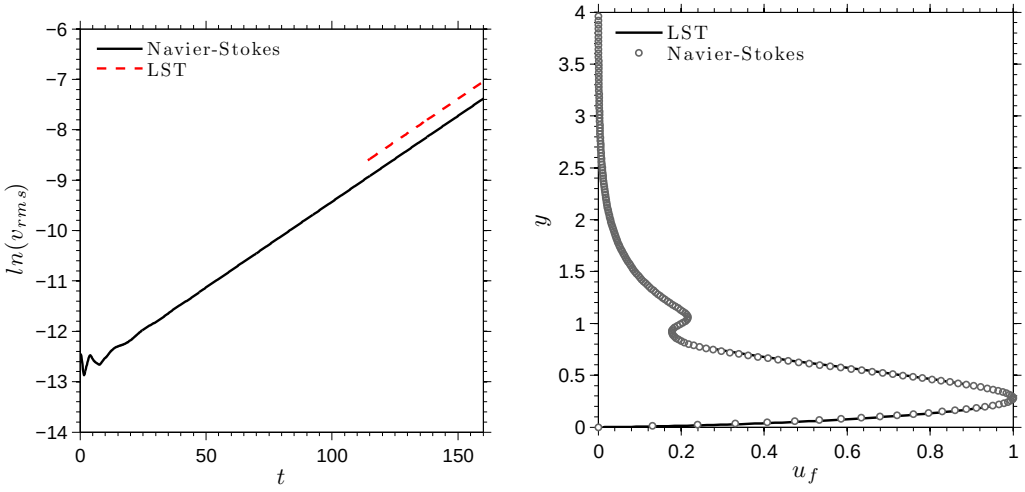

(a) (b)

Figure 2.5: Validation of the multi-block strategy employed. (a) Mack mode growth rate comparison (Navier-Stokes against LST), (b) comparison between Navier-Stokes amplitude function and LST eigenfunction for the Mack mode primary instability (u_f is the u-velocity Fourier mode amplitude function for the Navier-Stokes result and the u-velocity eigenfunction for the LST result).

Chapter 3

Small disturbance receptivity due to roughness[1]

This chapter and the next consider the effects of sharp-edged isolated roughness elements on the stability and transition of high-speed boundary layers. In particular, the investigation focuses on the breakdown of boundary layers in quiet environments, where the transition is initiated by the linear growth of small disturbances. In the present chapter, we concentrate on the receptivity and initial linear growth of disturbances by performing a parametric study focused on the effects of disturbance type and location (inside or outside the boundary layer), roughness height, Mach number ($M_\infty = 6.0$ and $M_\infty = 2.5$) and wall temperature. The chapter starts in section 3.3 with an introduction to the numerical simulations carried out for an extensive parametric study, in section 3.1. The different inflow disturbances considered are then characterised by looking at their behaviour in the free-stream, in section 3.2, and their effect on smooth flat plate boundary layers at $M_\infty = 6.0$ and $M_\infty = 2.5$ in section 3.3. The laminar steady-state flow over the roughness is analysed in section 3.5 under the different flow conditions and the results of the $M_\infty = 6.0$ and $M_\infty = 2.5$ roughness-induced receptivity are discussed in sections 3.6 and 3.7 respectively. The chapter ends with a synthesis of the results obtained in section 3.8. The study of roughness induced transition is completed in chapter 4 where the nonlinear stages of transition, leading to the development of a turbulent wedge behind the roughness element, are discussed.

[1]Part of this chapter was presented at NATO-RTO-MP-AVT-200, Paper No 22 (De Tullio & Sandham, 2012)

3.1 The parametric study

The details of the numerical simulations carried out for the parametric study are provided in Table 3.1. The computational domain dimensions considered for all the cases analysed in this chapter are those of domain B in figure 2.1. For the sake of clarity the cases are named using the following convention:

Case	Mach	$Re_{\delta_0^*}$	Re_h	Re_h^*	T_w	Disturbance forcing		Geomtery
						Type	Location	
$HSVI_a$	6.0	8200	-	-	7.022	type V	Internal	Smooth
$HSAI_a$	6.0	8200	-	-	7.022	type A	Internal	Smooth
$HSÆI_a$	6.0	8200	-	-	7.022	type Æ	Internal	Smooth
$HSVE_a$	6.0	8200	-	-	7.022	type V	External	Smooth
$HSAE_a$	6.0	8200	-	-	7.022	type A	External	Smooth
$HSÆE_a$	6.0	8200	-	-	7.022	type Æ	External	Smooth
$HR0.5AI_a$	6.0	8200	60	59	7.022	type A	Internal	$h = 0.5$
$HR1.0VI_a$	6.0	8200	331	328	7.022	type V	Internal	$h = 1.0$
$HR1.0AI_a$	6.0	8200	331	328	7.022	type A	Internal	$h = 1.0$
$HR1.0ÆI_a$	6.0	8200	331	328	7.022	type Æ	Internal	$h = 1.0$
$HR1.0VE_a$	6.0	8200	331	328	7.022	type V	External	$h = 1.0$
$HR1.0SE_a$	6.0	8200	331	328	7.022	type A	External	$h = 1.0$
$HR1.0ÆE_a$	6.0	8200	331	328	7.022	type Æ	External	$h = 1.0$
$CR1.0AI_a$	6.0	4135	331	349	3.5	type A	Internal	$h = 1.0$
$HSVI_b$	2.5	3300	-	-	2.055	type V	Internal	Smooth
$HSAI_b$	2.5	3300	-	-	2.055	type A	Internal	Smooth
$HSÆI_b$	2.5	3300	-	-	2.055	type Æ	Internal	Smooth
$HSVE_b$	2.5	3300	-	-	2.055	type V	External	Smooth
$HSAE_b$	2.5	3300	-	-	2.055	type A	External	Smooth
$HSÆE_b$	2.5	3300	-	-	2.055	type Æ	External	Smooth
$HR0.5AI_b$	2.5	3300	170	169	2.055	type A	Internal	$h = 0.5$
$HR1.0VI_b$	2.5	3300	791	788	2.055	type V	Internal	$h = 1.0$
$HR1.0AI_b$	2.5	3300	791	788	2.055	type A	Internal	$h = 1.0$
$HR1.0ÆI_b$	2.5	3300	791	788	2.055	type AE	Internal	$h = 1.0$
$HR1.0VE_b$	2.5	3300	791	788	2.055	type V	External	$h = 1.0$
$HR1.0SE_b$	2.5	3300	791	788	2.055	type A	External	$h = 1.0$
$HR1.0ÆE_b$	2.5	3300	791	788	2.055	type Æ	External	$h = 1.0$
$CR1.0_b$	2.5	1730	791	846	1.0	-	-	$h = 1.0$

Table 3.1: Cases included in the parametric study. Note that the wall temperature in the hot-wall cases ($T_w = 2.055$ and $T_w = 7.022$) is equal to the adiabatic wall temperature.

Case	Block	N_x	N_y (n_y^r)	N_z	b_y	Δx	Δz
HS_a	B1	751	191 (-)	51	3.40	0.2	0.2
	B2	751	191 (-)	49	3.40	0.2	0.2
$HR0.5_a$	B1	234	191 (26)	119	3.38	[0.21, 0.06]	0.05
	B2	99	166 (-)	119	3.38	0.06	0.05
	B3	564	191 (26)	119	3.38	[0.06, 0.21]	0.05
	B4	234	191 (26)	122	3.38	[0.21, 0.06]	[0.05, 0.2, 0.05]
	B5	99	191 (26)	122	3.38	0.06	[0.05, 0.2, 0.05]
	B6	564	191 (26)	122	3.38	[0.06, 0.21]	[0.05, 0.2, 0.05]
$HR1.0_a$ $CR1.0_a$	B1	234	205 (46)	119	3.20	[0.21, 0.06]	0.05
	B2	99	160 (-)	119	3.20	0.06	0.05
	B3	564	205 (46)	119	3.20	[0.06, 0.21]	0.05
	B4	234	205 (46)	122	3.20	[0.21, 0.06]	[0.05, 0.2, 0.05]
	B5	99	205 (46)	122	3.20	0.06	[0.05, 0.2, 0.05]
	B6	564	205 (46)	122	3.20	[0.06, 0.21]	[0.05, 0.2, 0.05]
HS_b	B1	501	191 (-)	51	3.40	0.2	0.2
	B2	501	191 (-)	49	3.40	0.2	0.2
$HR0.5_b$	B1	234	191 (26)	119	3.38	[0.21, 0.06]	0.05
	B2	99	166 (-)	119	3.38	0.06	0.05
	B3	326	191 (26)	119	3.38	[0.06, 0.21]	0.05
	B4	234	191 (26)	122	3.38	[0.21, 0.06]	[0.05, 0.2, 0.05]
	B5	99	191 (26)	122	3.38	0.06	[0.05, 0.2, 0.05]
	B6	326	191 (26)	122	3.38	[0.06, 0.21]	[0.05, 0.2, 0.05]
$HR1.0_b$	B1	234	205 (46)	119	3.20	[0.21, 0.06]	0.05
	B2	99	160 (-)	119	3.20	0.06	0.05
	B3	326	205 (46)	119	3.20	[0.06, 0.21]	0.05
	B4	234	205 (46)	122	3.20	[0.21, 0.06]	[0.05, 0.2, 0.05]
	B5	99	205 (46)	122	3.20	0.06	[0.05, 0.2, 0.05]
	B6	326	205 (46)	122	3.20	[0.06, 0.21]	[0.05, 0.2, 0.05]
$CR1.0_b$	B1	285	205 (46)	199	3.20	[0.21, 0.03]	0.03
	B2	199	160 (-)	199	3.20	0.03	0.03
	B3	340	205 (46)	199	3.20	[0.03, 0.21]	0.03
	B4	285	205 (46)	144	3.20	[0.21, 0.03]	[0.03, 0.2, 0.03]
	B5	199	205 (46)	144	3.20	0.03	[0.03, 0.2, 0.03]
	B6	340	205 (46)	144	3.20	[0.03, 0.21]	[0.03, 0.2, 0.03]

Table 3.2: Computational grids. N_x, N_y and N_z are the number of points in the streamwise, wall-normal and spanwise directions per block, while n_y^r is the number of points for $0 \leq y \leq h$. The values of Δx for the cases with roughness indicate the grid spacing at the beginning and at the end of the block. The multiple values of Δz indicate spanwise grid spacings at the beginning, at the centre and at the end of the domain.

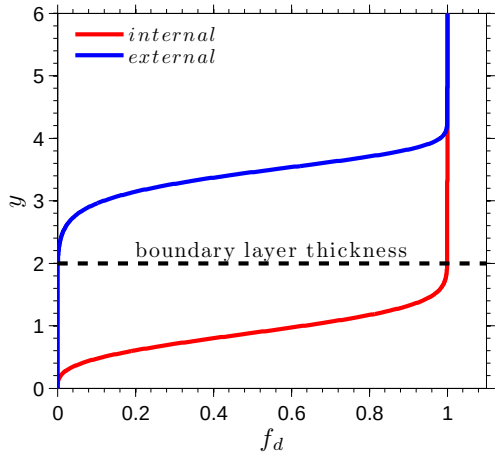

Figure 3.1: Position of non-zero inflow disturbances relative to the boundary layer for internal and external disturbances.

- The first letter indicates a hot (H) or a cold (C) wall temperature. Here, hot means adiabatic ($T_w = T_{ad}$) and cold means cooler, $T_\infty \leq T_w \leq T_{ad}$.
- The second letter defines the configuration considered, rough (R) or smooth (S). When rough, the letter is followed by a number indicating the height of the roughness.
- The third letter indicates the type of disturbances used (V, A or $Æ$).
- The last letter indicates whether disturbances are internal (I) or external (E) relative to the boundary layer. For internal disturbances the damping function f_d has $g = 1.0$, $p = 3.0$ and $l = 1.0$ in (2.12), whereas for external disturbances $g = 2.0$, $p = 12.0$ and $l = 22.0$. Figure 3.1 shows schematically how internal and external disturbances relate to the boundary layer 99% thickness.

Subscripts (a) and (b) are added to the designation to indicate the $M_\infty = 6.0$ and the $M_\infty = 2.5$ cases, respectively. The smooth wall cases are used as references to evaluate the effects of roughness. Cases prefixed *HR1.0* were carried out to investigate the effects of different disturbances, while cases prefixed *HR0.5* are useful to understand the effect of roughness height. Finally the cold wall cases are used to identify the influences of wall cooling on the boundary layer stability.

The simulation Reynolds numbers ($Re_{\delta_0^*} = 8200$ for the $M_\infty = 6.0$ cases and $Re_{\delta_0^*} = 3300$ for the $M_\infty = 2.5$ cases) were chosen to obtain a unit Reynolds number of $Re/m = 10^6$ when placing the roughness element at a distance of

$\tilde{x}_h^* = 0.08$ meters from the leading edge. The Reynolds number of the simulation was reduced in the cold wall cases to $Re_{\delta_0^*} = 4135$ for $M_\infty = 6.0$ and $Re_{\delta_0^*} = 1730$ for $M_\infty = 2.5$ to keep a constant roughness Reynolds numbers of $Re_h = 331$ and $Re_h = 791$ for the $M_\infty = 6.0$ and the $M_\infty = 2.5$ cases, respectively, thereby minimising local Reynolds number effects. All cases consider forced perturbations in the form of equation 2.12 for a frequency band $F = 0.02 - 0.32$ and amplitude $a = 2 \times 10^{-6}$.

Details of the different computational grids used for the parametric study are provided in Table 3.2. The number of points used for $0 \leq y \leq h$ in each case is given by n_y^r. In all cases the length $L = 6.0$ and width $W = 6.0$ of the roughness are resolved using $n_x^r = 101$ and $n_z^r = 121$ points respectively.

3.2 Characterisation of the disturbances in the free-stream

As shown by Chu and Kovasznay (Kovasznay, 1953; Chu & Kovasznay, 1958), small perturbations present in a uniform flow can be divided into independent vorticity, sound and entropy modes. The same framework is used here to characterise the disturbances introduced using the procedure explained in section 2.2.4, with the exception that entropy disturbances will be represented by internal energy. The characterisation of the different disturbance fields is carried out by considering the behaviour of each of their Fourier coefficients after an expansion into frequencies (F) and spanwise wavenumbers (k_z). We consider non-dimensional frequencies defined as $F = f^*\delta_0^*/U_\infty^*$, f^* being the dimensional frequency (cycles per second), and a Fourier decomposition is carried out according to the discrete Fourier transform (DFT) formula

$$\begin{aligned} \widehat{S}_{\eta,\xi}(x,y) &:= \frac{2}{LJ}\sum_{j=0}^{J-1}\sum_{l=0}^{L-1} s(x,y,z_l,t_j)e^{-2\pi i\frac{\eta}{J}j}e^{-2\pi i\frac{\xi}{L}l}, \\ \eta &= 0,1,\ldots,J-1 \text{ and } \xi = 0,1,\ldots,L-1, \end{aligned} \tag{3.1}$$

where J and L are the total time and space samples and s can be any flow variable. The indices η and ξ represent the discretised frequencies and spanwise wavenumbers, respectively. Non-dimensional frequencies can then be obtained as $F = \eta/\tau$, with $\eta = 0, 1, \ldots, J/2 - 1$, where $\tau = 50$ is one sampling period, corresponding to one forcing cycle. After reordering to place the zero-wavenumber component at

the centre of the spanwise wavenumber spectrum, we obtain $k_z = 2\pi\xi/L_z$, with $\xi = -(L/2-1), \ldots, -1, 0, 1, \ldots, L/2-1$, where $L_z = 20$ is the spanwise length of the computational domain. The normalisation factor $2/(LJ)$ gives unit amplitude Fourier modes for a disturbance signal given by a sum of temporal and spatial sinusoidal waves.

In addition to the amplitude of the single Fourier modes ($|\widehat{S}_{\eta,\xi}(x,y)|$), we define the amplitude associated with each frequency as

$$\mathcal{A}_\eta(x,y) := \sum_{\xi=-M}^{M} |\widehat{S}_{\eta,\xi}(x,y)|. \tag{3.2}$$

This definition is used to analyse the behaviour of disturbances at a particular y-location (e.g. in the free-stream).

The amplitudes of vorticity, sound and internal energy in the free-stream, associated with the three disturbances considered, are shown in figure 3.2, where $|\boldsymbol{\omega}|$, $|\nabla \cdot \mathbf{u}|$ and $|\nabla\sqrt{e}|$ are plotted as a function of frequency. Note that the quantities $\boldsymbol{\omega}^*$, $\nabla^* \cdot \mathbf{u}^*$ and $\nabla^*\sqrt{e^*}$ are dimensionally consistent. Type V and type A disturbances are dominated by vorticity and acoustic modes respectively, whereas type Æ perturbations are, for the most part, formed by sound and internal energy waves, the former being more energetic. The dominant free-stream acoustic disturbances propagate downstream at the speed of the slow acoustic waves ($c_{ph} = 1 - 1/M_\infty$) for the two Mach numbers considered, as shown in figure 3.3 for case *HSAI*, where the streamwise variation of phase divided by circular frequency ($\omega = 2\pi F$) is plotted for a selection of $\nabla \cdot \mathbf{u}$ modes. Note that, for constant $c_{ph} = \omega\,[d\phi(x)/dx]^{-1}$ and ω, $\phi(x)/\omega = x/c_{ph} + \phi(0)/\omega$. The $\phi(x)/\omega$ parameter is used instead of c_{ph} to avoid differentiation, which amplifies the small oscillations appearing in the Fourier transformed DNS results as a consequence of the superposition of modes with same frequency but different c_{ph}, and gives a clear visualisation of the phase speed of the dominant waves in the DNS signal.

The presence of fast acoustic waves in each case can be inferred from the pressure disturbance amplitude plots shown in figure 3.4. The oscillatory character of the mode amplitudes indicates that multiple modes with different phase speeds are contributing to the pressure signal. Assuming there are two modes at play, once the phase speed of the dominant wave is known, the oscillation period Δx can be used to calculate the phase speed of the additional wave by applying the following formula

$$F\Delta x \left|c^a_{ph} - c^b_{ph}\right| = c^a_{ph} c^b_{ph}, \tag{3.3}$$

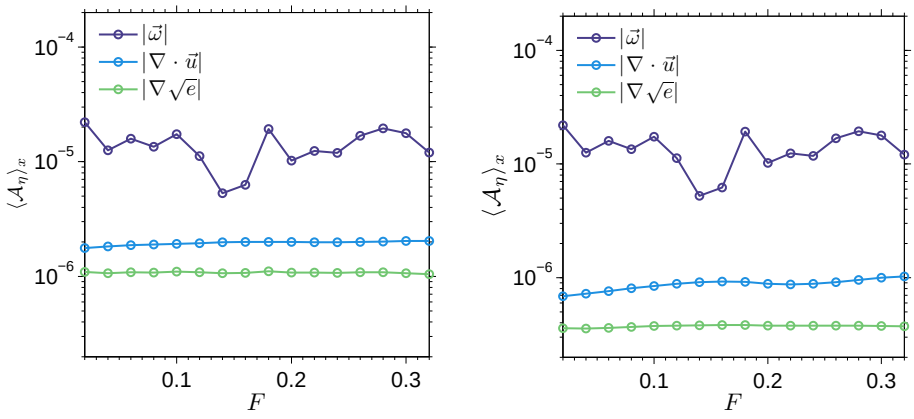

(a) type V disturbances (b) type V disturbances

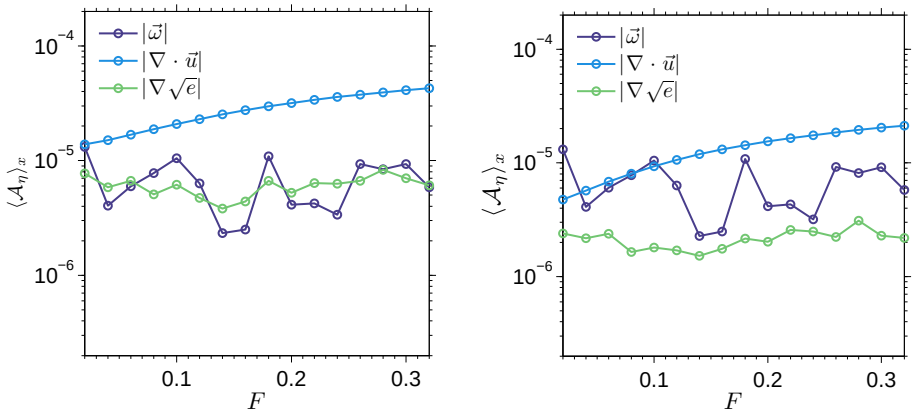

(c) type A disturbances (d) type A disturbances

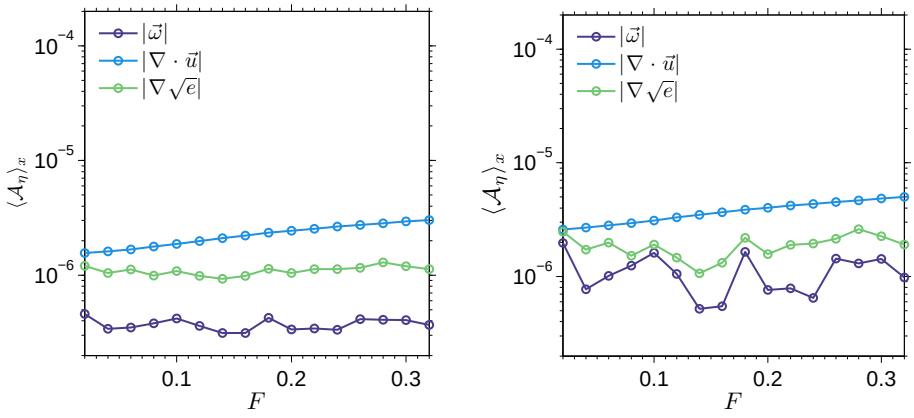

(e) type Æ disturbances (f) type Æ disturbances

Figure 3.2: Streamwise averaged disturbance amplitudes for $|\boldsymbol{\omega}|$, $|\nabla \cdot \mathbf{u}|$ and $|\nabla\sqrt{e}|$ in the free-stream. (a), (c), (e) $M_\infty = 6.0$ and (b), (d), (f) $M_\infty = 2.5$.

which holds for the superposition of two waves travelling at different speeds c^a_{ph} and c^b_{ph}. Equation (3.3) was obtained by noting that the amplitude of the signal composed by two waves $A_1 \exp(i\omega/c^a_{ph}x)$ and $A_2 \exp(i\omega/c^b_{ph}x)$, with equal frequencies but different phase speeds, varies in the streamwise direction according to the

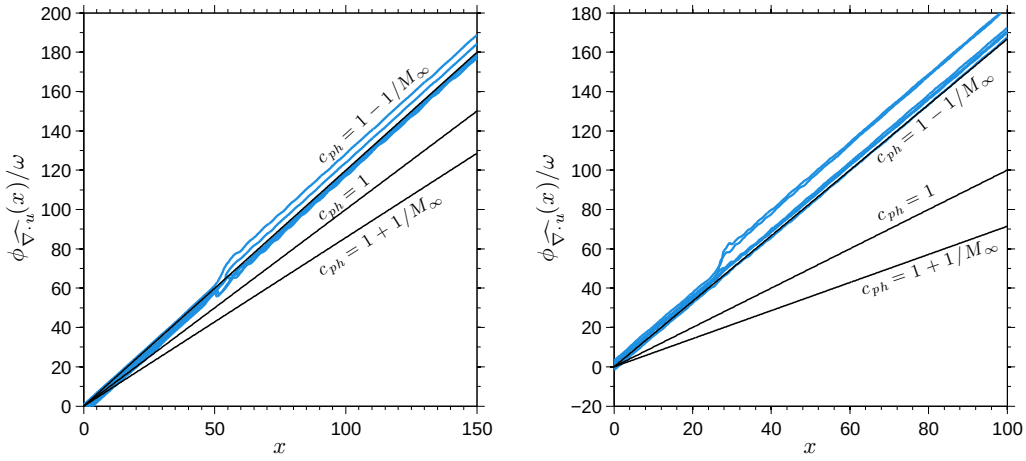

Figure 3.3: Streamwise $\phi(x)/\omega$ evolution for a selection of free-stream $\nabla \cdot u$ disturbances, showing the phase speed of the dominant free-stream acoustic waves. (a) type A disturbances, $M_\infty = 6.0$, (b) type A disturbances, $M_\infty = 2.5$.

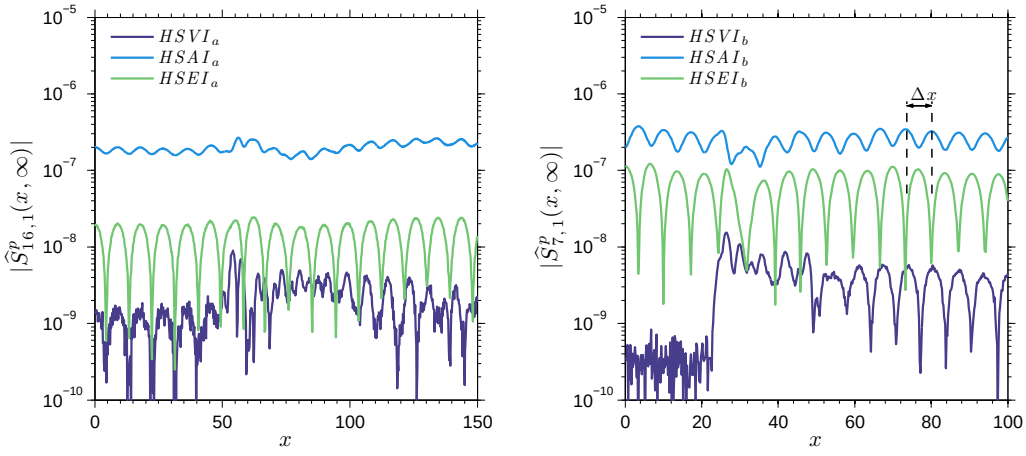

Figure 3.4: Amplitude of pressure disturbances in the free-stream. (a) $F = 0.32$ and $k = 0.314$ at Mach 6.0, (a) $F = 0.14$ and $k = 0.314$ at $M_\infty = 2.5$.

following

$$A(x) = \sqrt{A_1^2 + A_2^2 + 2A_1A_2\cos[\omega(1/c_{ph}^a - 1/c_{ph}^b)x]}, \tag{3.4}$$

which is a periodic function with period

$$\Delta x = \frac{1}{F\left|1/c_{ph}^a - 1/c_{ph}^b\right|}. \tag{3.5}$$

For simplicity we have assumed that the two waves have constant amplitudes and we have considered only positive phase speeds. The amplitude of the oscillation

in figure 3.4 also gives an indication of the relative amplitude of the two waves. This analysis shows that for type A forcing the slow acoustic wave amplitudes are about one order of magnitude higher than those of the fast acoustic waves. In the case of type Æ disturbances fast and slow acoustic waves present similar amplitudes. Type V disturbances present the lowest acoustic wave amplitudes of the three disturbance fields considered.

3.3 Receptivity and stability of the clean flat plate boundary layer

In this section we concentrate on the stability of the clean flat plate boundary layer, which will be studied both by LST and through the analysis of the DNS data obtained for the response of the boundary layer to the inflow disturbances introduced in section 2.2.4. These results will be compared with those obtained for the cases with rough flat plates to better understand the effects of roughness on the boundary layer stability.

Figures 3.5(a) and 3.5(b) show the temporal stability diagrams for the adiabatic-wall $M_\infty = 6.0$ (with $k_z = 0$) and $M_\infty = 2.5$ (with $k_z = 0.314$) boundary-layers

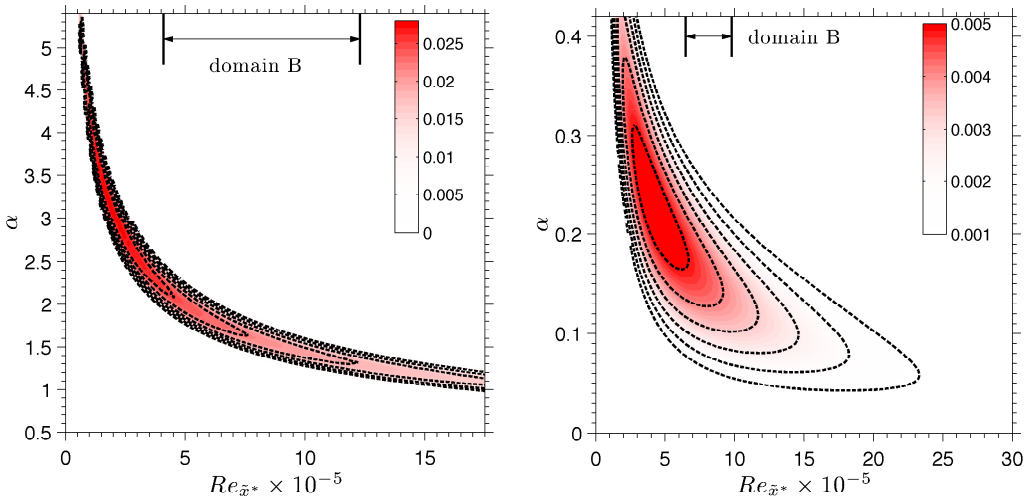

(a) (b)

Figure 3.5: Temporal LST stability diagrams. (a) $M_\infty = 6.0$ ($k_z = 0$), the dashed contourlines indicate $-\alpha_i = 0.010$ to 0.025 with steps of 3×10^{-3}, (b) $M_\infty = 2.5$ ($k_z = 0.314$), the dashed contourlines show $-\alpha_i = 0.0010$ to 0.005 with steps of 8×10^{-4}.

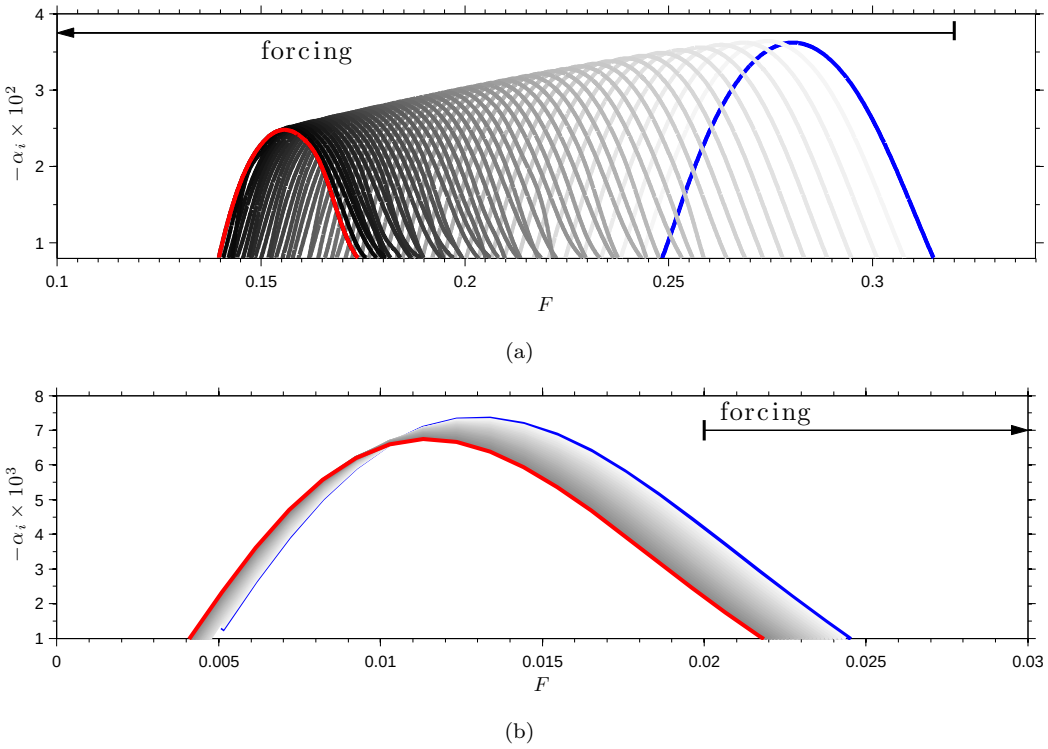

Figure 3.6: Spatial LST growth rates as a function of frequency. (a) $M_\infty = 6.0$ ($k_z = 0$), (b) $M_\infty = 2.5$ ($k_z = 0.314$).

respectively. At $M_\infty = 6.0$ the numerical simulations run from $Re_{\tilde{x}^*_{in}} \approx 4.0 \times 10^5$ to $Re_{\tilde{x}^*_{out}} \approx 16.4 \times 10^5$, and the computational domain inflow is placed downstream of the critical Reynolds number $Re_{\tilde{x}^*_{crit}} \approx 4.5 \times 10^4$. First and second modes are both unstable in the boundary layer region included in the domain. Two-dimensional Mack modes are the most unstable waves, while the most unstable first mode (not shown) is oblique ($k_z \approx 0.85$). The $M_\infty = 2.5$ cases show a region of first mode instability starting from $Re_{\tilde{x}^*_{crit}} = 1.0 \times 10^5$, while the second modes remain stable for all Reynolds numbers. The computational domain spans Reynolds numbers in the range $Re_{\tilde{x}^*} = 5.5 - 9.8 \times 10^5$. Figures 3.6(a) and 3.6(b) show the spatial LST growth rates as a function of frequency at different equally-spaced streamwise locations for a two-dimensional ($k_z = 0$) Mack mode in an $M_\infty = 6.0$ boundary layer and a three-dimensional first ($k_z = 0.314$) mode in an $M_\infty = 2.5$ boundary layer, respectively. The blue line shows the spatial stability diagram for the boundary layer at the inlet of the computational domain, while the red line refers to the outflow boundary. The well known tuning of Mack modes with the boundary layer thickness can be observed in figure 3.6(a), while the frequency of the most unstable first mode remains nearly constant. At $M_\infty = 6.0$ the frequencies of unstable Mack modes are contained in the frequency range of the

inflow disturbances, while for the $M_\infty = 2.5$ cases one forcing frequency ($F = 0.02$) falls within the frequency range of unstable first modes. The most unstable Mack mode for $M_\infty = 6.0$ at $x = 70$ has $F = 0.18$ and $-\alpha_i = 0.024$. At $M_\infty = 2.5$ the most unstable first mode has $F \approx 0.013$ and $-\alpha_i \approx 0.0075$, while the only unstable mode included in the simulation has $F = 0.02$ and $-\alpha_i = 0.005$, according to LST.

The results obtained from the direct solution of the Navier-Stokes equations show that, inside the boundary layer, type V perturbations lead to a transient disturbance growth immediately downstream of the inflow boundary, due to the v-velocity oscillations imposed by the forcing. The v' perturbations give rise to the non-modal growth of ρ', u' and T' at the edge of the boundary layer through a suboptimal lift-up mechanism, which is more effective at the low frequencies, as shown in figures 3.7(a) and 3.7(b) for $M_\infty = 6.0$ and $M_\infty = 2.5$ respectively. Cases with type A disturbances also show small amplitude perturbations at the edge of the boundary layer. Here, the boundary-layer response to the different inflow disturbances is analysed by considering an integrated norm for the disturbance amplitudes, defined as

$$\mathcal{I}_\eta(x) := \int_0^{\delta_{99}} \mathcal{A}_\eta(x, y) dy. \tag{3.6}$$

At $M_\infty = 6.0$, the three types of forced disturbances also give rise to a number of instability modes which grow and decay at different streamwise positions as they convect through their regions of instability. Figures 3.8(a) and 3.8(b) show that the amplitude functions of two growing Fourier modes with ($F = 0.06$, $k_z = 0.314$) and ($F = 0.18$, $k_z = 0.314$) respectively, extracted from the $M_\infty = 6.0$ DNS data at $x = 100$, match closely the eigenfunctions of a first mode with $c_{ph} = 0.88$ and a second mode with $c_{ph} = 0.92$. The $M_\infty = 2.5$ DNS data shows only one unstable mode, corresponding to ($F = 0.02$, $k_z = 0.314$). The LST eigenfunction of this mode is compared with the DNS amplitude function in figure 3.8(c), showing good agreement.

Contours of the real part of $\hat{p}_w$ (the Fourier transformed wall pressure) reveal that at $M_\infty = 6.0$ the disturbance field in the case of type A and type Æ disturbances is dominated by $\xi = 0$ (i.e. two-dimensional) first and second modes, while for type V perturbations the dominant modes are oblique. An example of this behaviour is given in figure 3.9, which shows the growth of the $\xi = 0$ Mack mode of instability for case $HSAI_a$ and a more three-dimensional disturbance field for case $HSVI_a$, characterised by the presence of oblique Mack modes, as will be shown later.

The excitation of unstable modes at $M_\infty = 6.0$ is registered for forcing frequencies $F \leq 0.22$, while at $M_\infty = 2.5$ for $F \geq 0.04$ all boundary layer disturbances are

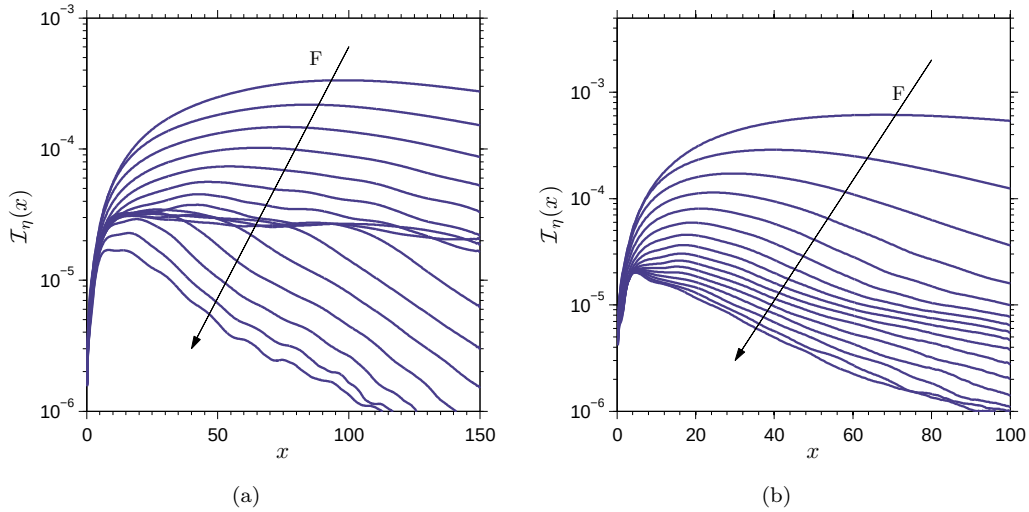

Figure 3.7: Transient growth of u' disturbances in the case of internal type V disturbances, sowing the boundary layer response for all the frequencies contained in the forcing signal ($0.02 \leq F \leq 0.32$). (a) $M_\infty = 6.0$, (b) $M_\infty = 2.5$.

stable. When the stable boundary layer modes decay the free-stream fast acoustic waves tend to dominate the near wall disturbance field, as shown in figure 3.10. This happens for $F > 0.28$ at $M_\infty = 6.0$ and for $F > 0.12$ at $M_\infty = 2.5$ and is more evident in the case of type Æ disturbances, since the perturbations present in the boundary layer edge, in the case of type V and type A disturbances, decay slowly downstream. The free-stream fast acoustic waves penetrate deeper inside the boundary layer than slow acoustic, vortical and entropy waves and excite boundary layer modes belonging to the fast acoustic continuous spectrum.

For inflow disturbances placed outside the boundary-layer, excitation of boundary-layer perturbations is weaker. This is shown in figures 3.11(a) and 3.11(b), where

$$|\mathcal{I}_\eta(\cdot)|_\infty := \max_{0 \leq x \leq L_x} [\mathcal{I}_\eta(x)] \tag{3.7}$$

is plotted for each forcing frequency and for the different inflow disturbances considered, giving the highest amplitude attained by the v' boundary-layer disturbances in each case. Internal type V and type A perturbations lead to higher amplitude disturbances compared to type Æ forcing, both at $M_\infty = 6.0$ and $M_\infty = 2.5$. The boundary-layer disturbance amplitudes obtained for type V forcing decrease about two orders of magnitude at $M_\infty = 6.0$ and more than three orders of magnitude at $M_\infty = 2.5$ when considering external disturbances. A similar, but lower magnitude effect, can also be noted for external type A and

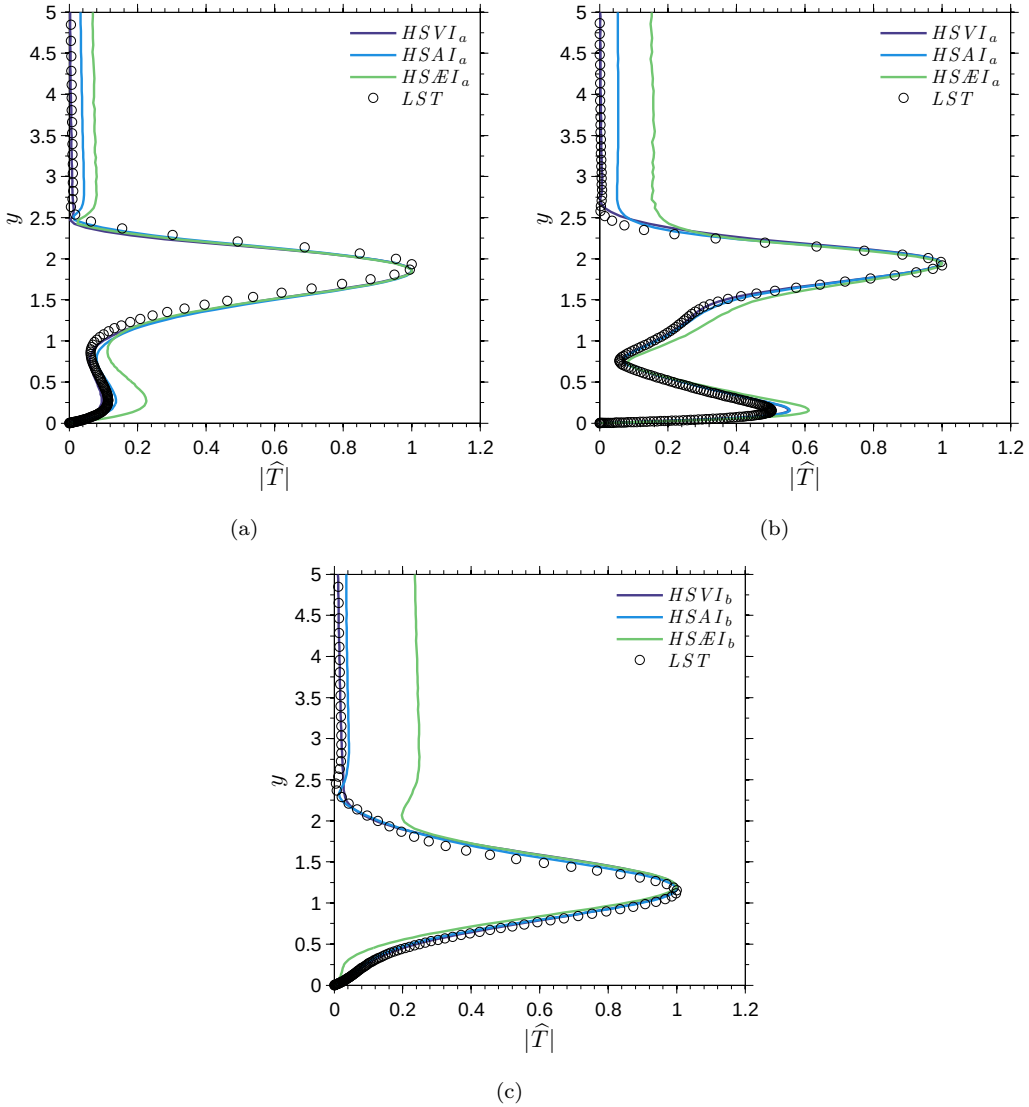

Figure 3.8: Comparison of DNS and LST eigenfunctions. (a) mode $F = 0.06$ and $k = 0.314$ at $M_\infty = 6.0$, (b) mode $F = 0.18$ and $k_z = 0.314$ at $M_\infty = 6.0$, (c) mode $F = 0.02$ and $k_z = 0.314$ at $M_\infty = 2.5$.

type Æ inflow perturbations, the trends being the same for the two Mach numbers considered.

To understand how the total disturbance amplitude is distributed over the spanwise modes we consider the parameter

$$\Lambda_{\eta,\xi} := \max_{0\le x\le L_x} \left[\frac{\int_0^{\delta_{99}} |\widehat{S}_{\eta,\xi}(x,y)|dy}{\mathcal{I}_\eta(x)} \right]. \tag{3.8}$$

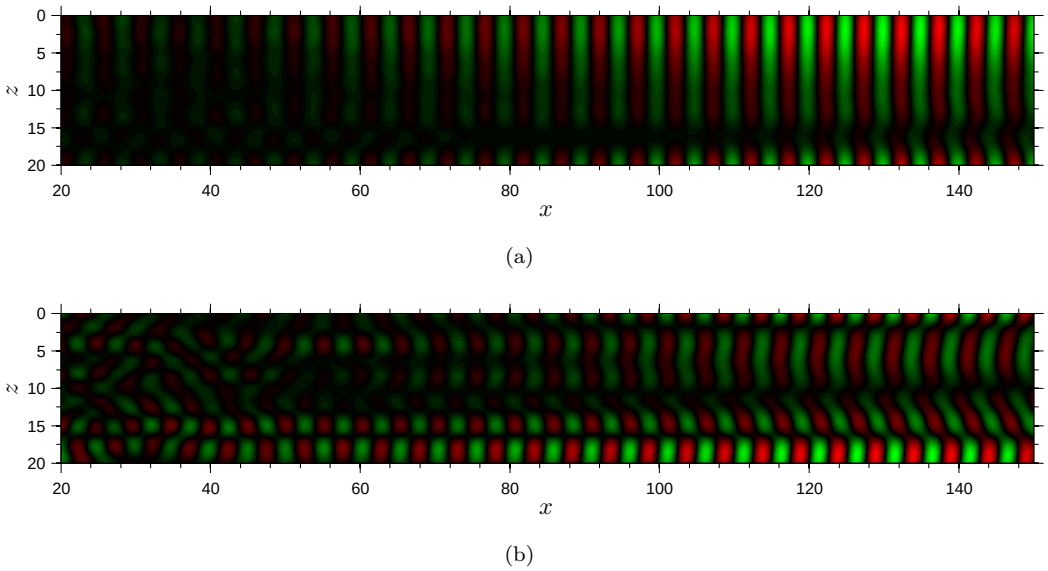

Figure 3.9: Contours of the real part of $\hat{p}_w$ for $F = 0.18$ showing the development of a Mack mode instability. (a) case $HSAI_a$ (contour limits $\Re\{\hat{p}_w\} = \pm 9.5 \times 10^{-5}$), (b) case $HSVI_a$ (contour limits $\Re\{\hat{p}_w\} = \pm 2.2 \times 10^{-5}$).

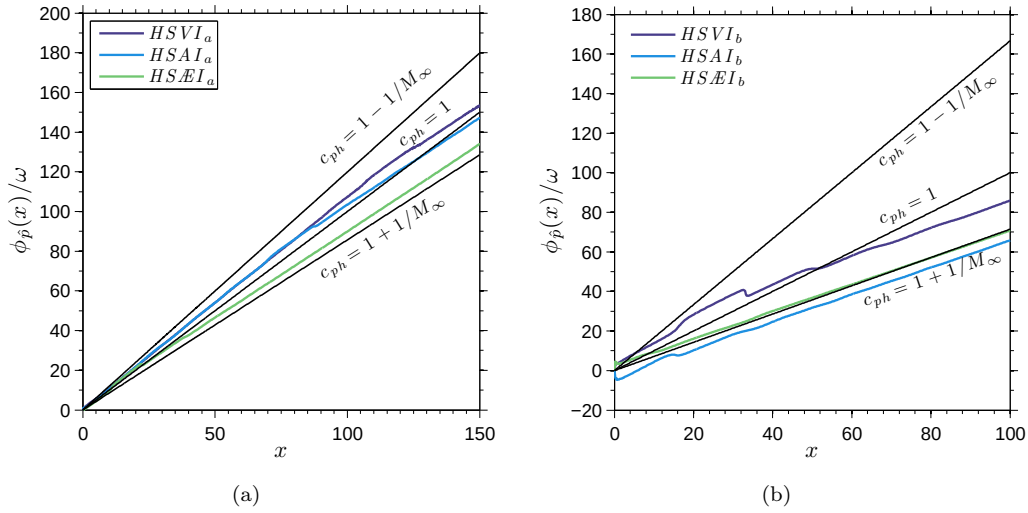

Figure 3.10: Streamwise $\phi(x)/\omega$ evolution for p' disturbances at the wall, showing that fast acoustic waves dominate the near wall disturbance field for certain frequencies. (a) $F = 0.28$ at $M_\infty = 6.0$, (b) $F = 0.12$ at $M_\infty = 2.5$.

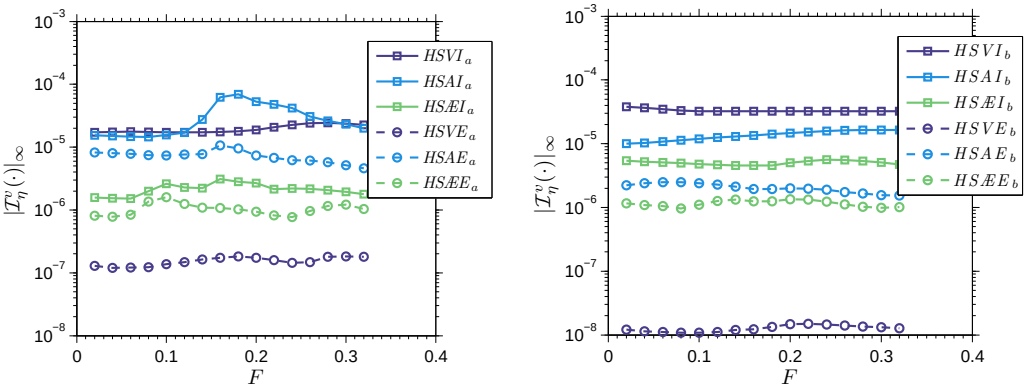

(a) (b)

Figure 3.11: Maximum total amplitude of boundary-layer disturbances for the different forcing frequencies. (a) $M_\infty = 6.0$, (b) $M_\infty = 2.5$.

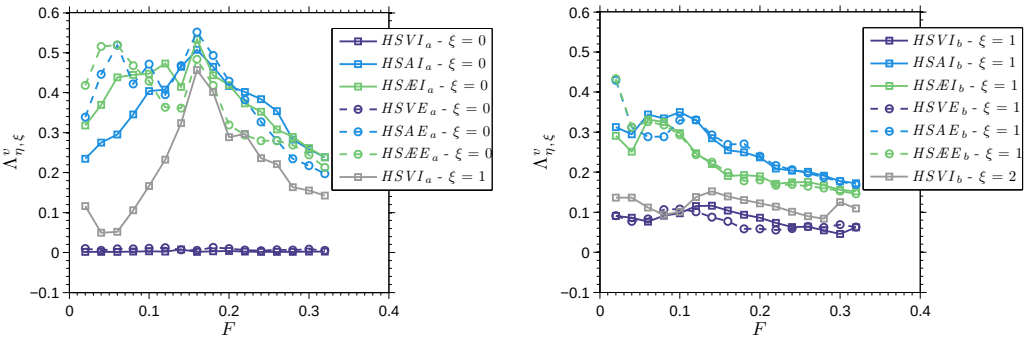

(a) (b)

Figure 3.12: Contribution of single spanwise modes to the total amplitude of disturbances inside the boundary-layer for the different forcing frequencies. (a) $M_\infty = 6.0$, (b) $M_\infty = 2.5$.

Figures 3.12(a) and 3.12(b) show $\Lambda_{\eta,\xi}^v$ for the different frequencies and inflow disturbances considered for $M_\infty = 6.0$ and $M_\infty = 2.5$, respectively. At $M_\infty = 6.0$, the $\xi = 0$ mode plays a crucial role for internal and external type A and type Æ perturbations. In particular, a peak is visible for frequencies in the range $0.14 \leq F \leq 0.24$, corresponding to the frequency range of the unstable Mack modes. The Mack mode amplitudes decrease for these two types of disturbances in the case of external forcing. These cases also show dominant $\xi = 0$ modes at the low frequencies as a consequence of the excitation of $\xi = 0$ first modes. As can be seen, the contribution of the $\xi = 0$ mode for internal and external type V disturbances is insignificant. For case $HSVI_a$ high amplitude $\xi = 1$ modes, relative to the total disturbance amplitude inside the boundary layer, appear for frequencies in the range of the unstable Mack modes. This behaviour correlates with

the presence of unstable Mack modes for $\xi = 1$, already shown in figure 3.8(b). On the other hand, external type V disturbances do not lead to any significant Mack modes inside the boundary layer. At $M_\infty = 2.5$ the $\xi = 1$ modes have high relative amplitudes at the low frequencies for type A and type Æ disturbances. However, due to the absence of unstable boundary layer modes, with the exception of the unstable first mode at $F = 0.02$, the total disturbance energy is more evenly spread among the different spanwise wavenumbers, particularly in the case of type V disturbances.

The same disturbances used here to perturb the smooth flat plate boundary layer are also employed to study the stability of the steady-state laminar flow over isolated roughness elements under different conditions, the details of which are presented in section 3.5.

3.4 Grid convergence study and influence of filtering

In this section, we test the effects of different grid resolutions and choice of filtering parameter σ in equation 2.14. The test is carried out for cases *HR1.0AI*$_a$ and *HR1.0AI*$_b$ which, as will be shown later, are the cases showing the highest disturbance amplification. The effects of grid resolution are considered by testing

Case	Block	N_x	N_y (n_y^r)	N_z	b_y	Δx	Δz
HR1.0$_a$	B1	128	103 (31)	74	3.80	[0.4, 0.1]	0.08
	B2	59	73 (-)	74	3.80	0.10	0.08
	B3	299	103 (31)	74	3.80	[0.10, 0.40]	0.08
	B4	128	103 (31)	66	3.80	[0.40, 0.10]	[0.08, 0.40, 0.08]
	B5	59	103 (31)	66	3.80	0.10	[0.08, 0.40, 0.08]
	B6	299	103 (31)	66	3.80	[0.10, 0.40]	[0.08, 0.40, 0.08]
HR1.0$_b$	B1	128	103 (31)	74	3.80	[0.4, 0.1]	0.08
	B2	59	73 (-)	74	3.80	0.10	0.08
	B3	174	103 (31)	74	3.80	[0.10, 0.40]	0.08
	B4	128	103 (31)	66	3.80	[0.40, 0.10]	[0.08, 0.40, 0.08]
	B5	59	103 (31)	66	3.80	0.10	[0.08, 0.40, 0.08]
	B6	174	103 (31)	66	3.80	[0.10, 0.40]	[0.08, 0.40, 0.08]

Table 3.3: Coarse computational grids used to to quantify the effects of different grid resolutions.

two grids; the reference grid (details of which can be found in table 3.2 on page 33) and a coarse grid (given in table 3.3) for each case. The filtering parameters considered for the analysis of the effects introduced by filtering are $\sigma = 0.14$ and $\sigma = 0.28$ for $M_\infty = 6.0$ and $\sigma = 0.05$ and $\sigma = 0.10$ for $M_\infty = 2.5$. Two quantities will be considered for the test; the streamwise evolution of the Fourier transformed pressure amplitude at the wall ($\mathcal{A}^p_\eta(x,0)$) and the same quantity integrated in the

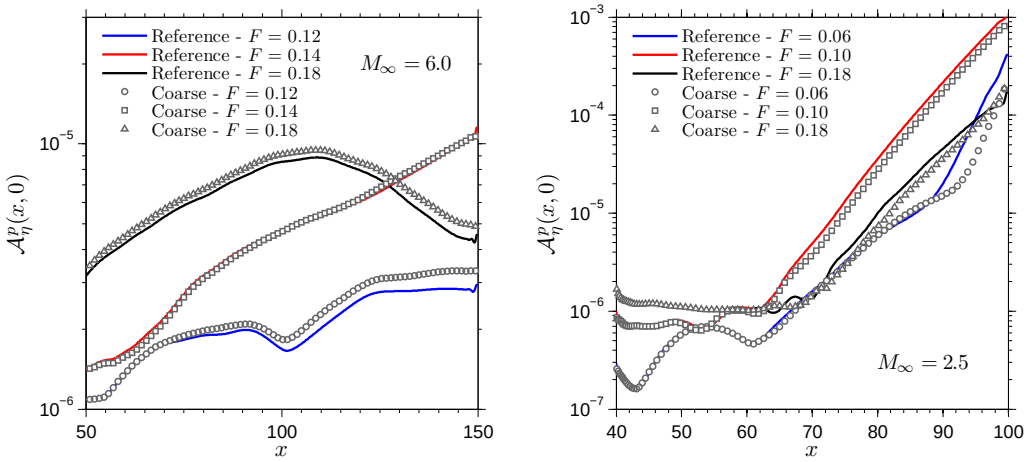

(a) (b)

Figure 3.13: Effect of grid resolution on the streamwise evolution of disturbances downstream of the roughness element. (a) *HR1.0AI*$_a$, (b) *HR1.0AI*$_b$

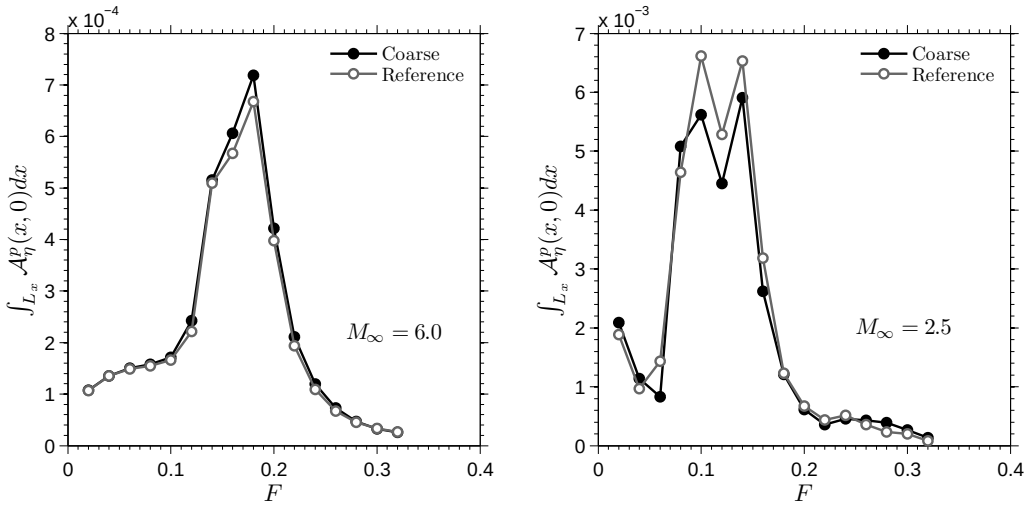

(a) (b)

Figure 3.14: Effect of grid resolution on the overall boundary layer response to the incoming disturbances. (a) *HR1.0AI*$_a$, (b) *HR1.0AI*$_b$

streamwise direction ($\int_{L_x} \mathcal{A}_\eta^p(x,0)dx$). Figures 3.13(a) and 3.13(b) show the effect of grid resolution on $\mathcal{A}_\eta^p(x,0)$ for a selection of frequencies at $M_\infty = 6.0$ and $M_\infty = 2.5$ respectively. It can be seen that the different grid resolutions do not lead to significant differences in the growth rates of disturbances developing downstream of the roughness element. Some differences in disturbance amplitudes can be observed, particularly for $F = 0.12$ at $M_\infty = 6.0$ starting from $x = 100$ and for $F = 0.06$ at $M_\infty = 2.5$ for $x > 90$ (note that the growth of $F = 0.06$ disturbances for $x > 90$ in this case is associated with weakly nonlinear interactions which are not of interest in this part of the study). The effect of grid resolution over the entire frequency range of inflow disturbances is given in figures 3.14(a) and 3.14(b) for $M_\infty = 6.0$ and $M_\infty = 2.5$ respectively. It can be seen that, overall, the response of the laminar flow to the forced disturbances is well captured by the two grids considered, both at $M_\infty = 6.0$ and $M_\infty = 2.5$.

The effect of filtering is shown in figures 3.15(a) and 3.15(b) for $M_\infty = 6.0$ and $M_\infty = 2.5$ respectively. The boundary layer response to the incoming disturbances is practically identical for the two levels of filtering considered. This was also the case for the streamwise variation of disturbance amplitude (not shown).

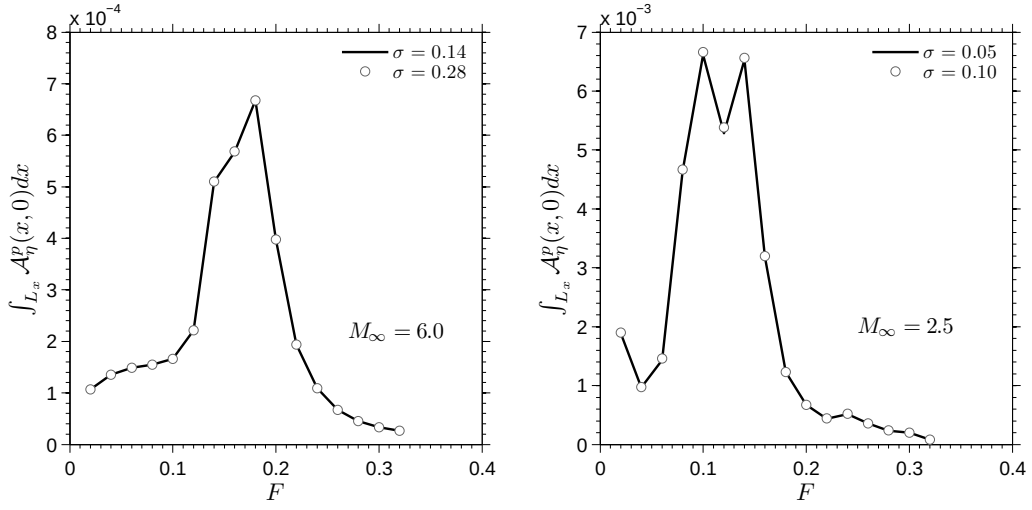

(a) (b)

Figure 3.15: Effect of filtering parameter on the overall boundary layer response to the incoming disturbances. (a) *HR1.0AI*$_a$, (b) *HR1.0AI*$_b$

3.5 Analysis of the basic flow in the presence of roughness

The steady-state laminar flow over the roughness element is analysed here by comparison with the flow over a clean flat plate. Our interest is to highlight the modifications induced by the roughness element, which will determine the stability characteristics of the laminar flow, and how these vary with Mach number, roughness height and wall temperature.

The roughness element induces two regions of separated flow, located immediately upstream and downstream of it, as can be seen in figure 3.16 for cases $HR1.0_a$ ($M_\infty = 6.0$) and $HR1.0_b$ ($M_\infty = 2.5$) through isosurfaces of small negative streamwise velocity in blue. The centreline bubble lengths for the three configurations are provided in Table 3.4. Cases with $h = 1.0$ show comparable upstream and downstream bubble lengths, with the downstream bubble being only slightly longer. A reduction of roughness height by a factor of two leads to an upstream bubble length

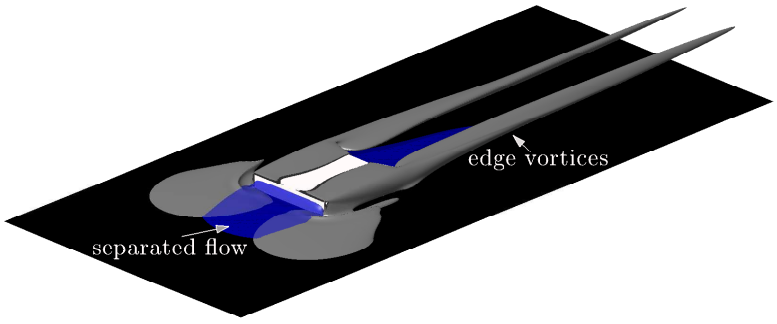

(a)

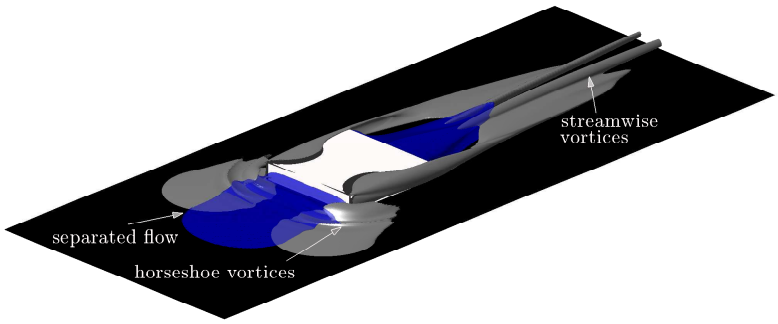

(b)

Figure 3.16: Flow topology around the roughness element: (a) $HR1.0_a$, (b) $HR1.0_b$. Isosurfaces of small negative u show the separated flow regions in blue. Grey isosurfaces of ω_x, positive on the right and negative on the left part of the computational domain looking downstream, show the roughness-induced vortices.

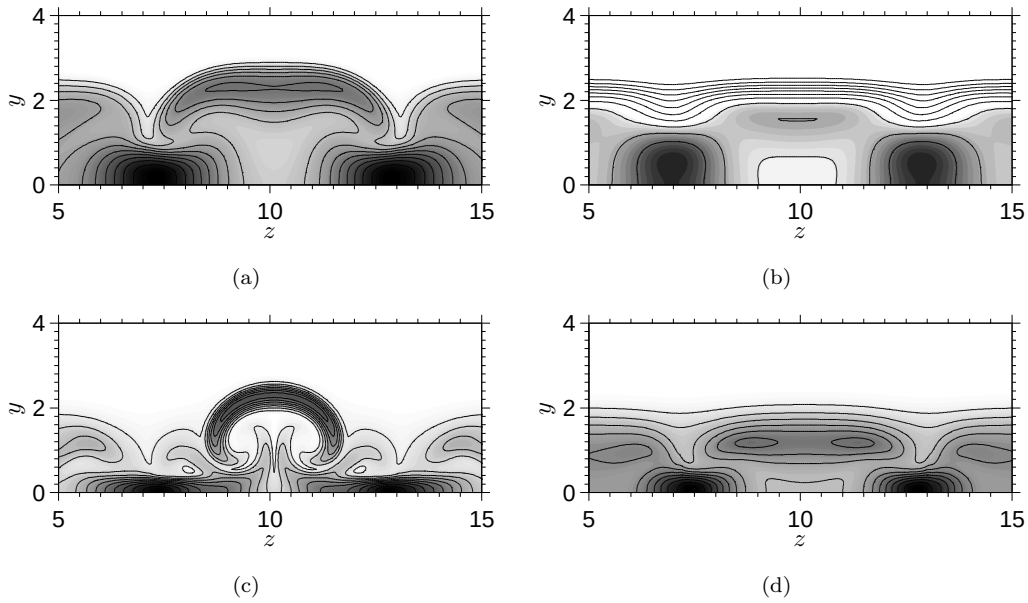

Figure 3.17: Contours of $u_S := \sqrt{(\partial u/\partial y)^2 + (\partial u/\partial z)^2}$ showing the localised shear generated by the roughness-induced counter-rotating vortices. (a) $M_\infty = 6.0$, $h = 1.0$ at $x = 120$, (b) $M_\infty = 6.0$, $h = 0.5$ at $x = 120$, (c) $M_\infty = 2.5$, $h = 1.0$ at $x = 80$, (d) $M_\infty = 2.5$, $h = 0.5$ at $x = 80$.

reduction of about 62% for $M_\infty = 2.5$ and about 61% for $M_\infty = 6.0$. The length of the separation bubble induced downstream of the roughness element reduces by about 25% for $M_\infty = 2.5$ and about 73% for $M_\infty = 6.0$. For both Mach numbers wall cooling seems to only affect the downstream separation bubble and reduces its length slightly. As will be discussed later, no steady solution was obtained for case *HR1.0*$_b$, hence the bubble lengths were time averaged.

The roughness wake is characterised by the presence of regions of high streamwise vorticity. A pair of streamwise vortices are generated at the roughness edges due to a small difference in pressure between the top (lower) and the sides (higher) of

Case	L_{sep} (Upstream)	L_{sep} (Downstream)
HR1.0$_a$	5.9	9.9
HR0.5$_a$	2.3	2.7
CR1.0$_a$	6.0	9.0
HR1.0$_b$	7.7	9.6
HR0.5$_b$	2.9	7.2
CR1.0$_b$	7.7	9.3

Table 3.4: Separation bubble lengths for the three different configurations considered.

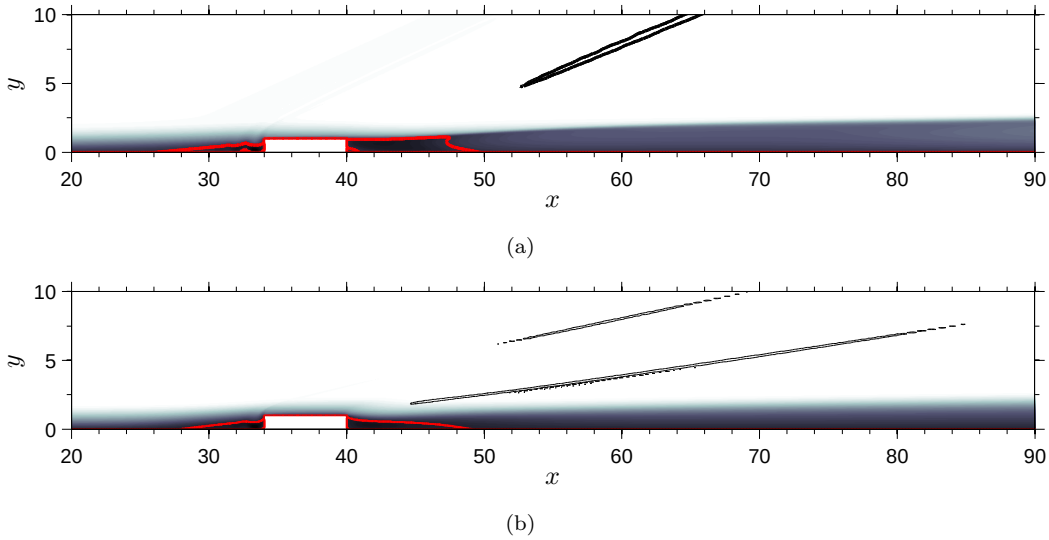

Figure 3.18: Contours of u. Separated flow regions and reattachment shock shown as $u = 0$ (red line) and negative $\nabla \cdot \mathbf{u}$ (black line) respectively. (a) case *HR1.0*$_a$, (b) case *CR1.0*$_b$.

the roughness, as shown in figure 3.16(a) for case *HR1.0*$_a$, which appear in all the cases analysed. Cases *HR1.0*$_b$ and *CR1.0*$_b$ show, in addition to the edge vortices, a pair of strong counter-rotating streamwise vortices forming as the flow reattaches downstream of the roughness. These vortices can be observed in figure 3.16(b) near the roughness mid-plane for case *HR1.0*$_b$. The vortices present in the roughness wake lift-up low momentum fluid from the near wall region, generating a low velocity streak away from the wall, and induce regions of localised high $\partial u/\partial y$ and $\partial u/\partial z$ shear, shown in figure 3.17 as contours of $u_S := \sqrt{(\partial u/\partial y)^2 + (\partial u/\partial z)^2}$ for the different Mach numbers and roughness heights considered. Convective instabilities may easily develop in high detached shear layers.

The flow displacement caused by the roughness induces a compression in the upstream region of the flow, which for the $M_\infty = 6.0$ cases eventually develops into an oblique shock further downstream, followed by an expansion as the flow turns over the top of the roughness. When the flow reattaches downstream a fan of compression waves forms and merges into a weak oblique shock both for $M_\infty = 2.5$ and $M_\infty = 6.0$. The roughness induced shocks are shown in figure 3.18 for cases *HR1.0*$_a$ and *CR1.0*$_b$. The strength of these shocks decreases with the height of the roughness and with increasing wall temperature due to local Mach number effects. Shock-waves can interact with the incoming disturbance field and influence the development of instability modes downstream of the roughness.

3.6 Roughness receptivity at $M_\infty = 6.0$

This section focuses on the results obtained for roughness-induced receptivity and transition at $M_\infty = 6.0$. The analysis starts with a discussion of the effects of roughness height on the boundary layer stability under the action of type A disturbances. The analysis of the results obtained for the different inflow disturbances in the presence of a roughness element with $h = 1.0$ follows and the section ends with a discussion of the effects of wall cooling on the flow stability in the case of type A inflow disturbances.

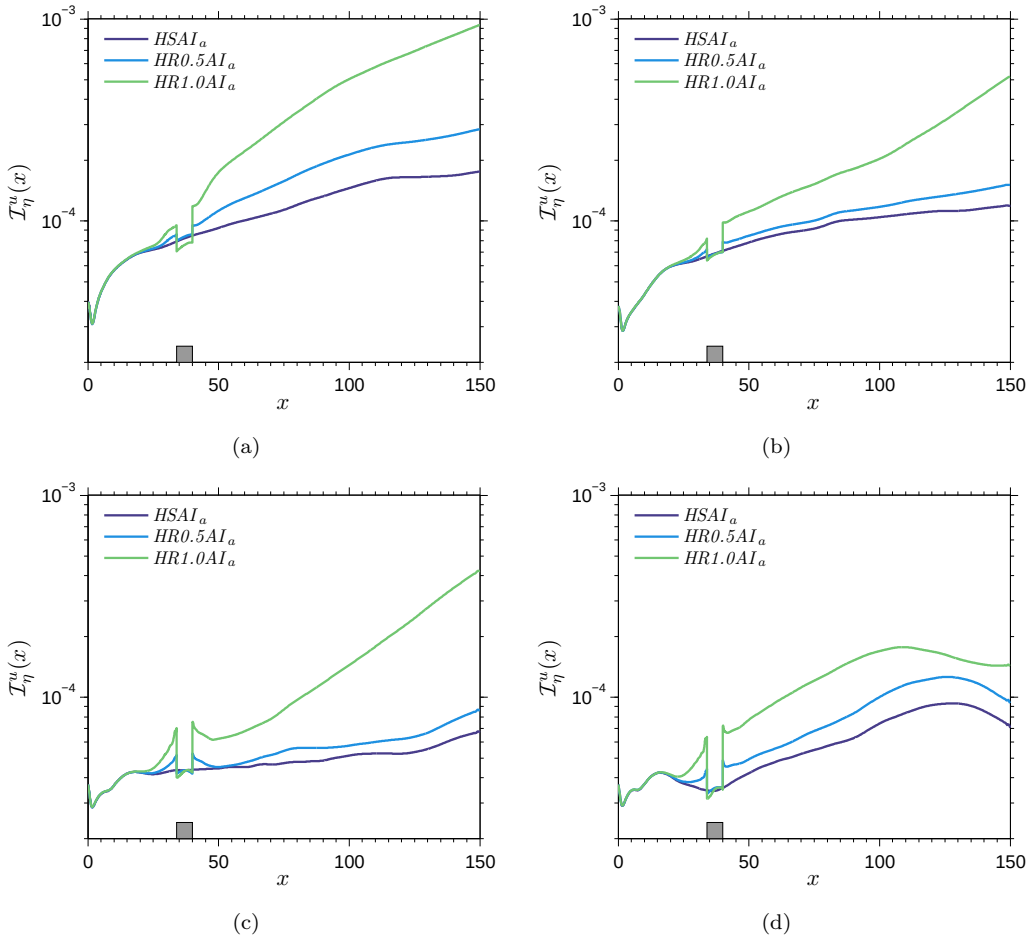

Figure 3.19: Streamwise evolution of u' disturbances inside the boundary-layer for cases $HSAI_a$, $HR0.5AI_a$ and $HR1.0AI_a$. (a) $F = 0.02$, (b) $F = 0.06$, (c) $F = 0.14$, (d) $F = 0.18$.

3.6.1 Effect of roughness height

The influence of roughness height on the boundary-layer stability is analysed by comparing cases $HSAI_a$, $HR0.5AI_a$ and $HR1.0AI_a$, which consider the effects of type A perturbations for a smooth flat plate and for two different roughness heights. The boundary-layer response to frequencies $F = 0.02$, $F = 0.06$, $F = 0.14$ and $F = 0.18$ is shown in figure 3.19 for the three cases considered. The disturbances enter the boundary-layer near the inflow boundary and are weakly amplified in the upstream separation bubble. In the region immediately downstream of the roughness element the boundary-layer disturbances redistribute into the modes of the new basic flow, leading to a short amplification or decay depending on the frequency considered. For the frequencies shown in figure 3.19 this results in an overall disturbance amplification which is more prominent for the taller roughness elements. Further downstream, the disturbance evolution for case $HR0.5AI_a$ tends to follow the same behaviour shown by the smooth flat plate case, indicating that the small roughness element mainly acts as a disturbance amplifier. Inspection of the boundary-layer disturbance field in the presence of the small roughness element reveals that the disturbance amplification observed is mainly due to an increased receptivity of the boundary-layer modes developing away from the roughness wake.

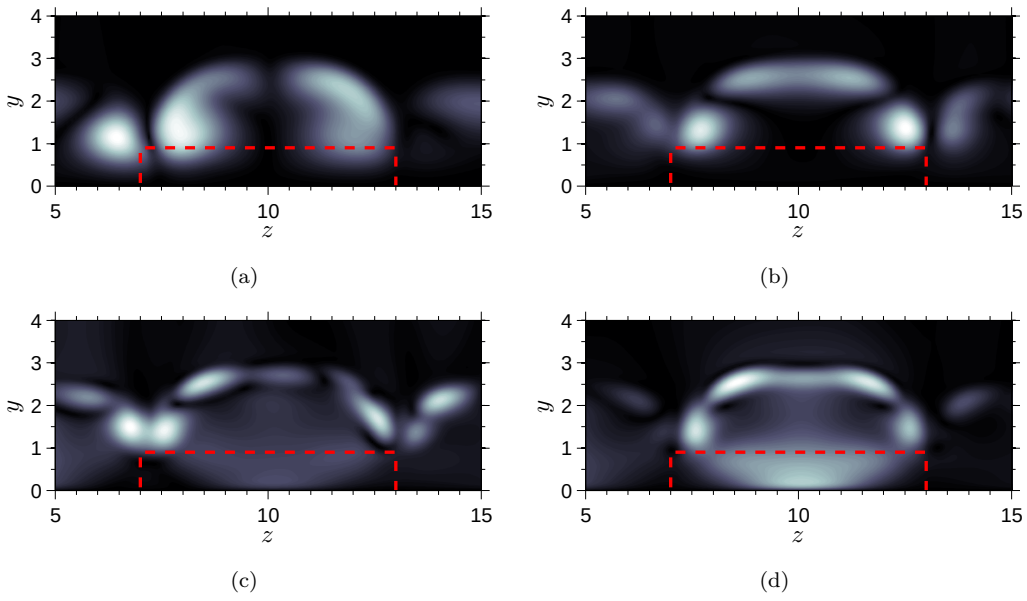

Figure 3.20: Contours of $|\hat{u}|$ in a crossflow plane at $x = 140$ showing the shape of the instability modes developing in the roughness wake for case $HR1.0AI_a$. The red dashed line indicates the roughness position. (a) $F = 0.02$, (b) $F = 0.06$, (c) $F = 0.12$, (d) $F = 0.14$.

The boundary layer disturbances for case $HR0.5AI_a$ have higher amplitudes than those observed in case $HSAI_a$ but show the same growth rates.

A different scenario appears for $h = 1.0$. The difference in disturbance growth rates registered between case $HR1.0AI_a$ and $HSAI_a$, particularly for $F \leq 0.16$, reveals the presence of additional instability modes induced by the localised roughness element. At low frequencies (see for example $F = 0.02$ in figure 3.19a), disturbances experience a strong amplification, reminiscent of algebraic growth, and as a result low frequency modes are the most energetic in the boundary-layer region spanned by the computational domain. On the other hand, disturbances grow faster at higher frequencies, hence the final stages of transition are more likely to be driven by these more unstable modes. In particular, two linear growth rate maxima appear for $F = 0.06$ and $F = 0.14$, shown in figures 3.19(b) and 3.19(c) respectively. The disturbance amplification observed for $F = 0.18$ in all cases is associated with a Mack mode instability developing in the lateral boundary layer regions away from the roughness wake with a growth rate of $-\alpha_i \approx 0.024$, which

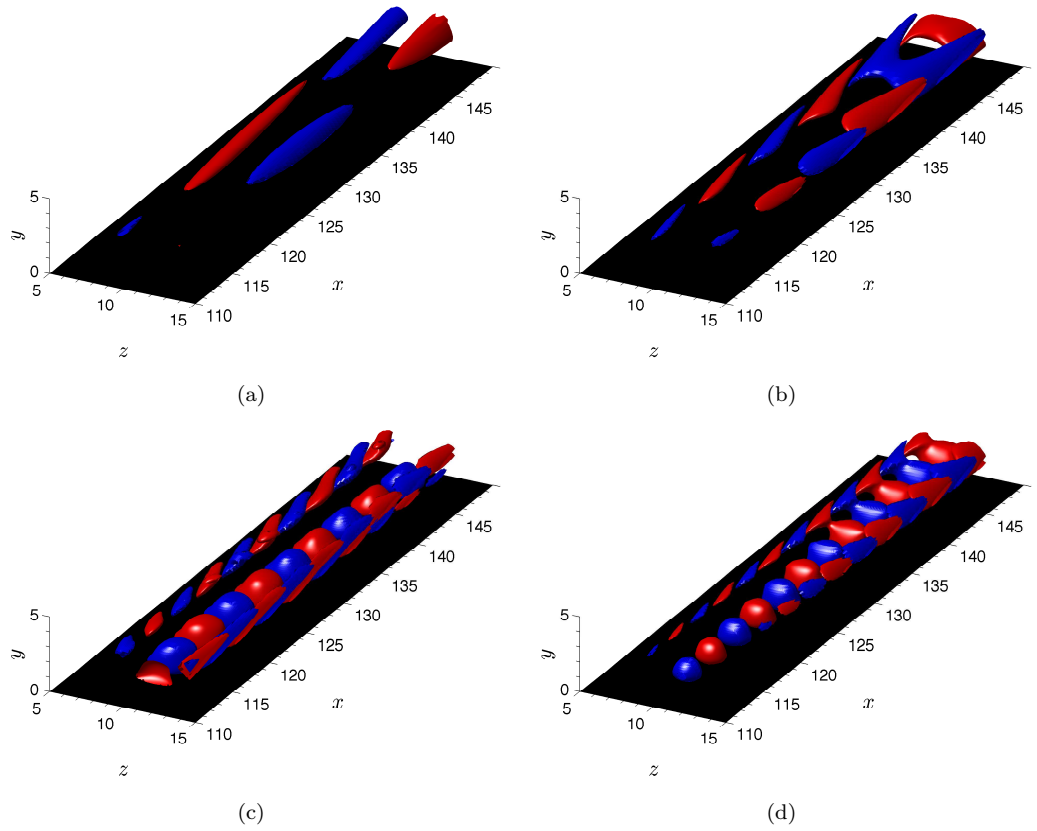

Figure 3.21: Isosurfaces of $\Re\{\hat{v}\}$ showing the three-dimensional structure of the wake modes for case $HR1.0AI_a$. (a) $F = 0.02$, (b) $F = 0.06$, (c) $F = 0.12$, (d) $F = 0.14$.

agrees well with the LST prediction for the Mack mode growth rates at $x = 70$, as already discussed in the previous section. Both the $h = 0.5$ and $h = 1.0$ roughness elements lead to an amplitude boost and a shortening of the region of instability for disturbances with $F = 0.18$ and $F = 0.20$. The amplitude boost seems to be associated with an enhanced receptivity of the Mack modes. At higher frequencies boundary-layer disturbances are damped by the roughness.

The nature of the instability modes developing downstream of the roughness for case *HR1.0AI*$_a$ is shown in figures 3.20 and 3.21 for some of the most amplified frequencies. The plots in figure 3.20 show contours of $|\hat{u}|$ in a crossflow plane at $x = 140$, while figure 3.21 shows the three-dimensional structure of the modes through isosurfaces of the real part of $\hat{v}$ (the Fourier transformed v-velocity). For $F = 0.02$, high disturbance amplitudes are registered near the lateral shear layer at ($y \approx 1.0$, $z \approx 7.0$) in figure 3.20(a) and the instability mode manifests itself as a sinuous deformation of the low velocity streak, as can be inferred from figure 3.21(a). For $F = 0.06$ disturbances grow in the two lateral shear layers at ($y \approx 1.0$, $z \approx 7.0$) and ($y \approx 1.0$, $z \approx 14.0$) in figure 3.20(b). The non-zero u' disturbances at the roughness mid-plane reveal the presence of a varicose instability mode for this frequency, and this is corroborated by the isosurfaces of $\Re\{\hat{v}\} = \pm 1.5 \times 10^{-4}$ in figure 3.21(b). At higher frequencies, a different type of instability mode, which is associated with a near wall amplitude maximum at the roughness mid-plane, develops in the wake of the roughness. This mode starts becoming visible for $F = 0.12$ in figures 3.20(c) and 3.21(c), and dominates the instability of the wake at $F = 0.14$, as shown in figure 3.20(d), and at $F = 0.16$, leading to a varicose streak deformation.

The sinuous and varicose modes observed for $F = 0.02$ and $F = 0.06$ respectively, are a consequence of instabilities growing in the lateral shear layers induced by the roughness in its wake. In this case, sinuous and varicose modes seem to develop when the shear layer instabilities, developing on opposite sides of the roughness wake, are in or out of phase, respectively. For future reference, we name the $F = 0.02$ and $F = 0.06$ modes as Sinuous Lateral (SL) and Varicose Lateral (VL), respectively. The varicose mode observed for $F = 0.14$ seems to be of a different nature. Its amplitude function shows similarities with that of mode VL, with amplitude maxima at the edges of the streak. However, it also shows a near wall amplitude maximum at the centre of the roughness wake. The origin of this mode, which will be referred to as Varicose Centred (VC), is unclear, however it seems to be closely linked with the development of Mack mode instabilities inside the boundary layer, as will be better explained later. Interestingly, figure

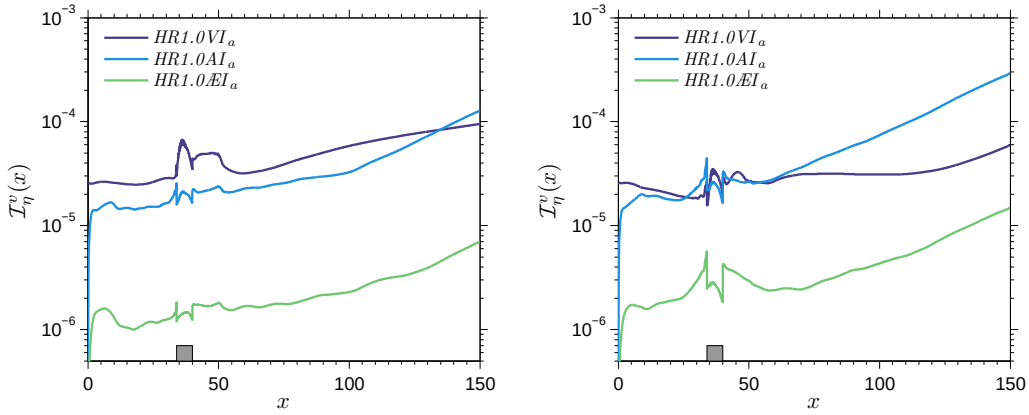

Figure 3.22: Streamwise evolution of v' disturbances inside the boundary-layer for cases $HR1.0VI_a$, $HR1.0AI_a$ and $HR1.0ÆI_a$. (a) $F = 0.06$, (b) $F = 0.14$.

3.21(c) shows that the near wall maximum first grows and later decays towards the end of the computational domain, where the lateral maxima continue growing. This seems to indicate that the range of unstable frequencies for modes VC and VL overlap and in some cases the amplitude functions observed might be the result of superpositions of multiple modes. Mode superposition may also explain the asymmetric amplitude functions observed for certain modes, as for example in figure 3.20(a), as it can potentially lead to destructive and/or constructive interferences and cause local amplitude maxima and minima.

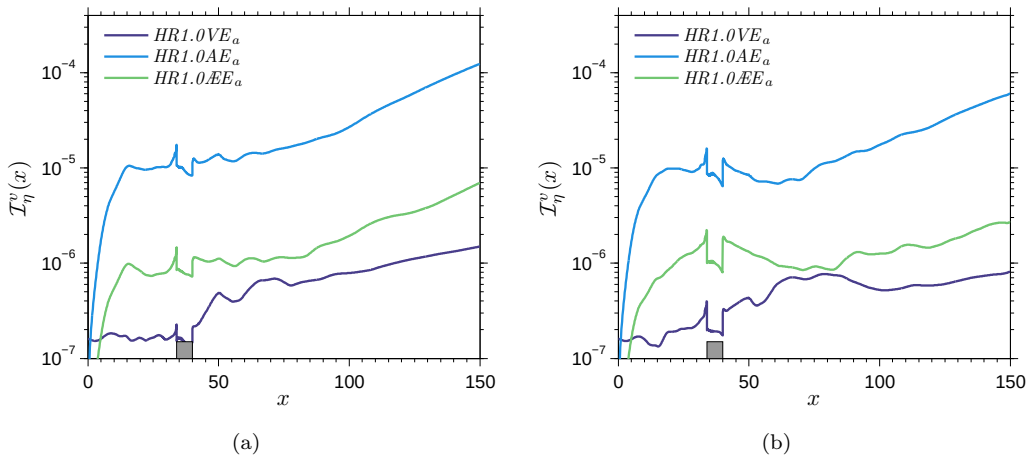

Figure 3.23: Streamwise evolution of v' disturbances inside the boundary-layer for cases $HR1.0VE_a$, $HR1.0AE_a$ and $HR1.0ÆE_a$. (a) $F = 0.06$, (b) $F = 0.14$.

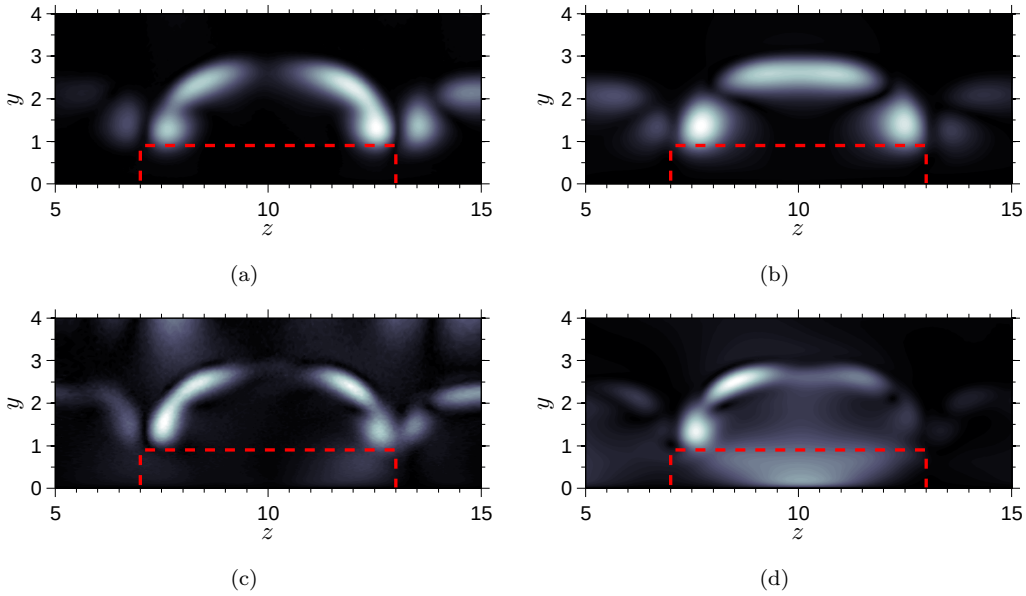

Figure 3.24: Contours of $|\hat{u}|$ in a crossflow plane at $x = 140$ showing the shape of the instability modes developing in the roughness wake for different inflow disturbances. The red dashed line indicates the roughness position. (a) $F = 0.06$ for case $HR1.0VE_a$, (b) $F = 0.06$ for case $HR1.0AE_a$, (c) $F = 0.14$ for case $HR1.0VE_a$, (d) $F = 0.14$ for case $HR1.0AE_a$.

3.6.2 Effect of disturbance type and position

The effect of different inflow disturbances on the flow instability is analysed here for a roughness element with $h = 1.0$. We consider both the effects of forcing functions with zero (external) and nonzero (internal) amplitudes inside the boundary-layer. Figure 3.22 shows the boundary-layer response to internal disturbances of type V, A and Æ for $F = 0.06$ and $F = 0.14$, through the streamwise evolution of v' disturbances inside the boundary-layer. Differences appear in the initial excitation of disturbances, with cases $HR1.0VI_a$ and $HR1.0AI_a$ showing considerably higher disturbance amplitudes inside the boundary-layer than those observed for case $HR1.0ÆI_a$. Although growth of instability modes for case $HR1.0VI_a$ can be seen in figure 3.22(b) from $x \approx 120$, this tends to be buried inside the weakly damped v' perturbations introduced at the edge of the boundary-layer. Interestingly, these perturbations, and the associated algebraic growth of ρ', u', w' and T', seem to have little effect on the receptivity of downstream instability modes, which are more amplified in case $HR1.0AI_a$, despite the total disturbance amplitudes upstream of the roughness being lower than for case $HR1.0VI_a$. Far enough downstream of the roughness the three cases show similar disturbance growth rates

for certain frequencies (i.e. $F = 0.14$ in figure 3.32(d)), while for other frequencies (i.e. $F = 0.06$ in figure 3.22(a)) lower growth rates are registered for case *HR1.0VI*$_a$. An inspection of the $\hat{u}$ amplitude functions indicates that mode SL is the dominant instability at $F = 0.06$ for case *HR1.0VI*$_a$, while for cases *HR1.0AI*$_a$ and *HR1.0ÆI*$_a$ mode VL drives the wake instability at the same frequency. The different growth rates are then explained by the different dominant modes and indicate that mode VL is more unstable than mode SL.

The effect of disturbance position is analysed by comparing the previous results for internal disturbances with cases *HR1.0VE*$_a$, *HR1.0AE*$_a$, *HR1.0ÆE*$_a$, which are initially external to the boundary layer. The results show that type A and type Æ perturbations penetrate the boundary-layer and excite the boundary-layer modes to higher amplitudes than in the case of type V disturbances. This in turn affects the receptivity of shear layer modes in the region downstream of the roughness. The overall picture shows that the range of unstable frequencies is the same for internal and external perturbations, while the disturbance amplitudes inside the boundary-layer are smaller for the case of external forcing. This behaviour correlates with the excitation of boundary-layer instability modes upstream of the roughness, which was found to be weaker in the case of external disturbances. The three forcing functions considered show similar disturbance growth downstream of the roughness. However, there are differences between case *HR1.0VE*$_a$ and the other two cases in the disturbance growth rates for some frequencies, as can be noted in figure 3.23 for $F = 0.06$ and $F = 0.14$. Amplitude functions in a cross-flow plane at $x = 140$, shown in figure 3.24 for cases *HR1.0VE*$_a$ and *HR1.0AE*$_a$, reveal that the growth of disturbances registered behind the roughness for case *HR1.0VE*$_a$ is associated with a mode SL instability, while for cases *HR1.0AE*$_a$ and *HR1.0ÆE*$_a$ the wake instability is driven by modes VL and VC for $F = 0.06$ and $F = 0.14$, respectively. It is interesting to note that for internal type V disturbances the dominant wake mode for $F = 0.14$ is mode VC, while mode SL dominates for external disturbances of the same type. The streamwise evolution of $\mathcal{I}_\eta^v$, shown in figures 3.22 and 3.23, can be used to estimate the growth rates of the most unstable wake modes. The growth rate of mode VL at $F = 0.06$ is $-\alpha_i \approx 0.029$ while for mode VC at $F = 0.14$, $-\alpha_i \approx 0.027$. On the other hand, the growth of mode SL is $-\alpha_i \approx 0.012$ for $F = 0.06$ and $-\alpha_i \approx 0.010$ for $F = 0.14$. Sinuous and varicose instability modes were also found recently by Choudhari *et al.* (2009, 2012) growing in the wakes of an array of ramp trips and diamond shaped roughness elements in a $M_\infty = 6.0$ boundary layer. Contrary to what was found in this work, their bi-global eigenvalue analysis shows that sinuous modes

are more unstable than varicose ones. The roughness Reynolds number considered by Choudhari *et al.* (2012) in the case of diamond shaped trips was $Re_h = 567$ (for a hot wall), higher than that considered here. As will be shown in chapter 4, for $Re_h = 726$ the dominant linear instability seems to be of sinuous type.

A possible explanation for the excitation of different wake instability modes (modes SL, VL and VC) under different disturbance fields is provided in figure 3.25, which gives contour plots of the real part of $\hat{u}$ in a x-z plane at $y = 0.9$. The excitation of varicose modes, found to be dominant for internal and external type A and type Æ disturbances, seems to be related to the high amplitude two-dimensional ($\xi = 0$)

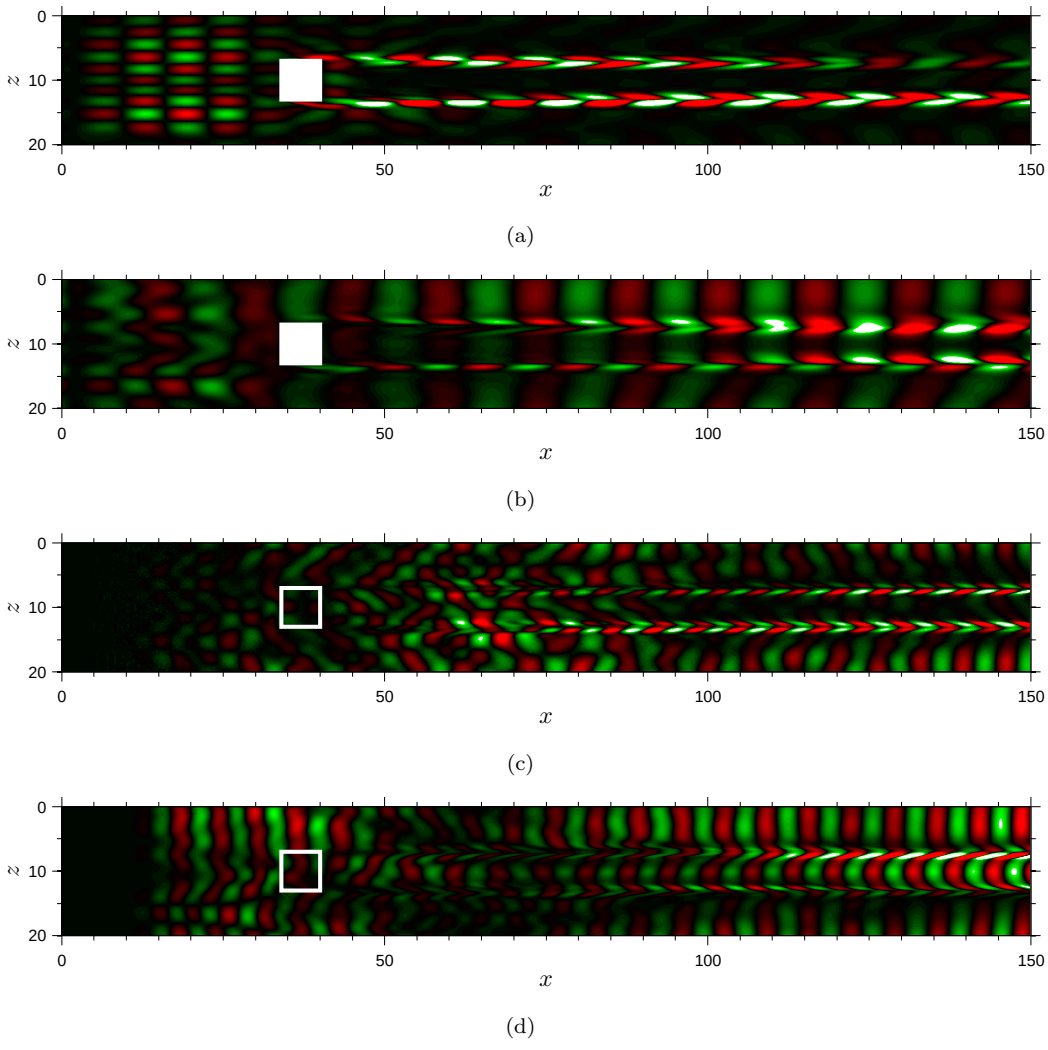

Figure 3.25: Contours of the real part of $\hat{u}$ showing the excitation of wake instability modes. The white squares indicate the roughness location. (a) $F = 0.06$ for case $HR1.0VI_a$ at $y = 0.88$, (b) $F = 0.06$ for case $HR1.0AI_a$ at $y = 0.88$, (c) $F = 0.14$ for case $HR1.0VE_a$ at $y = 1.2$, (d) $F = 0.14$ for case $HR1.0AE_a$ at $y = 1.2$.

boundary-layer modes observed in these cases. At $F = 0.06$, boundary layer disturbances with high spanwise wavenumbers dominate for case *HR1.0VI*$_a$ upstream of the roughness and the wake instability downstream is sinuous, see figure 3.25(a). The two-dimensional disturbances observed in figure 3.25(b) are $\xi = 0$ first mode instabilities, which dominate at the low frequencies for type A and type Æ disturbances, as already shown in Section 3.3. These modes seem to be responsible for the preferred excitation of varicose modes, as they tend to force a symmetric wake response. A similar scenario appears for $F = 0.14$, as show in figures 3.25(c) and 3.25(d). This time, however, the dominant two-dimensional perturbations found for type A and type Æ disturbances are manifestations of unstable $\xi = 0$ Mack modes growing inside the boundary layer. Sinuous and varicose lateral (SL and VL) wake modes share the same range of unstable frequencies and one mode may be dominant over the other depending on the disturbance field upstream of the roughness. Generic three-dimensional disturbances lead to the excitation of mode SL, while two-dimensional disturbance fields force the wake response towards mode VL. Mode VC, found to play an important role for $0.12 \leq F \leq 0.16$ in the case of disturbances dominated by sound (type A and type Æ perturbations), is closely linked to the growth of Mack modes inside the boundary-layer. In fact, this mode was observed in all cases except for the vortical case *HR1.0VE*$_a$, which showed no Mack mode excitation.

3.6.3 Wall temperature effects

Wall temperature effects were analysed by considering a cooled-wall flat plate with a constant wall temperature of $T_w = 3.5$ and a roughness element with height $h = 1.0$. The Reynolds number of the simulation ($Re_{\delta_0^*} = 4135$) was reduced compared to the hot wall cases to keep a constant roughness Reynolds number of $Re_h = 331$. The effects of wall cooling on the receptivity to internal type A perturbations are analysed by comparing the growth of disturbances in cases *HR1.0AI*$_a$ and *CR1.0AI*$_a$. Figure 3.26 shows a comparison of the downstream disturbance evolution inside the boundary-layer for a selection of frequencies. For modes developing in the roughness wake, both cases show two distinct maximum growth rates at the lower and at the higher end of the frequency spectrum. The low frequency maximum, shown in figure 3.26(b), is obtained for $F = 0.06$ in both cases, while at higher frequencies the maximum growth rate, shown in figure 3.26(c), is registered for $F = 0.14$ and $F = 0.10$ for cases *HR1.0AI*$_a$ and *CR1.0AI*$_a$ respectively. At the low frequencies the growth rates of the modes developing in the

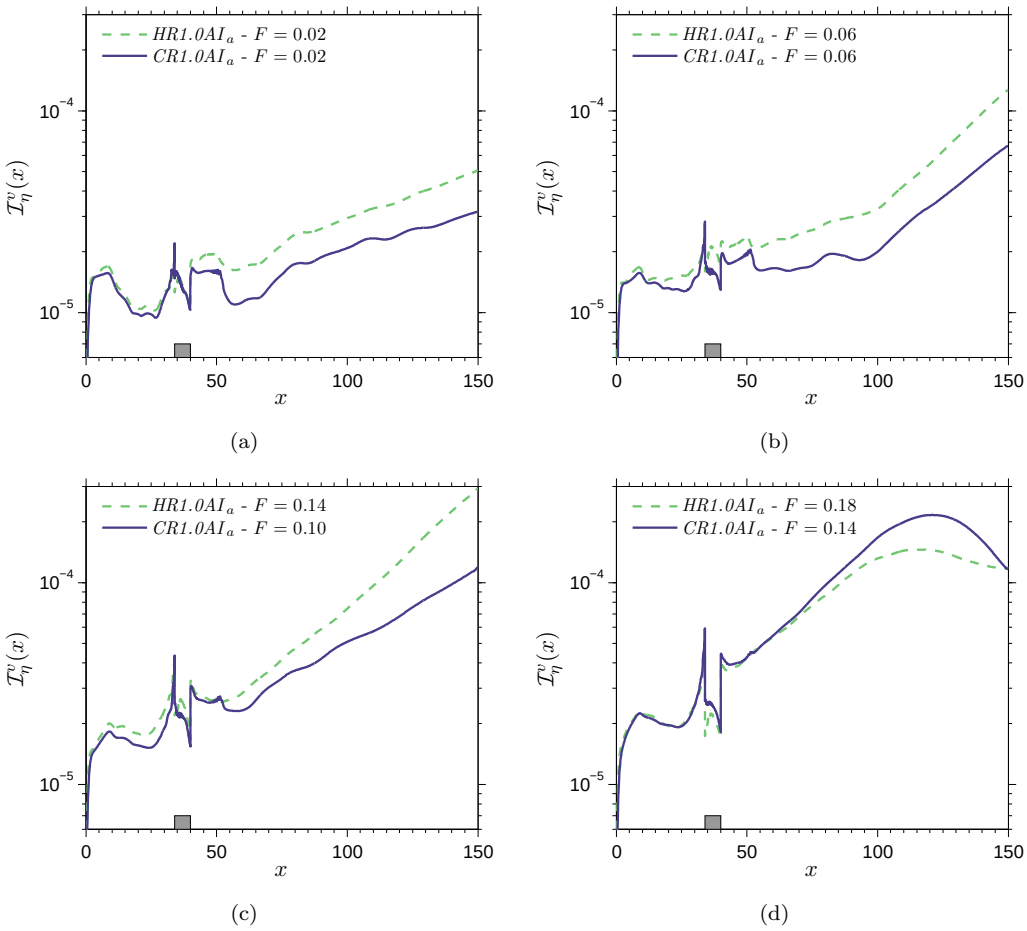

Figure 3.26: Streamwise evolution of v' disturbances inside the boundary-layer for cases $HR1.0AI_a$ and $CR1.0AI_a$. (a) $F = 0.02$, (b) $F = 0.06$, (c) $F = 0.14$ for case $HR1.0AI_a$ and $F = 0.10$ for case $CR1.0AI_a$, (d) $F = 0.18$ for case $HR1.0AI_a$ and $F = 0.14$ for case $CR1.0AI_a$.

roughness wake are comparable in the two cases, as shown in figures 3.26(a) and 3.26(b) for $F = 0.02$ and $F = 0.06$, however the wake mode amplitudes are lower in the cooled-wall case. The amplitude functions associated with these frequencies reveal that modes SL and VL dominate for $F = 0.02$ and $F = 0.06$, respectively, in both the hot and cooled cases. Mode VC drives the wake instability for $F = 0.14$ in the hot case and $F = 0.10$ in the cooled case, however the measured mode VC growth rate for case *CR1.0AI* ($-\alpha_i \approx 0.018$) is lower than for case *HR1.0AI*. It seems that wall cooling leads to a more stable shear layer, with a linear stability curve centred at a frequency lower than that obtained for the hot-wall case.

The disturbance growth observed for $F = 0.14$ for case $CR1.0AI_a$ and for $F = 0.18$ for case $HR1.0AI_a$ in figure 3.26(d) is associated with Mack mode instabilities developing in the lateral laminar boundary-layer away from the roughness wake

and follow a trend similar to that observed in the smooth flat plate case, growing and decaying as they enter and leave their regions of instability. Cooling has a damping effect on these modes, in agreement with theory. In the cooled wall case the Mack mode growth rate is higher than the growth rate of the most unstable wake mode (found for $F = 0.06$).

3.7 Roughness receptivity at $M_\infty = 2.5$

As in the $M_\infty = 6.0$ case, this section starts with a discussion of the results obtained for two different roughness heights. The analysis of the effects of different disturbances follows and the section ends with a discussion of the effects of cooling on the stability of the flow over a roughness element with $h = 1.0$.

3.7.1 Effect of roughness height

The influence of roughness height on the $M_\infty = 2.5$ boundary layer stability is analysed by comparing cases $HSAI_b$, $HR0.5AI_b$ and $HR1.0AI_b$, where the effects

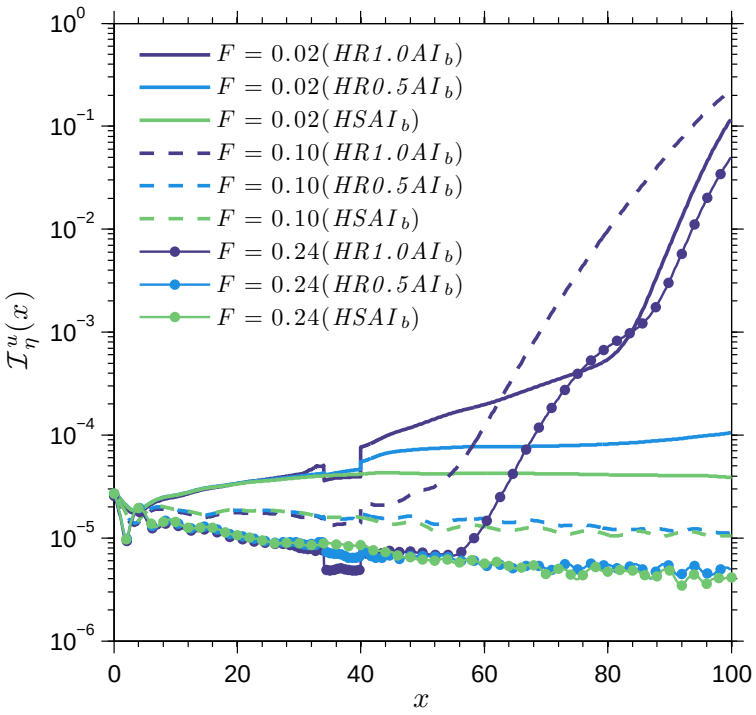

Figure 3.27: Streamwise evolution of u' disturbance amplitude for cases $HSAI_b$, $HR0.5AI_b$ and $HR1.0AI_b$.

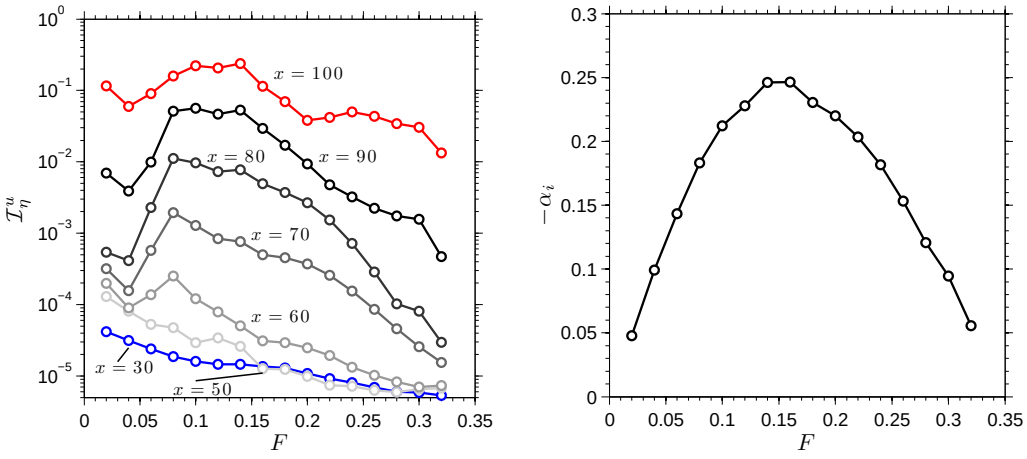

(a) (b)

Figure 3.28: Growth of u' disturbances inside the boundary layer as a function of frequency for case $HR1.0AI_b$. (a) amplitude of boundary layer disturbances at different streamwise positions, (b) maximum disturbance growth rate in the region $73 < x < 75$, calculated from $\mathcal{I}^u_\eta(x)$.

of type A perturbations on the laminar flow over roughness elements with different heights are considered. Figure 3.27 shows the boundary layer response to frequencies $F = 0.02$, $F = 0.1$ and $F = 0.24$. After the initial boundary-layer receptivity, taking place immediately downstream of the inflow boundary, near-wall disturbances enter the upstream separation bubble and amplify. This amplification is not evident from the wall-normal integrated norm used in figure 3.27, but might play a role in the development of disturbances downstream of the roughness. In the downstream separation bubble a secondary receptivity process takes place as the mean flow changes abruptly, leading to a redistribution of disturbance energy into modes of the new basic flow. This can be seen as a sudden amplification at about $x = 40$, noticeable for $F = 0.02$ in figure 3.27, which is more pronounced for the low frequencies and for the taller roughness. Both this and the subsequent linear growth rate increase with roughness height. As the frequency increases the effect of the small roughness weakens until it becomes completely negligible. In fact, the $F = 0.1$ and $F = 0.24$ disturbances experience the same amplitude decay for cases $HSAI_b$ and $HR0.5AI_b$. The effect of the small roughness on the boundary-layer stability is weak and is limited to $F \leq 0.04$. For $F > 0.04$ disturbance amplitudes decay in both cases at a rate which increases with frequency.

The roughness wake response to the incoming disturbances is drastically different in the case of a roughness element with $h = 1.0$. Disturbances grow quickly

in this region of the boundary layer, showing a growth of more than three orders of magnitude between inflow and outflow boundaries, so that some of the most unstable modes have already reached finite amplitudes before the end of the computational domain. This leads to the increased growth rate of $F = 0.02$ and $F = 0.24$ modes for $x > 80$ for case *HR1.0AI*$_b$, which is due to nonlinear interactions of $F = 0.10$, $F = 0.12$ and $F = 0.14$ disturbances. The roughness wake is receptive to a broad frequency band, as can be seen in figure 3.28(a), which shows the disturbance amplitude associated with the different forcing frequencies at different streamwise locations. At $x = 30$ (blue line in figure 3.28a) the disturbance amplitudes inside the boundary layer are high at $F = 0.02$, corresponding to the only unstable boundary layer mode excited, and decrease with frequency. Immediately downstream of the roughness element ($x = 50$), low frequencies experience a sudden amplification while the high frequencies are either damped by the roughness or keep decreasing due to their inherent stability. At $x = 60$ a peak centred at $F = 0.08$ appears in figure 3.28(a), which indicates that the roughness wake mode with $F = 0.08$ has the highest receptivity. However, further downstream higher frequencies start to grow quickly and by $x = 90$ disturbances in the range $0.08 \leq F \leq 0.14$ are the most amplified. The high amplitudes shown in figure 3.28(a) at the low and high end of the frequency spectrum are a consequence of nonlinear interactions between the most amplified linear modes. Figure 3.28(b) gives the maximum linear growth rate, calculated form the function $\mathcal{I}_\eta^u(x)$ in the region $60 \leq x \leq 80$, for each frequency. Disturbances with $F = 0.14$ are the most unstable, with a maximum growth rate of $-\alpha_i \approx 0.25$. This is more than thirty times higher than the smooth flat plate primary instability for the same Mach and Reynolds numbers, for which $F \approx 0.013$.

The excitation of instability modes downstream of the roughness is visualised in figures 3.29(a) and 3.29(b), which show contours of the real part of $\hat{u}$ for the $F = 0.04$ and $F = 0.10$ disturbance fields, for cases *HR0.5AI*$_b$ and *HR1.0AI*$_b$ respectively. The contours are taken in $x-z$ planes at two different distances from the wall, $y \approx 0.75$ for case *HR0.5AI*$_b$ and $y \approx 1.1$ for case *HR1.0AI*$_b$, in order to better visualise the disturbance development in the roughness wake for the two cases. For $h = 0.5$ the boundary-layer disturbances affect the lateral regions of the roughness wake, with relatively high $\partial u/\partial z$ shear. These disturbances seem to be neutral or slightly unstable. In case *HR1.0AI*$_b$ the disturbances first enter a region of shear surrounding the downstream separation bubble and excite the highly unstable wake modes. An interesting feature can be noted in figure 3.29(b), where the wavelength of the disturbances upstream of the roughness increases, starting

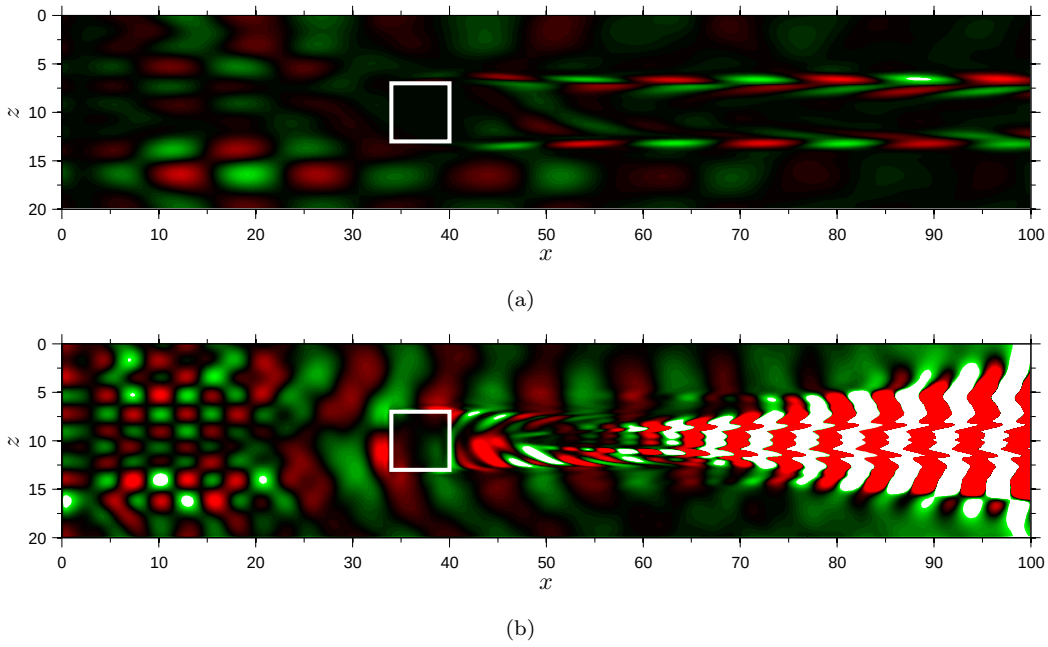

(a)

(b)

Figure 3.29: Contours of $\Re\{\hat{u}\}$ showing the excitation of instabilities downstream of the roughness. The white squares indicate the roughness position. (a) case *HR0.5AI*$_b$ for $F = 0.04$ at $y = 0.75$, (b) case *HR1.0AI*$_b$ for $F = 0.1$ at $y = 1.1$. The two horizontal planes show the region of maximum disturbance amplitude in the two cases.

from $x \approx 20$. Generic three-dimensional boundary layer disturbances dominate near the inflow boundary, while further downstream the disturbance field shows the effect of the free-stream fast acoustic waves, which are able to penetrate the boundary layer.

The nature of the instability modes developing in the roughness wake for case *HR1.0AI*$_b$ is shown for $F = 0.08$ and $F = 0.26$ in figure 3.30, which gives the $|\hat{u}|$, $|\hat{v}|$ and $|\hat{w}|$ amplitude functions in a crossflow plane at $x = 70$. The different shapes observed for the two frequencies suggest the presence of two different instability modes which dominate at different frequencies. For $F = 0.08$ the wake instability is driven by an instability mode developing in the $\partial u/\partial y$ shear layer induced by the pair of counter-rotating streamwise vortices at the roughness mid-plane, while at $F = 0.26$ the amplitude function can be interpreted as the effect of an instability growing in the lateral $\partial u/\partial z$ shear layers located at the edges of a low-speed streak. Contour plots of the real part of $\hat{w}$ at a $y = 1.4$ plane, shown in figure 3.31, reveal that the dominant mode at $F = 0.08$ is characterised by an antisymmetric w' disturbance field, consistent with the growth of a Kelvin-Helmholtz instability on the top part of the shear layer, leading to a varicose deformation of the streak. In contrast, the disturbance field at $F = 0.26$ shows a

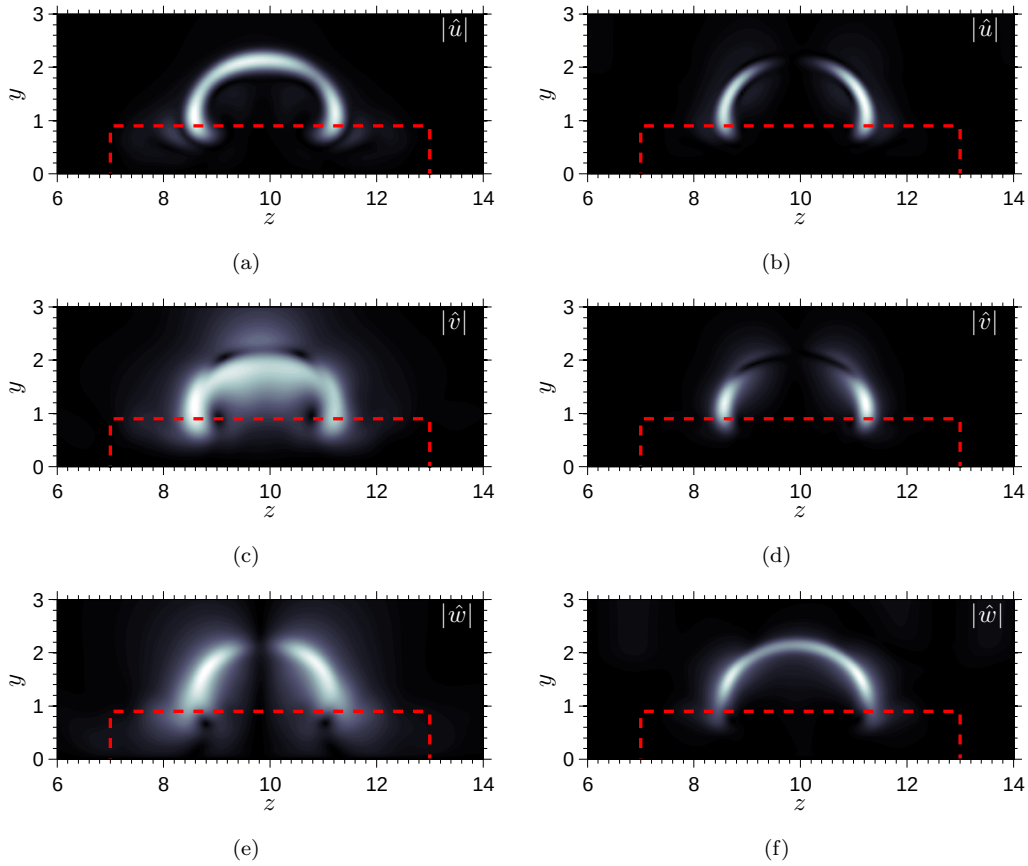

Figure 3.30: Shear layer instability amplitude functions for $F = 0.08$ and $F = 0.26$ in a crossflow plane at $x = 70$ (case *HR1.0AI*$_b$). The red dashed line indicates the roughness position. (a) $|\hat{u}|$ for $F = 0.08$, (b) $|\hat{u}|$ for $F = 0.26$, (c) $|\hat{v}|$ for $F = 0.08$, (d) $|\hat{v}|$ for $F = 0.26$, (e) $|\hat{w}|$ for $F = 0.08$, (f) $|\hat{w}|$ for $F = 0.26$

symmetric w', suggesting that an additional sinuous mode grows on the edge of the streak. We refer to the mode developing in the $\partial u/\partial y$ shear layer as Varicose Top (VT) and, by analogy with the results obtained for $M_\infty = 6.0$, the mode developing at the edges of the streak will be called Sinuous Lateral (SL). These two modes appear for all frequencies, however amplitude functions indicate that mode VT dominates for frequencies in the range $0.08 \leq F \leq 0.14$, while mode SL drives the transition at the higher frequencies ($F > 0.14$). Similarly to what was found for $M_\infty = 6.0$, for certain frequencies the two modes present similar amplitudes, in which case the amplitude function becomes asymmetric. This shows that the unstable frequency ranges for the two modes overlap and the asymmetric shape of the amplitude function can be understood as a result of the phase-locked superposition of the two modes, which may lead to a destructive interference on one side and a constructive interference on the other. Choudhari *et al.* (2010); Kegerise *et al.* (2012) recently found similar varicose and sinuous modes in the wake of a

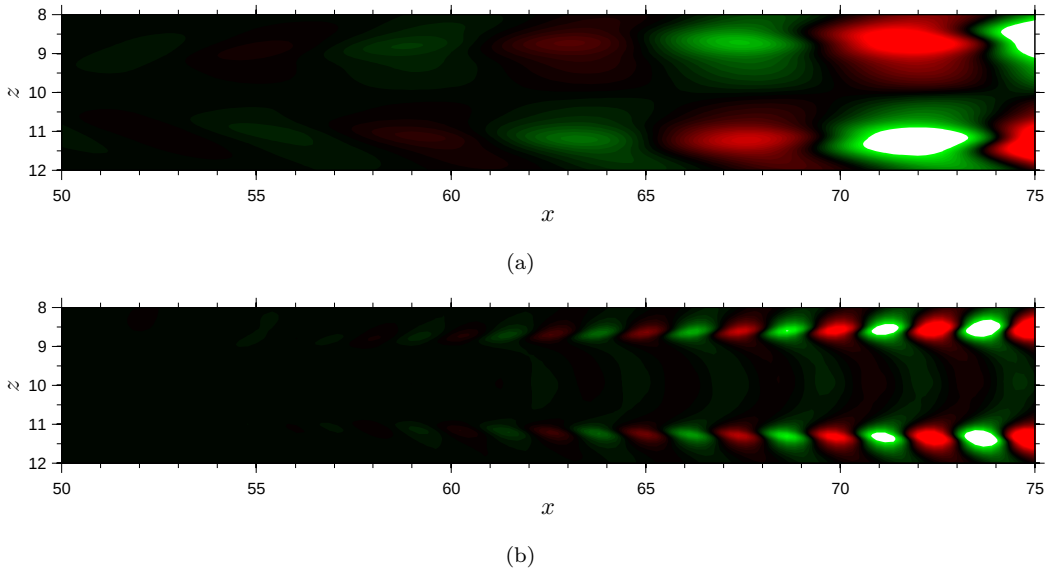

Figure 3.31: Showing the nature of the shear layer and the streak modes. Contours of $\Re\hat{w}$ at $y = 1.4$. (a) $F = 0.08$, where the shear layer mode is dominant, (b) $F = 0.26$, dominated by the streak instability, shows the sinuous nature of the mode.

localised diamond-shaped roughness element at $M_\infty = 3.5$. They analysed the stability of the wake by solving the bi-global eigenvalue problem and found that initially varicose modes have higher growth rates than sinuous modes, however the latter become more unstable than the former further downstream. Their results also show that sinuous modes become dominant as the roughness Reynolds number decreases. Varicose and sinuous modes with amplitude functions similar to those of the two-dimensional eigenfunctions were also found experimentally (Kegerise *et al.*, 2012).

3.7.2 Effect of disturbance type and position

Case *HR1.0AI*, analysed in the previous section, shows that a roughness element with $h = 1.0$ promotes transition by introducing a highly unstable wake. The most dangerous instability modes are characterised by frequencies about one order of magnitude higher than the most unstable smooth flat plate boundary layer modes and their grow rate is more than thirty times higher. In this section we consider the same flow configuration ($HR1.0_b$) to analyse the modifications introduced by the different inflow disturbances on the flow instability.

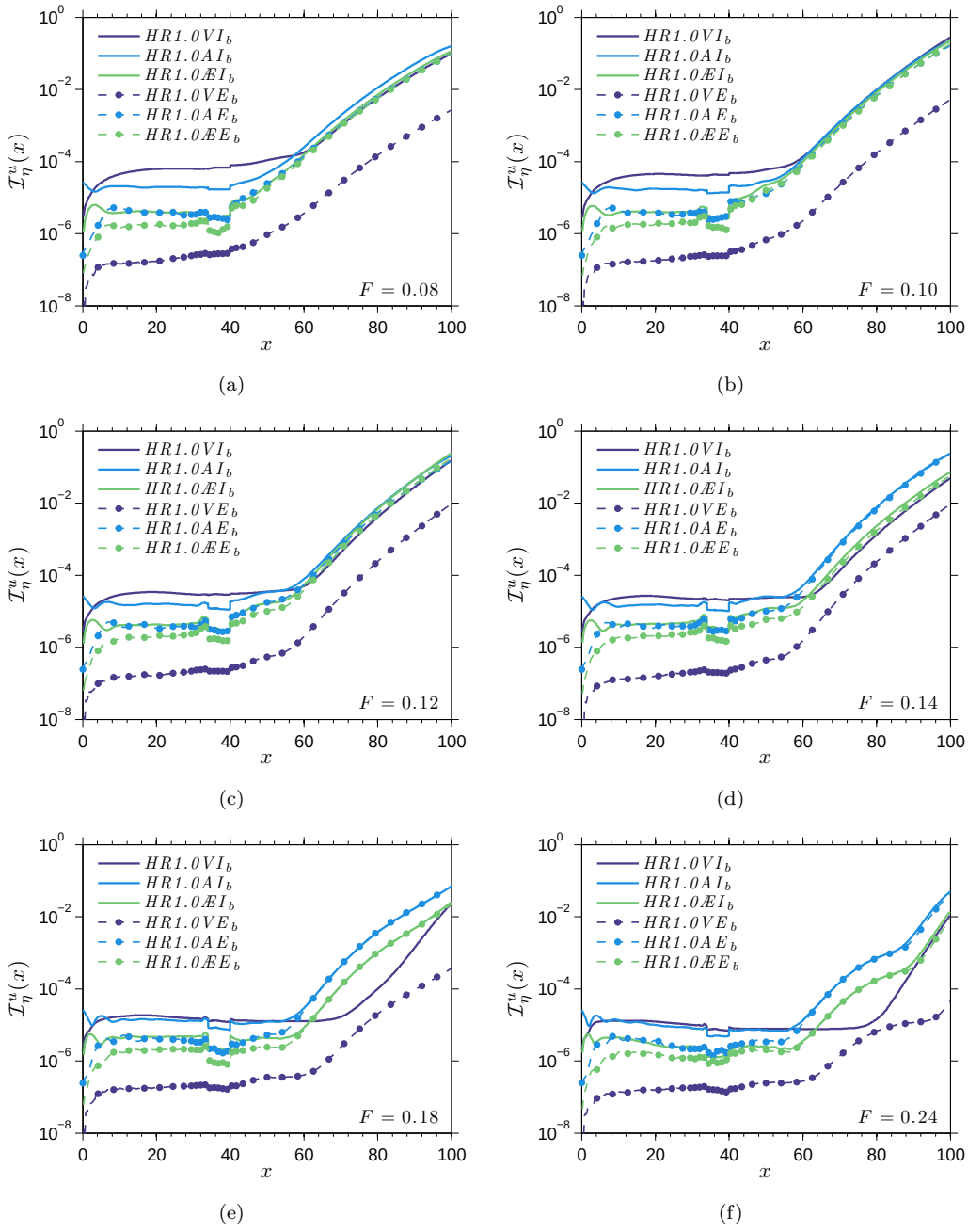

Figure 3.32: Streamwise evolution of disturbance amplitude for cases $HR1.0VI_b$, $HR1.0AI_b$ and $HR1.0EI_b$. (a) $F = 0.08$, (b) $F = 0.1$, (c) $F = 0.12$, (d) $F = 0.14$, (e) $F = 0.18$, (f) $F = 0.24$.

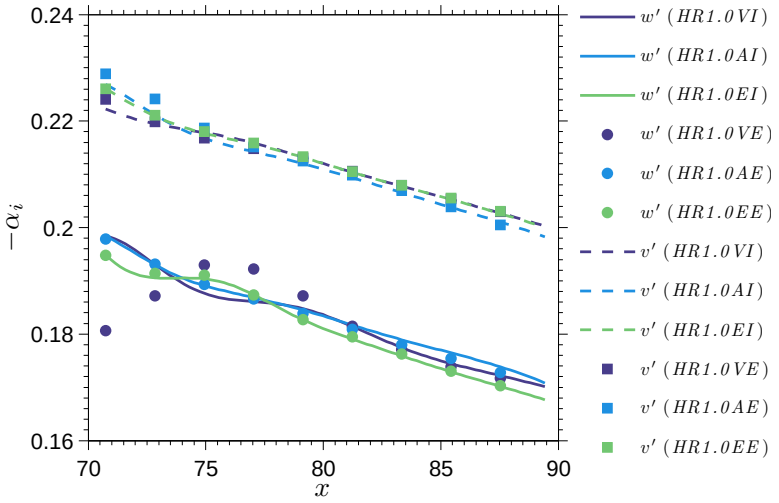

Figure 3.33: Comparing the growth rates of mode VT and mode SL. The plot gives growth rate as a function of streamwise distance, calculated at the roughness centreline plane.

Figure 3.32 shows the u' disturbance amplitude growth for a selection of frequencies inside the boundary layer for cases $HR1.0VI_b$, $HR1.0AI_b$, $HR1.0ÆI_b$, $HR1.0VE_b$, $HR1.0AE_b$ and $HR1.0ÆE_b$. Case $HR1.0VI_b$ does not show earlier transition despite the initial transient growth, which induces vortical waves near the boundary layer edge and takes the total disturbance amplitude to levels considerably higher than those obtained in the other cases. These waves affect the near wall region only marginally, as they follow the boundary layer edge while travelling downstream. In addition, their distance from the wall and rate of decay both increase with frequency. There seems to be a correlation between this behaviour and the decay of shear layer mode amplitudes with frequency seen in case $HR1.0VI_b$, especially since the shear layer instability for case $HR1.0VE_b$, where no transient growth is recorded, does not show a strong frequency dependence. For frequencies $F < 0.14$ the boundary layer response downstream of the roughness element is similar in all cases, with the exception of case $HR1.0VE_b$, despite the different upstream disturbance amplitudes. This aspect can be explained by considering that the wall-normal integrated norm takes into account the amplitude of disturbances developing near the boundary layer edge. The wake response, however, seems to be driven mainly by the near wall disturbances. Despite the similar amplitudes, subtle differences can be observed in the growth rates of disturbances downstream of the roughness for this frequency range, which will be analysed in more detail later.

A clear discrepancy in the amplitude of disturbances developing in the roughness

wake appears for $F \geq 0.14$, where type A perturbations always lead to higher amplitudes, followed by type Æ and type V disturbances. Interestingly, this happens with frequencies for which the near wall disturbance field is dominated by the free-stream fast acoustic waves in all cases. In addition, in the case of type A and type Æ disturbances the wake response is identical for external and internal perturbations when $F > 0.14$, although the total boundary layer disturbance amplitudes are different upstream of the roughness. Therefore, for the high frequencies, the excitation of wake instability modes is determined by the level of fast acoustic waves in the free-stream. This, in fact, explains the different wake mode amplitudes recorded for the different cases. At the high frequencies, the fast acoustic waves lead to the excitation of mode SL.

Overall, the range of unstable frequencies is the same for all cases. A deeper analysis of the boundary layer response to the different disturbances for $F \leq 0.14$, however, shows differences in the growth rates of some of the most unstable modes, which may be explained as the influence of the superposition of modes VT and SL on the Fourier amplitudes calculated from the DNS data. For example, at $F = 0.6$ the disturbance growth rate is slightly higher for cases $HR1.0VI_b$ and $HR1.0ÆI_b$ compared to case $HR1.0AI_b$, while at $F = 0.14$ disturbances grow faster for cases $HR1.0VI_b$ and $HR1.0AI_b$ than for case $HR1.0ÆI_b$. This behaviour correlates with the different amplitudes of modes VT and SL found for the different cases, and indicates that these two modes grow at different rates. Growth rates can be extracted by comparing the growth of v' and w' disturbances at the roughness mid plane, which is also the symmetry plane for mode VT. In this region w' disturbances follow the growth of mode SL and are not affected by the mode VT, which, on the other hand, determines the v' disturbance field. The growth rates of both modes peak at $F \approx 0.14$. As shown in figure 3.33, at $F = 0.14$ mode VT grows, on average, about 17% faster than mode SL. It seems that any generic boundary layer disturbance leads to the excitation of both mode SL and mode VT. Contrary to what was found for $M_\infty = 6.0$, no excitation of mode VL can be observed for $M_\infty = 2.5$. This seems to be due to the absence of $\xi = 0$ modes in the forced disturbances in this case and indicates that the wake tends to select mode SL over mode VL, as was already suggested during the discussion of the $M_\infty = 6.0$ results.

3.7.3 Wall temperature effects

Wall temperature effects were analysed by considering a flat plate with a constant wall temperature equal to the free-stream temperature and a roughness element with height $h = 1.0$. The Reynolds number of the simulation ($Re_{\delta_0^*}$) was reduced in this case to keep the same roughness Reynolds number (Re_h) of the hot-wall cases. The computation of the laminar flow around the roughness element becomes particularly challenging under these flow conditions. This is because the cold temperature near the wall leads to high local Mach numbers, which translates for example into a stronger shock developing at the roughness leading edge. Therefore, to resolve both the shock and the high gradients dictated by the sharp roughness, the grid was substantially refined both in the streamwise and spanwise directions compared to the hot-wall cases. Despite this, no steady laminar solution was found. In fact, the boundary layer undergoes a strong transition process without the need for external disturbances. Close inspection of the flow field shows the development of self-sustained oscillations in the roughness-induced upstream separation bubble, shown in figure 3.34 as contours of v-velocity at $y = 0.4$. These propagate downstream and feed the instability of the shear layer induced by the roughness. The same qualitative behaviour was found for two different wall temperatures, namely $T_w = T_\infty$ (reported in figure 3.34) and $T_w = 1.5 \times T_\infty$, whereas for $T_w = T_{ad} = 2.055 \times T_\infty$ the flow was steady in the absence of the inflow disturbances. It is likely that the disturbances developing in the upstream bubble in the cooled wall cases come from the development of an absolute instability developing in the separated region, which might be seen as an upstream near wall heated jet. However, further analysis would be needed before definite conclusions can be drawn.

3.8 Synthesis and discussion of receptivity results

The parametric study performed in the previous sections has shed some light onto the mechanisms driving the initial (linear) stages of the transition to turbulence of $M_\infty = 6.0$ and $M_\infty = 2.5$ boundary layers in the presence of localised sharp-edged roughness elements of two different heights and under the action of small external disturbances of different types. The main study considers a fixed wall temperature of $T_w = T_{ad}$. The influence of wall cooling has also been analysed with

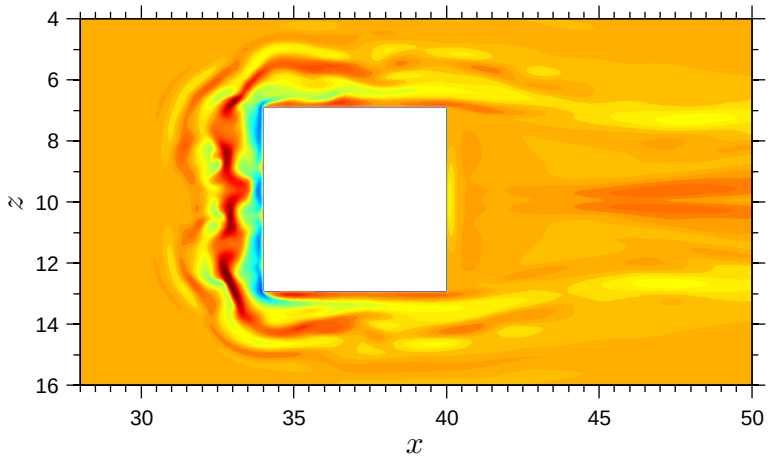

Figure 3.34: Oscillations in the upstream separation bubble, shown by v-velocity contours at $y = 0.4$.

one additional case per Mach number, where the roughness Reynolds number was kept fixed to $Re_h = 331$ and $Re_h = 791$ for $M_\infty = 6.0$ and $M_\infty = 2.5$ respectively.

At the two Mach numbers considered, the roughness elements introduce changes in the mean flow, which can lead to a drastic modification of the stability characteristics of the flow depending on the roughness height considered. Of particular importance is the generation of pairs of counter-rotating streamwise vortices, which, through the lift-up of low momentum fluid from the near wall region, give rise to a low velocity streak surrounded by regions of high wall-normal and lateral shear, forming the roughness wake. Separation bubbles are induced upstream and downstream of the roughness, opening the possibility for the onset of absolute instabilities.

The two small roughness elements considered have $h = 0.5$ when normalised with the displacement thickness at the inflow of the computational domain. This corresponds to $h/\delta_h^* \approx 0.35$ and $h/\delta_h \approx 0.27$ for the $M_\infty = 6.0$ cases and $h/\delta_h^* \approx 0.45$ and $h/\delta_h \approx 0.22$ at $M_\infty = 2.5$. Here, δ_h^* and δ_h are, respectively, the displacement thickness and boundary layer thickness at the roughness streamwise location for a clean flat plate. For both Mach numbers the results show that the effects of these small roughness elements are weak. At $M_\infty = 6.0$ the roughness mainly leads to a slight enhancement of the receptivity of boundary layer modes developing away from the wake. On the other hand, for $M_\infty = 2.5$ roughness effects are only visible at low frequencies, for which oscillations developing in the lateral shear layers surrounding the streak contribute to the boundary layer disturbance amplitudes.

In both cases the effects of roughness are negligible and early transition is not expected.

The scenario changes drastically when considering the taller roughness elements. At $M_\infty = 6.0$ the roughness height compares to the local boundary layer as $h/\delta_h^* \approx 0.71$ and $h/\delta_h \approx 0.54$. For this case the computational domain encloses a region of the boundary layer where both first and second mode instabilities develop. In addition to these, the results highlight the presence of three unstable modes developing in the roughness wake, named here as modes SL (Sinuous Lateral), VL (Varicose Lateral) and VC (Varicose Centred). Both modes SL and VL are characterised by the growth of instabilities in the lateral shear layers induced by the roughness in its wake and lead to a sinuous and a varicose deformation of the streak, respectively. Mode VC also leads to a varicose streak deformation, however its origin is not clear. Generic three-dimensional boundary layer disturbances lead to the excitation of mode SL. In the presence of two-dimensional boundary layer modes, however, the roughness wake response is forced towards the varicose modes, which are also more unstable. Mode VC appears for $0.12 \leq F \leq 0.16$ and seems to be closely linked to the Mack modes developing in the undisturbed flow regions away from the roughness wake. Mode VL for $F = 0.06$ and mode VC for $F = 0.14$ grow at similar rates and are the most unstable modes observed, with $-\alpha_i \approx 0.029$ and $-\alpha_i \approx 0.027$ respectively. Their excitation is more effective in the case of disturbances dominated by sound (type A and type Æ), which are also the perturbations leading to the highest amplitudes of two-dimensional first and second modes. On the contrary, streamwise vorticity disturbances (type V) do not lead to significant two-dimensional boundary layer modes, hence, in this case, mode SL dominates. Sinuous and varicose modes were also found at $M_\infty = 6.0$ by Choudhari *et al.* (2009, 2012) by eigenvalue analysis, although in their case sinuous modes are dominant.

At $M_\infty = 2.5$ the wake behind the roughness is highly unstable (in this case $h/\delta_h^* \approx 0.89$ and $h/\delta_h \approx 0.44$). Instability modes grow in the roughness wake for all frequencies of the forcing, the most unstable of which has a frequency $F = 0.14$ and growth rate $-\alpha_i \approx 0.25$, which is about one order of magnitude higher than that of the most unstable wake mode at $M_\infty = 6.0$. A more unstable behaviour was expected given the difference in Re_h. An inspection of the mode amplitude functions reveals that the driving instabilities grow in the lateral shear layers placed at the sides of the low velocity streak, leading to the sinuous mode SL, and in the shear layer along the roughness centreline, which lead to a varicose deformation of the streak (mode VT). Contrary to what was found for $M_\infty =$

6.0, no VL modes have been observed, which seems to be due to the absence of $\xi = 0$ modes in the inflow forcing signal. The range of unstable frequencies of modes SL and VT overlap, however, mode VT is the most unstable and drives the instability of the wake for $0.08 \leq F \leq 0.14$. An important finding was that, in the absence of boundary layer modes, the free-stream fast acoustic waves are the only disturbances able to penetrate the boundary layer and trigger the instability of the wake. Similar wake modes to those found in this work were also found experimentally by Kegerise *et al.* (2012) at $M_\infty = 3.5$.

Finally, all the main flow configurations analysed (*HR0.5*, *HR1.0* and *CR1.0* for $M_\infty = 6.0$ and $M_\infty = 2.5$) are shown in figures 3.35(a) and 3.35(b) in the context of the transition criteria proposed by Redford *et al.* (2010) and Bernardini *et al.* (2012) respectively. The transition-map plane is divided into two regions by the two black lines (critical lines) in figure 3.35, one where roughness does not have an effect on transition (left) and one where transition is dominated by roughness effects (right). Relative to the results obtained in this work, both the transition criteria predict well the effect of roughness for the cases with $h = 0.5$ and for case $HR1.0_b$. The results obtained here for case $HR1.0_a$ suggest that early transition is promoted by the roughness element considered. This case, however, lies well on the left part of the transition map in figure 3.35(b) and very close to the critical line when using the criterion proposed by Redford *et al.* (2010). Wall cooling was found to lead to a more stable behaviour of the roughness wake at $M_\infty = 6.0$ (case $CR1.0_a$). This effect is predicted by the Redford's criterion, while Bernardini's criterion, in fact, predicts a small destabilisation. Note that this criterion always predicts a destabilising effect of cooling. It is interesting to note that the predictions made by the two roughness-induced transition criteria discussed here are mostly based on the stability characteristics of the flow behind the roughness. However, as suggested by the results obtained here for case $CR1.0_b$, additional mechanisms like for example the onset of absolute instabilities in the separation bubble induced upstream of the roughness element can take over and drive the transition to turbulence under certain conditions.

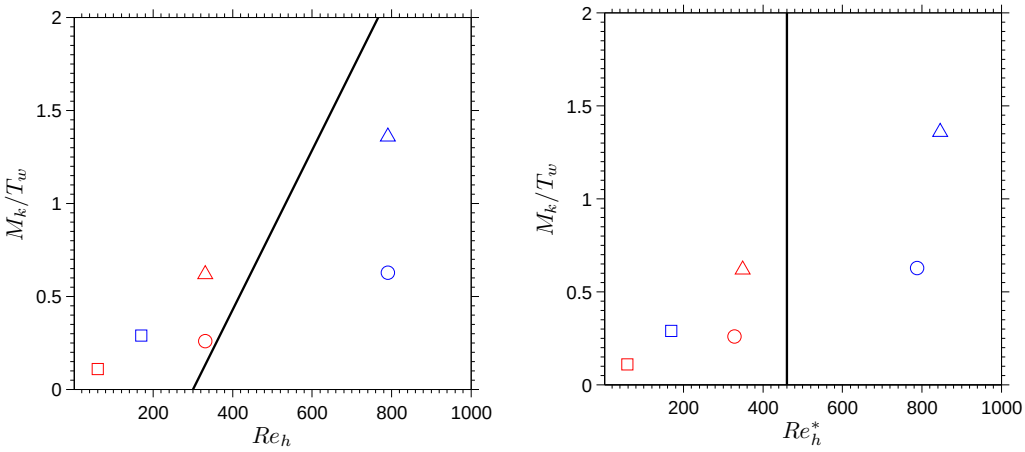

Figure 3.35: Position of the numerical simulations carried out for the receptivity study relative to the transition criteria proposed by Redford *et al.* (2010) (a) and Bernardini *et al.* (2012) (b). Circles indicate hot wall cases with $h = 1.0$, triangles indicate cooled wall cases with $h = 1.0$ and squares indicate hot wall cases with $h = 0.5$. Red symbols are for the $M_\infty = 6.0$ cases and blue symbols for the $M_\infty = 2.5$ cases.

Chapter 4

Nonlinear stages in supersonic roughness-induced transition[1]

The parametric study carried out in the previous chapter has clarified the mechanisms responsible for the receptivity and initial linear growth of instability modes in the roughness wake. As these modes grow, reaching finite amplitudes, nonlinear interactions become important and disturbances start interacting with each other and with the mean flow, leading to a breakdown into turbulence. In this chapter we concentrate on the final stages of transition to turbulence, where nonlinear processes dominate. We analyse the mechanisms responsible for the breakdown to turbulence and study the development of a turbulent wedge behind the roughness element by performing direct numerical simulations of the compressible Navier-Stokes equations (2.2). The study also analyses how the breakdown process and the turbulent wedge evolution may be modified by the interaction between the boundary layer and an impinging oblique shock. The chapter starts with a description of the numerical simulations carried out, given in section 4.1, followed by a discussion of the results obtained for the roughness induced breakdown to turbulence at $M_\infty = 6.0$ and $M_\infty = 2.5$, provided in sections 4.2 and 4.3 respectively. Finally, a comparison between the $M_\infty = 6.0$ and $M_\infty = 2.5$ results and a discussion of the main findings are provided in section 4.4.

[1]Part of this chapter was presented at 28th International Symposium on Shock Waves, 2011

	NL6.0	*NL6.0S*	*NL2.5*	*NL2.5S*
Mach number	6.0	6.0	2.5	2.5
$Re_{\delta_0^*}$	14000	14000	3300	3300
Re_h	726	726	791	791
Re_h^*	719	719	788	788
Wall temperature, T_w	7.022	7.022	2.055	2.055
Shock generator angle (degrees)	0.0	1.70	0.0	1.93
$L_x \times L_y \times L_z$	300×20×50	300×20×50	250×20×60	250×20×60
Grid resolution, Δx^+, Δy^+_{min}, Δz^+	4.0, 0.50, 1.70	6.6, 0.8, 2.8	6.3, 0.7, 2.6	7.5, 0.9, 3.1
Observation period, $T_s = T_s^* U_\infty^* / \delta_0^*$	2100	2100	2100	2100
Sampling frequency, $f_s = f_s^* \delta_0^* / U_\infty^*$	0.075	0.1	0.1	0.1
Time step, $\Delta t = \Delta t^* U_\infty^* / \delta_0^*$	0.015	0.02	0.02	0.02

Table 4.1: Flow conditions, simulation parameters, grid resolution and sampling information. Note that the wall temperature is equal to the laminar adiabatic wall temperature in all cases. The asterisk in Re_h^* indicates that the kinematic viscosity is taken at the wall.

4.1 Numerical simulations

In this second part of the study of supersonic roughness-induced transition to turbulence we perform a set of direct numerical simulations in which the boundary layer undergoes all the transition stages, from the initial linear evolution of disturbances to the final breakdown to turbulence. As for the receptivity study presented in chapter 3, the investigations are carried out for $M_\infty = 6.0$ and $M_\infty = 2.5$ flat plate boundary layers, with an isolated roughness element of height $h = 1.0$. In order to follow the boundary layer all the way to turbulence, we use a large computational domain (domain A in figure 2.1), the dimensions of which are provided in Table 4.1 along with additional details of the numerical simulations carried out for this part of the study. As explained in section 2.2.2, the domain sizes were chosen to accomodate the turbulent wedge growth in all directions. A total of four cases were carried out for the analysis presented here. Cases *NL6.0* and *NL2.5* deal with the breakdown to turbulence at $M_\infty = 6.0$ and $M_\infty = 2.5$ respectively, while the effects of a shock-wave/boundary-layer interaction (SBLI) in the transitional region of the boundary layer are analysed with cases *NL6.0S* and *NL2.5S*. For the $M_\infty = 6.0$ cases the simulation Reynolds number $Re_{\delta_0^*} = 14000$ was increased compared to the receptivity study in order to obtain breakdown to turbulence within the computational domain. This leads to a roughness Reynolds number of $Re_h = 726$. The flow conditions for the $M_\infty = 2.5$ cases are the same as those considered for the receptivity study, for which $Re_h = 791$.

The numerical grids employed were designed to resolve both the laminar flow around the sharp-edged roughness element and the wedge of turbulence developing in the downstream region. Computational domain sizes and grid resolution in viscous wall units are reported in Table 4.1, while a more detailed description of the numerical grids employed in the different cases is given in Table 4.2. Grid generation follows the procedure explained in section 2.2.6, whereby regions of constant grid spacing are joined by ninth degree polynomials. Streamwise and spanwise grid spacings around the roughness element are the same as those used for the receptivity study. The values of Δx^+, Δy^+_{min} and Δz^+, calculated near the roughness mid-plane and the outflow boundary of the computational domain, in a region of turbulent flow, are better than most fully resolved DNS studies (see for example Pirozzoli *et al.*, 2004; Muppidi & Mahesh, 2012). The small Δx^+, Δy^+_{min} and Δz^+ values obtained for case *NL6.0S* are due to the fact that the boundary layer does not reach a fully turbulent state by the end of the computational domain, as will be shown later. As reported in Table 4.1, case *NL6.0S* also requires a

Case	Block	N_x	N_y (n_y^r)	N_z	b_y	Δx	Δz
	B1	245	205 (57)	119	3.96	[0.30, 0.06]	0.05
	B2	99	149 (-)	119	3.96	0.06	0.05
NL6.0	B3	2062	205 (57)	119	3.96	[0.06, 0.12]	0.05
NL6.0S	B4	245	205 (57)	361	3.96	[0.30, 0.06]	[0.05, 0.15, 0.05]
	B5	99	205 (57)	361	3.96	0.06	[0.05, 0.15, 0.05]
	B6	2062	205 (57)	361	3.96	[0.06, 0.12]	[0.05, 0.15, 0.05]
	B1	245	222 (61)	119	3.94	[0.30, 0.06]	0.05
	B2	99	162 (-)	119	3.94	0.06	0.05
NL2.5	B3	1645	222 (61)	119	3.94	[0.06, 0.12]	0.05
NL2.5S	B4	245	222 (46)	428	3.94	[0.30, 0.06]	[0.05, 0.15, 0.05]
	B5	99	222 (46)	428	3.94	0.06	[0.05, 0.15, 0.05]
	B6	1645	222 (46)	428	3.94	[0.06, 0.12]	[0.05, 0.15, 0.05]

Table 4.2: Computational grids. N_x, N_y and N_z are the number of points in the streamwise, wall-normal and spanwise directions per block, while n_y^r is the number of points for $0 \leq y \leq h$. The values of Δx indicate the grid spacing at the beginning and at the end of the block. The multiple values of Δz indicate spanwise grid spacings at the beginning, at the centre and at the end of the domain respectively.

smaller time step than that used for the other three cases due to the appearance of strong contact discontinuities in the initial breakdown region near the sides of the turbulent wedge. A TVD scheme (Yee *et al.*, 1999), coupled with the modified Ducros (Ducros *et al.*, 1999) sensor given in 2.9, was used starting from $x = 70$, in the numerical simulations presented here in order to capture contact discontinuities occurring in the transitional region of the boundary layer shortly after breakdown to turbulence and to resolve the imposed shocks in the cases with SBLI.

In all cases the transition process is initiated by subjecting the laminar flow to an acoustic disturbance given by equation (2.13). For both the Mach numbers considered, the frequency band of the forced perturbations ($F = 0.06 - 0.4$) includes the range of most unstable frequencies identified during the receptivity study. The amplitude of the forcing function was increased to $a = 6 \times 10^{-5}$ (from $a = 2 \times 10^{-6}$ used in the previous chapter) in order to move the point of breakdown to turbulence upstream, while having a clear linear stage of disturbance growth in both cases.

4.2 Roughness-induced breakdown to turbulence at $M_\infty = 6.0$

The discussion of the results obtained for the $M_\infty = 6.0$ case begins with a description of the boundary layer transition to turbulence. This will be followed by an investigation into the mechanisms leading to breakdown to turbulence after the linear growth of disturbances in the roughness wake and a discussion aimed at clarifying the main features of the lateral spreading of turbulence after breakdown. Finally we present results that shed some light into the flow dynamics leading to an acceleration of the transition process in the presence of an interaction between an oblique shock wave and a transitional boundary layer.

4.2.1 Main features of the laminar-turbulent transition process

Before entering upon a discussion of the main feature of the boundary layer after breakdown to turbulence, it is instructive to analyse the modifications introduced by the Reynolds number increase from $Re_{\delta_0^*} = 8200$ ($Re_k = 331$) considered for the receptivity study to $Re_{\delta_0^*} = 14000$ ($Re_k = 726$) considered here, on the laminar flow around the roughness, given that small changes in the laminar basic flow may greatly affect the linear growth of disturbances. The main basic flow modification introduced by the variation of Reynolds number is shown in figures 4.1(a) and 4.1(b), which show shaded contours of streamwise vorticity superimposed by line contours of $u_S := \sqrt{(\partial u/\partial y)^2 + (\partial u/\partial z)^2}$ highlighting regions of high detached shear, for cases *NL6.0* and $HR1.0_a$ (the equivalent case from the previous chapter) respectively. The pair of counter-rotating streamwise vortices induced by the roughness leads, in both cases, to a redistribution of the vorticity field and the generation of regions of high detached shear. As evidenced by the receptivity study, the shear layers forming the roughness wake play a crucial role in the linear stages of transition as they sustain the growth of convective instabilities. In the high Reynolds number case the roughness-induced vortices are stronger than in the low Reynolds number case and lead to thinner and more intense (and hence more unstable) shear layers. Based on these observations, the linear growth of disturbances is expected to be faster for case *NL6.0* than for case $HR1.0_b$. In addition to this, an increase in Reynolds number also leads to larger separation

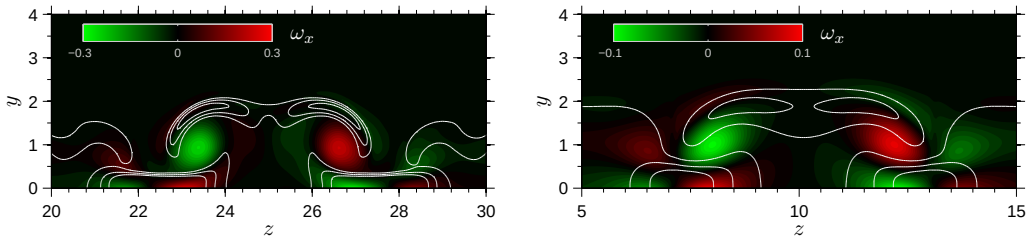

(a) (b)

Figure 4.1: Contours of streamwise vorticity (ω_x) in a crossflow plane placed 40 displacement thicknesses downstream of the roughness (shaded contours), showing the modifications introduced on the roughness wake by the Reynolds number increase. Contours of u_S (white lines) show regions of high detached shear. (a) case *NL6.0* ($Re_h = 726$, $u_S = 0.38, 0.74, 1.1$), (b) case *HR1.0*$_b$ ($Re_h = 331$, $u_S = 0.65, 1.025, 1.4$). Different u_S levels were used to highlight the structure of the high shear layers in the two cases.

bubbles immediately upstream and downstream of the roughness. Large separation bubbles may lead to the onset of absolute instabilities, although this was not the case here.

Having indentified the main differences in the basic laminar flow between cases *NL6.0* and case *HR1.0*$_a$ we now focus on case *NL6.0* alone. Figures 4.2(a) and 4.2(b) give instantaneous temperature contours in a vertical plane along the roughness centreline and in a horizontal plane at $y = 1.2$, respectively, showing a general view of the full transition to turbulence for case *NL6.0*. Finite amplitude disturbances, indicating the nonlinear development, are visible starting from $x \approx 150$. Further downstream, mixing of hot and cold fluid increases gradually, indicating that the initially laminar boundary layer transitions to a chaotic state. The state of the boundary layer at different streamwise positions is given more quantitatively in figure 4.3 through the time averaged skin friction, calculated using non-dimensional variables as

$$c_f := \frac{2\mu_w}{Re_{\delta_0^*}} \frac{\partial u}{\partial y}|_w, \tag{4.1}$$

and plotted at three different locations across the span. Breakdown to turbulence leads to a gradual rise in skin friction, visible in figure 4.3 for $x > 200$, which is similar at all three spanwise positions and continues up to the end of the computational domain, indicating that transition is not complete. The differences in c_f registered between the sides and the centre of the roughness are the effect of the roughness induced streamwise vortices, which lift-up low momentum near-wall

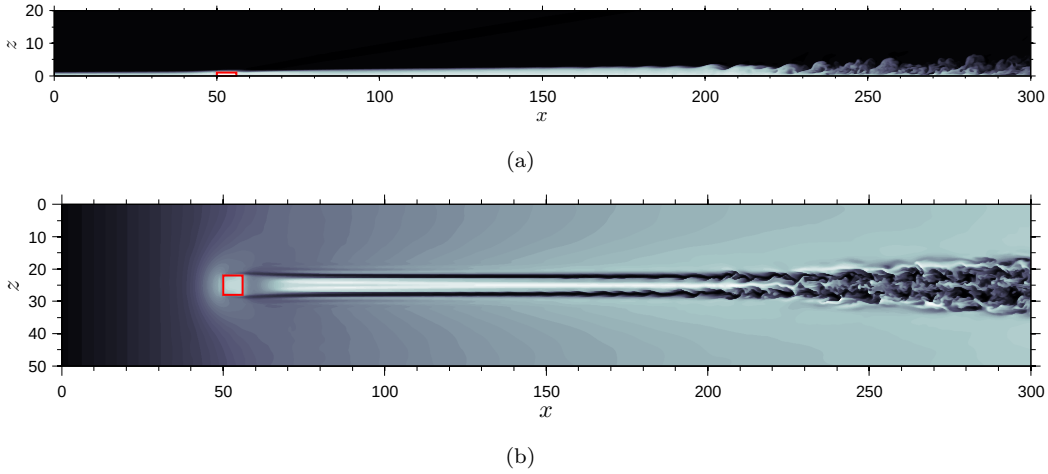

Figure 4.2: Contours of instantaneous temperature. The red squares indicate the roughness position. (a) side view at the roughness mid-plane ($z = 25$), (b) top view in a horizontal plane at $y = 1.2$.

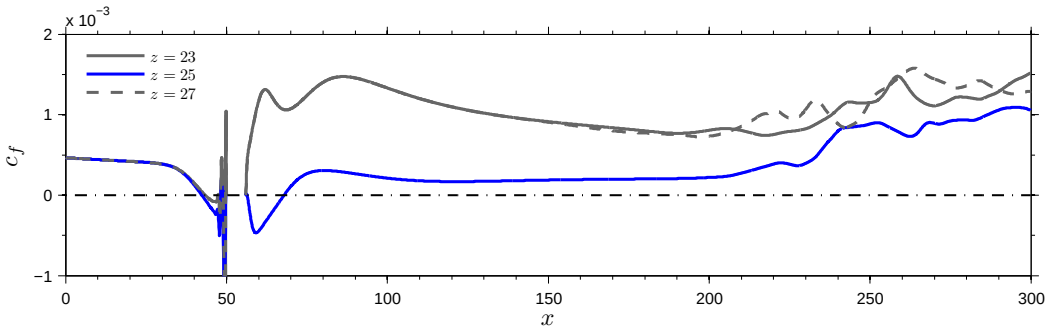

Figure 4.3: Streamwise evolution of time-averaged skin friction at three positions across the span.

fluid at the roughness mid-plane and push fast moving flow towards the wall near the sides of the wake. The effect of these vortices on the mean flow is more prominent in the laminar regions, however it appears to remain significant also after breakdown to turbulence, as can be observed more clearly in figure 4.4 showing contours of the time-averaged v-velocity in a crossflow plane at $x = 292$, and leads to a thicker boundary layer at the roughness mid-plane (see the $\overline{u} = 0.99$ contour in figure 4.4).

Figures 4.5(a) and 4.5(b) show contours of wall normal velocity gradient and temperature gradient at the wall ($y = 0$), giving an indication of the effects introduced by the isolated roughness element on the wall heat transfer. The increased wall shear stress induced by the pair of counter-rotating streamwise vortices at the sides of the roughness wake (see high $\partial\overline{u}/\partial y$ regions near $z = 23$ and $z = 27$) takes the

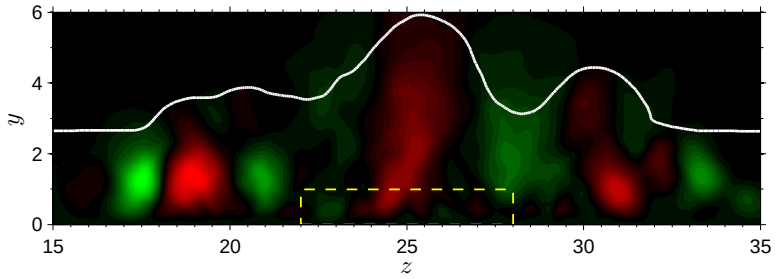

Figure 4.4: Contours of time averaged v-velocity (green for negative and red for positive) in a crossflow plane at $x = 292$ showing how the upwash generated by the roughness induced streamwise vortices near the roughness mid-plane ($z = 25$) persists after breakdown to turbulence. The white line indicates the local boundary layer thickness ($\overline{u} = 0.99$) and the dashed yelow square shows the roughness position.

near wall fluid to temperatures higher than the laminar adiabatic-wall temperature (see high $\partial\overline{T}/\partial y$ regions near $z = 23$ and $z = 27$), used here for the constant temperature wall boundary condition. As expected, transition to turbulence leads to a temperature increase near the wall, visible as high $\partial T/\partial y$ near $x = 230$ in figure 4.5(b), associated with the increased friction caused by the breakdown to turbulence. In the same transitional boundary layer regions, unsteady pressure loads are also high, as expected. This is shown in figure 4.5(c) as contours of the rms of the fluctuating pressure at the wall, normalised by the free-stream pressure. Peak values are found at about $x = 230$ and $z = 28$, immediately downstream of the beginning of breakdown to turbulence, where the mean wall-pressure fluctuations reach amplitudes of about 15% of the free-stream pressure, and decay down to about 8% of the free-stream pressure as the flow evolves towards a turbulent state (note that the flow behind the roughness is still transitional at the computational domain outflow boundary).

4.2.2 Mechanisms responsible for the breakdown to turbulence

As shown in the previous section, the interaction of small disturbances with the laminar flow around a sharp-edged isolated roughness element at $M_\infty = 6.0$ leads to a breakdown to turbulence characterised by the generation of a turbulent wedge behind the roughness element. More insight into the mechanisms leading to the laminar-turbulent transition can be gained by looking more closely at the evolution (both linear and nonlinear) of disturbances in the roughness wake. Figures 4.6(a)

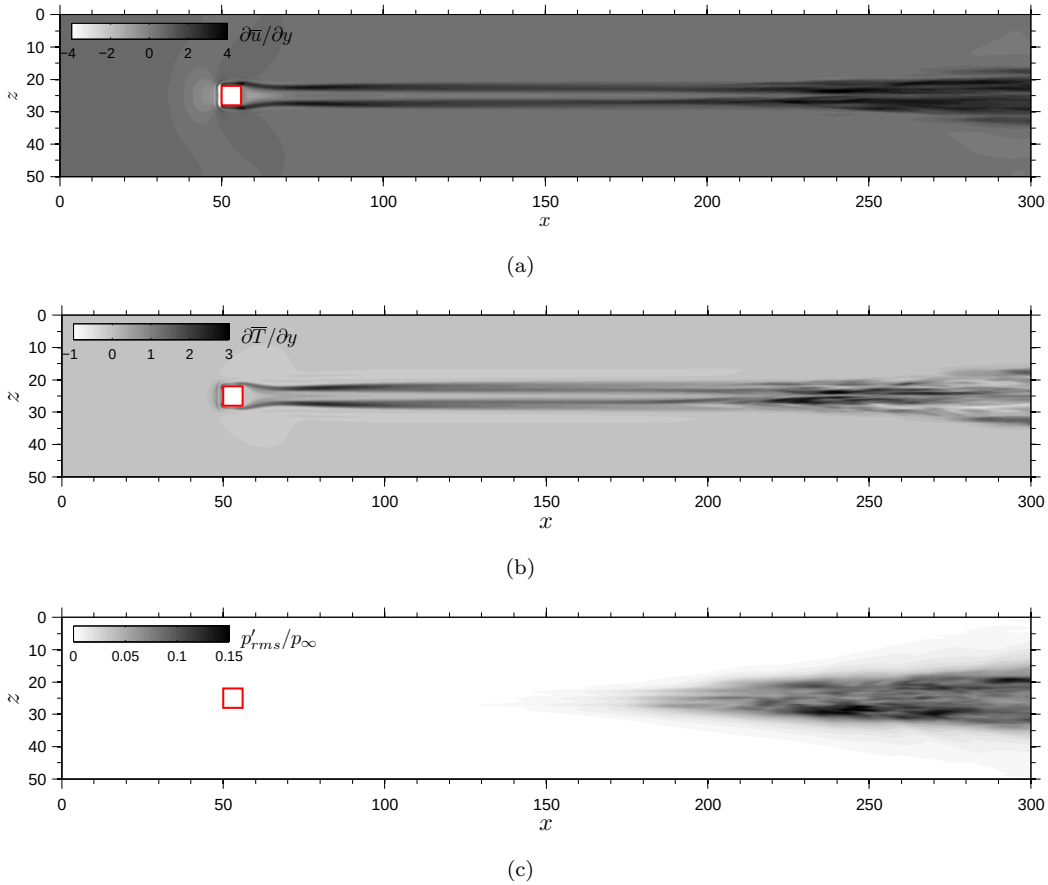

(a)

(b)

(c)

Figure 4.5: Effect of the isolated roughness, and the induced transition to turbulence, on the wall heat transfer and wall pressure fluctuations. (a) contours of wall-normal mean velocity gradient, (b) contours of wall-normal mean temperature gradient, (c) contours of the rms of the fluctuating wall-pressure normalised by free-stream pressure.

to 4.6(c) show, respectively, the streamwise variation of the maximum u'_{rms}, v'_{rms} and w'_{rms} inside the boundary layer at three different positions across the span, namely $z = 23$, $z = 25$ (the roughness mid-plane) and $z = 27$. Shortly after entering the roughness wake, disturbances grow in the lateral wake regions, particularly u' and v'-velocity fluctuations. While significant growth of u'_{rms} and v'_{rms} appears from about $x = 70$ at $z = 27$ and about $x = 80$ at $z = 23$, at the roughness mid-plane ($z = 25$) disturbance growth is only registered for $x > 100$. Growth rates are found to be higher at $z = 27$ than at the other two spanwise positions considered for $x < 130$, particularly for the u' and v' fluctuations. The absence of u' and v' disturbance growth for $x < 100$, together with the growth of w'_{rms} at the same spanwise position for $60 < x < 85$, seen in figure 4.6(c), suggests that the initial instability is dominated by a sinuous wake mode (this aspect will be shown more clearly later). The growth of disturbances slows down for $x \geq 130$

at $z = 27$ and saturation is reached at about $x = 150$. Further downstream, near $x = 200$, all the disturbances growing in the wake of the roughness saturate, indicating the breakdown to turbulence. Disturbance saturation divides the linear and weakly nonlinear stages of transition from the final stage before turbulence, dominated by nonlinear interactions. The beginning of this final stage ($x \approx 200$) coincides with the beginning of the skin friction rise towards the fully turbulent value, as shown in figure 4.3. Figure 4.6(d) gives a comparison of the streamwise growth of the maximum (over y and z) u', v' and w' disturbances inside the roughness wake. Fluctuations of the u-velocity component are dominant throughout the transition region. For $x < 200$, in the linear and weakly nonlinear transition stages, $v'_{rms} > w'_{rms}$. In fact, u' and v' disturbances grow at a higher rate than w' fluctuations. In the strongly nonlinear stage ($x > 200$), however, the amplitude of w' fluctuations becomes higher than that of v' fluctuations. The pattern $u'_{rms} > w'_{rms} > v'_{rms}$, typical of fully developed turbulent flows, indicates that the boundary layer is approaching a fully turbulent state.

The flow dynamics leading to breakdown to turbulence are visualised in figure 4.7, which shows contours of $u' = u - \overline{u}$ and u'_{rms} at different crossflow planes along the streamwise direction. As already reported during the receptivity study in Chapter 3, disturbances enter the wake of the roughness and excite instability modes growing in regions of high detached shear surrounding the roughness induced low velocity streak. This aspect can be inferred from figure 4.7(a) by noting that u'_{rms} maxima appear in regions of high u_S. At the same streamwise position the antisymmetric u' disturbance field shown in figure 4.7(b) suggests that the linear instability of the boundary layer is driven by a sinuous mode growing in the wake of the roughness. The shape of the wake changes as it evolves downstream, while disturbances grow in amplitude, see figure 4.7(c), and at $x = 94.5$ the dominant wake mode is still of the sinuous type, as shown in figure 4.7(d). Further downstream, the sequence provided in figures 4.7(e), 4.7(g) and 4.7(i), indicates that a u'_{rms} peak develops near $z = 27$ and $y = 0.9$ and quickly grows in the streamwise direction, eventually leading to breakdown to turbulence. As can be observed in figures 4.7(f), 4.7(h) and 4.7(j), starting from about $x = 115$ the instantaneous u' disturbance field can be seen to clearly depart from the antisymmetric behaviour shown further upstream. As already seen in figure 4.6, the high amplitude u' disturbances developing in the lateral wake region near $z = 27$ grow faster than disturbances developing in other regions of the wake. This behaviour may be understood as the effect of the linear superposition of non-normal wake

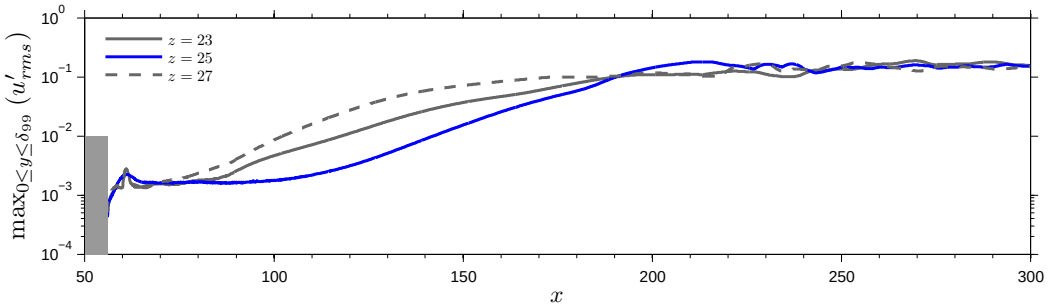

(a)

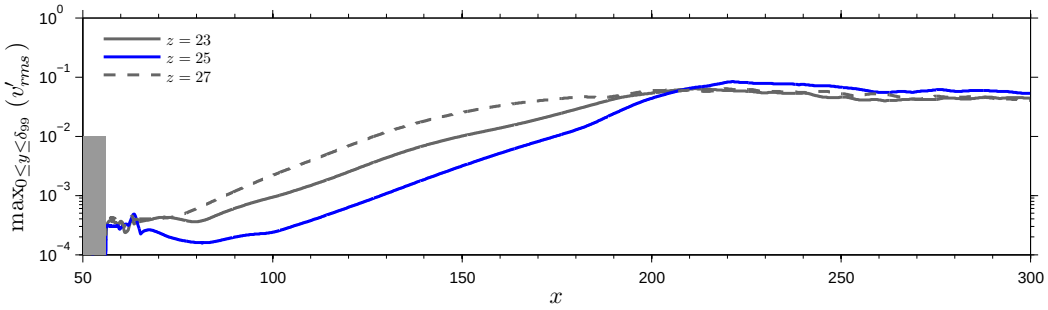

(b)

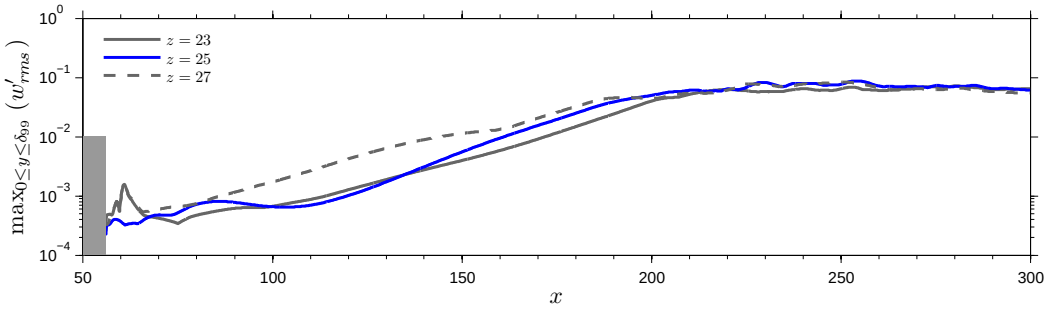

(c)

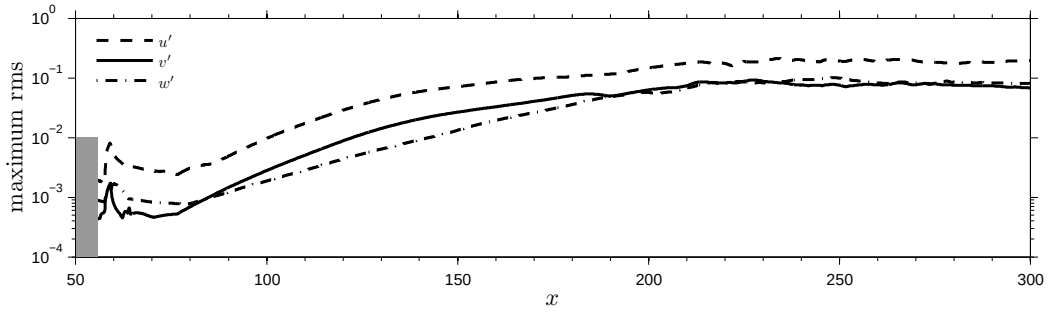

(d)

Figure 4.6: Linear and nonlinear evolution of disturbances in the roughness wake. The grey rectangle indicates the roughness position. (a) maximum u'_{rms} inside the boundary layer, (b) maximum v'_{rms} inside the boundary layer, (c) maximum w'_{rms} inside the boundary layer, (d) maximum (over y and z) rms velocity fluctuations inside the roughness wake.

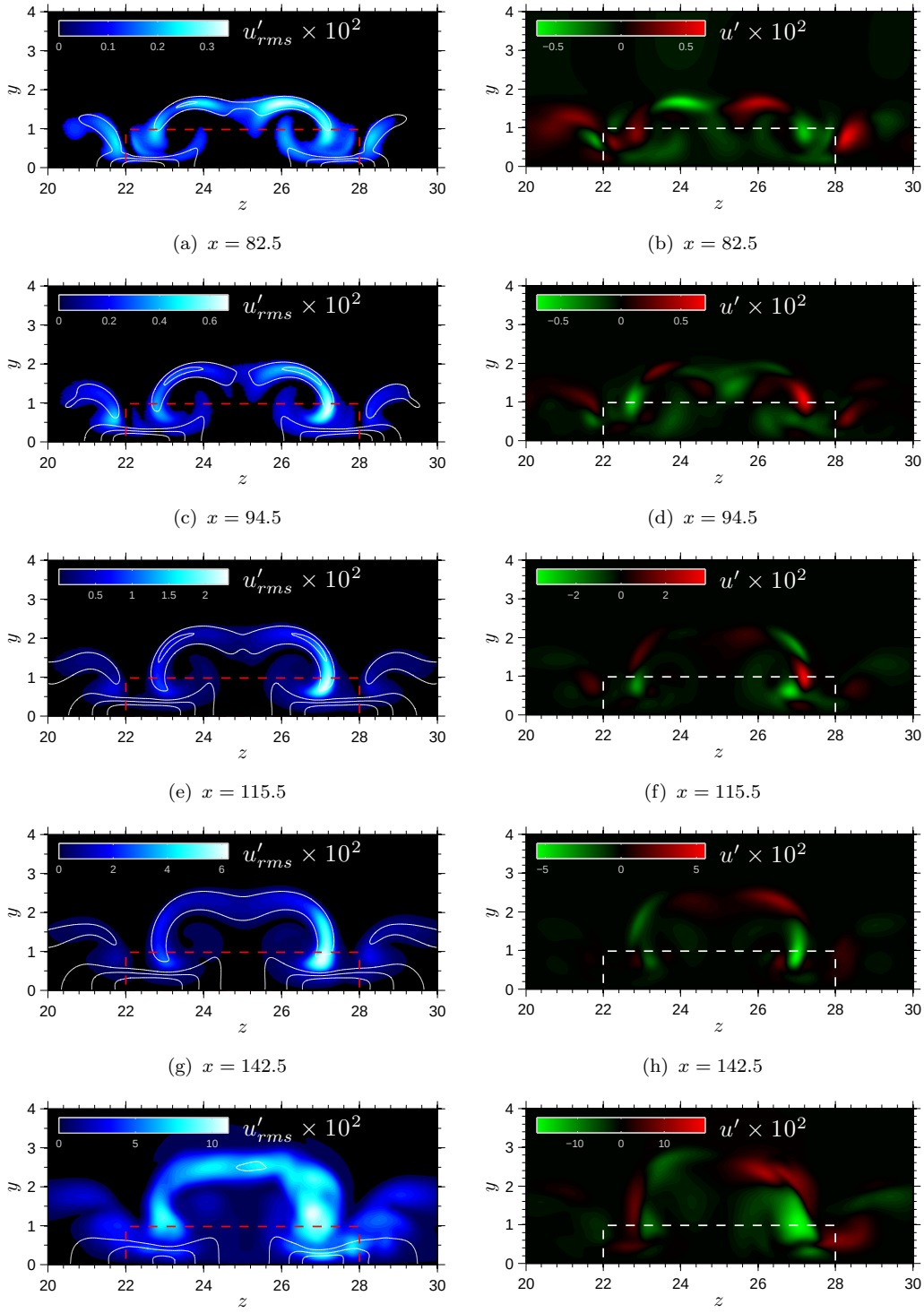

(a) $x = 82.5$ (b) $x = 82.5$

(c) $x = 94.5$ (d) $x = 94.5$

(e) $x = 115.5$ (f) $x = 115.5$

(g) $x = 142.5$ (h) $x = 142.5$

(i) $x = 184.5$ (j) $x = 184.5$

Figure 4.7: Visualisation of the downstream development of roughness wake instabilities. (a), (c), (e), (g), (i) contours of u'_{rms} (shaded), superimposed by $u_S = 0.65, 1.025, 1.4$ contours and (b), (d), (f), (h), (j) contours of u'.

modes, but it could also be a consequence of the onset of weakly nonlinear interactions of localised perturbations. In practice, the former mechanism may quickly lead to the latter. We also note that the quick change in wake shape observed from $x = 82.5$ to $x = 94.5$ (see figures 4.7a and 4.7c) may introduce considerable non-parallel flow effects, which can favour the onset of algebraic growth by inducing a redistribution of the disturbance energy into the modes of the modified basic flow.

An insight of the onset of significant nonlinear interactions, leading to a modification of the basic laminar flow, can be gained by making use of the asymmetric growth of disturbances observed in the roughness wake, together with the perfect symmetry of the basic laminar flow about the roughness mid-plane. The idea is to calculate the streamwise variation of an asymmetry parameter, defined here as

$$\mathcal{S}_\phi(x) := \max_{0\leq y\leq \delta_{99}} \left\{ \left| \int_0^{L_z} |\overline{\phi}\,(x,y,z)\,|\cos(z\pi/L_z)dz \right| \right\}, \tag{4.2}$$

where $\overline{\phi}$ can be any time-averaged flow variable, which becomes greater than zero in regions where the time-averaged flow becomes asymmetric about the roughness mid-plane. In other words, $\mathcal{S}_\phi$ grows as the mean flow departs from the basic laminar flow. Figure 4.8 shows the streamwise variation of $\mathcal{S}_\phi$ for $\phi = \rho, u, v, w$, with the streamwise variation of maximum v'_{rms} inside the roughness wake (blue line) plotted for reference. The asymmetry parameter rises from zero as the forced disturbances hit the boundary layer near $x = 25$ and remains approximately constant until about $x = 100$, where it starts a fast growth before reaching another plateau near $x = 200$. Figure 4.8 suggests that nonlinear interactions become significant only after $x \approx 100$, considerably downstream of the initial growth of disturbances in the roughness wake (see the evolution of maximum v'_{rms} in figure 4.8). It is argued that the linear instability of the wake is driven by the growth of a sinuous wake mode and that the asymmetry in the disturbance field initially grows due to linear effects (e.g. non-parallel flow effects followed by a superposition of non-normal modes), which give way to nonlinear interactions as the disturbances reach finite amplitudes further downstream.

The growth of sinuous instability modes in the wake of the roughness was also observed in the receptivity study presented in section 3.6. The investigation, however, also revealed the presence of varicose instability modes (i.e. modes VL and VC), which are closely linked to the presence of two-dimensional first modes and second (Mack) modes in the disturbance field surrounding the roughness wake. At least for $Re_{\delta_0^*} = 8200$, varicose modes are slightly more unstable than sinuous

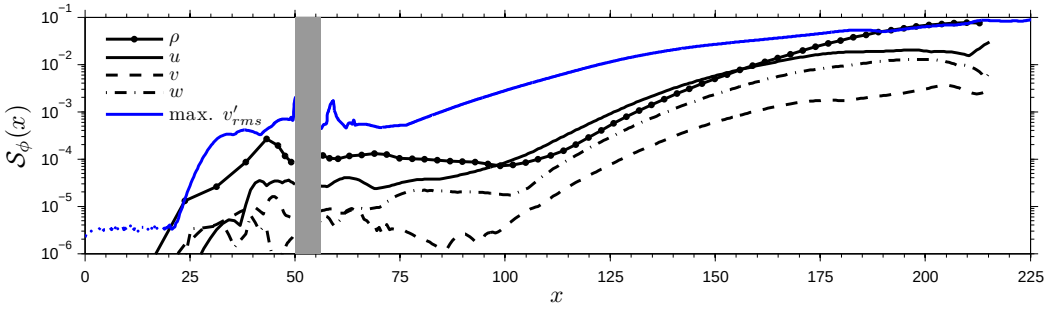

Figure 4.8: Streamwise evolution of the asymmetry parameter $\mathcal{S}_\phi$, giving an indication of the onset of considerable nonlinear interactions. The blue line shows the streamwise variations of maximum v'_{rms} inside the roughness wake and is plotted for reference. The grey rectangle shows the roughness position.

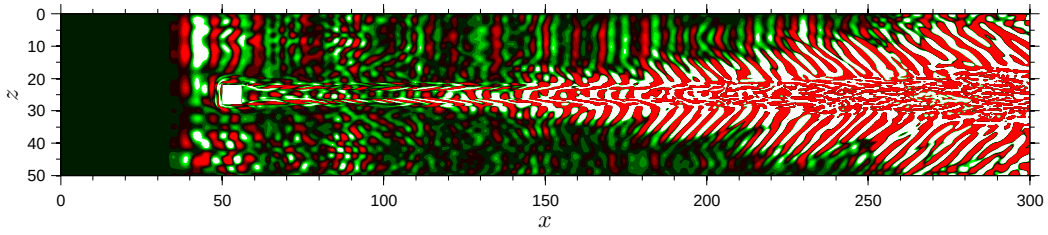

Figure 4.9: Development of two-dimensional waves inside the boundary layer. Contours of fluctuating v'-velocity in a horizontal plane at $y = 0.3$.

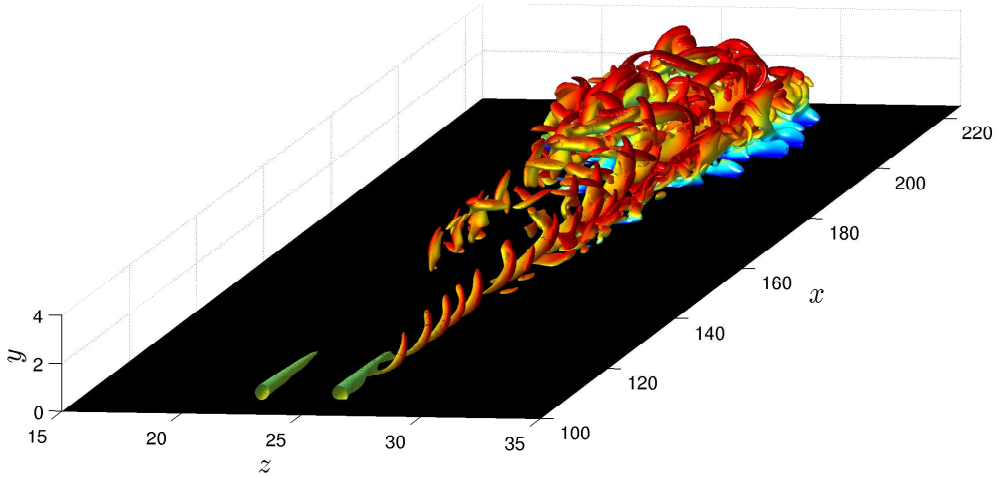

Figure 4.10: Isosurfaces of $Q = 0.0055$, coloured by streamwise velocity, showing the flow structures appearing during breakdown to turbulence.

ones. In the case considered here, visualisations of the disturbance field inside the boundary layer reveal the presence of two-dimensional waves, see the contours of v' shown in figure 4.9, which, judging from the dominant streamwise wavenumbers, may well be the sign of Mack mode instabilities. These, however, are only

evident starting from about $x = 140$ and do not seem to interfere with the initial instability of the wake. This observation highlights the important role played by the receptivity mechanisms in the laminar-turbulent transition.

The dominant flow structures appearing in the flow during the final transition stages are shown in figure 4.10 through isosurfaces of the second invariant of the velocity gradient tensor (Q-criterion Chong *et al.*, 1990), given by

$$Q := \frac{\partial u}{\partial x}\frac{\partial v}{\partial y} + \frac{\partial u}{\partial x}\frac{\partial w}{\partial z} + \frac{\partial v}{\partial y}\frac{\partial w}{\partial z} - \left(\frac{\partial u}{\partial y}\frac{\partial v}{\partial x} + \frac{\partial u}{\partial z}\frac{\partial w}{\partial x} + \frac{\partial v}{\partial z}\frac{\partial w}{\partial y}\right). \tag{4.3}$$

The breakdown to turbulence starts with the roll-up of the lateral shear layer at $z \approx 27$. As a result, a series of vortices become visible in figure 4.10 starting from about $x = 110$, the legs of which form strong quasi-streamwise vortices and quickly drive the flow to an unpredictable chaotic state. The opposite side of the wake goes through a similar process, with roll-up of the lateral shear layer visible from $x \approx 150$. By about $x = 200$ strong quasi-streamwise vortices appear also in this region of the wake. Further downstream strong vortex interactions lead to the development of a wedge of transitional/turbulent flow, the features of which will be discussed in the following section.

4.2.3 Turbulent wedge development

Following the breakdown to turbulence described above, a region of turbulent flow appears downstream of the roughness element, forming a wedge of turbulence which expands laterally with increasing streamwise distance. The lateral spreading of turbulence in turbulent wedges is currently not well understood and the literature on this subject is limited (Schubauer & Klebanoff, 1955; Gad-el Haq *et al.*, 1981; Clark *et al.*, 1993; Zhong *et al.*, 2003; Fiala & Hillier, 2005). The aim of this section is to present results which will shed some new light into the processes leading to the lateral growth of a turbulent wedge at $M_\infty = 6.0$.

The turbulent wedge is visualised in figure 4.11(a) through an isosurface plot of $Q = 0.02$. It can be seen that the edges of the wedge are populated mostly by elongated streamwise vortices, while smaller structures can be found near the core of the wedge. Top and crossflow views of turbulent kinetic energy (TKE) contours, respectively at $y = 1.17$ and $x = 281$, showing the extent of the turbulent wedge, are provided in figures 4.11(b) and 4.11(c). As expected, high TKE values are found at the edges of the turbulent wedge, in regions where laminar flow

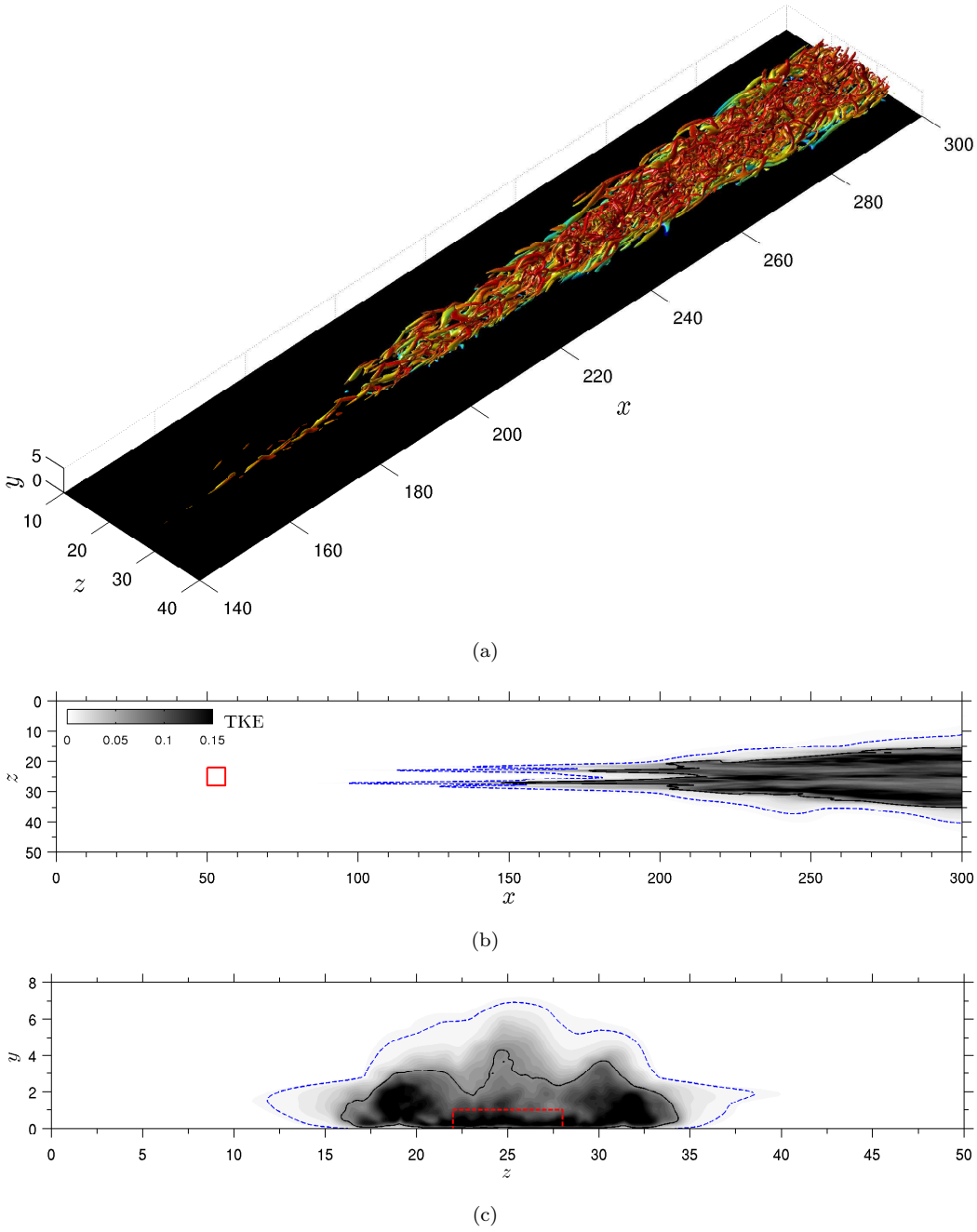

Figure 4.11: Visualisation of the turbulent wedge developing downstream of the roughness. The solid and dashed contourlines in (b) and (c) indicate, respectively, $TKE = 0.08$ and $TKE = 0.007$. (a) Isosurfaces of $Q = 0.02$, coloured by streamwise velocity, (b) TKE contours in the horizontal plane at $y = 1.1$, (c) crossflow TKE contours at $x = 281$.

undergoes transition to turbulence, and in the near wall region. The solid and dashed contourlines indicate, respectively, $TKE = 0.07$ and $TKE = 0.008$ and clearly show the existence of a region of intermittent flow bounding the core of the wedge. Regions of intermittent flow near the sides of turbulent wedges have been

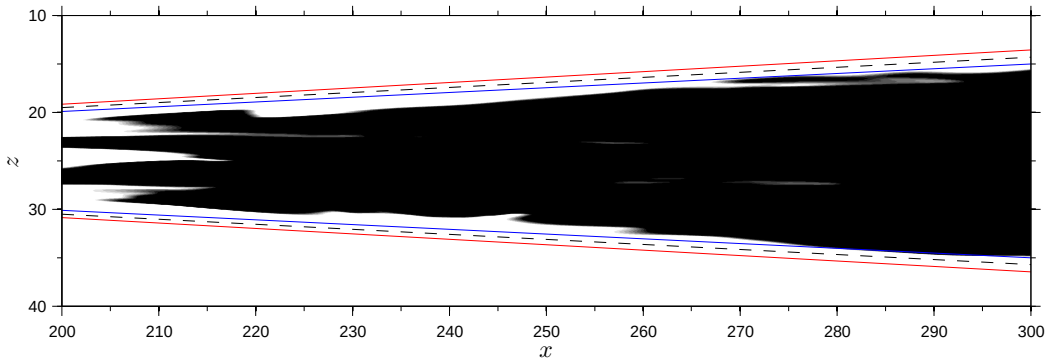

(a)

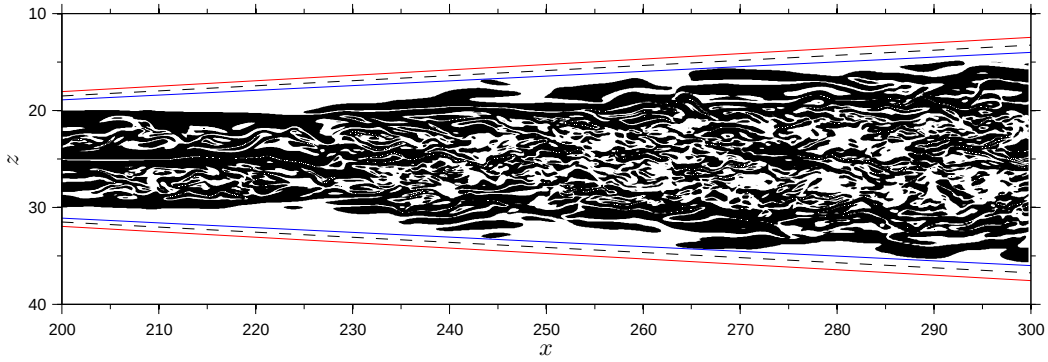

(b)

Figure 4.12: Measuring the lateral spreading half angle of the turbulent wedge. The solid blue, dashed black and solid red lines are inclined at $\alpha = 2.8°$, $\alpha = 3.0°$ and $\alpha = 3.2°$ to the horizontal, respectively. (a) contours of $TKE \geq 0.07$ at $y = 1.1$, (b) contours of $0.06 \leq |\omega_y| \leq 0.08$ at $y = 1.1$.

found experimentally, both at low (Schubauer & Klebanoff, 1955; Clark *et al.*, 1993; Zhong *et al.*, 2003) and high speeds (Fiala & Hillier, 2005). The rate at which the turbulent wedge grows laterally is measured as the half angle of the wedge, which is estimated here to be $\alpha = 3.0 \pm 0.2°$. This value was obtained after measuring the spreading angle in two different ways. The first method entails visually measuring the lateral growth of a region of TKE ≥ 0.07 in a plan view at $y = 1.17$ (where TKE is maximum) while the second method looks at the lateral spreading of instantaneous plots of $0.06 \leq |\omega_y| \leq 0.08$. The TKE and $|\omega_y|$ cut-off values were chosen since they are representative of the values attained in the core of the wedge. The procedures are shown in figures 4.12(a) and 4.12(b), where the solid blue, dashed black and solid red lines are inclined, respectively, at $\alpha = 2.8°$, $\alpha = 3.0°$ and $\alpha = 3.2°$ to the horizontal. The value obtained here for the spreading half angle of the turbulent wedge lies within the interval proposed by Fischer (1972) for the spreading half angle of compressible turbulent spots, which was derived from experimental data. In addition, our result agrees well with the

spreading half angle reported by Redford *et al.* (2012) for a turbulent spot in a hot wall ($T_w = T_{ad}$) $M_\infty = 6.0$ boundary layer. It is interesting to note that the intermittent flow region (defined by TKE ≥ 0.008) surrounding the turbulent core of the wedge grows laterally with a spreading half angle of $\alpha = 4.0 \pm 0.4°$, close to the upper limit proposed by Fischer (1972) for the Mach number considered here. Differences in lateral growth rates between the intermittent and the fully turbulent regions of the wedge were found in a number of experiments (Schubauer & Klebanoff, 1955; Gad-el Haq *et al.*, 1981; Clark *et al.*, 1993; Zhong *et al.*, 2003; Fiala & Hillier, 2005). Here, the intermittent region is associated with the presence of a mean spanwise flow from the core of the wedge to the surrounding laminar flow, a feature which will be analysed later.

The agreement between the lateral growth rates of turbulent wedges and turbulent spots makes it interesting to understand whether the mechanisms dictating the growth of turbulent wedges are similar to those responsible for the lateral growth of turbulent spots. Redford *et al.* (2012) investigated the evolution of turbulent spots in $M_\infty = 3.0$ and $M_\infty = 6.0$ boundary layers and found, in agreement with previous studies (see for example Gad-el Haq *et al.*, 1981), that the dominant lateral spreading mechanisms are twofold; destabilisation of the surrounding laminar flow and lateral convection of turbulent structures from the centre of the spot outwards. The destabilisation mechanism was found to be dominant at $M_\infty = 3.0$, while at $M_\infty = 6.0$ the spot was found to grow mainly by convection. Hence, the well documented reduction of spreading angle with Mach number was attributed to the damping of the growth by destabilisation mechanism. Redford *et al.* (2012) found that the destabilisation of the surrounding laminar flow is due to the instability of lateral jets present at the edges of the spot, forced continuously by the turbulent core of the spot. These jets are also responsible for the convection of turbulent structures out into the laminar region of the boundary layer, and hence play an important role in the lateral spreading of turbulence. The spanwise flow observed by Redford *et al.* (2012) was characterised by lateral velocities that reached up to 10% of the free-stream velocity. Such lateral flows near the spot tips are generally believed to be a consequence of fluid entering the spot core at the top and rear of the spot and exiting sideways.

The present results show that the mean flow inside the turbulent wedge is characterised by the presence of quasi-streamwise vortices, believed to be responsible for the spanwise distribution of turbulent structures. The appearance of large vortices in the mean velocity field is shown in figure 4.13, where the time-averaged crossflow velocity vectors are plotted over $\overline{w} = \pm 5 \times 10^{-3}$ contours at different streamwise

positions. In order to provide a more detailed visualisation the figures only show half of the turbulent wedge. As the roughness wake breaks down into turbulence, the pair of counter rotating streamwise vortices induced by the roughness, one of which can be seen in figure 4.13(a) near $z = 24$, gain strength and two secondary streamwise vortices appear at the two edges of the newly formed turbulent wedge. One of these vortices is visible in figure 4.13(a) near $z = 21$. Further downstream, the roughness induced streamwise vortices lose strength as the core of the wedge

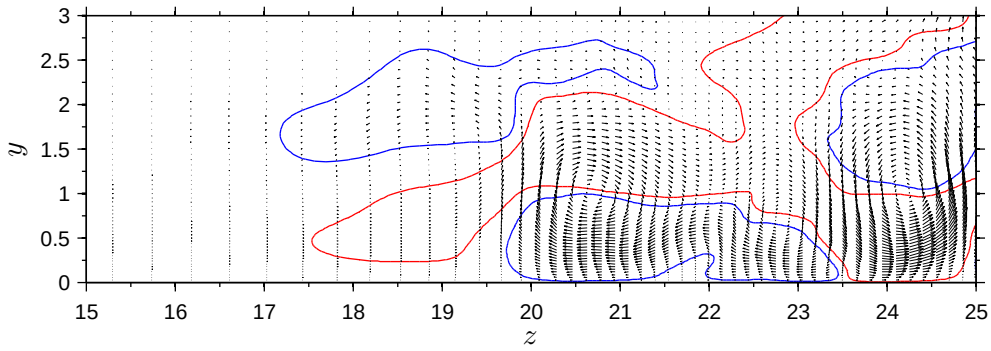

(a)

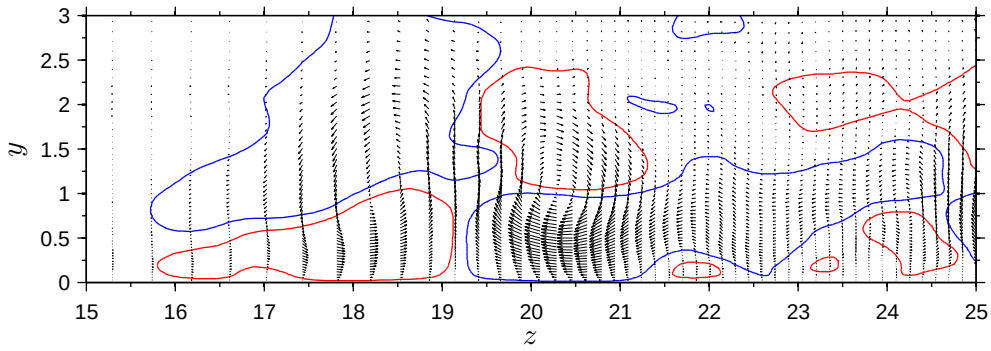

(b)

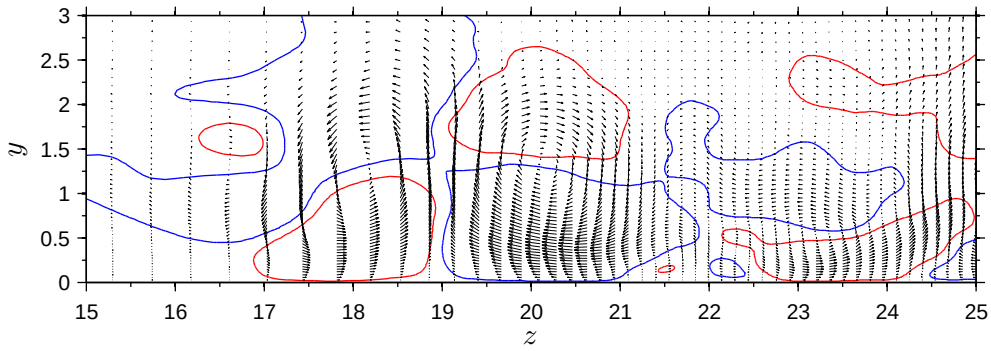

(c)

Figure 4.13: Contours of $\overline{w} = \pm 5 \times 10^{-3}$ (red for positive and blue for negative), superimposed by mean crossflow velocity vectors. (a) $x = 241$, (b) $x = 277$, (c) $x = 289$.

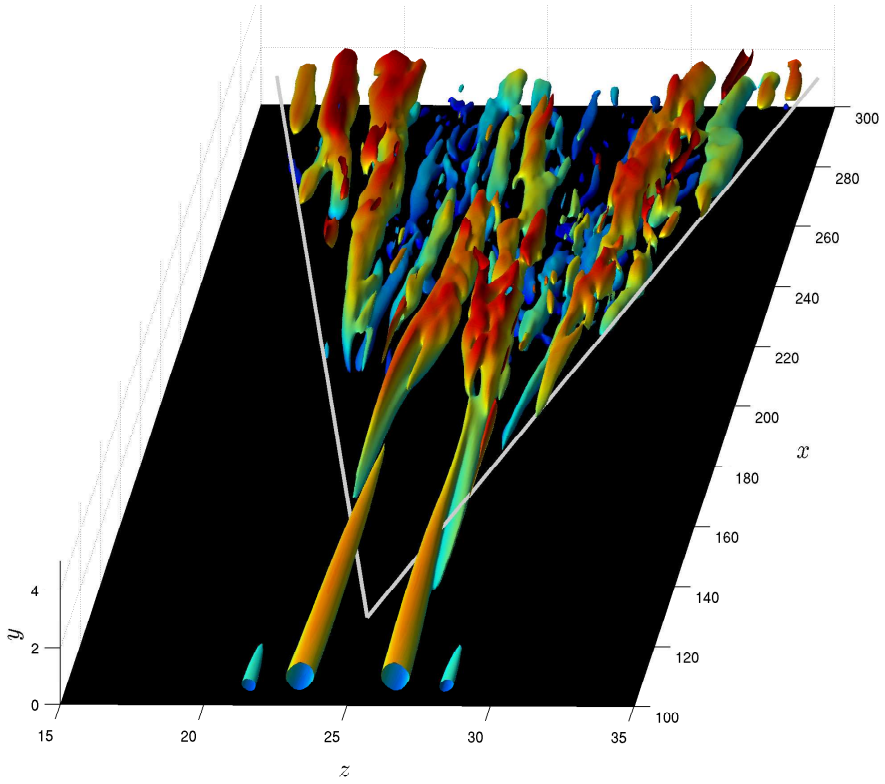

Figure 4.14: Isosurfaces of mean $Q = 0.001$, coloured by wall-normal distance. The light grey lines are inclined at $\alpha = 3.0°$ to the streamwise direction.

evolves towards a fully turbulent state. Meanwhile, the two secondary vortices become stronger and drift laterally outwards. For increasing streamwise distance new quasi-streamwise vortices appear in succession near the edges of the turbulent wedge, each counter rotating with respect to its neighbour. The generation of a new vortex of opposite sign can be observed in figure 4.13(b) at about $z = 18.5$ and the initial stages of the roll up of an additional vortex can be seen in figure 4.13(c) near $z = 16.5$. A better visualisation of the development of large mean vortical structures inside the turbulent wedge is given in figure 4.14 through isosurfaces of mean $Q = 0.001$, coloured by wall-normal distance. The quasi-streamwise vortices found at the sides of the wedge are inclined laterally at aproximately 1° to the streamwise direction and sit at the boundary between turbulent and laminar flow. It seems clear from figure 4.14 that the lateral displacement of these vortices and the generation of new vortices both contribute to the spanwise growth of the turbulent wedge. In fact, using the development of these structures to calculate the lateral spreading rate of turbulence gives $\alpha \approx 3.0°$ (see light grey line in figure 4.14), which agrees with measurements obtained from the TKE and instantaneous vertical vorticity contours discussed earlier. The lateral drift of the secondary vortices suggests the presence of considerable spanwise mean flow from the core

of the wedge outwards. Some evidence of this secondary flow can be observed for example in figure 4.13(b) near $z = 23$ and $y = 1.0$ and $z = 16.5$ and $y = 1.0$. However, the mean lateral velocities observed here are lower than those reported in turbulent spots studies (Wygnanski *et al.*, 1982; Redford *et al.*, 2012). It should be noted that, since the wedge under consideration is transitional, the observation period ($T_s = 2100$) used here for the computation of the time averages, might not be sufficient to capture the full details of the time-averaged flow. In fact, as will be shown in the next section and for the $M_\infty = 2.5$ case, mean lateral flow clearly appears in crossflow mean w-velocity contour plots in regions where the turbulent wedge is fully developed. The other dominant mechanism of lateral spreading observed, that is, the generation of new steady quasi-streamwise vortices at the sides of the wedge, seems here to be simply due to the roll-up of streamwise vorticity generated by the action of the above mentioned lateral mean flow, combined with the upwash or downwash induced by the steady vortex placed at the edge of the wedge. This mechanism always leads to the formation of successive counter-rotating vortices.

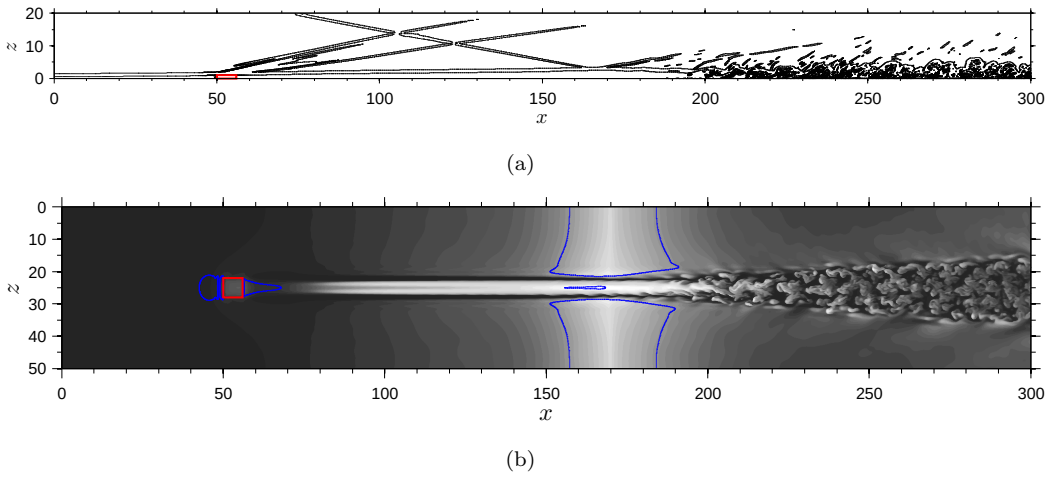

Figure 4.15: Flow features induced by the SBLI. (a) contours of $\sqrt{(\partial\rho/\partial x)^2 + (\partial\rho/\partial y)^2}$ at the roughness mid-plane, (b)contours of instantaneous temperature in a horizontal plane at $y = 1.2$. The red squares indicate the roughness position and the blue line shows regions of separated flow ($\overline{u} = 0$ at the first grid point above the wall).

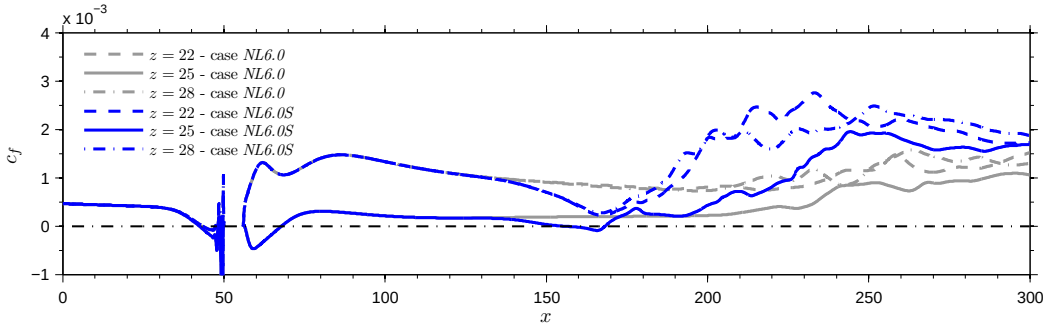

Figure 4.16: Streamwise evolution of time-averaged skin friction at the roughness mid-plane, showing the effect of the SBLI on the breakdown to turbulence.

4.2.4 Effects of a shock wake impinging on the transitional boundary layer

Although interactions between shock-waves and boundary layers are a common feature of high-speed flight, our current knowledge of the fundamental physical mechanisms involved in unsteady shock-wave/boundary-layer interactions (SBLI) is far from complete and a number of aerospace applications would benefit from a deeper understanding of the subject. Most of the research efforts in this field have been directed to the analysis of shock-waves interacting with nominally two-dimensional turbulent boundary layers (Dolling, 2001), mainly to explain the onset of large unsteady thermal and pressure loads induced by SBLI and the characteristic low frequency unsteadiness associated with such interactions (Touber & Sandham, 2009, 2011). However, flows over high-speed vehicles and, in particular, inside the intakes of their air-breathing propulsion systems are very complex and include interactions of shock-waves with three-dimensional transitional boundary layers. The transition process at high speeds may be greatly affected by the interaction with shock-waves through mechanisms that are largely unknown. The limited number of studies available in the literature on transitional SBLI show that for strong interactions (in the convective instability regime) small-amplitude disturbances experience strong amplification across the shock-induced separation bubble due to the instability of the separated shear layer (Yao *et al.*, 2007). In addition, transitional interactions induce higher levels of unsteadiness and stronger thermal loads than in the fully turbulent case (Benay *et al.*, 2006; Murphree *et al.*, 2006).

The results presented here are aimed at shedding some light on the modifications introduced by a relatively weak oblique shock impingement on a boundary layer

undergoing the final stages of transition to turbulence. The interaction analysed is highly unsteady, as the shock impinges onto the boundary layer immediately downstream of the initial breakdown to turbulence, in a region of three-dimensional transitional flow. As reported in table 4.1, we consider a shock generator angle of $\theta = 1.70$ and the shock is set to reach the wall at $x_{imp} = 180$ by imposing the appropriate jump conditions on the upper boundary of the computational domain at $x = 74.15$.

Figure 4.15 provides a visualisation of the flow features induced by the SBLI. An oblique shock can be seen to reach the edge of the boundary layer near $x = 165$ in figure 4.15(a), which shows contours of $\sqrt{(\partial\rho/\partial x)^2 + (\partial\rho/\partial y)^2}$ at the roughness mid-plane. The shocks associated with the upstream and downstream roughness induced separation bubbles are also visible for $x > 60$. Figure 4.15(b) shows temperature contours (shaded contours) on the horizontal plane at $y = 1.2$, superimposed by $\overline{u} = 0$ contours (blue line) at the first grid point above the wall, showing regions of mean separated flow. The shock system is strong enough to lead to a small separation bubble in the laminar boundary layer away from the roughness wake, with a bubble length varying from about 30 inflow displacement thicknesses at the edges of the computational domain to about 40 close to the transitional region. On the other hand, the transitional region of the boundary layer remains mostly attached, with the exception of a small region of separated flow near the roughness mid-plane, visible near $x = 160$.

By comparing figure 4.15(b) with figure 4.2(b) one can already notice that the shock moves the transition point upstream and leads to a wider turbulent wedge. This observation is supported by the streamwise evolution of skin friction coefficient, shown in figure 4.16 for three different positions across the span. It can be seen that the shock leads to a significant reduction of the transition region length. This effect is more evident for the two lateral positions considered, where the skin friction rise can be seen to occur considerably further upstream (about 30 displacement thicknesses) than for the case without a shock. The skin friction rises sharply from $x \approx 170$, roughly starting from the centre of the separation bubble, and reaches a maximum before decreasing again near the outflow boundary, indicating that transition is complete. At the roughness mid-plane transition to turbulence occurs faster than in the case without a shock, however the skin friction rise in this region is more gradual than in the lateral positions. The effects of the shock/boundary layer interaction on heat transfer and unsteady pressure loads at the wall are shown in figure 4.17. Regions of high wall-normal temperature gradient and wall pressure fluctuations appear for case *NL6.0S* in

figures 4.17(b) and 4.17(d), respectively, near the sides of the roughness wake at $x \approx 200$, which are not present for case *NL6.0* (see figures 4.17(a) and 4.17(c)) and correlate with the strong skin friction increase shown in figure 4.16 at the same spanwise locations. Overall, peak values of $\partial\overline{T}/\partial y$ and p'_{rms}/p_∞ registered for case *NL6.0S* in the breakdown region are comparable to those observed in case *NL6.0*. In the case with shock interaction the breakdown to turbulence seems to be fixed by the shock impingement point and occurs immediately downstream of

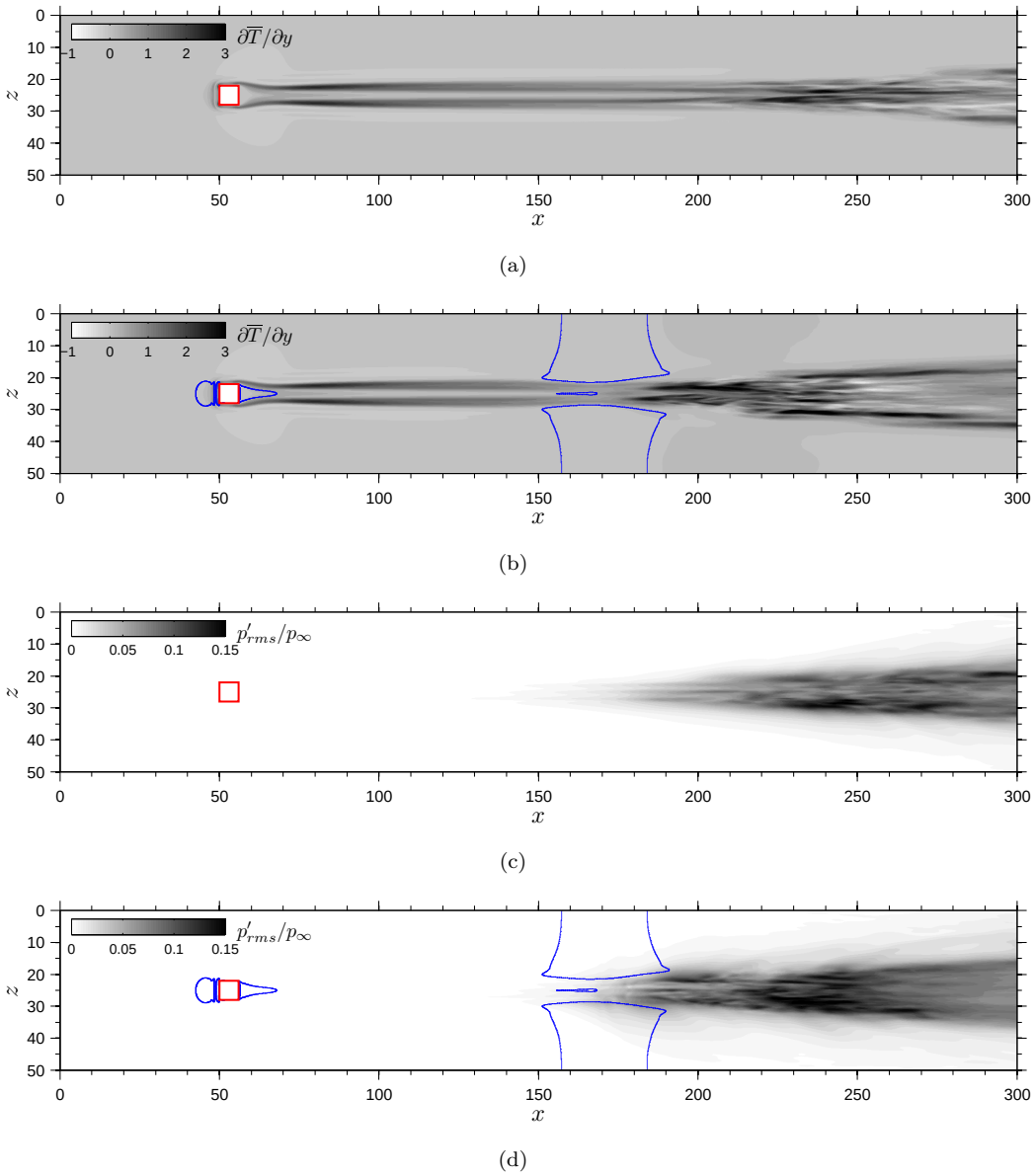

Figure 4.17: Effects of SBLI on heat transfer and unsteady pressure loads at the wall. Blue lines show regions of separated flow ($\overline{u} = 0$ at the first grid point above the wall). (a) $\partial\overline{T}/\partial y$ for case *NL6.0*, (b) $\partial\overline{T}/\partial y$ for case *NL6.0S*, (c) p'_{rms}/p_∞ for case *NL6.0*, (d) p'_{rms}/p_∞ for case *NL6.0S*.

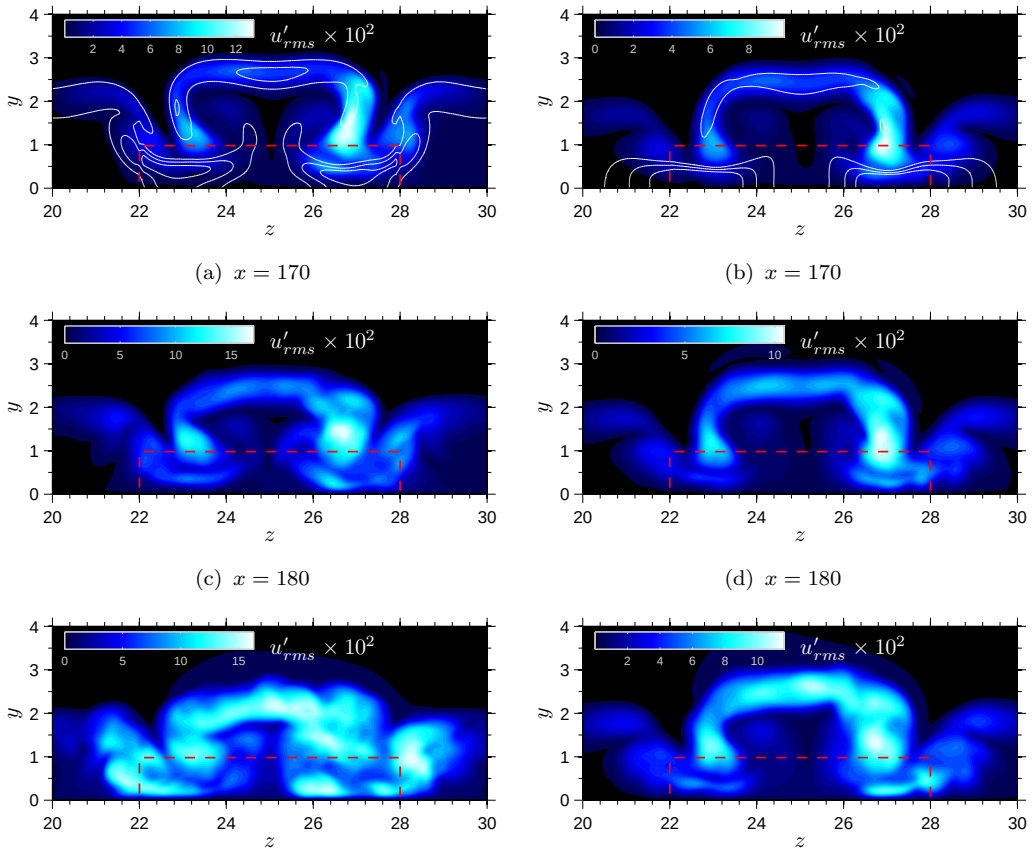

(a) $x = 170$ (b) $x = 170$

(c) $x = 180$ (d) $x = 180$

(e) $x = 190$ (f) $x = 190$

Figure 4.18: Effect of the SBLI on the growth of disturbances inside the roughness wake. White lines in (a) and (b) show $u_S = 0.65, 1.025, 1.4$. (a), (c), (e) case *NL6.0S* and (b), (d), (f) case *NL6.0*.

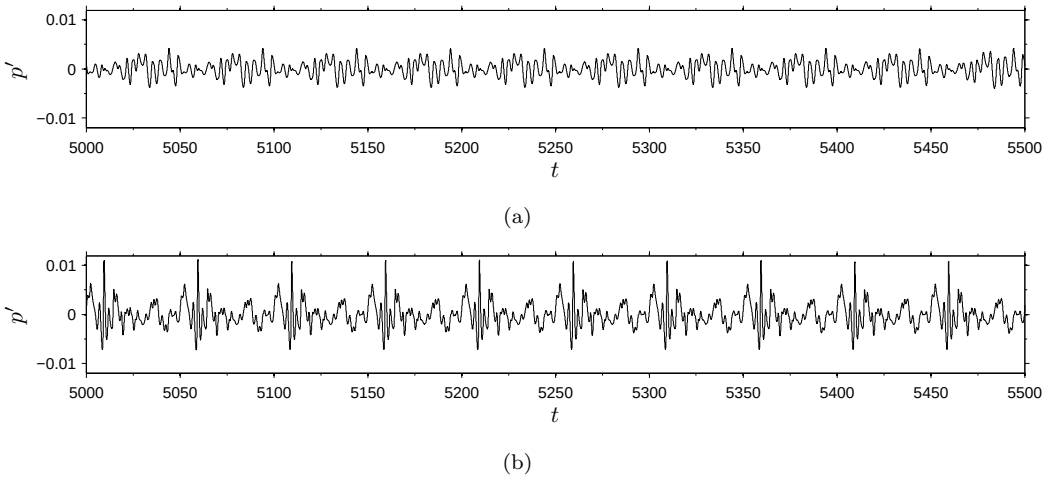

(a)

(b)

Figure 4.19: Pressure probe at $x = 210$ and $z = 25$ showing the amplification of low frequencies by the shock system. (a) *NL6.0*, (b) case *NL60S*.

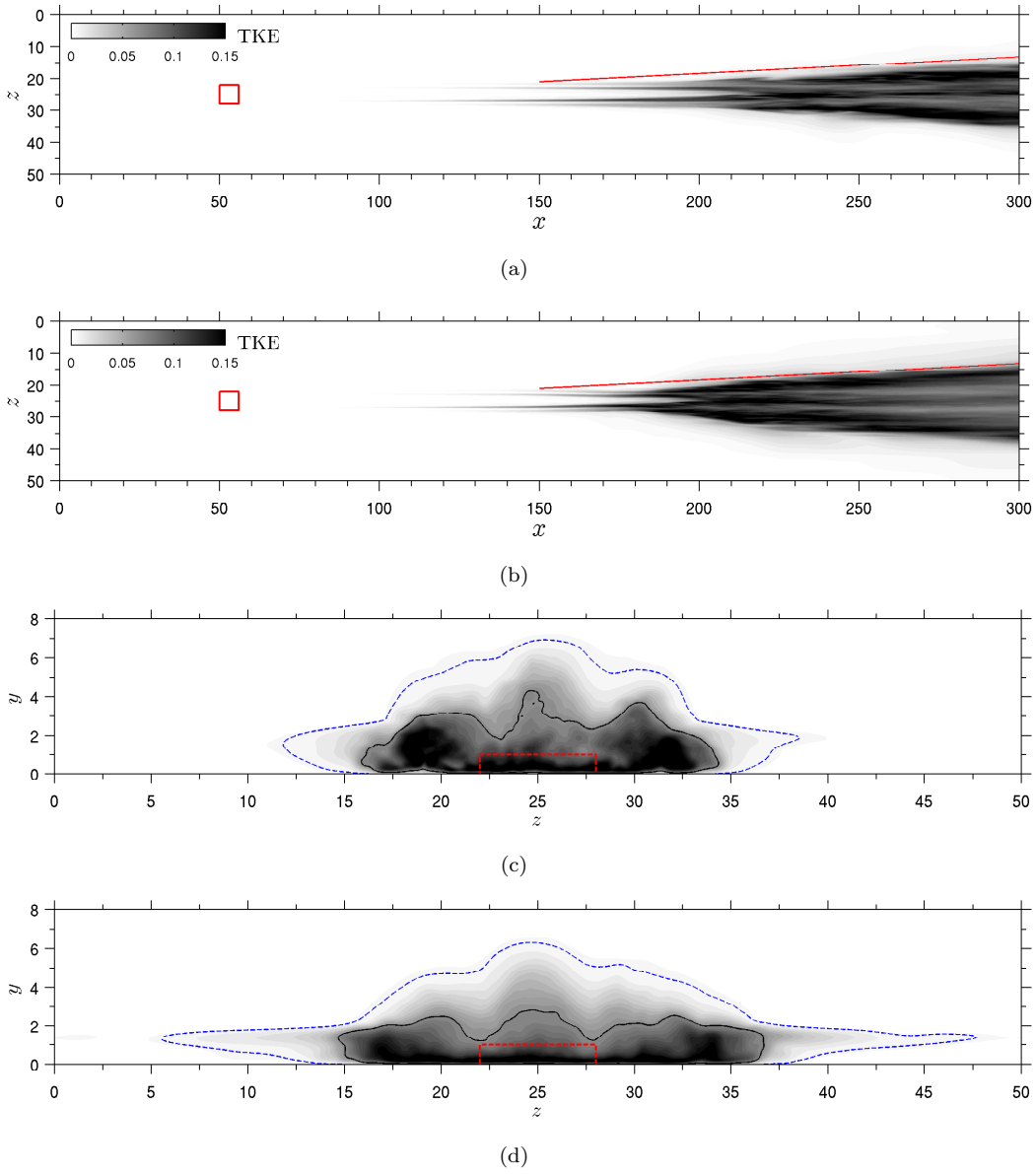

Figure 4.20: Comparison of the turbulent wedge structure for cases *NL6.0* and *NL6.0S*. The solid and dashed contourlines in (c) and (d) indicate, respectively, $TKE = 0.07$ and $TKE = 0.008$. (a) TKE contours in the horizontal plane at $y = 1.1$ for case *NL6.0*, (b) TKE contours in the horizontal plane at $y = 1.1$ for case *NL6.0S*, (c) crossflow TKE contours at $x = 281$ for case *NL6.0*, (c) crossflow TKE contours at $x = 281$ for case *NL6.0S*.

the shock-induced separation bubble.

More insight into the mechanisms leading to early transition in the presence of SBLI can be gained by analysing how the shock modifies the flow inside the wake

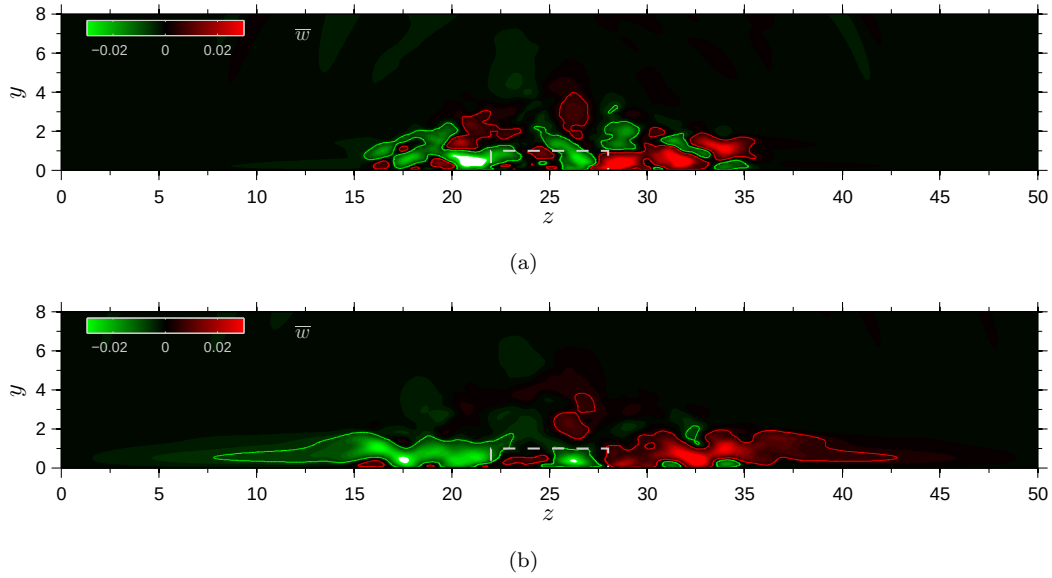

Figure 4.21: Crossflow contours of mean lateral velocity. Red and green contourlines show respectively $\overline{w} = +5 \times 10^{-3}$ and $\overline{w} = -5 \times 10^{-3}$. The dashed white line indicates the roughness position. (a) $x = 250$, (b) $x = 280$.

of the roughness. Figure 4.18 shows crossflow contours of u'_{rms} at three different positions along the shock-induced separation bubble, giving a comparison between cases *NL6.0S* (left) and *NL6.0* (right) for the growth of disturbances in the roughness wake. It can be seen that the shock system changes the shape of the roughness wake. By comparing figures 4.18(a) and 4.18(b), one can note that the shock leads to the generation of lateral shear layers near the sides of the wake (see figure 4.18(a) near $z = 21.8$ and $z = 28.2$), which appear due to the separation induced in the surrounding laminar boundary layer. Disturbances grow rapidly in these lateral shear layers for increasing streamwise distance, as shown in figures 4.18(c) and 4.18(e). On the other hand, figures 4.18(d) and 4.18(f) show that in the absence of shock impingement the wake instability is contained within the shear layers bounding the roughness induced streamwise vortices. It is therefore believed that the lateral shear layers induced by the shock system play an active role in the acceleration of the transition process by the SBLI. Pressure signals registered by numerical probes located at $x = 210$ and $z = 25$ (roughness mid-plane) are shown in figures 4.19(a) and 4.19(b) for case *NL6.0* and *NL6.0S* respectively. The shock leads to the amplification of a rage of frequencies, however a distinctive tone appears for $F \approx 0.02$, which corresponds to the ΔF of the forced acoustic disturbances. Flow visualisations suggest that this peak is associated with the vortex shedding from the edge of the separation bubble. A mechanism involving the amplification of low frequencies by the shock system was proposed by Touber

& Sandham (2011) for turbulent SBLI. The observation made here for transitional SBLI would need to be studied in more detail in the future.

Finally, we analyse the effects of SBLI on the development of the turbulent wedge forming downstream of the roughness element. Figure 4.20 gives top and crossflow views of the TKE contours, respectively at $y = 1.1$ and $x = 281$, for cases *NL6.0* and *ML6.0S*, showing a comparison of the turbulent wedge structure. It can be seen that the lateral spreading of turbulence is higher for case *NL6.0S* in a region immediately downstream of the separation bubble (from $x \approx 190$ to $x \approx 220$ in figure 4.20b), while further downstream the turbulent wedge recovers the spreading rate of the case without a shock (see the fixed red line in figures 4.20a and 4.20b). The net result is a wider turbulent wedge for case *NL6.0S*. The agreement in lateral growth rates between a transitional turbulent wedge (case *NL6.0*) and a fully developed turbulent wedge (case *NL6.0S*) is somewhat surprising. However, a similar result was reported by Clark *et al.* (1993) for incompressible turbulent wedges. As shown in figures 4.20(c) and 4.20(d), at $x = 281$ the region of intermittent flow bounding the core of the wedge protrudes deeper into the surrounding laminar boundary layer for case *NL6.0S*, suggesting the presence of a stronger lateral flow than that observed for case *NL6.0*. Figures 4.21(a) and 4.21(b), showing crossflow contours of mean lateral velocity respectively at $x = 250$ and $x = 280$ for case *NL6.0S*, provide evidence that, in fact, lateral jets clearly form near the edges of the turbulent wedge as it evolves from a transitional to a fully turbulent state. The average $\overline{w}$-velocities observed in this case are about 1% of the free-stream velocity, with instantaneous peaks reaching up to 3%. Visualisations of the instantaneous velocity field show that lateral jets with w-velocities of the order of 10% of the free-stream velocity appear sporadically near the edges of the wedge. These jets, however, do not seem to contribute significantly to the lateral spreading of turbulence. It is interesting to note that, in the case analysed in this section, the mean lateral jets lead to the generation of steady co-rotating vortices (see near $z = 16$, $z = 18$, $z = 31$ and $z = 34$ in figure 4.21b), similar to those one would expect to arise from a crossflow instability.

In the light of the results presented in this section, it appears that the mechanisms responsible for the lateral growth of turbulent wedges and turbulent spots in $M_\infty = 6.0$ boundary layers present some similarities but also differences. In both cases, the spanwise displacement of turbulent structures due to the presence of a lateral flow from the turbulent core out into the laminar boundary layer seems to be the dominant mechanism. Moreover, the results analysed here did not show any strong evidence of the spreading by destabilisation of lateral jets, which was also found

by Redford *et al.* (2012) to be almost entirely suppressed at $M_\infty = 6.0$ (as will be shown later, this mechanism is active at $M_\infty = 2.5$). The present investigation also sheds some new light into the lateral spreading mechanisms of turbulent wedges. It appears that in the transitional stages of the wedge steady quasi-streamwise vortices, placed at the boundary between laminar and transitional flow, play an active role in the growth of the wedge. It is found that the mean spanwise flow from the core of the wedge outwards induces a lateral drift of these vortices and also participates in the generation of new structures. On the other hand, as noted above, the appearance of steady co-rotating vortices near the sides of fully developed turbulent wedges suggest that crossflow instability could contribute to the lateral growth of the wedge.

4.3 Roughness-induced breakdown to turbulence at $M_\infty = 2.5$

In this section we discuss the results obtained for the roughness-induced transition to turbulence in a $M_\infty = 2.5$ boundary layer. As for the $M_\infty = 6.0$ case discussed in the previous sections, we first provide a description of the main features of the time-averaged flow, followed by a discussion of the mechanisms leading to breakdown to turbulence and a study of the evolution of the turbulent wedge induced downstream of the roughness element as a result of the breakdown to turbulence. The section ends with a discussion of the results obtained for an investigation into the modifications introduced by an oblique shock impinging on the transitional boundary layer developing downstream of the roughness element.

4.3.1 Mean flow features

In the absence of upstream disturbances, the case analysed in this section is identical to case *HR1.0$_b$*, considered for the receptivity study (see section 3.5). The laminar flow around the roughness in this case is characterised by strong counter-rotating streamwise vortices which give rise to a highly unstable, three-dimensional detached shear layer, as seen in figure 3.17(c), in the wake of the roughness element. When subjected to external perturbations, the roughness wake develops instabilities which eventually lead to breakdown to turbulence. Figure 4.22 gives plan and side views of the transitional flow through contours of temperature. Regions of high (near the roughness centreline) and low (at the sides of the wake)

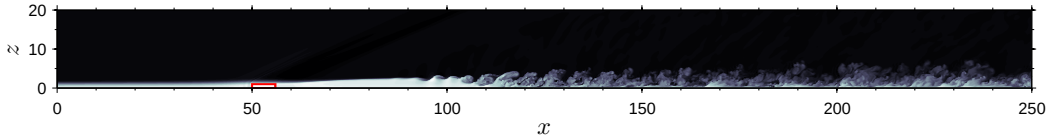

(a)

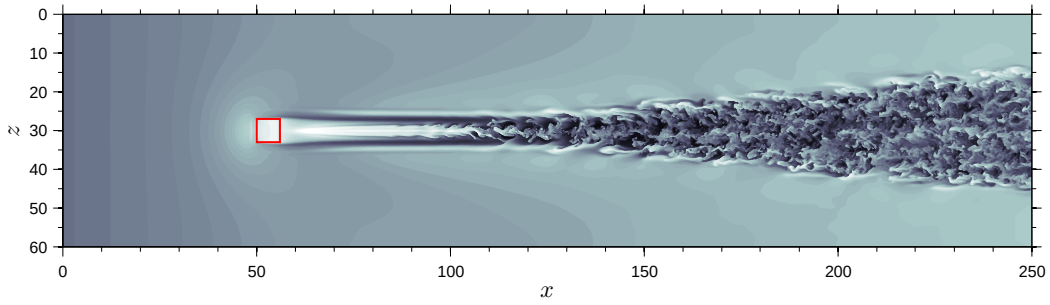

(b)

Figure 4.22: Contours of instantaneous temperature. The red squares indicate the roughness position. (a) side view at the roughness mid-plane, (b) top view in a horizontal plane at $y = 1.2$.

temperature fluid downstream of the roughness show the lift-up effect created by the strong counter-rotating streamwise vortices. Judging from the mixing of hot and cold fluid, breakdown to turbulence can be seen to start in the wake of the roughness at $x \approx 110$. Turbulent flow spreads laterally for increasing downstream distance, leading to the generation of a turbulent wedge downstream of the roughness.

Figure 4.23 shows the streamwise variation of the time-averaged skin friction coefficient at three positions across the span, namely $z = 27$, $z = 30$ (the mid-span location) and $z = 33$, chosen here to represent the transitional flow behaviour at the centre ($z = 30$) and at the sides ($z = 27$ and $z = 33$) of the roughness wake. In the roughness mid-plane, the skin friction rises sharply starting from $x \approx 100$ due to the breakdown to turbulence; it peaks at $x \approx 125$ and decays further downstream as the turbulent boundary layer grows. At $z = 27$ and $z = 33$ breakdown to turbulence leads to a gradual skin friction increase starting from $x \approx 110$. The c_f values attained at these two lateral wake positions after breakdown to turbulence are higher than those obtained at the roughness mid-plane, which indicates that the effect of the streamwise vortices on the mean flow persists after transition, similarly to what was found for case *NL6.0*.

Figures 4.24(a) to 4.24(c) show contours of, respectively, $\partial\overline{u}/\partial y$, $\partial\overline{T}/\partial y$ and p'_∞/p_∞ at the wall. An increase in skin friction near the wall translates into an increased

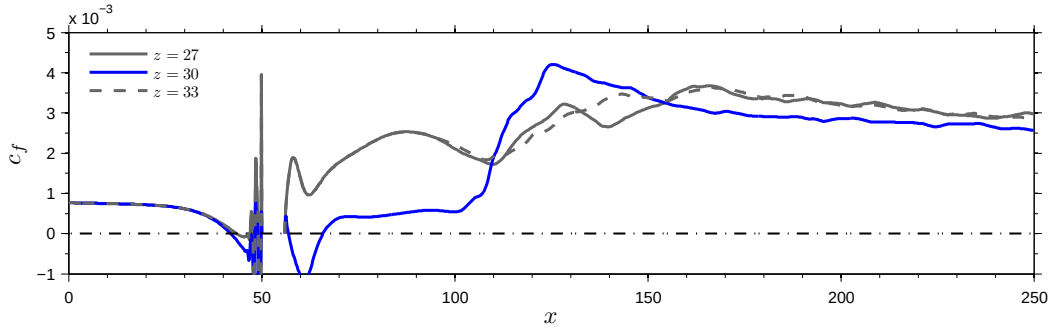

Figure 4.23: Streamwise evolution of time-averaged skin friction at the different positions across the span.

wall-normal temperature gradient. Figures 4.24(a) and 4.24(b) show the footprints of the pair of counter-rotating streamwise vortices induced by the roughness element (near $z = 27$ and $z = 33$) and the location of the initial breakdown to turbulence, visible near $x = 110$ where $\partial\overline{T}/\partial y$ reaches its peak. A relatively large region of negative wall-normal temperature gradient, which can be seen near $x = 130$ in figure 4.24(b), appears as cold free-stream fluid is pushed towards the wall by the breakdown of the boundary layer. Breakdown to turbulence also leads to a local increase of unsteady pressure loads, as shown in figure 4.24(c). The rms of the fluctuating wall pressure peaks in regions placed immediately downstream of the initial breakdown to turbulence, near $x = 110$ and $z = 30$, reaching values of about 8% of the free-stream pressure. In the fully developed turbulence region further downstream, the mean wall-pressure fluctuations decay to about 3% of the free-stream pressure.

4.3.2 Mechanisms responsible for the breakdown to turbulence

The results presented in the previous section show that the linear evolution of disturbances in the roughness wake eventually gives way to a nonlinear breakdown into turbulence. In this section, we look more closely at the evolution of disturbances in the roughness wake during the weakly and strongly nonlinear stages of transition, which drive the boundary layer to a turbulent state. Figure 4.25 shows contours of $u' = u - \overline{u}$ and u'_{rms} at different crossflow planes along the streamwise direction. The plots illustrate a sequence of events which describe the development of wake instability modes from the linear stages of transition until breakdown to turbulence. Figures 4.25(a) to 4.25(d) show that, as already discussed during the

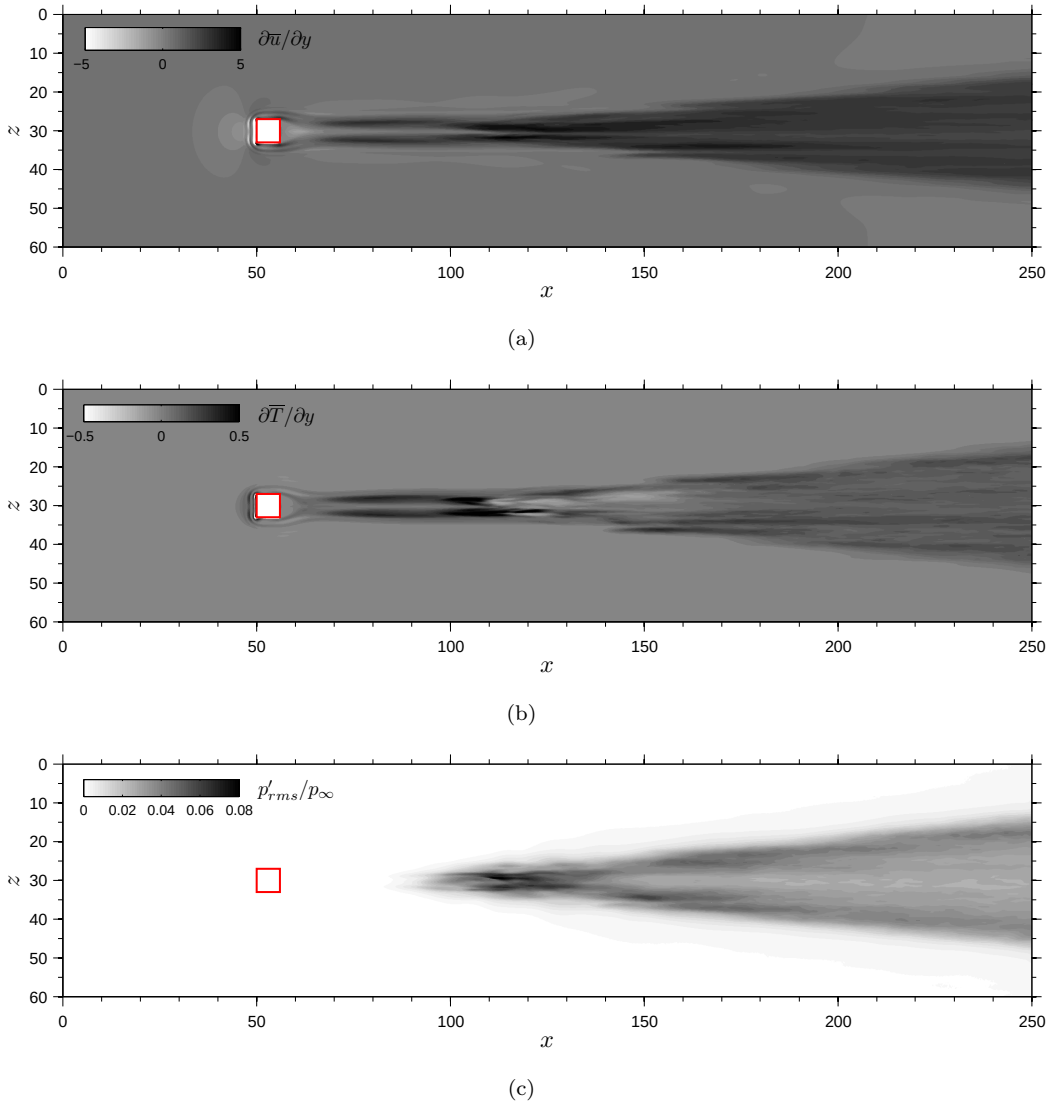

Figure 4.24: Effect of the isolated roughness, and the induced transition to turbulence, on the wall heat transfer and wall pressure fluctuations. (a) contours of wall-normal mean velocity gradient, (b) contours of wall-normal mean temperature gradient, (c) contours of the rms of the fluctuating wall-pressure normalised by free-stream pressure.

receptivity study in section 3.7, during the linear stages of transition the wake sustains the growth of sinuous and varicose modes. The varicose mode can be observed in the fluctuating u'-velocity field in figure 4.25(b) (notice the symmetric u' field), while the sinuous mode can be seen to appear shortly downstream in figure 4.25(d) (notice the nearly antisymmetric u' field). The contours of u'_{rms} in figures 4.25(a) and 4.25(c), on the other hand, show that the varicose mode is dominant at all streamwise locations, in agreement with the findings reported for the receptivity study, where varicose modes were found to be more unstable than

sinuous ones. The dominant varicose modes grow quickly in amplitude for increasing streamwise distance, as can be inferred from figures 4.25(e) and 4.25(f), leading eventually to the onset of nonlinear interactions and breakdown to turbulence (see 4.25g to 4.25j).

The streamwise variation of maximum (over y and z) u', v' and w' disturbances inside the roughness wake is shown in figures 4.26(a) and 4.26(b) on a logarithmic and on a linear scale, respectively. It can be seen that fluctuations of the u-velocity component are dominant throughout the transition region and in the fully turbulent boundary layer downstream. Disturbances grow in the roughness wake starting from $x \approx 60$ and initially evolve linearly. The maximum u', v' and w' perturbations grow at similar rates up to about $x = 75$, where the growth of v' and w' disturbances can be seen to accelerate considerably. This increase in growth rate signals the start of weakly nonlinear interactions. Note that the growth rate of u' perturbations does not change up to until $x = 80$, by which point nonlinear disturbances have grown large enough to dominate the instability of the wake. This quickly leads to a disturbance amplitude saturation at $x \approx 100$ and to the subsequent breakdown to turbulence. Note that the saturation of disturbances growing in the wake of the roughness is associated with the start of the skin friction rise in figure 4.23. Similarly to what was observed for the $M_\infty = 6.0$ case, during the linear and weakly nonlinear stages of transition before breakdown to turbulence, $u'_{rms} > v'_{rms} > w'_{rms}$, while, as expected, in the fully turbulent region further downstream $u'_{rms} > w'_{rms} > v'_{rms}$. This aspect can be seen clearly in figure 4.26(b).

A visualisation of the flow structures taking part in the breakdown to turbulence is given in figure 4.27 through isosurface of $Q = 0.01$ coloured by distance from the wall. The varicose instability mode observed above leads to the roll-up of the three-dimensional shear layer induced by the isolated roughness element, which can be seen starting from $x \approx 75$. This leads to the formation of a series of hairpin vortices whose legs connect with the streamwise vortices induced by the roughness element. Further downstream the hairpin vortices quickly break down, leading to a turbulent wedge which grows laterally for increasing streamwise distance. More details about the lateral spreading of turbulence after the breakdown process are provided in the next section.

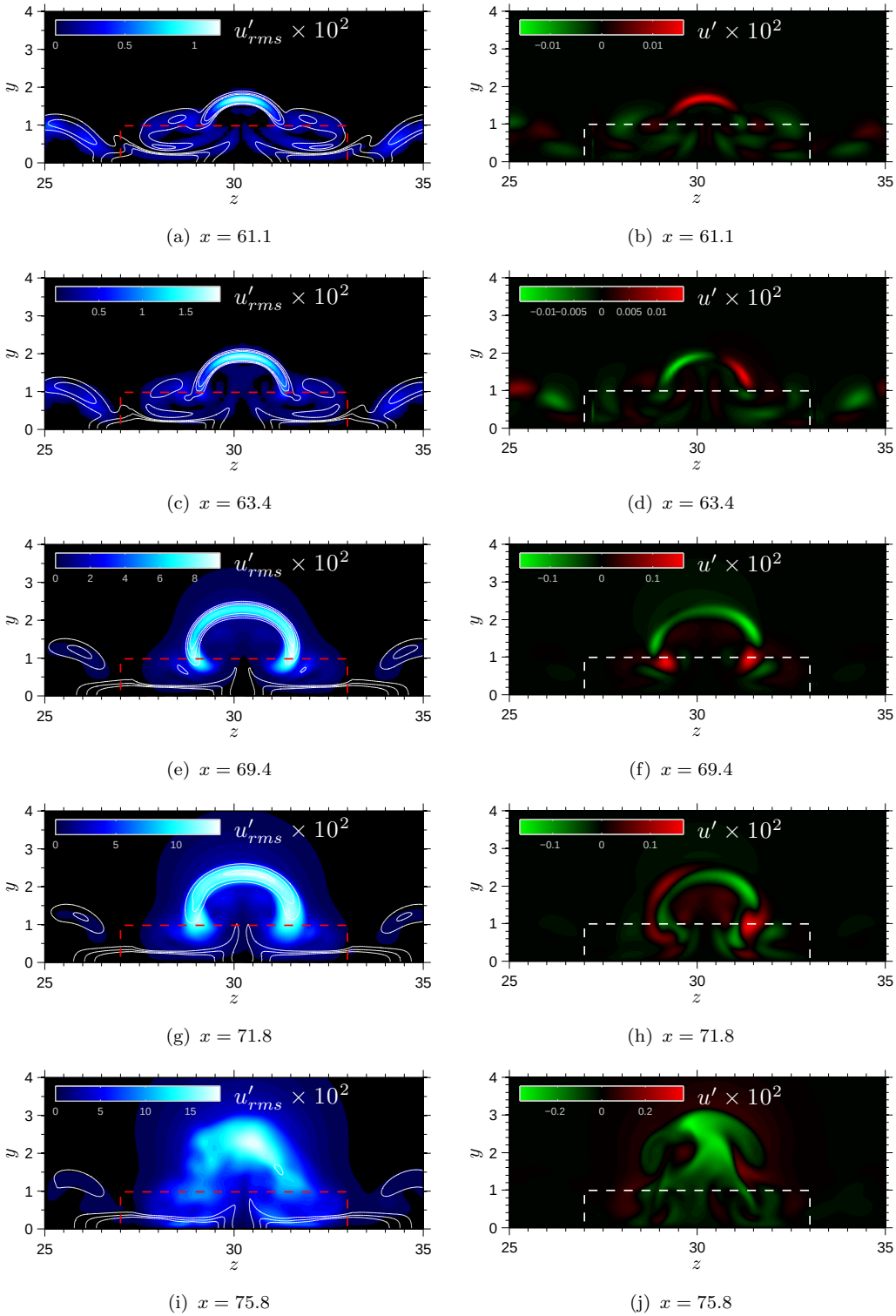

(a) $x = 61.1$ (b) $x = 61.1$

(c) $x = 63.4$ (d) $x = 63.4$

(e) $x = 69.4$ (f) $x = 69.4$

(g) $x = 71.8$ (h) $x = 71.8$

(i) $x = 75.8$ (j) $x = 75.8$

Figure 4.25: Visualisation of the downstream development of roughness wake instabilities. (a), (c), (e), (g), (i) contours of u'_{rms} (shaded), superimposed by $u_S = 0.65, 1.025, 1.4$ contours and (b), (d), (f), (h), (j) contours of u'.

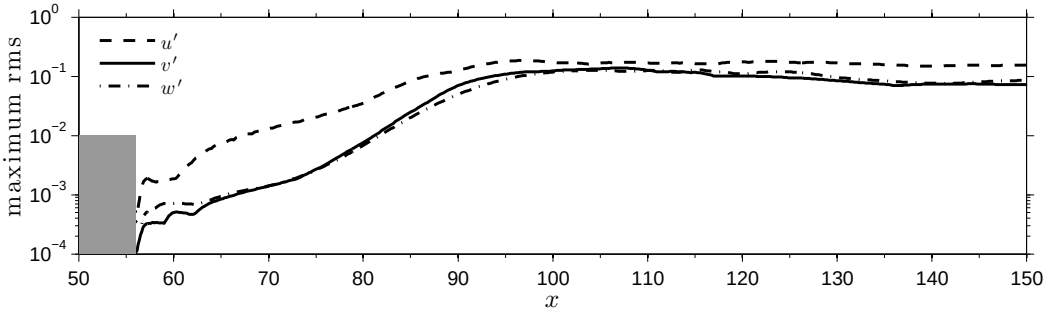

(a)

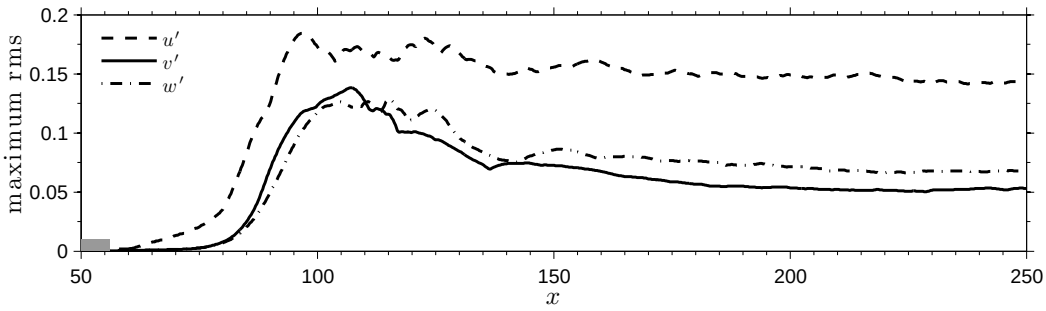

(b)

Figure 4.26: Linear and nonlinear evolution of disturbances in the roughness wake, shown by the streamwise evolution of maximum disturbance amplitude inside the wake of the roughness. (a) logarithmic scale, (b) linear scale.

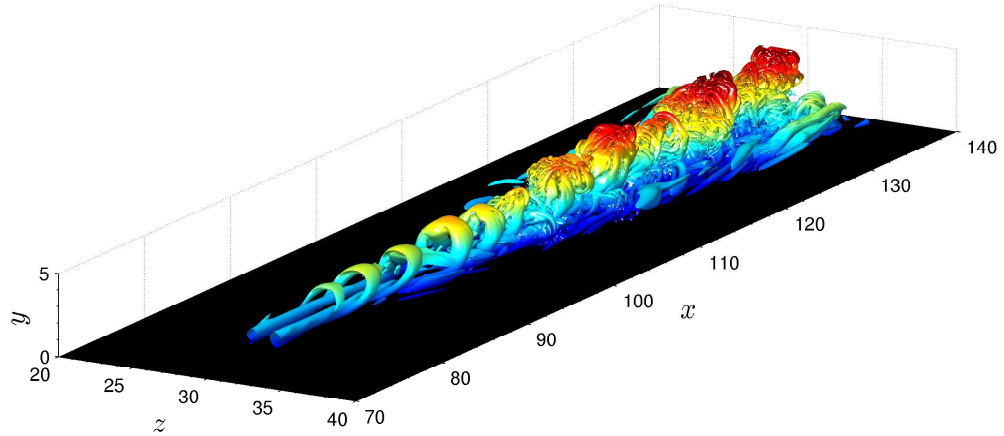

Figure 4.27: Isosurfaces of $Q = 0.01$, coloured by wall-normal distance, showing the flow structures appearing during breakdown to turbulence.

4.3.3 Turbulent wedge development

The wedge of turbulence forming downstream of the roughness element is visualised in figure 4.28(a) through isosurfaces of $Q = 0.02$ coloured by distance from the wall. It can be seen that the edges of the wedge are populated by streamwise

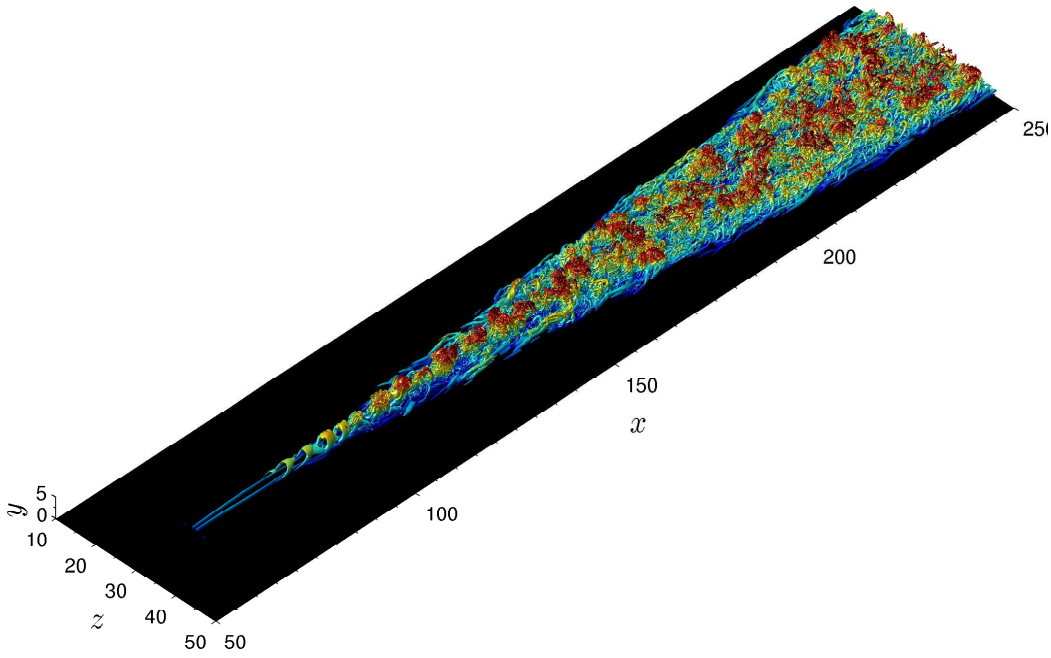

(a)

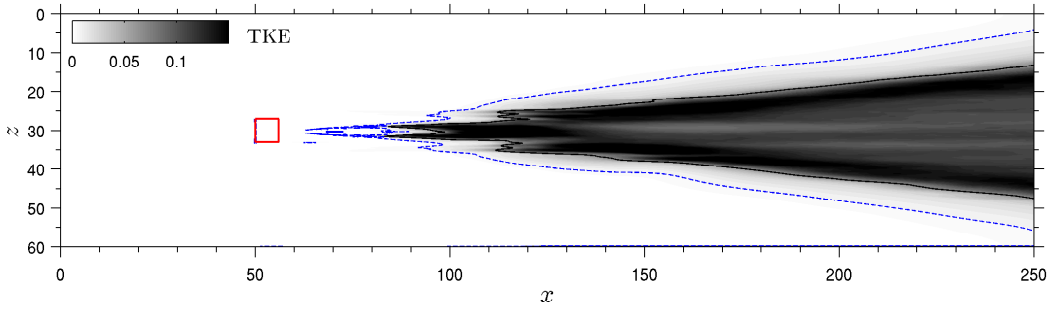

(b)

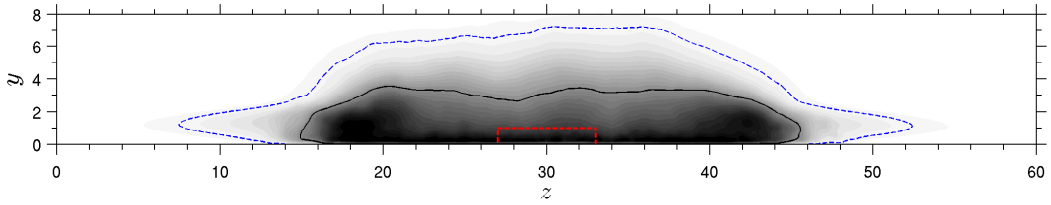

(c)

Figure 4.28: Visualisation of the turbulent wedge developing downstream of the roughness. The solid and dashed contourlines in (b) and (c) indicate, respectively, $TKE = 0.07$ and $TKE = 0.008$: (a) Isosurfaces of $Q = 0.02$, coloured by wall-normal distance, (b) TKE contours in the horizontal plane at $y = 1.2$, (c) crossflow TKE contours at $x = 230$.

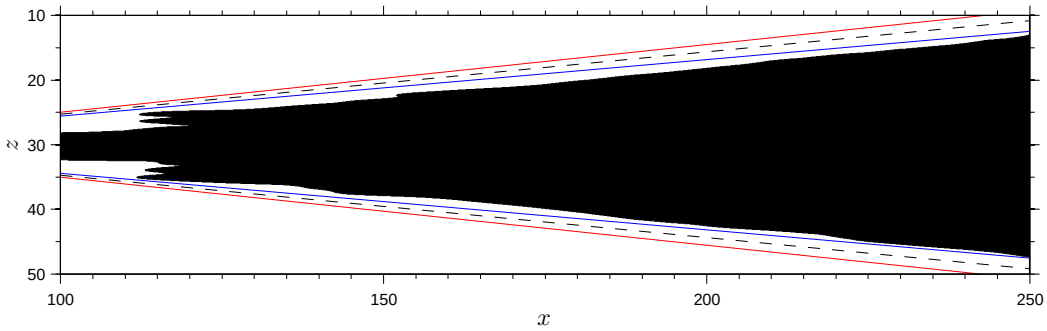

(a)

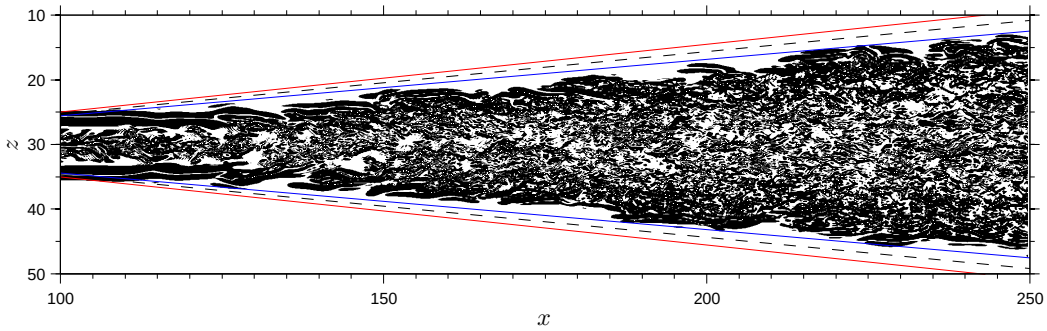

(b)

Figure 4.29: Measuring the lateral spreading half angle of the turbulent wedge. The solid blue, dashed black and solid red lines are inclined at $\alpha = 5.3°$, $\alpha = 5.5°$ and $\alpha = 5.7°$ to the horizontal, respectively. (a) contours of $TKE \geq 0.07$ at $y = 1.2$, (b) contours of $0.06 < |\omega_y| < 0.08$ at $y = 1.2$.

vortices, while the turbulent core is formed by hairpin vortices protruding upwards and smaller scale structures closer to the wall. Turbulence is continuously generated in the breakdown region (near $x = 100$) and spreads laterally with increasing streamwise distance, also in a continuous fashion. Figures 4.28(b) and 4.28(c) show, respectively, top and crossflow views of TKE contours at $y = 1.2$ and $z = 240$, with black continuous and blue dashed lines giving TKE = 0.07 and TKE = 0.008 contours defining the inner and outer edges of the turbulent wedge, respectively. As expected, TKE maxima are found near the inner edges and in the near-wall region. On the other hand, velocity fluctuations extend for a about eight inflow laminar displacement thicknesses out into the surrounding laminar flow.

The wedge lateral spreading rate is calculated following the same procedures used for the $M_\infty = 6.0$ case. The results, shown in figure 4.29, give a half spreading angle of $\alpha = 5.5 \pm 0.2°$, which agrees well with predictions of Fischer (1972). Measurements of the half spreading angle of the intermittent flow region (not shown), performed using the cut-off value of TKE = 0.008, give $\alpha = 7.8 \pm 0.2°$.

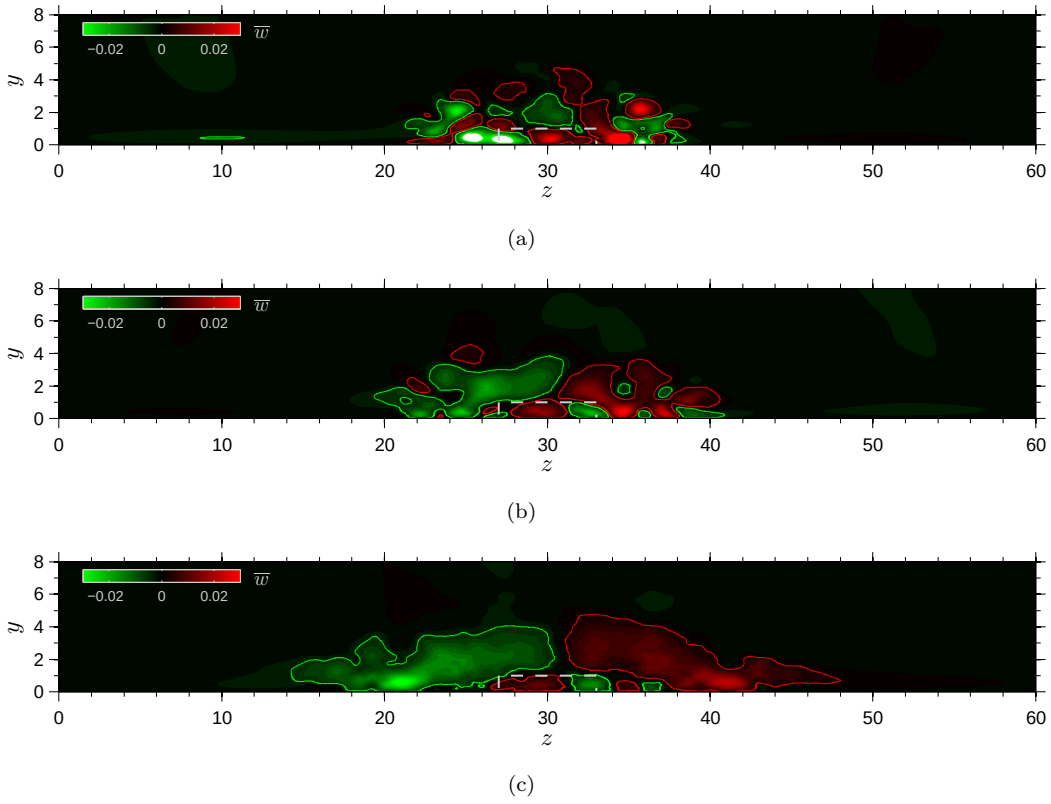

Figure 4.30: Crossflow contours of mean lateral velocity. Red and green contourlines show respectively $\overline{w} = +3 \times 10^{-3}$ and $\overline{w} = -3 \times 10^{-3}$. The dashed white line indicates the roughness position. (a) $x = 148$, (b) $x = 172$, (c) 220.

Similarly to what was observed for the $M_\infty = 6.0$ case, the half spreading angle of the intermittent region lies just outside the interval proposed by Fischer (1972).

Having measured the lateral growth rate of the turbulent wedge, the analysis now concentrates on shedding some light onto the mechanisms responsible for the lateral spreading of turbulence. Figures 4.30(a) to 4.30(c) show mean lateral velocity contours respectively at $x = 148$, $x = 172$ and $x = 220$. It can be seen that, as already shown for case *NL6.0S*, following the wedge evolution from a transitional to a fully turbulent state a mean spanwise flow from the turbulent core into the surrounding laminar boundary layer appears in mean w-velocity contour plots. Lateral velocities reach about $2 - 3\%$ of the free-stream velocity near the core and are about one order of magnitude lower near the edges of the wedge, i.e. near $z = 14$ and $z = 46$ in figure 4.30(c). Visualisations of the instantaneous w-velocity field at different streamwise locations provided in figures 4.31(a) to 4.31(c) for $x = 196$, $x = 208$ and $x = 215$, respectively, show that lateral jets protruding into the surrounding laminar boundary layer appear and disappear near the sides of the turbulent wedge (note the presence of lateral jets pointing outwards near

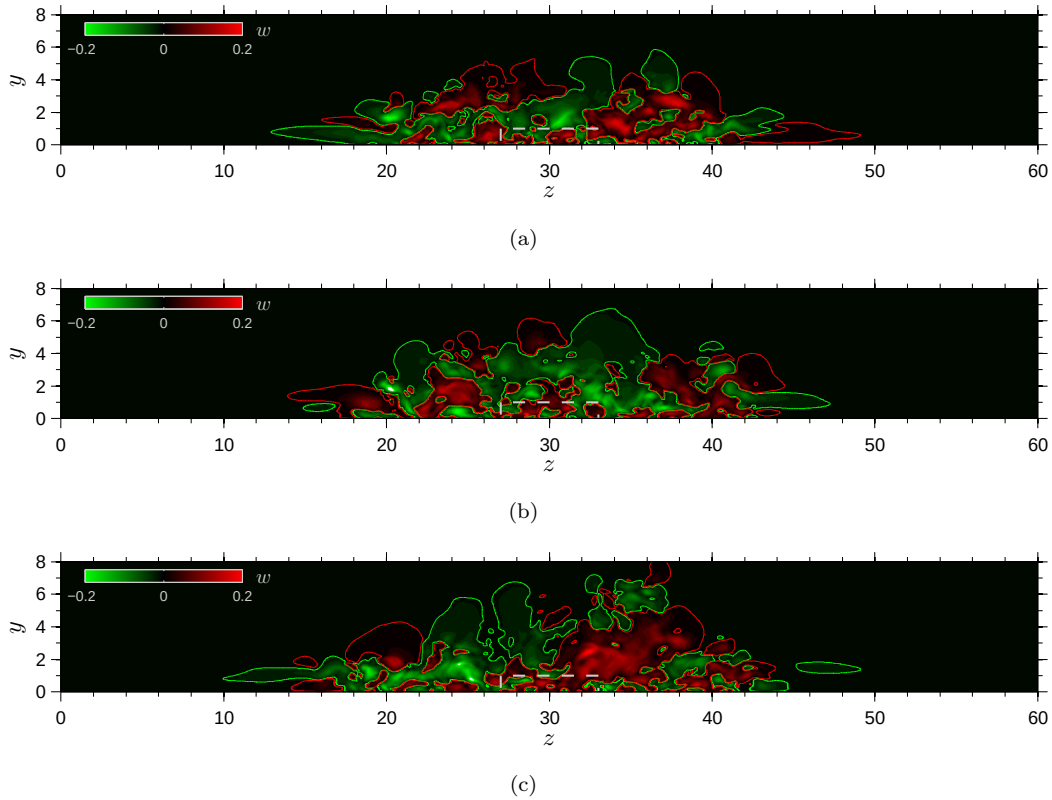

(a)

(b)

(c)

Figure 4.31: Crossflow contours of instantaneous lateral velocity. Red and green contourlines show respectively $\overline{w} = +5 \times 10^{-3}$ and $\overline{w} = -5 \times 10^{-3}$. The dashed white line indicates the roughness position. (a) $x = 148$, (b) $x = 172$, (c) 220.

$z = 14$ and $z = 48$ in figure 4.31a, while fluid flows from the laminar boundary layer towards the core of the wedge near $z = 14$ and $z = 46$ in figure 4.31b). Enhancement and suppression of these lateral jets may be due to local events or to a global breathing mode of the wedge. Here we limit ourselves to pointing out that, as shown in figure 4.31(c), outward jets on one side of the wedge (see near $z = 12$) may correspond to inward flow on the opposite side (see $z = 47$), which would indicate a suppression of the lateral jet near $z = 47$ by a local event at the edge of the wedge. Events of this type repeat periodically, so that lateral flow averages out near the edges of the wedge, explaining the low mean w-velocities found in this region of the flow. As in the $M_\infty = 6.0$ case, the jets observed in the instantaneous flow field reach lateral velocities of up to about 10% of the free-stream velocity, similarly to what was found for turbulent spots (Wygnanski *et al.*, 1982; Redford *et al.*, 2012).

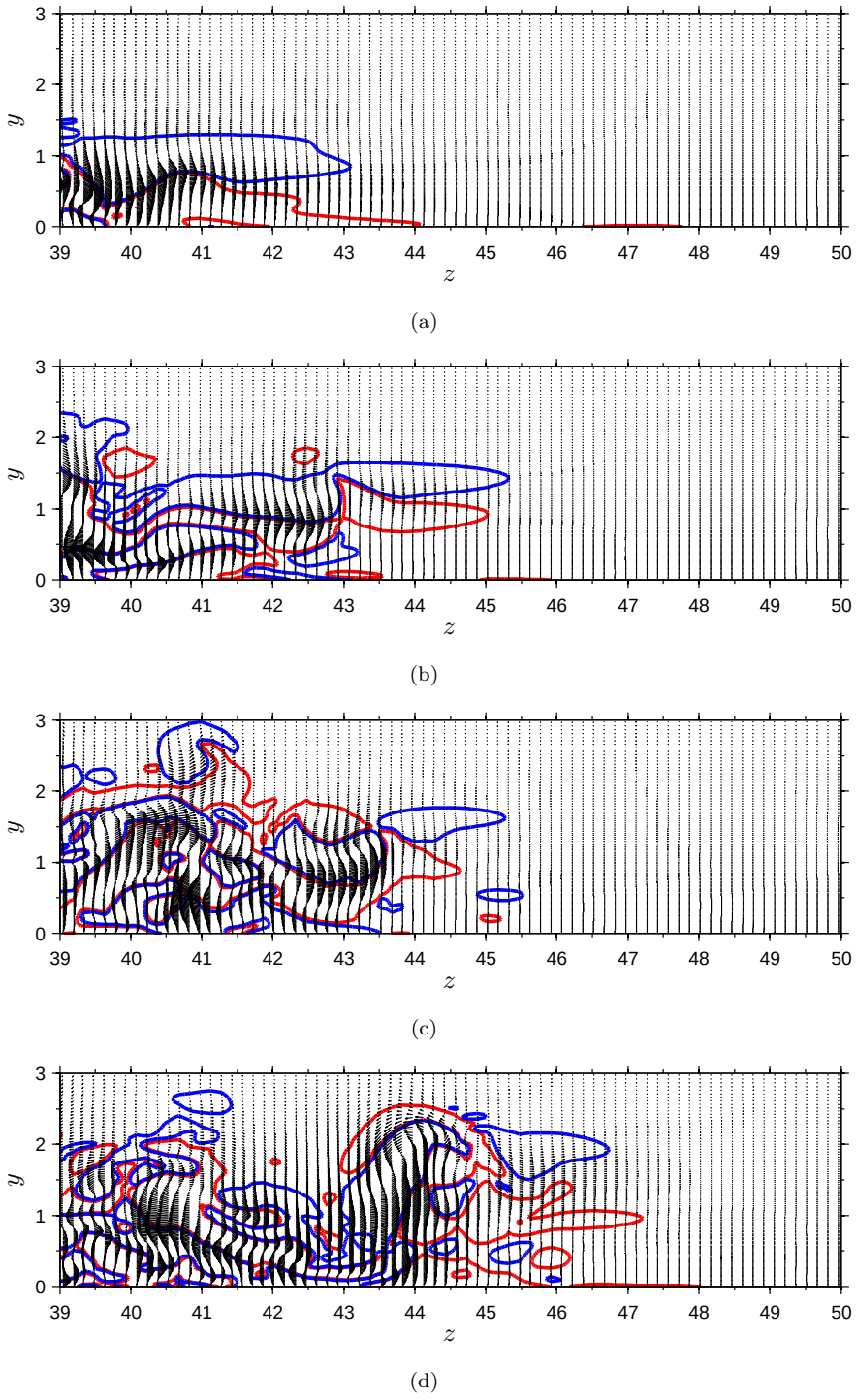

Figure 4.32: Generation of new vortices by destabilisation of surrounding laminar flow. Crossflow velocity vectors superimposed streamwise vorticity contours $\omega_x = \pm 0.05$, red for positive and blue for negative. (a) $x = 180$ and $t = 2852$, (b) $x = 200$ and $t = 2880$, (c) $x = 220$ and $t = 2904$, (d) $x = 240$ and $t = 2924$.

The mean lateral flow from the core of the wedge outwards described above suggests that the turbulent wedge is growing due to the convection of turbulent structures into the surrounding boundary layer. This mechanism, however, only partly

explains the lateral spreading of turbulence, especially given the low mean w-velocities observed. Looking back at figure 4.28(a), it is clear that new structures (mostly streamwise vortices) are continuously being created near the sides of the turbulent wedge, following the destabilisation of the surrounding laminar flow (see for example near $x = 130$ and $z = 35$ and near $x = 150$ and $z = 25$). One of these events is captured in figure 4.32, which shows crossflow velocity vectors superimposed over streamwise vorticity contours ($\omega_x = \pm 0.05$) at different times and streamwise positions. Figure 4.32(a) shows that at time $t = 2852$ a spanwise jet is present at $x = 180$ on one edge of the turbulent wedge ($z = 41$). Note that the jet is perturbed downwards by the presence of a vortex near $z = 39.2$ and takes a meandering shape. At $x = 200$ and 28 time units later, figure 4.32(b) shows a near wall jet for $z > 40$, a strong lateral jet for $z > 41$ and $y \approx 1$ and a vortex centred at $z = 42.5$ and $y = 1$. The roll-up of streamwise vorticity which leads to the generation of this vortex appears to follow an anti-symmetric deformation and subsequent instability of the lateral jet. The same vortex is seen in figure 4.32(c), now centred at $z = 43$ and $y = 1$, inducing an upward tilting of the lateral jet. Finally, figure 4.32(d) shows the same vortex displaced upwards and laterally, see near $z = 43.5$ and $y = 1.5$, surrounded by turbulent structures. These results seem to confirm the findings of Redford *et al.* (2012), who proposed the instability of the lateral jets as a mechanism for the destabilisation of the surrounding laminar flow. However for the wedge of turbulent fluid these jets only occur transiently.

4.3.4 Effects of a shock wave impinging on the transitional boundary layer

The study of the effects induced by an oblique shock on the laminar-turbulent transition occurring downstream of the roughness element, which began in section 4.2.4 with the analysis of case *NL6.0S*, continues here with a discussion of the results obtained for $M_\infty = 2.5$. In this case, the shock generator angle is $\theta = 1.93°$ (see table 4.1) and the RankineHugoniot conditions are applied at $x = 75$ so that, in the absence of a boundary layer, the shock reaches the wall at $x \approx 118$.

The flow features induced by the SBLI are visualised in figures 4.33(a) and 4.33(b), showing, respectively, contours of $\sqrt{(\partial\rho/\partial x)^2 + (\partial\rho/\partial y)^2}$ at the roughness mid-plane and shaded temperature contours in the horizontal plane at $y = 1.2$, superimposed by $\overline{u} = 0$ contours (blue line) at the first grid point above the wall. The oblique shock impinges onto the boundary layer at $x \approx 110$, in a region where the roughness wake is undergoing breakdown to turbulence, and induces a separation

bubble in the laminar boundary layer regions at the sides of the computational domain. The streamwise length of the separation bubble is about 30 inflow displacement thicknesses in the laminar boundary layer and reaches about 45 near the transitional roughness wake. The interaction does not lead to separation in the transitional flow behind the roughness element. Figure 4.33(b) shows that the turbulent wedge developing downstream of the roughness element undergoes a rapid lateral growth immediately downstream of the separation bubble, leading to a wider turbulent wedge than that observed in case *NL2.5*. This aspect will be analysed later in more detail.

Figure 4.34 shows a comparison of the streamwise variation of the time-averaged skin friction obtained for cases *NL2.5* and *NL2.5S* inside the wake of the roughness element. The adverse pressure gradient created by the SBLI leads to a gradual decrease in skin friction visible from $x \approx 75$. The flow does not separate for the spanwise positions plotted, hence c_f remains positive across the interaction region. At the roughness mid-plane ($z = 30$) the skin friction increases sharply, starting from about $x = 100$ for both cases (*NL2.5* and *NL2.5S*). The skin friction rise associated with the breakdown to turbulence at the roughness mid-plane is practically identical up to $x \approx 115$ for the cases with and without shock. Downstream of this point case *NL2.5S* shows an earlier transition peak and a faster breakdown

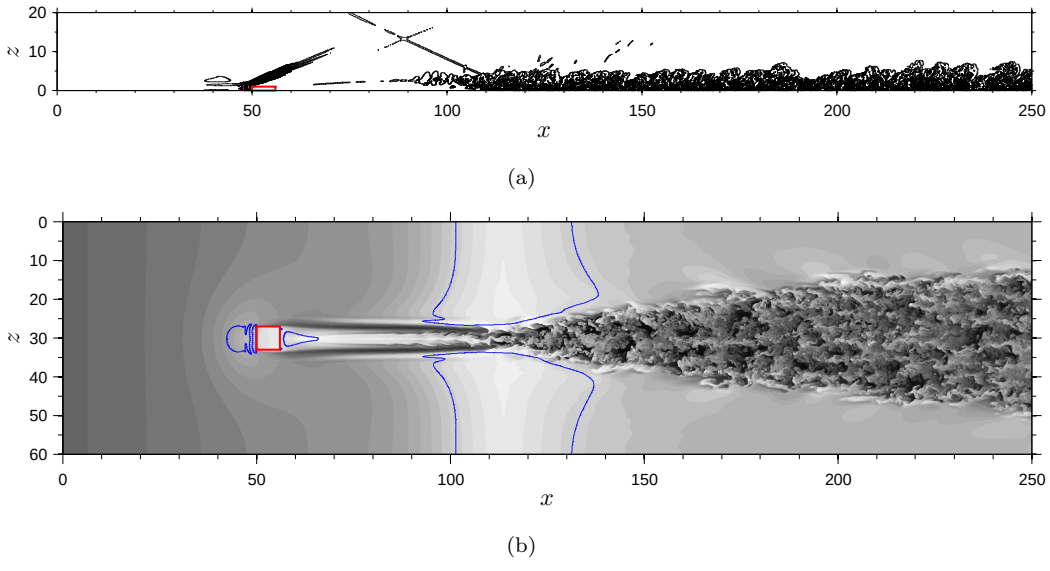

Figure 4.33: Flow features induced by the SBLI. (a) contours of $\sqrt{(\partial\rho/\partial x)^2 + (\partial\rho/\partial y)^2}$ at the roughness mid-plane, (b)contours of instantaneous temperature in a horizontal plane at $y = 1.2$. The red squares indicate the roughness position and the blue line shows regions of separated flow ($\overline{u} = 0$ at the first grid point above the wall).

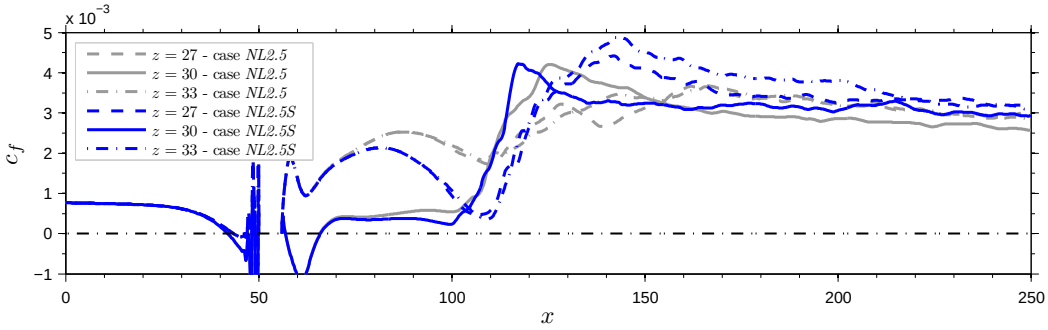

Figure 4.34: Streamwise evolution of time-averaged skin friction at the roughness mid-plane, showing the effect of the SBLI on the breakdown to turbulence.

to turbulence. The effect of the SBLI is more evident near the sides of the roughness wake. At the two lateral wake positions considered in figure 4.34, c_f for case *NL2.5S* can be seen to rise suddenly starting from $x \approx 110$, reaching a transition peak near $x = 145$. Peak skin friction values are higher near the sides of the wake than at the roughness mid-plane for this case. The skin friction at $z = 27$ and $z = 33$ for case *NL2.5* also starts increasing from $x \approx 110$ but the rise towards the turbulent value is more gradual than for case *NL2.5S*.

The wall-normal temperature gradient and the pressure fluctuations at the wall for cases *NL2.5* and *NL2.5S* are compared in figure 4.35. Overall, peak values of $\partial\overline{T}/\partial y$ and p'_{rms}/p_∞ are similar for the two cases under consideration. However, the SBLI induces two regions of high near-wall temperature and wall-pressure fluctuations at the edges of the roughness wake (near $z = 22$ and $z = 38$) immediately downstream of the shock-induced separation bubble (near $x = 140$). As already noted from the instantaneous temperature contours in figure 4.33(b), and similarly to what was reported for the $M_\infty = 6.0$ cases, the lateral spreading of turbulence in this region of the boundary layer is considerably faster for case *NL2.5S* than for case *NL2.5*.

To analyse more closely the fast lateral spreading of turbulence observed for case *NL2.5S* downstream of the interaction region we focus our attention on how the shock modifies the growth of disturbances inside the roughness wake. Figure 4.36 gives a comparison of crossflow u'_{rms} contours for cases *NL2.5S* and *NL2.5* at different streamwise positions along the transition region. Figures 4.36(a) and 4.36(b) show that at $x = 93$, immediately upstream of the shock-induced separation bubble, the amplitude of disturbances in the roughness wake is similar for the two cases considered. On the other hand, similarly to what was found for the $M_\infty = 6.0$ case, the SBLI leads to a modification of the mean flow consisting mainly in

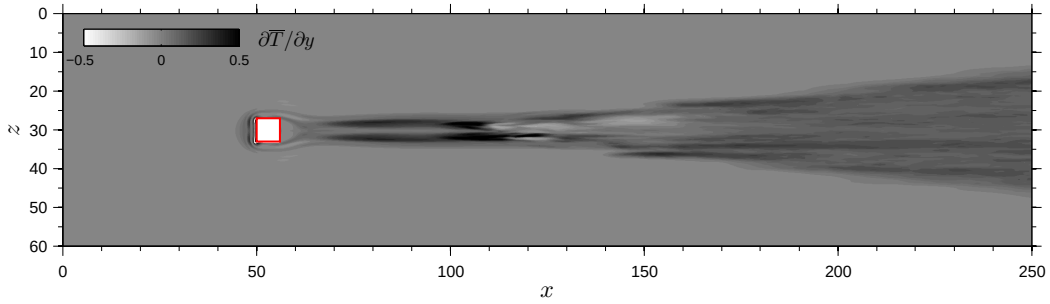

(a)

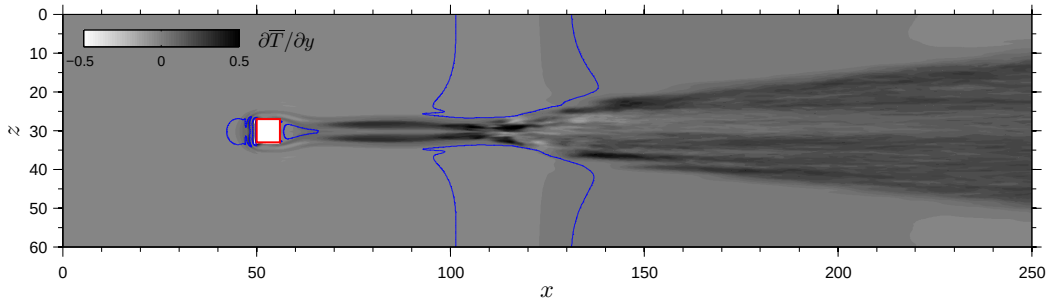

(b)

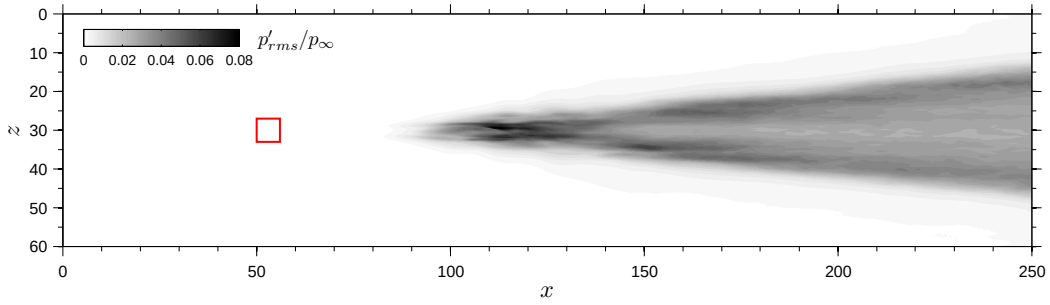

(c)

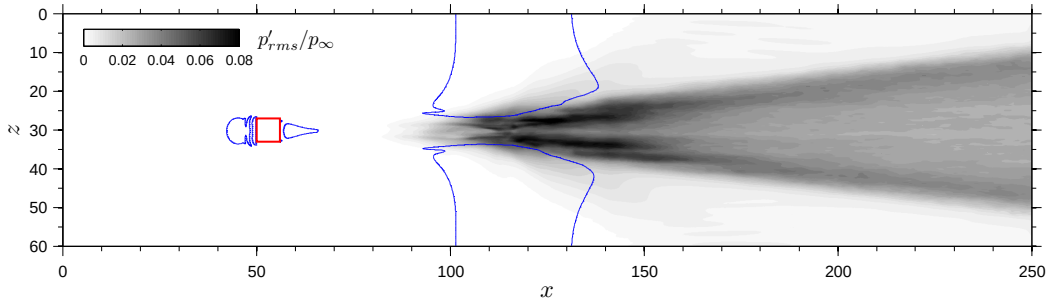

(d)

Figure 4.35: Effects of SBLI on heat transfer and unsteady pressure loads at the wall. Blue lines show regions of separated flow ($\overline{u} = 0$ at the first grid point above the wall). (a) $\partial\overline{T}/\partial y$ for case *NL2.5*, (b) $\partial\overline{T}/\partial y$ for case *NL2.5S*, (c) p'_{rms}/p_∞ for case *NL2.5*, (d) p'_{rms}/p_∞ for case *NL2.5S*.

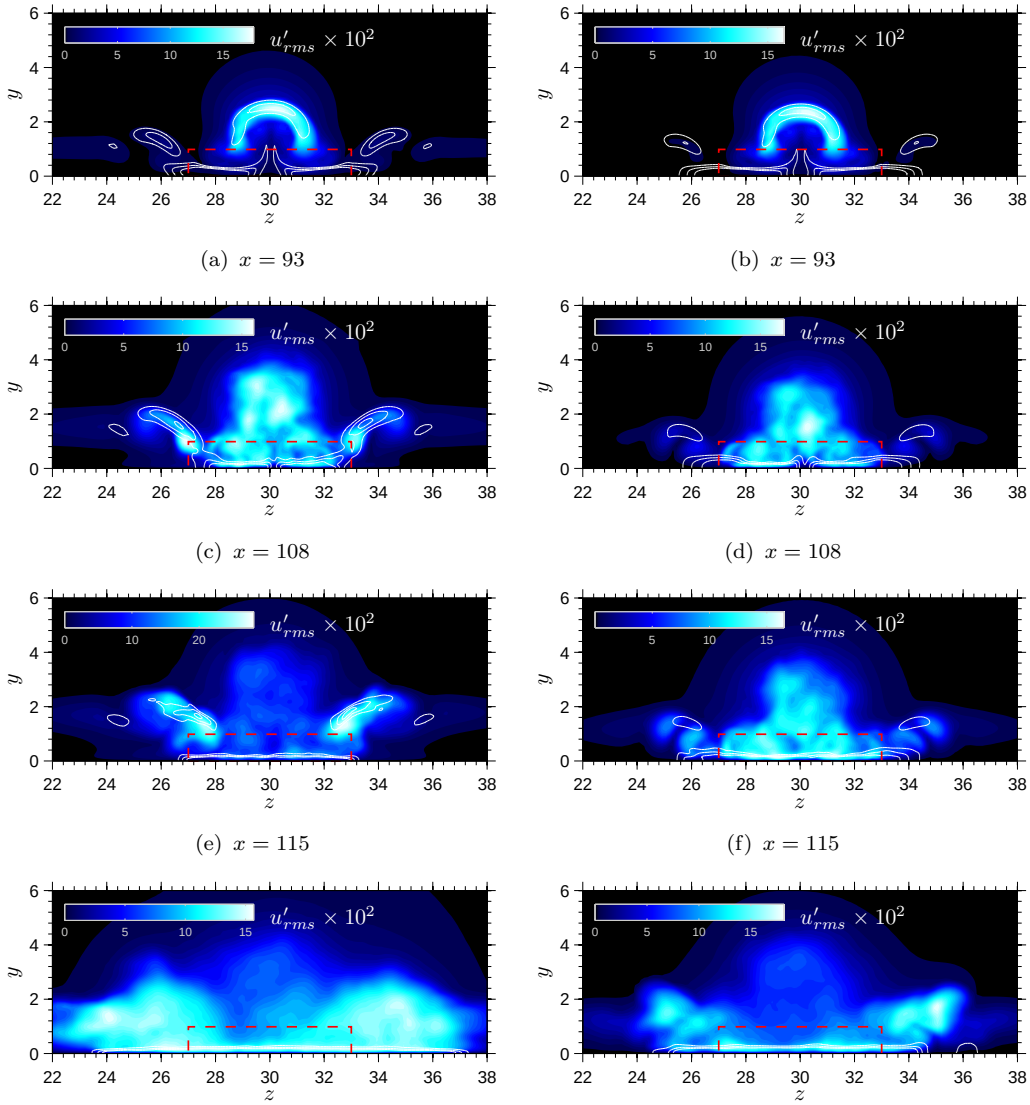

(a) $x = 93$ (b) $x = 93$

(c) $x = 108$ (d) $x = 108$

(e) $x = 115$ (f) $x = 115$

(g) $x = 134$ (h) $x = 134$

Figure 4.36: Effect of the SBLI on the growth of disturbances inside the roughness wake. White lines in (a) and (b) show $u_S = 0.70, 1.05, 1.4$. (a), (c), (e), (g) case *NL6.0S* and (b), (d), (f), (h) case *NL6.0*.

the generation of lateral shear layers near the sides of the roughness wake. This effect becomes more evident further downstream, as can be seen by comparing figures 4.36(c) and 4.36(d), showing regions of high mean shear inside the roughness wake together with the amplitude of u' perturbations at $x = 105$, for cases *NL2.5S* and *NL2.5* respectively. It can be seen that lateral shear layers appear for case *NL2.5S* at the boundaries between attached transitional flow and separated laminar flow near $z = 24$ and $z = 26$. Maximum disturbance amplitudes are still similar for the two cases, however u'_{rms} peaks appear for case *NL2.5S* near $z = 27$ and $z = 33$, indicating the growth of disturbances in the above mentioned

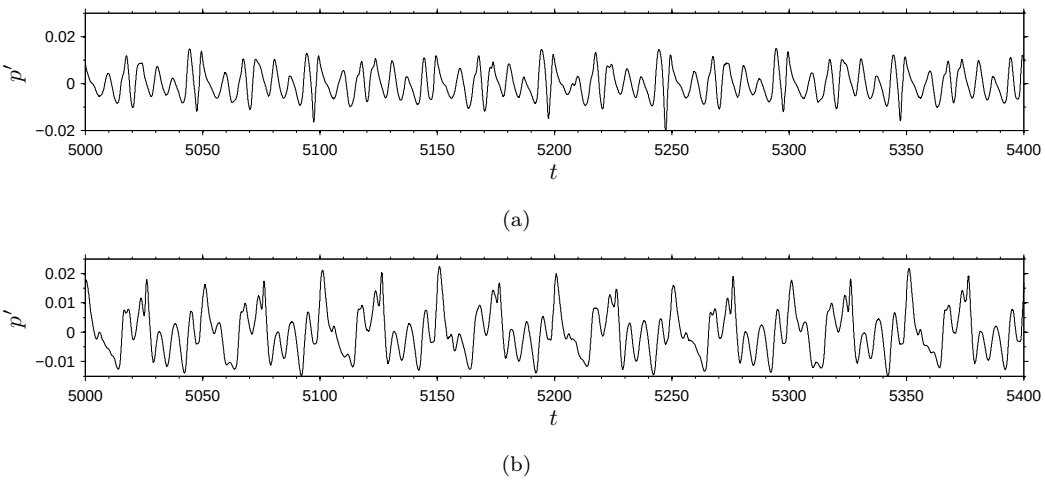

Figure 4.37: Pressure probe at $x = 110$ and $z = 28$ showing the amplification of low frequencies by the shock system. (a) *NL2.5*, (b) case *NL2.5S*.

lateral shear layers. In fact, these are the only disturbances still growing in the roughness wake at $x = 105$, since disturbances developing in the central region of the roughness wake have reached saturation and the flow is in the final stages of breakdown to turbulence. The instability of the lateral shear layers dominates the u'_{rms} field for case *NL2.5* at $x = 115$ (see figure 4.36e) and, further downstream, breakdown to turbulence is seen to occur also near the edges of the separation bubble, as shown in figure 4.36(g). This behaviour is not observed for case *NL2.5* in figures 4.36(f) and 4.36(h). Wall pressure signals registered by numerical probes located at $x = 110$ and $z = 28$ are shown in figures 4.37(a) and 4.37(b) for case *NL2.5* and *NL2.5S*, respectively. As already observed in the $M_\infty = 6.0$ case, the shock system seems to induce an amplification of the low frequencies. Movies of the flow in this region of the wake show vortex shedding from the bubble edge at a frequency of $F \approx 0.02$ for case *NL2.5S*, in agreement with what was found for the $M_\infty = 6.0$ case.

The turbulent wedge evolution downstream of the breakdown region is shown in figures 4.38(a) and 4.38(b) through TKE contours in horizontal planes at $y = 1.2$ for cases *NL2.5* and *NL2.5S* respectively. After the initial fast lateral growth, the turbulent wedge can be seen to recover the spreading rate of the case without shock (see red line in figures 4.38a and 4.38b), similarly to what was found for case *NL6.0S*. Therefore, the main effect of SBLI is to induce a fast initial widening of the turbulent wedge, which in turn leads to a shortening of the transition region. Crossflow contours of TKE at $x = 230$, shown in figures 4.38(c) and 4.38(d) respectively for cases *NL2.5* and *NL2.5S*, show that, while leading

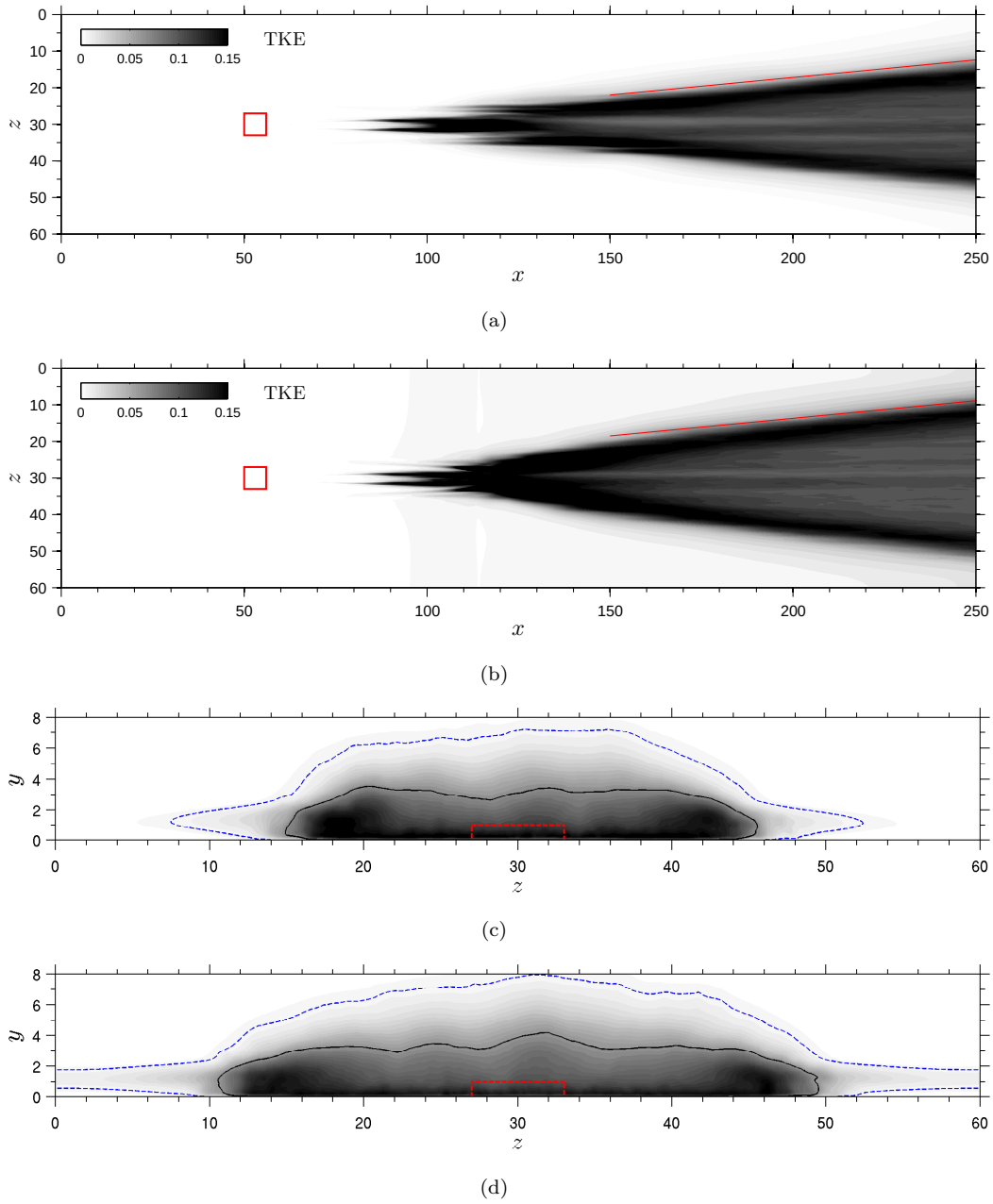

Figure 4.38: Comparison of the turbulent wedge structure for cases *NL2.5* and *NL2.5S*. The solid and dashed contourlines in (c) and (d) indicate, respectively, $TKE = 0.08$ and $TKE = 0.007$. (a) TKE contours in the horizontal plane at $y = 1.2$ for case *NL2.5*, (b) TKE contours in the horizontal plane at $y = 1.2$ for case *NL2.5S*, (c) crossflow TKE contours at $x = 230$ for case *NL2.5*, (c) crossflow TKE contours at $x = 230$ for case *NL2.5S*.

to a considerably wider turbulent wedge, the SBLI does not induce a substantial thickening of the boundary layer in regions near the roughness mid-plane. Similarly to what was found for the $M_\infty = 6.0$ case, the region of intermittent flow

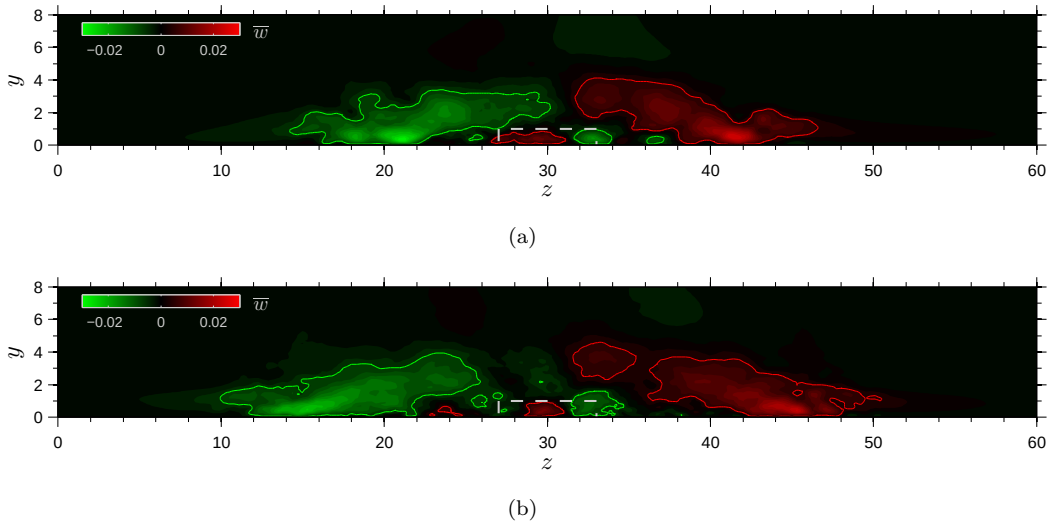

(a)

(b)

Figure 4.39: Crossflow contours of mean lateral velocity at $x = 230$. Red and green contourlines show respectively $\overline{w} = +5 \times 10^{-3}$ and $\overline{w} = -5 \times 10^{-3}$. The dashed white line indicates the roughness position. (a) case *NL2.5*, (b) case *NL2.5S*.

bounding the fully turbulent core of the wedge is more widely spread in the presence of SBLI. In fact, while the half width of the wedge core is about four inflow displacement thicknesses larger for case *NL2.5S* than for case *NL2.5* at $x = 230$, at the same streamwise position the intermittent flow region increases more than eight displacement thicknesses and spreads over the full spanwise extent of the computational domain. This behaviour might be due to either the more violent breakdown to turbulence observed in the presence of SBLI or the amplification of disturbances in the laminar separation bubble (see figure 4.36(c) near $z \approx 22$ and $z = 38$), or a combination of the two effects. Finally, figures 4.39(a) and 4.39(b), showing contours of mean w-velocity at $x = 230$ for cases *NL2.5* and *NL2.5S*, respectively, indicate that, after transition to turbulence in the core of the wedge is complete, similar lateral mean flow develops in the two cases, with peak mean w-velocities reaching up to about 3% of the free-stream velocity. This behaviour is consistent with the agreement in lateral half spreading angles observed for the two cases.

4.4 Synthesis and discussion of key findings

The mechanisms leading to breakdown to turbulence in $M_\infty = 6.0$ and $M_\infty = 2.5$ boundary layers in the presence of a localised sharp-edged roughness element, with

height of the order of the local boundary layer thickness and under the effect of small external disturbances, have been analysed in this chapter. The study focused on the nonlinear stages of the laminar-turbulent transition process and considered also the effects of an oblique shock wave impinging on the transitional part of the boundary layer dowsntream of the roughness element. This study is a continuation of chapter 3, which focused on the linear stages of transition.

The results show that, for both the Mach numbers considered, the initial linear growth of disturbances in the roughness wake eventually leads to breakdown to turbulence, which starts at the roughness wake and results in a wedge of turbulent flow that spreads laterally with increasing streamwise distance. At $M_\infty = 6.0$ the linear growth of disturbances in the wake of the roughness is dominated by a sinuous wake instability mode, similar to mode SL observed during the $M_\infty = 6.0$ receptivity study in section 3.6, which initially leads to an anti-symmetric deformation of the roughness wake. Interestingly, as this mode evolves in the streamwise direction it appears that linear processes, including non-parallel flow effects or non-normal mode superposition (or a combination of the two), lead to the asymmetric growth of disturbances in the roughness wake, with a disturbance peak appearing on one of the two lateral shear layers generated by the roughness induced pair of counter-rotating streamwise vortices. The idea is that as the basic flow changes in the streamwise direction, the disturbance energy is re-distributed into the modes of the new basic flow, potentially leading to asymmetric amplitude increase due to the spanwise asymmetry of the forced perturbations. Non-parallel flow effects can also lead to the excitation of additional wake modes (stable and/or unstable) which, if non-orthogonal, may lead to algebraic disturbance growth. Further downstream the finite amplitude disturbances trigger nonlinear interactions, leading to the roll-up of the lateral shear layers which drive the breakdown to turbulence of the roughness wake.

By contrast, at $M_\infty = 2.5$ the linear stages of transition show the presence of both varicose (mode VT) and sinuous (mode SL) modes, the former being dominant as already found during the receptivity study in section 3.7. The growth of mode VT leads to the rapid onset of nonlinear interactions, which manifest themselves as the roll-up of the strong three-dimensional detached shear layer induced by the counter-rotating streamwise vortices associated with the roughness element. The final stages of the laminar-turbulent transition are driven by the breakdown of the hairpin-like structures appearing as a consequence of the above mentioned shear layer roll-up. At $M_\infty = 2.5$ transition to turbulence occurs considerably closer to the roughness element than at $M_\infty = 6.0$ (recall that for case *NL6.0* the flow

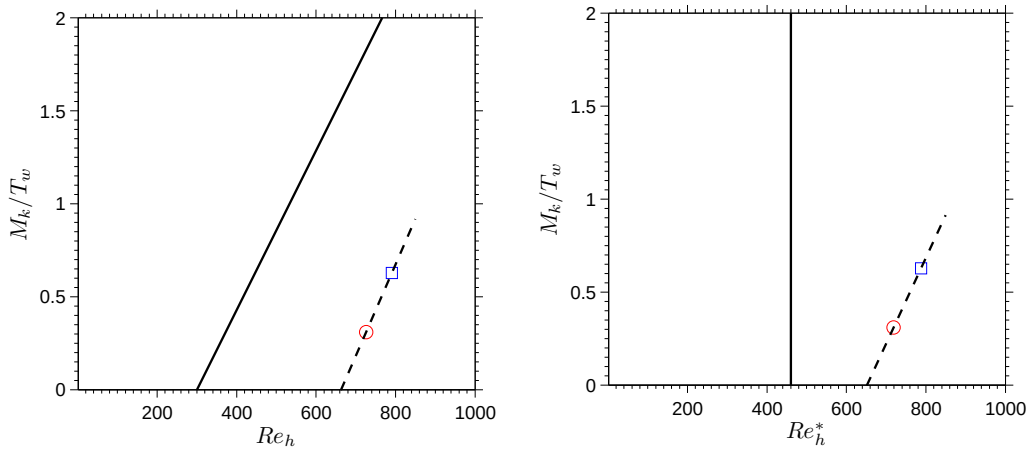

Figure 4.40: Cases *NL6.0* (red circles) and *NL2.5* (blue squares) in the context of the transition criteria proposed by Redford *et al.* (2010) (a) and Bernardini *et al.* (2012) (b). The dashed black lines are straight lines going through the two markers and are plotted to highlight the distance of each case from the critical line (solid black line).

behind the roughness element is still transitional at the computational outflow boundary). This aspect is consistent with the higher roughness Reynolds number and lower wall-temperature considered for case *NL2.5*, which leads to a more unstable flow than for case *NL6.0*. Figure 4.40 puts the cases considered in this chapter in the context of the transition maps proposed by Redford *et al.* (2010) and Bernardini *et al.* (2012). In these maps a dividing line is used to separate flows that remain laminar (to the left of the line) from those undergoing transition to turbulence (to the right of the line). Note that for case *NL6.0* $M_k/T_w = 0.31$, $Re_h = 726$ and $Re_h^* = 719$, while for case *NL2.5* $M_k/T_w = 0.63$, $Re_h = 791$ and $Re_h^* = 788$. Both transition criteria correctly predict transition to turbulence for the two cases analysed.

Following breakdown to turbulence a wedge of turbulent flow forms behind the roughness element. The rate at which turbulence spreads laterally for increasing streamwise distance in the two cases considered here (half spreading angles are $\alpha = 3.0 \pm 0.2°$ for case *NL6.0* and $\alpha = 5.5 \pm 0.2°$ for case *NL2.5*) agrees well with experimental (Fischer, 1972) and numerical (Redford *et al.*, 2012) results obtained for the lateral spreading rate of turbulent spots in compressible boundary layers. A distinctive lateral flow from the wedge core to the surrounding laminar boundary layer is present, similar to that observed in turbulent spots. This behaviour is clearest for case *NL6.0S*, where SBLI leads to a fully turbulent wedge core, and

for the two $M_\infty = 2.5$ cases. However, peak mean w-velocities are somewhat smaller than those reported in turbulent spots studies (about 3% of the free-stream velocity both for the $M_\infty = 6.0$ and $M_\infty = 2.5$ cases analysed here against about $7 - 10\%$ found in turbulent spots). A close look at the mechanisms driving the lateral spreading of the turbulent wedges also reveals similarities with turbulent spots. At $M_\infty = 2.5$ the wedge is found to grow both by convection of turbulent structures from the wedge core outwards and by destabilisation of the surrounding laminar flow. Flow visualisations suggest that the latter mechanism occurs, at least in part, as a consequence of the instability of the lateral jets, which are continuously forced by the turbulent core of the wedge. The same mechanism was found to be active in turbulent spots by Redford *et al.* (2012). At $M_\infty = 6.0$ the growth by destabilisation mechanism was found to be strongly damped, also in agreement with the observations of Redford *et al.* (2012), and the wedge appears to grow mainly due to the lateral convection of turbulent structures by the mean spanwise flow.

Finally, the effects induced by an oblique shock wave impinging on the transitional boundary layer developing downstream of the roughness element were analysed both at $M_\infty = 6.0$ and $M_\infty = 2.5$. The shock/boundary layer interaction induces a separation in the laminar boundary layer surrounding the transitional wake of the roughness, where the flow remains attached, and leads to an acceleration of the transition process. This effect is particularly evident at the sides of the roughness wake, near the edges of the laminar separation bubble, characterised by high lateral shear. Disturbances are found to grow quickly in these lateral shear layers and eventually lead to the breakdown to turbulence in the lateral regions of the roughness wake. Consequently, lateral spreading of turbulence is found to be greatly enhanced immediately downstream of the shock-induced separation bubble. Similar behaviour was reported by Krishnan & Sandham (2007), who studied the influence of SBLI on the evolution of compressible turbulent spots and found an increment of the spot spreading angle as it passed through the shock induced separation bubble. Further downstream the turbulent wedge recovers the spreading rate of the case without shock.

Chapter 5

Transition control using surface porosity[1]

5.1 Introduction

It was shown in chapter 3 that Mack modes can influence the receptivity of instability modes in the wake of a roughness element. In this investigation our attention is focused on the effects of a porous surface on the transition to turbulence over a flat plate due to small external disturbances at $M_\infty = 6$. Smooth and porous walls are considered. The damping effect of porosity on the Mack modes is analysed by comparisons with smooth wall results. The purpose of the present study is to continue the work of Sandham & Lüdeke (2009) by analysing the transition process all the way through the secondary instability to the final turbulent breakdown.

The numerical calculations were carried out using the temporal DNS approach (TDNS), see for example Kleiser & Zang (1991). In this technique the Navier-Stokes equations are solved using periodic boundary conditions in the directions parallel to the wall. This means that the evolution of disturbances in the boundary layer is followed in time for a much smaller computational domain than would be required for the full spatially-developing boundary layer. This is especially advantageous when details of surface geometry such as pores need to be resolved. In a spatially developing boundary layer a wave travelling at a certain phase speed encounters different velocity profiles at each instant. From a frame of reference moving with the wave, the rate at which the boundary layer grows depends on the boundary layer spatial growth and the phase speed of the wave. Without a

[1]The work presented in this chapter has been published in De Tullio & Sandham (2010)

forcing term the boundary layer would grow over time at a rate which is unrelated to the disturbance phase speed. In addition, while growing, the laminar profile would change shape and stability characteristics due to the imposed periodicity, which reduces the u-momentum equation to

$$\frac{\partial \rho_b U_b}{\partial t} = \frac{1}{Re}\frac{\partial}{\partial y}\left(\mu_b \frac{\partial U_b}{\partial y}\right). \tag{5.1}$$

A possible solution is to use similarity profiles at different downstream locations to prescribe the temporal growth of the laminar boundary layer, taking into account the phase speed of the disturbances. However, as the boundary layer grows the wavelengths of the disturbances change, along with their growth rates, making the interpretation of disturbance interaction and growth rates difficult. For these reasons it was decided to focus on the evolution of disturbances in a specific laminar boundary layer and to apply forcing terms to the momentum and energy equations to keep the initial laminar base flow fixed in time. The forcing terms are found by the numerical evaluation of the Navier-Stokes equations at the first time step, after initializing the flow with the similarity solutions for compressible boundary layers, and take the following form

$$\begin{aligned} F_{M1} &= -\frac{1}{Re}\frac{d}{dy}\left(\mu_b \frac{dU_b}{dy}\right) \quad ; \quad F_{M2} = F_{M3} = 0 \\ F_E &= -\frac{1}{Re}\frac{d}{dy}\left(U_b \mu_b \frac{dU_b}{dy}\right) - \frac{1}{(\gamma-1)M_\infty^2 Pr Re}\frac{d}{dy}\left(\mu_b \frac{dT_b}{dy}\right), \end{aligned} \tag{5.2}$$

where the subscript (b) refers to the basic laminar flow. The terms F_{Mi}, with $i = 1$, 2, 3, are the forcing terms for the x, y and z-momentum equations respectively whereas F_E is the forcing term for the energy equation. The main drawbacks of TDNS are that only a selection of discrete modes, which have to be chosen a priori by performing preliminary linear stability analysis, are allowed in the calculation and that, as already mentioned, boundary layer growth effects are not included. This latter omission is less important when the rapid breakdown stages of transition are studied as in the present work. When comparing smooth and porous surfaces an additional difficulty arises from the possibility that the effects of porosity may be different for different primary and secondary wavelengths. This aspect was investigated for the primary instability and is reported in Section 5.5.

5.2 Numerical simulations

This investigation is focused on the transition to turbulence in the boundary layer over a flat plate at $M_\infty = 6$ due to small initial disturbances. Smooth and porous walls are considered. The stabilizing effects of porous surfaces can be analyzed by comparison with the smooth wall results. The Navier-Stokes equations are solved using the TDNS approach with no-slip and constant temperature boundary conditions at the walls. The wall temperature is set to be equal to the adiabatic wall temperature, $T_w = 7.027$. At the outer boundary $y = L_y$, characteristic boundary conditions were used and periodicity is imposed in the x and z directions. The variation of viscosity μ due to temperature is modeled using Sutherland's law (2.8) with a constant of $S^* = 110.4K$ and a reference temperature of $T_r^* = 216.65K$. A constant ratio of specific heats, $\gamma = 1.4$, was considered. Two different Reynolds numbers based on the displacement thickness of the initial laminar boundary layer were analyzed for the smooth and the porous wall cases, namely $Re_{\delta^*} = 6000$ and $Re_{\delta^*} = 20000$. The Prandtl number was set to $Pr = 0.72$ in all the simulations. The rest of the simulation parameters are presented in Table 5.1 and a sketch of the computational domain is shown in figure 5.1. In the main simulations (R2S, R2P, R6S, R6P) the streamwise extent of the computational domain gives a streamwise wavenumber of $\alpha = 2\pi/3$, which, according to LST calculations performed by Sandham & Lüdeke (2009), with a $M_\infty = 6$ and $Re_{\delta^*} = 20000$ base flow, places the fundamental wave near the maximum growth rate of the second Mach mode. This configuration allows the fundamental type of secondary instability to be analyzed. The spanwise extent of the computational domain was chosen to allow the growth of an unstable secondary wave. Ng & Erlebacher (1992) and El-Hady

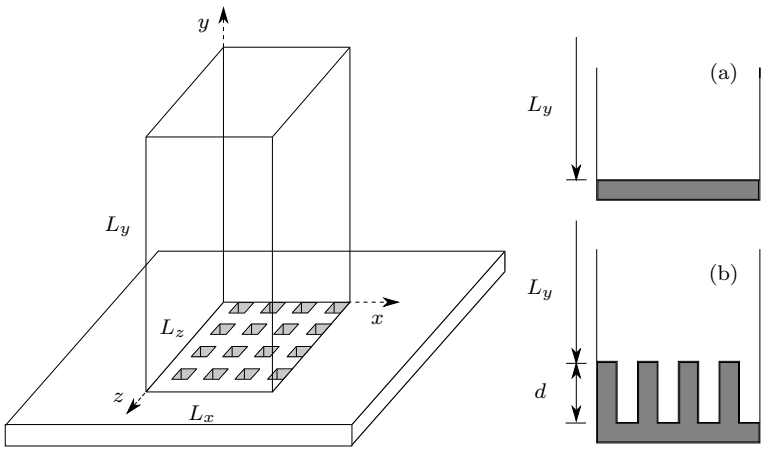

Figure 5.1: Computational domain. (a) smooth wall, (b) porous wall.

Case	Re_{δ^*}	$L_x \times L_y \times L_z$	$N_x \times N_y \times N_z$	Type
Main simulations				
R2S	20000	3×10×3	128×356×128	Smooth
R2P	20000	3×10×3	128×356×128	Porous
R6S	6000	3×10×3	64×356×64	Smooth
R6P	6000	3×10×3	64×356×64	Porous
Additional simulations				
R6S-6×3	6000	6×10×3	128×356×64	Smooth
R6S-6×9	6000	6×10×9	128×356×192	Smooth
R2S-9×6	20000	9×10×6	192×356×128	Smooth
R2P-9×6	20000	9×10×6	192×356×128	Porous

Table 5.1: Simulation parameters.

(1992) have shown that the spanwise wavenumber of the most dangerous secondary instability tends to the streamwise wavenumber of the primary instability as the Mach number increases from 1.6 to 7 and that there is a broad band of spanwise wavenumbers for which the secondary growth rates are large. Based on this the spanwise extent of the domain was chosen to be equal to the streamwise primary wavelength.

The smooth wall calculations were started with a computational grid of $N_x = 32$, $N_y = 356$, $N_z = 32$ points. As the calculations advanced the grids were refined to meet the resolution requirements. For the $Re_{\delta^*} = 6000$ and $Re_{\delta^*} = 20000$ cases the finest grid used was of 64×356×64 and 128×356×128 points respectively.

The porous wall calculations were performed with 4 pores in the streamwise and spanwise directions, giving a total of 16 pores. Based on the findings of Sandham & Lüdeke (2009), who showed that, for the same pore hydraulic diameter considered here, the pores reached an asymptotic behavior after $d = 1$, a pore depth of $d = 1$ was used in this study. The pores were square with length and width of 0.375 which gives a hydraulic diameter of $d_h = 0.375$. In real applications the porous sheet is expected to have a higher number of pores per Mack mode wavelength. See for example the experiments of Rasheed *et al.* (2002) where a sheet with $10 - 20$ pores per disturbance wavelength was used. On the other hand, LST (Fedorov *et al.*, 2001) and DNS (Sandham & Lüdeke, 2009) suggest that the damping effect of the pores on the Mack mode increases with their hydraulic diameter. The present calculations are relevant since they may help reveal whether big pores

could trigger early transition due to roughness effects, a problem which may be critical for the design of porous surfaces. All the porous wall calculations have a porosity of $n = 0.25$, which is achieved by considering the same number of grid cells inside and outside the pores in the streamwise and spanwise directions. The grid is uniform in these two directions. As reported by Sandham & Lüdeke (2009), due to the simplicity of the flow inside the pores, the number of grid points within the pores can be reduced to the minimum allowed by the spatial discretisation scheme. The Carpenter scheme employed near solid boundaries allows a minimum number of $N_g = 8$ streamwise or spanwise grid points inside the pores. Here 9 grid points (8 cells) per pore were considered giving an initial grid of 64×356×64 points. For the $Re_{\delta^*} = 20000$ case this grid was refined to 128×356×128 points as for the smooth wall case. To verify grid convergence a calculation with a fine grid (128×356×128) was started from $t = 0$, giving a Mack mode growth rate ($\omega_i = 0.0128$) only 3% lower than the coarse grid result. Note that the porous wall cases have 112 additional grid points within the pores in the vertical direction. A non-dimensional time step of $\Delta t = 0.002$ was used for all the simulations.

The additional simulations stated in Table 5.1 were carried out to complete the study. In particular cases R6S-6×3 and R6S-6×9 were used to analyze the behavior of the subharmonic secondary instabilities during transition and to assess the importance of the domain size in the low Reynolds number cases, respectively. Simulations R2S-9×6 and R2P-9×6 were carried out in order to verify the importance of oblique first mode waves in the presence of pores.

The presence of periodic boundary conditions in the streamwise and spanwise directions allowed the use of Fourier interpolation for refining the grids. This interpolation method provides the highest possible accuracy. For the porous wall cases Fourier interpolation was applied away from the pores. Within the pores the flow field was interpolated by a cubic spline method.

Grid stretching was only applied in the y direction in order to place more points near the flat plate ($y = 0$). The stretching function used is given by

$$y = L_y \frac{\sinh(c\eta)}{\sinh c}, \tag{5.3}$$

where $\eta_{min} < \eta < 1$ is the vertical coordinate in the computational grid. For the smooth wall cases $\eta_{min} = 0$ and $c = 3.15$. For the porous wall cases η_{min} and c were iteratively determined imposing $y(\eta_{min}) = -d$ and an integer number of grid points within the pore. Here c was chosen to be close to the value used in the smooth wall cases. All the test cases were initialized with the laminar similarity

solution at $M_\infty = 6$. For the porous wall simulations the smooth wall similarity solution was used to initialize the flow field over the pores, whereas inside the pores all the flow variables were kept constant and equal to their values at the wall ($y = 0$). The flow was initially perturbed by introducing random noise in the v-velocity component with maximum amplitude of the order of $10^{-3} \times U_\infty$. A damping function given by

$$D = y^2 e^{-y^2}, \tag{5.4}$$

was used to damp the amplitude of the noise close and far away from the wall. In the porous wall cases D was set to zero for $y < 0$. The objective here is to excite all the boundary layer modes resolved by the grid employed in order not to favor any particular wavenumber. The random disturbances are introduced into the v-component of velocity and during the subsequent integration of the governing equations all the conservative variables develop fluctuations. The maximum amplitude of the disturbances was chosen small enough to include the linear regime in the calculations.

In order to allow comparisons between the different simulations all the results shown in Fourier space are referred to a grid with $N_x = 64$ and $N_z = 64$ points.

5.3 Transition to turbulence due to second mode waves

5.3.1 Evolution and interactions of boundary layer modes

The disturbance evolution for cases R2S and R2P is shown in figure 5.2. It can be seen that in the smooth wall case (figure 5.2a) the random noise decays rapidly and after about ten non-dimensional time units the primary instability mode (1,0) starts growing linearly. The growth rate calculated from the numerical solution was found to be $\omega_i = 0.0341$, which is in agreement (to 3 significant figures) with the LST result. When mode (1,0) reaches finite amplitudes it starts interacting nonlinearly with itself giving rise to mode (2,0), which, as expected, grows twice as fast as mode (1,0). Nonlinear interactions of modes (1,0) and (2,0) then lead to mode (3,0) and so on for the higher harmonics. The total energy contained in each mode is calculated as follows

$$E_\phi(k_x, k_z, t) = \int_0^{L_y} \hat{\phi}(k_x, k_z, y, t)\hat{\phi}^\dagger(k_x, k_z, y, t)dy, \tag{5.5}$$

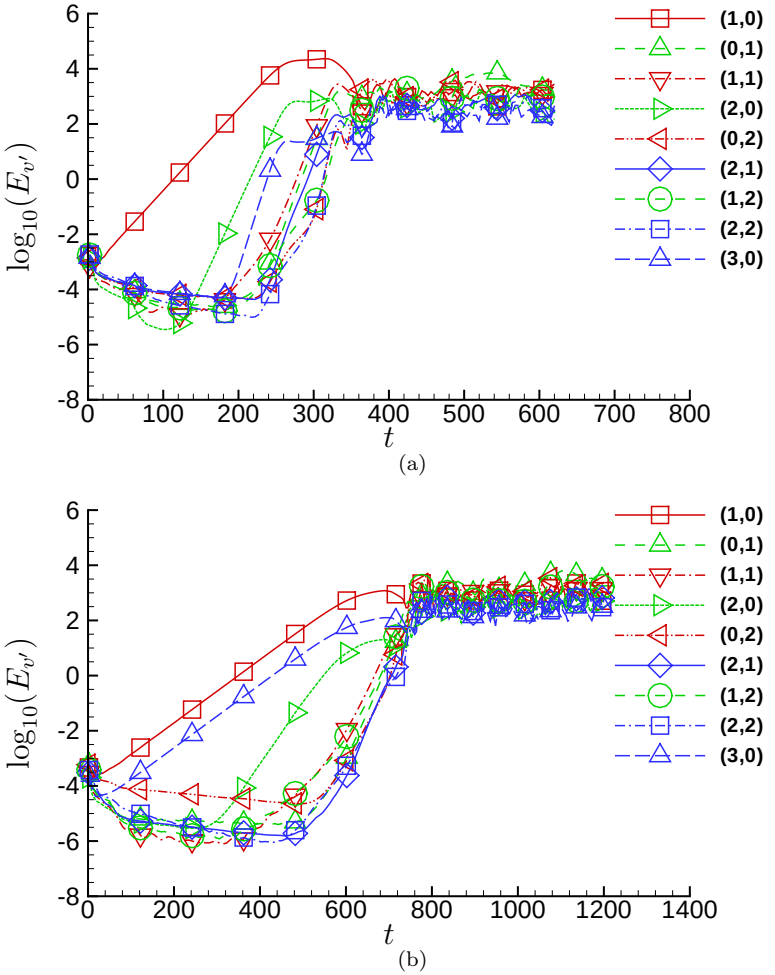

Figure 5.2: Time history of selected v' Fourier modes. (a) case R2S, (b) case R2P

where $\phi = \{u', v', w', \rho', T'\}$ and the the superscript (†) denotes a complex conjugate. At about $t = 180$ mode (1,1) starts growing, closely followed by modes (0,1) and (2,1). At time $t = 250$ the primary instability mode saturates and there is an increase in the growth rate of mode (1,1). At this point the transition process is driven by modes (1,1), (0,1) and (2,1) which all grow at the same rate.

Flow visualisations for case R2S reveal that mode (1,0) is a second mode wave (the Mack mode), which, in the region close to the boundary layer edge, is represented by a spanwise vortex. When the final breakdown to turbulence starts, the secondary instability breaks the two-dimensional structure of this vortex introducing spanwise variations in the disturbance amplitude, represented by a series of peaks and valleys and giving rise to characteristic Λ-vortices as seen in figure 5.3(a). The vortices are identified as regions of positive second invariant (Q-criterion) of the velocity gradient tensor (given by equation 4.3), and represent the dominant

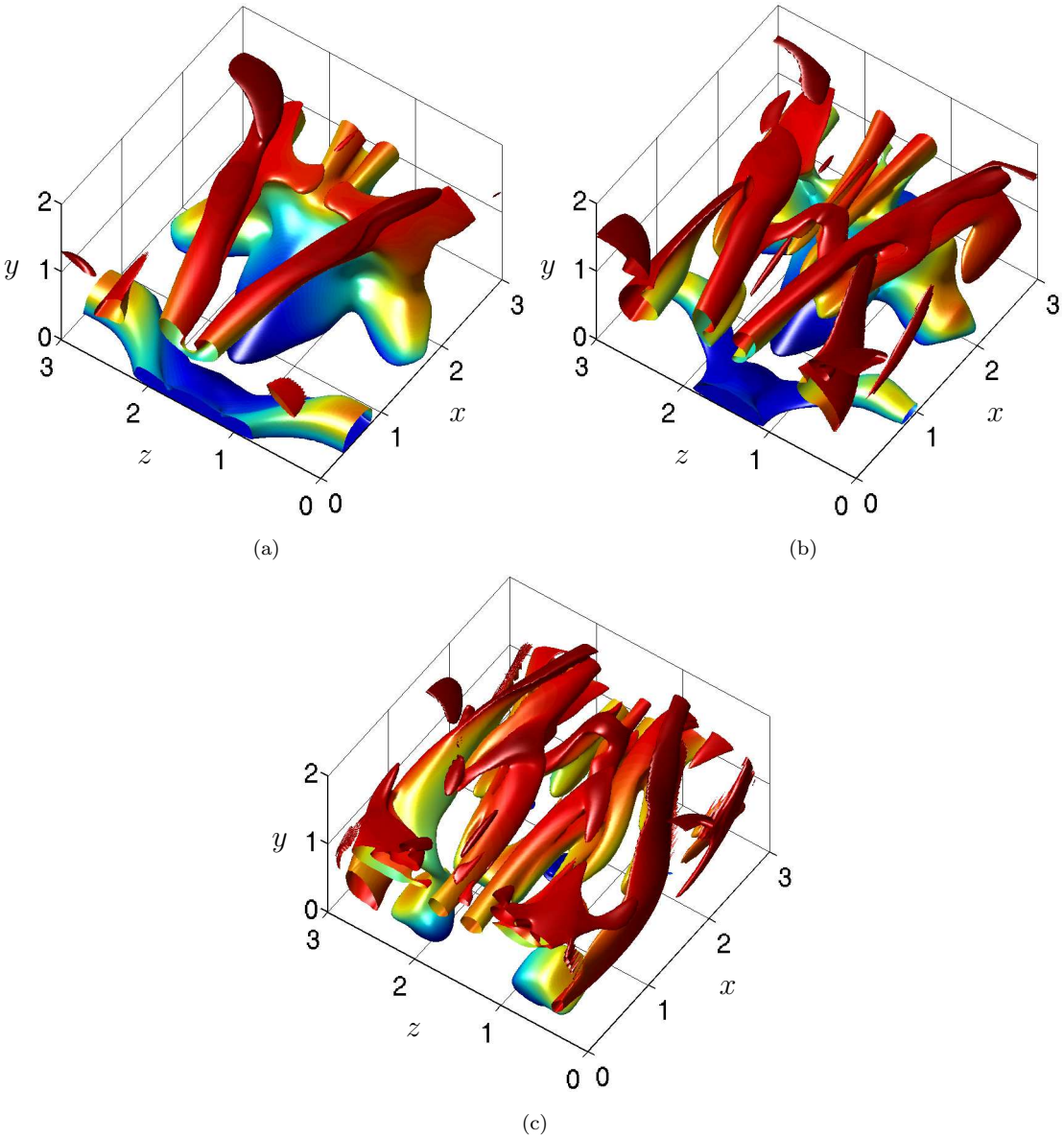

Figure 5.3: Coherent structures during transition for case R2S (Q-criterion), colored by streamwise velocity increasing from blue to red. (a) $t = 350$, (b) $t = 360$, (c) $t = 368$.

mode (1,1) taking part in the secondary instability. In all the cases the presence of vortices was verified by plotting velocity vectors in the regions indicated by the vortex visualisation criterion used. The Λ-vortices redistribute the mean shear and give rise to localised regions of high shear. The mechanism driving this is consistent with the findings of Stuart (1965), Sandham & Kleiser (1992) and Adams & Kleiser (1996), who showed, for both low speed and high speed flows, the importance of vortex stretching ($\omega_z \partial w/\partial z$) and convection in the generation of additional vorticity (notice that positive $\partial w/\partial z$ is associated with counter-rotating

streamwise vortices as seen in figure 5.3a). The shear layers roll up into the additional streamwise vortices visible in figure 5.3(b) at $z \approx 0.5$ and $z \approx 2.5$. The strength of these new vortices increases until they dominate the flow field together with the legs of the initial Λ-vortices, which can be seen in the region $1.0 < z < 2.0$ in figure 5.3(c). Further interactions of these streamwise vortices drive the flow to a chaotic state.

The variation of mode energy with time for case R2P shown in figure 5.2(b) reveals that, as expected, mode (1,0) (the Mack mode) starts growing linearly at a rate of $\omega_i = 0.0132$, which is about 2.5 times lower than in the smooth wall case. In this case, the DNS primary mode growth rate does not agree perfectly with the LST result of $\omega_i = 0.0107$, which is about 19% smaller than the DNS. The nonlinear interaction of mode (1,0) with itself leading to mode (2,0) is also visible along with the secondary instability growth starting from about $t = 350$. From the behavior seen on figure 5.2(b) modes (1,1) and (1,2) both are involved in the secondary instability.

The LST growth rates of the porous wall cases were calculated following the study of Wartemann *et al.* (2009), which corrected an error in the earlier LST calculations reported by Sandham & Lüdeke (2009). Wartemann *et al.* (2009) compared the temporal/spatial stability code used in this work with the DLR NOLOT spatial stability code showing very good agreement. The DLR NOLOT code was also found to agree well with Fedorov's original code (Fedorov *et al.*, 2001). However, it should be noted that, here and in Wartemann *et al.* (2009), the boundary conditions at the porous wall were calculated following the procedure proposed by Fedorov *et al.* (2001) for circular pores, using the hydraulic diameter as the characteristic pore size. Fedorov (2009) has recently shown that it is possible to reduce the discrepancies between the LST and the DNS by using the acoustic properties of square pores in the calculation of the porous-layer admittance.

The temporal evolution of mode (3,0) in figure 5.2(b), which grows linearly at the same rate as mode (1,0), was not expected. In fact, there is a whole family of discrete modes that shows the same behavior. The modes that were observed to follow this trend are the same that one would expect to see from the nonlinear interaction of modes (1,0) with the (4,0) and (0,4) standing waves, which represent the four pores per wavelength in the streamwise and spanwise directions. A physical explanation of this phenomenon can be found in the scattering of sound from the interaction of the Mack mode with the pores. The basic mechanism is similar to the scattering of sound from rough surfaces, studied by Brekhovskikh

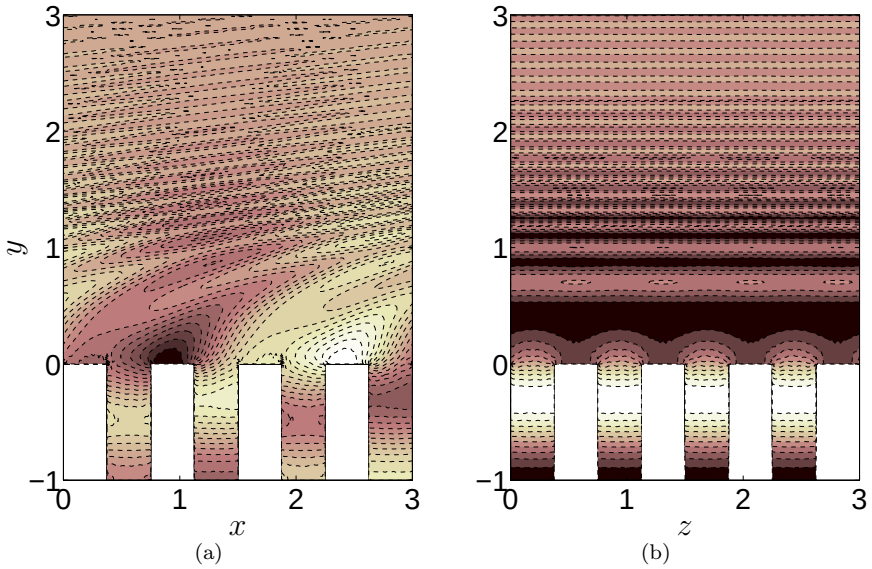

Figure 5.4: Scattering of sound waves for case R2P (contours of pressure: increasing from dark to light). (a) $x-y$ plane, (b) $y-z$ plane

& Lysanov (1994). For a simplified problem involving a rough surface with small slopes and small roughness elements the method of small perturbations (MSP) can be used to obtain an analytical solution for the scattered field. We consider an incident plane wave moving in the direction $\{\zeta_0, \gamma_0\}$, with ζ_0 and γ_0 being the horizontal and vertical components of the wave vector. Then by representing the rough surface, defined as $y = \Psi(\mathbf{r})$ with $\mathbf{r} = \{x, z\}$, as a Fourier integral

$$\Psi(\mathbf{r}) = \int_{-\infty}^{+\infty} A(\xi) e^{i\xi\mathbf{r}} d\xi, \tag{5.6}$$

it is possible to show that each of its Fourier components ξ gives rise to a scattered plane wave with $\zeta = \zeta_0 + \xi$. Here ζ_0 would be the horizontal wavenumber of the Mack mode. A complete derivation of this result can be found in Brekhovskikh & Lysanov (1994). The sound waves scattered from the porous surface can be appreciated in figure 5.4, which shows pressure contours in the $x-y$ and $y-z$ planes.

At the beginning of the simulation transient growth of spanwise modes can be observed in the density, temperature and streamwise velocity component for both R2S and R2P cases, as can be noted in figure 5.5 where the time history of $E_{u'}$ is shown. The growth of these modes represents the formation of streaks in the vicinity of the boundary layer edge, as shown in figure 5.6. Similar behavior was reported by Kim & Moser (1989) in their calculations of transition in plane

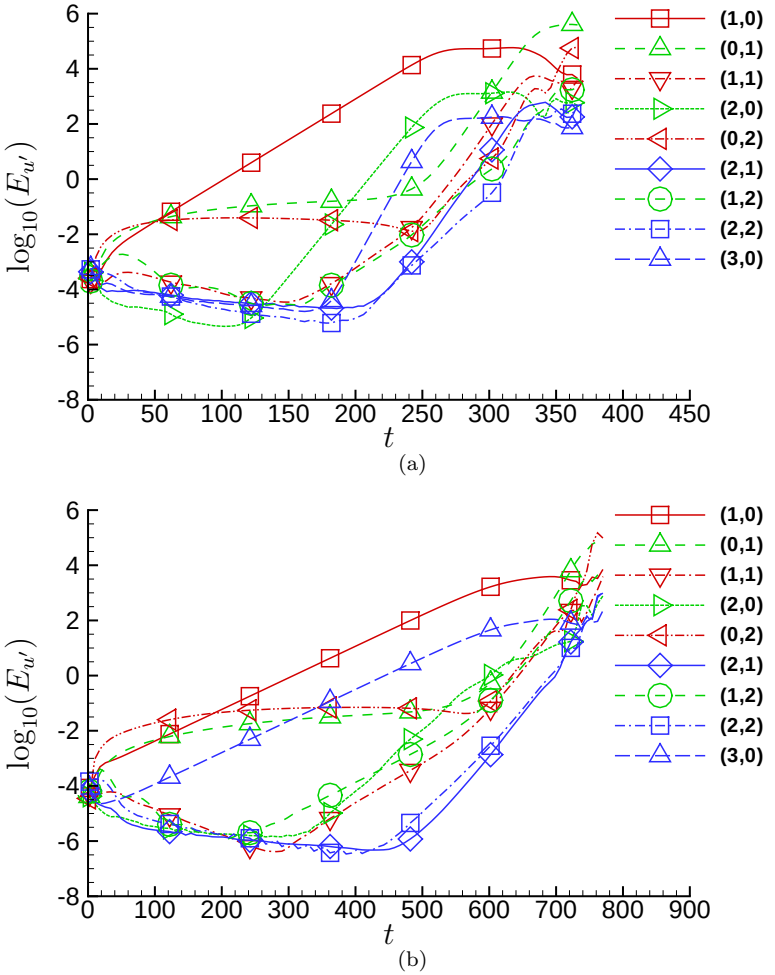

Figure 5.5: Time history of selected u' Fourier modes. (a) case R2S, (b) case R2P

Poiseuille flow. A direct consequence of the initial growth of spanwise modes (streaks) is the excitation of the fundamental three-dimensional modes, which arise due to nonlinear interactions of the primary mode (1,0) and the spanwise modes ($k_x = 0$,$k_z \neq 0$). Since the streaks are only slightly damped, the growth rate of mode (1,1) is initially similar to that of mode (1,0), as can be noted in figures 5.2 and 5.5. It should be noted that the initial growth of mode (1,1) and other fundamental three-dimensional modes (until about $t = 250$ for the smooth wall case and $t = 550$ for the porous wall case) seems to be associated with the aforementioned nonlinear interactions rather than with the secondary instability, which only develops at later times. The effects of the transient growth observed on the secondary instability are discussed further in Section 5.4.

At saturation the primary wave has an amplitude of $A = 6\%$ of the free-stream velocity for the smooth wall (case R2S), whereas for the porous wall (case R2P)

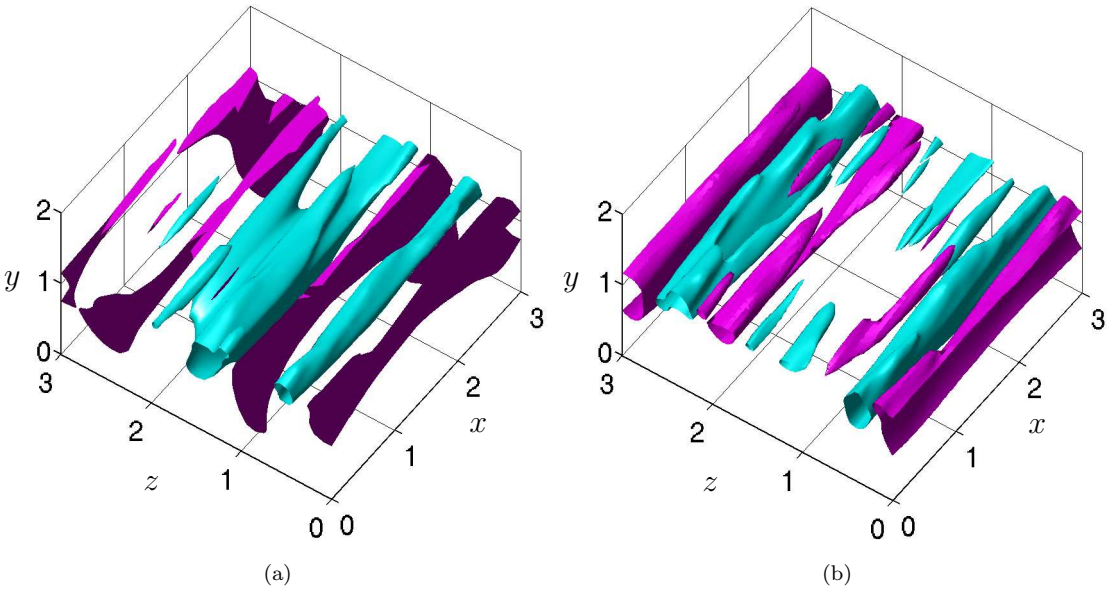

Figure 5.6: Streaks in the u-velocity profile due to transient growth, isosurfaces of u' (cyan: low speed streaks; magenta: high speed streaks). (a) case R2S, (b) case R2P

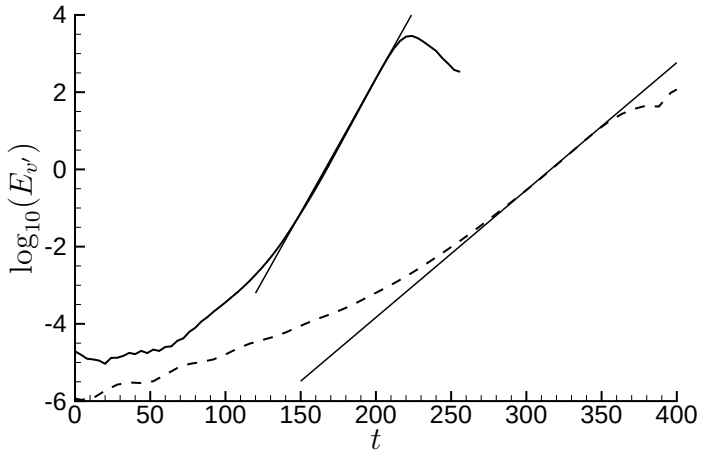

Figure 5.7: Comparison of secondary instability mode (1,1) growth rates: — , Smooth wall; – – – , Porous wall. Note that the curves where moved along the temporal axis to help the comparison.

$A = 3\%$. This drop in primary wave amplitude affects the growth rate of the secondary instability as shown in figure 5.7 for mode (1,1). The growth rate reduction factor is 0.475. Floquet analysis carried out by Ng & Erlebacher (1992) for a Mach 4.5 secondary instability showed a secondary growth rate reduction factor of about 0.56 when the primary amplitude dropped from $A = 6\%$ to $A = 3\%$. This behavior compares well with what is observed here. It is concluded that the pores mainly affect the secondary instability growth rate indirectly by limiting the

energy of the saturated primary wave. In order to understand the direct effect of porosity on the secondary instability it is useful to compare the mode energy distribution across the boundary layer, given by

$$e_\phi(k_x, k_z, y, t) = \hat{\phi}(k_x, k_z, y, t)\hat{\phi}^\dagger(k_x, k_z, y, t). \tag{5.7}$$

The energy profiles of the secondary wave in the smooth and porous cases are shown in figure 5.8, where the total mode energy is the same for the porous and the smooth wall results. The damping effect of the pores in the near wall region is clear. In the smooth wall case the secondary wave energy is mainly concentrated in the near wall region, whereas in the porous wall case there is a big peak near the critical layer. Damping of the secondary wave energy near the wall was observed for all the components of the disturbance field (u', v', w', ρ', T'). A possible explanation for this change of shape in the disturbance energy profiles is given in Section 5.3.2.

The coherent structures involved in the transition process in case R2P are similar to those discussed for case R2S. The secondary instability distorts the primary wave leading to the Λ-vortices shown in figure 5.9(a). Soon after the formation of these vortices additional Λ-shaped vortices pointing downstream form close to the boundary layer edge, as can be seen in figure 5.9(b). These two Λ-vortices represent modes (1,1) and (1,2) which, as shown in figure 5.2(b), dominate the secondary instability. At this stage the flow is dominated by strong quasi-streamwise vortices, which drive the flow to the breakdown to turbulence.

Figure 5.10 shows the temporal evolution of selected Fourier modes for the $Re_{\delta^*} =$

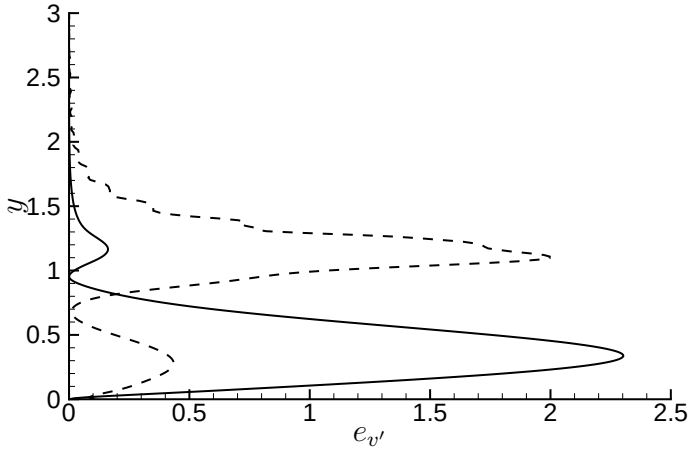

Figure 5.8: Secondary mode energy profiles: — , Smooth wall; – – – , Porous wall.

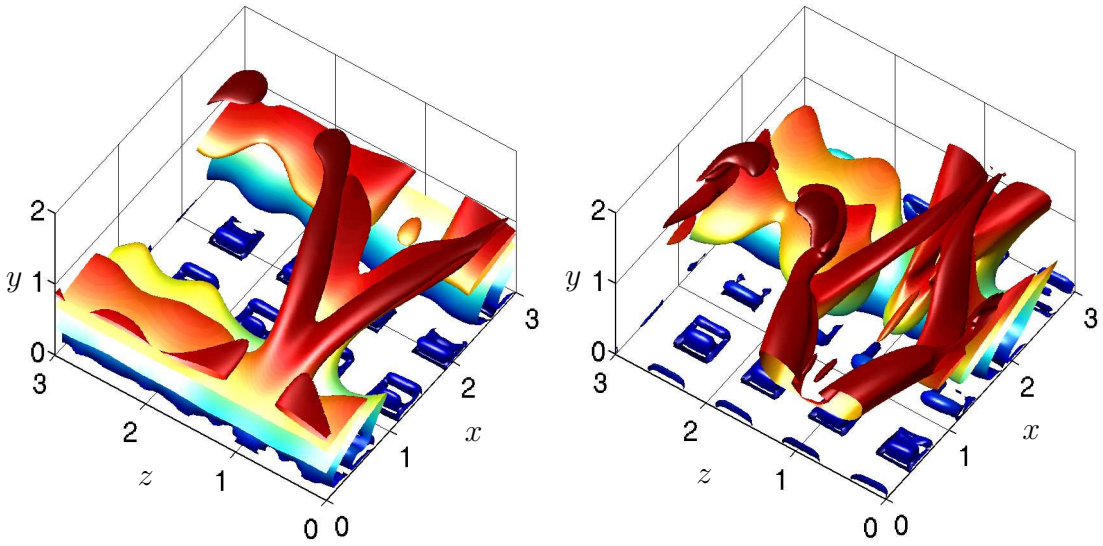

Figure 5.9: Coherent structures during transition for case R2P (Q-criterion), colored by streamwise velocity increasing from blue to red. (a) $t = 712$, (b) $t = 730$.

6000 smooth and porous walls (cases R6S and R6P). As can be seen the boundary layer is still unstable at this Reynolds number and the Mack mode grows linearly at a rate $\omega_i = 0.02084$ in the smooth wall case and $\omega_i = 0.00889$ in the presence of pores. The LST prediction for the primary growth rate gives $\omega_i = 0.02085$ and $\omega_i = 0.00576$ for smooth and porous wall respectively, i.e. in the porous wall case the LST result is about 35% lower than the DNS solution. In both cases the growth rate of the Mack mode has decreased in comparison with the $Re_{\delta^*} = 20000$ case, in agreement with theory. The flow undergoes all the stages of transition observed in the higher Reynolds number cases, including the secondary instability dominated by modes (1,1), (0,1) and (2,1) in case R6S and modes (1,1) and (1,2) in case R6P. The amplitude of the saturated primary waves is similar to the higher Reynolds number counterpart in both cases. The porous wall simulation (case R6P) shows the characteristic growth of scattered waves due to the interaction of the Mack mode with the pores. Transient growth of the u', ρ' and T' spanwise modes is also present for both the smooth and the porous wall cases. The effect of porosity on the secondary instability compares well with what is observed in the higher Reynolds number case. The reduction of growth rate due to porosity is very similar. In fact, the reduction factor recorded at $Re_{\delta^*} = 6000$ is $f_{sec} = 0.5$. Following the secondary instability all the boundary layer modes grow rapidly and the spectrum fills up, indicating the start of a chaotic state, only to quickly decay soon after. From visualisations of the flow it is seen that the turbulence does

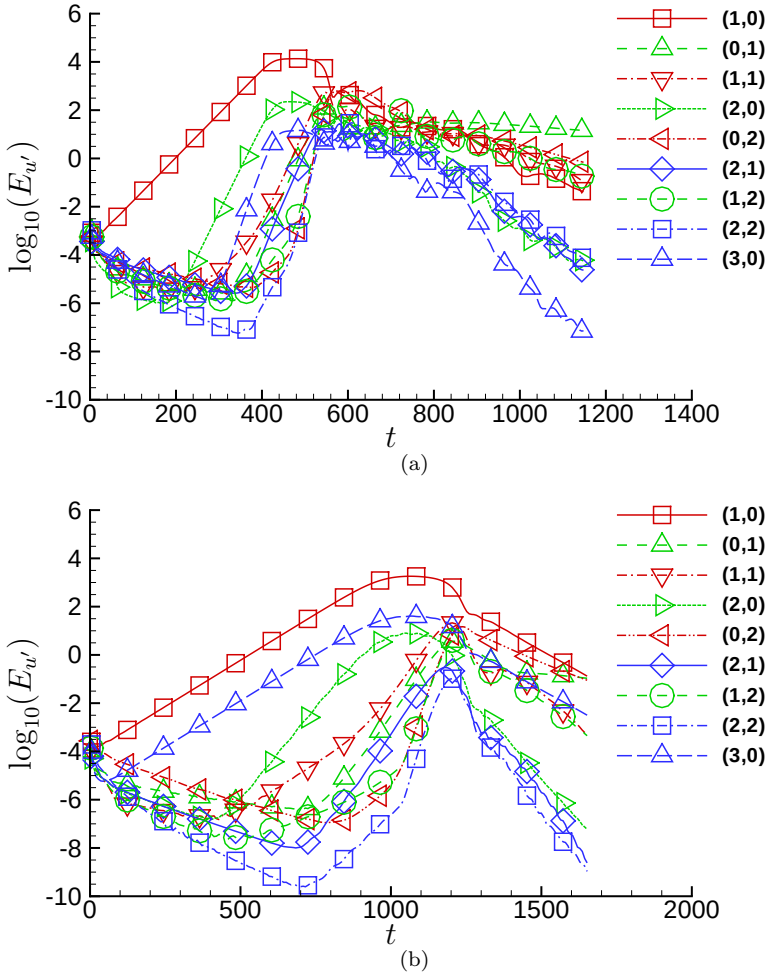

Figure 5.10: Time history of selected v' Fourier modes. (a) case R6S, (b) case R6P.

not penetrate to the near wall region and does not sustain. The reason for this sudden decay is that, given the low Reynolds number and high temperature, and hence viscosity, near the wall, the computational box is too small to accommodate the mechanisms that sustain the near wall turbulence (Jiménez & Moin, 1991; Waleffe, 1997). The spanwise extent of the computational domain in wall units, at $t \approx 600$, is $L_z^+ \approx 45$, which is below the limit of $L_z^+ \approx 100$ identified by Jiménez & Moin (1991) for self sustaining turbulence in incompressible channel flows. The situation is even worse when considering the streamwise domain length.

In order to investigate this particular behaviour further, an additional calculation was carried out for the smooth wall case with a domain of $L_x \times L_y \times L_z = 6 \times 10 \times 9$ (case R6S-6×9), which gives $L_z^+ \approx 120$ and $L_x^+ \approx 80$ at $t \approx 600$. Although still relatively short in the streamwise direction, the new domain is able to sustain the turbulence. As shown in figure 5.11, the new configuration allows the presence of

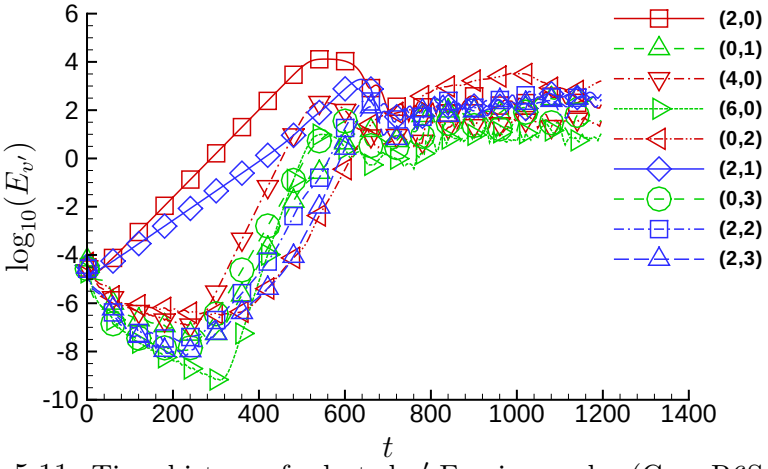

Figure 5.11: Time history of selected v' Fourier modes (Case R6S-6×9).

an oblique second mode with $\alpha = 2\pi/3$ and $k_z = 2\pi/9$ which grows linearly at a lower rate than the two-dimensional Mack mode, in accordance with LST. The Mack mode dominates the linear stages of transition growing at the same rate reported for the case with the smaller domain. As expected the presence of an oblique wave in the flow field affects the secondary instability. The fundamental secondary instability, represented by modes (2,1), (2,2) and (2,3), still dominates this stage of the transition process, however the growth rate is now significantly lower than for the smaller domain case. It should be noted that, due to the presence of the oblique second mode (2,1) and its nonlinear interaction with the two-dimensional Mack mode, which gives rise to modes (0,1) and (2,2), the flow is already three-dimensional when it undergoes secondary instability. Nevertheless, besides the appearance of an unstable oblique second mode, which seems to be of secondary importance in the transition process, the new simulation has not brought up any fundamentally new transition mechanism, hence the small computational domain used in cases R6S and R6P seems to capture the main features of the transition process prior to the final turbulent breakdown. The waves dominating the transition to turbulence are the two-dimensional second mode in the linear stages and the fundamental secondary modes, followed by spanwise modes and mode (4,3) in the late stages. Note that mode (4,3) coincides with mode (2,1) in the small domain. At the same time, we conclude that the relaminarisation observed in cases R6S and R6P is an artifact of the small computational domain used and not a fundamental physical mechanism.

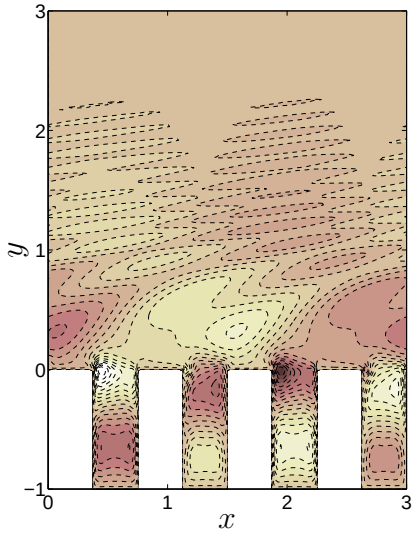

Figure 5.12: Contours of v for case R2P during the primary instability stage (increasing from dark to light).

5.3.2 Dissipation of disturbance energy inside the pores

Porous surfaces were originally proposed as a passive method for transition control in high-speed flows due to their ability to absorb acoustic energy (Fedorov *et al.*, 2001). It was thought that damping of the higher modes of Mack could be achieved by dissipating some of their energy inside the pores. This was then verified both numerically and experimentally, as already explained in Section 1.6. The results obtained in this work corroborate further this hypothesis. The acoustic waves which constitute the Mack mode are partially absorbed by the pores due to viscous losses. This can be seen in figure 5.12 for case R2P in the form of v' perturbations moving towards the bottom of the pores and represents the main mechanism responsible for the Mack mode damping. A similar effect is observed in figure 5.13(a) during the secondary instability stage. The pores seem to suppress the near wall v' modulations, visible in figure 5.13(b) for case R2S, due to the oblique acoustic waves shed by the secondary vortices and trapped in the relative supersonic region near the wall. This explains the difference in the energy profiles in figure 5.8. It is not clear how this process affects the secondary wave, however, as already mentioned, we believe that the main cause of secondary growth rate reduction is the reduced primary saturation.

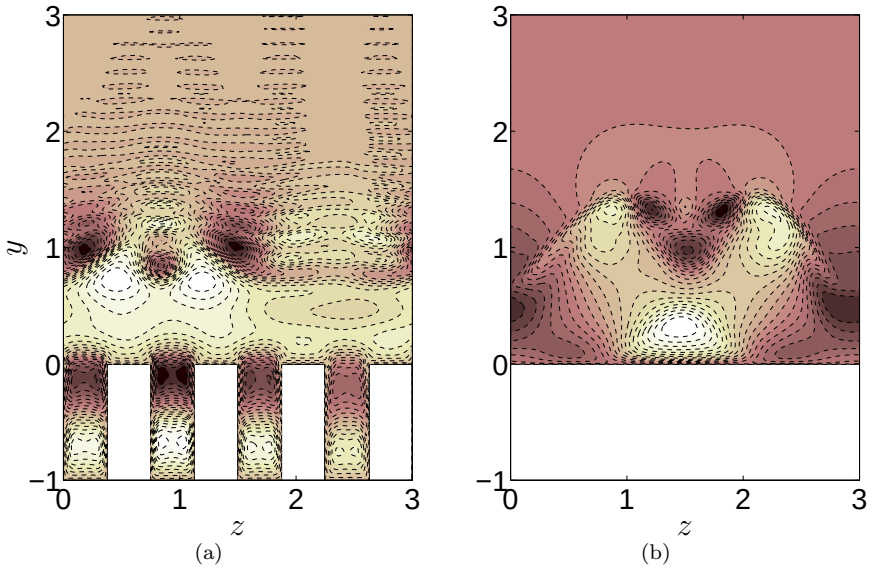

Figure 5.13: Contours of v during the secondary instability stage (increasing from dark to light). (a) case R2P, (b) case R2S.

5.3.3 Evolution of the averaged boundary layer quantities

To understand better how the mode interactions affect the averaged boundary layer an analysis of the boundary layer integral quantities is considered. The displacement thickness (δ^*) and momentum thickness (θ) are defined by

$$\delta^* = \int_0^\infty \left(1 - \frac{\rho u}{\rho_\infty U_\infty}\right) dy, \quad \theta = \int_0^\infty \frac{\rho u}{\rho_\infty U_\infty}\left(1 - \frac{u}{U_\infty}\right) dy, \tag{5.8}$$

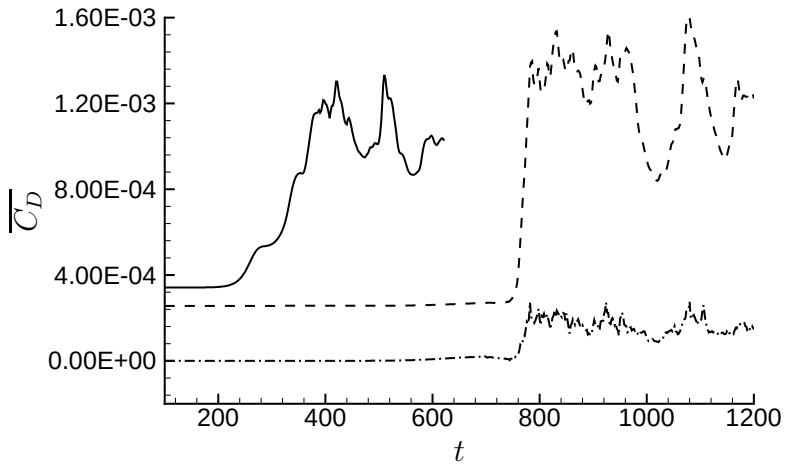

Figure 5.14: Time history of drag coefficient for the $Re^*_\delta = 20000$ cases: — , total drag C_D (case R2S); – – – , skin friction drag C_{Df} (case R2P); – · – pressure drag C_{Dp} (case R2P).

and the skin friction coefficient is calculated using non-dimensional variables as

$$c_f = \frac{2\mu_w}{Re}\frac{\partial u}{\partial y}|_w. \tag{5.9}$$

Figure 5.14 shows a comparison between the instantaneous spatially-averaged drag coefficients for the high Reynolds number cases. In the porous wall case the total drag is given by the sum of friction and pressure drag $C_D = C_{Df} + C_{Dp}$, where C_{Df} was calculated by integrating c_f over the entire horizontal area of the computational domain, whereas to calculate C_{Dp} the pressure was integrated over the vertical areas facing the streamwise direction inside the pores. C_{Df} and C_{Dp} where normalized with the same area. The first thing to note is that in the porous wall case the rise in C_D from the laminar to the turbulent value is much more sudden than in the smooth wall case. In the smooth wall case C_D increases in three stages. The skin friction first increases with the onset of the secondary instability at $t \approx 220$. The second rise is a consequence of the nonlinear interactions between the secondary waves, which start at $t \approx 300$. The third and final skin friction jump coincides with the final stages of transition when the turbulence reaches the wall. In the porous wall case the secondary as well as the primary waves are damped near the wall, so that the growth of the disturbances is not reflected in the drag coefficient, which only grows when the turbulence, after developing away from the wall, finds its way into the near wall region. Another feature worth noting is the difference in C_D before transition, which depends on the porosity considered and it is due to the fact that the basic flow in the porous wall case consists of zero velocity and constant pressure inside the pores. The laminar

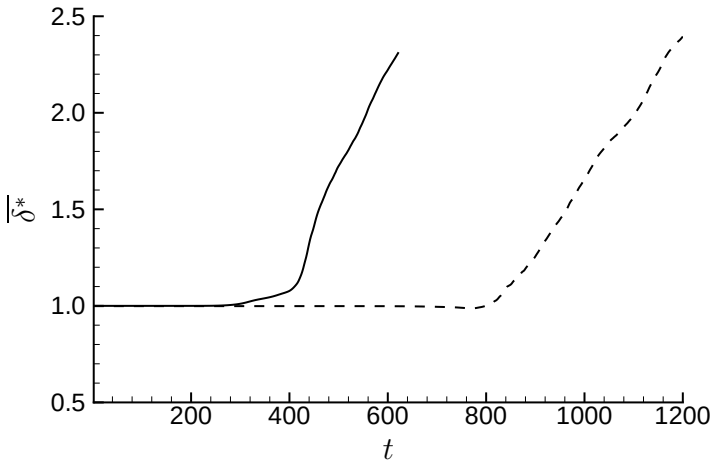

Figure 5.15: Time history of averaged displacement thickness: — , case R2S; – – – , case R2P.

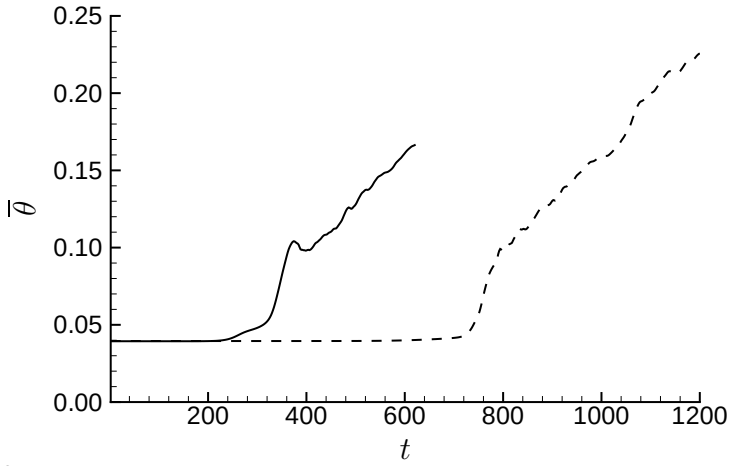

Figure 5.16: Time history of averaged momentum thickness: — , case R2S; – – – , case R2P.

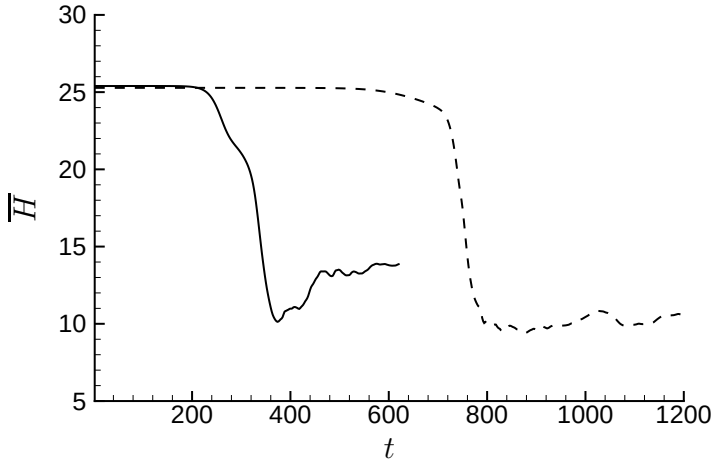

Figure 5.17: Time history of averaged shape factor: — , case R2S; – – – , case R2P.

total drag in the porous wall case is 25% smaller than in the smooth wall case. This difference corresponds to the 25% porosity and is a direct consequence of the forcing used to maintain the base flow. Calculations of a spatially-developing flow over pores are needed to study the effect of porosity on the laminar boundary layer. When the turbulence reaches the wall in the porous wall case a streamwise pressure difference establishes within the pores so that the pressure drag increases and brings the turbulent total drag to a higher value than in the smooth wall case. The total drag is influenced by the hydraulic diameter of the pores, which is quite large in the present simulations.

The evolution of the spatially-averaged displacement thickness, momentum thickness and shape factor, $H = \delta^*/\theta$, is shown in figures 5.15, 5.16 and 5.17. The

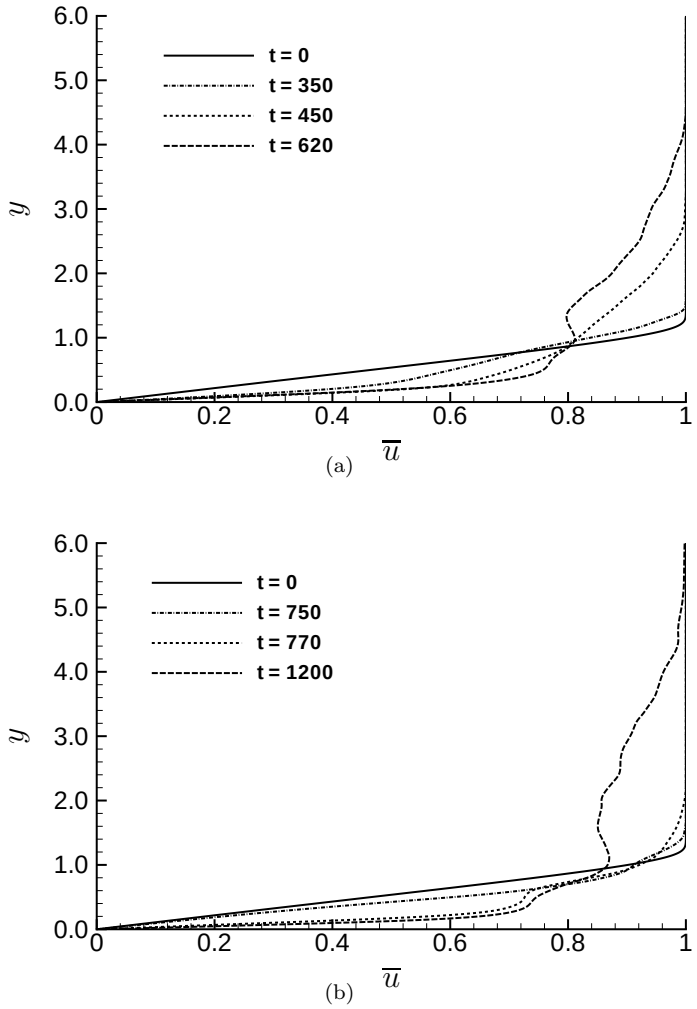

Figure 5.18: Boundary layer averaged u-velocity profiles during transition. (a) case R2S, (b) case R2P.

behavior observed at $Re_{\delta^*} = 20000$ (cases R2S and R2P) presents all the general features of boundary layer transition, with an increase in δ^* and θ and a decrease in shape factor. While in the smooth wall case skin friction and shape factor depart from their respective laminar value at about the same time, in the porous wall case the shape factor has already dropped significantly before the turbulence starts affecting the skin friction. Again, this indicates the effectiveness of the

porous surface in damping the disturbances in the near wall region.

An impression of the evolution of the boundary layer during the simulations is provided in figure 5.18 where boundary layer profiles are plotted at different times. The velocity profiles become steeper close to the wall and flatter away from the wall as the boundary layer grows and turbulence develops from the boundary layer edge all the way to the near wall region. The damping effect of the pores can also be noticed by observing that at $t = 750$ in figure 5.18(b) the mean velocity profile is still very close to the initial laminar profile. The heat transfer properties of the boundary layer during transition can be analyzed by plotting the Stanton number, written in dimensionless form as

$$St = \frac{(\gamma - 1)M_\infty^2 \overline{q}_w}{(T_w - 1)}, \tag{5.10}$$

which is a measure of the heat transferred from the fluid to the structure or vice versa. Given the normalisation used in this work the dimensionless density $\rho_\infty = 1$. Here, negative values of St indicate heat being transferred from the fluid to the structure.

Figure 5.19 shows the evolution of Stanton number for cases R2S and R2P. Although the wall is kept at a constant high temperature (equal to the laminar adiabatic temperature) in the smooth wall case there is still a heat transfer peak, characteristic of transitional high speed boundary layers. The same is not true for the porous wall case where heat transfer is negligible. The sudden drop in Stanton number for the smooth wall case coincides with the initial growth of skin friction due to the evolution and interactions of the three-dimensional secondary

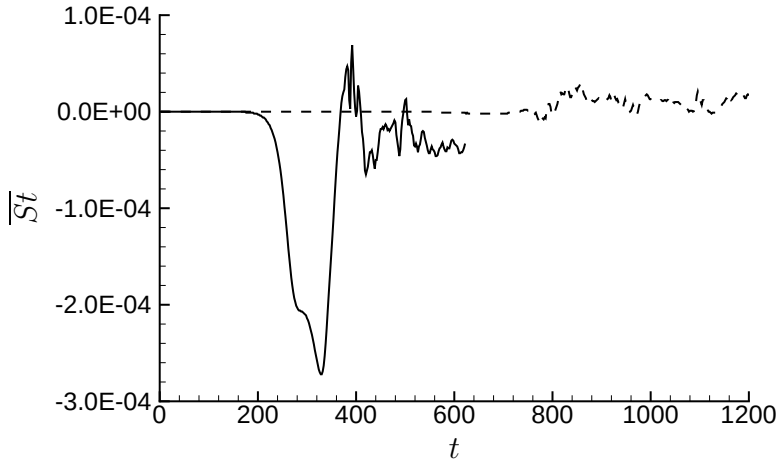

Figure 5.19: Variation of Stanton number during transition: — , case R2S; – – – , case R2P.

waves. Since these waves are damped by the pores in the near wall region the same behavior is not observed in the porous wall case.

5.4 The role of the fundamental secondary waves

The limited available literature on boundary layer secondary instability for compressible flows seems to suggest that the H-type (subharmonic) transition is the most likely transition scenario at high speeds. Ng & Erlebacher (1992) performed linear calculations using a Floquet model and found no evidence of the fundamental type of transition following a second-mode primary instability with streamwise wavenumber of $\alpha = 2.52$ at $M_\infty = 4.5$. This result was later verified by Adams & Kleiser (1996) for the same configuration through TDNS. On the other hand, Erlebacher & Hussaini (1990) carried out temporal direct numerical simulations of the fundamental secondary instability of the $M_\infty = 4.5$ flow over a flat plate and showed that the K-type (fundamental) breakdown to turbulence is possible. The initial simulations carried out in the present work focused on the fundamental type of transition, since the streamwise extent of the computational domain was set to be equal to the primary wave streamwise wavelength. The importance of subharmonic secondary waves was evaluated in case R6S-6×3, where a domain with a streamwise extent twice as large as the primary wave wavelength was used. Figure 5.20 shows the temporal evolution of the Fourier mode energy. In this new configuration mode (2,1) represents the fundamental secondary instability whereas mode (1,1) is the subharmonic. It can be seen that the energy of the subharmonic secondary wave remains at low levels throughout the transition process. This

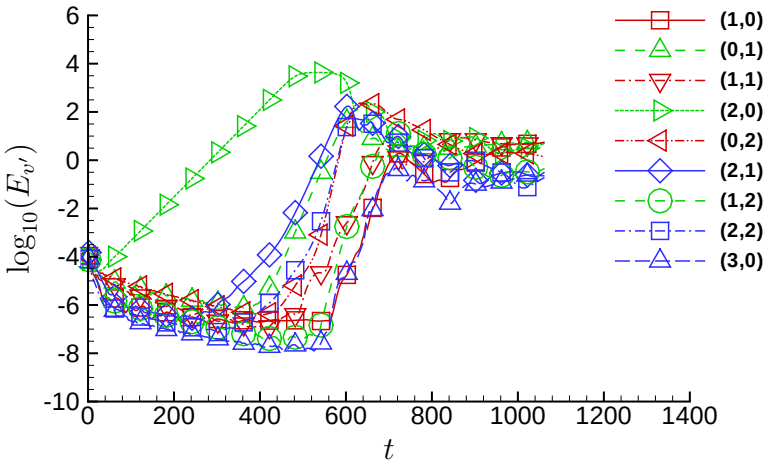

Figure 5.20: Time history of selected v' Fourier modes (Case R6S-6×3).

behavior was corroborated by the calculation carried out in order to assess the importance of the computational domain size discussed in Section 5.3 (see figure 5.11). The additional subharmonic secondary waves included in that case were also found to have small amplitudes during the transition process.

It should be noted that the initial growth of mode (2,1), starting from $t \approx 250$, is not a consequence of the secondary instability. As already mentioned in Section 5.3, the fundamental wave initially grows solely due to the interaction of the primary wave with the slightly damped spanwise modes present in the flow after the initial transient growth, which in turn is a consequence of the excitation of all the boundary layer modes through the introduction of random noise. In particular, the initial excitation of v' drives the transient growth of streaks through the lift-up mechanism, as already shown in figure 5.6.

It is concluded that the early excitation of mode (2,1) tends to favor the fundamental secondary instability. For this reason the subharmonic secondary instability can be excluded from the present simulations, although it may still play an important role in the $M_\infty = 6$ boundary layer transition to turbulence, depending upon upstream conditions.

5.5 The importance of first mode waves

Linear stability theory predicts that at $M_\infty = 6$ the second Mack mode waves, in particular the two-dimensional waves, are the most unstable. At these speeds the first mode is also unstable, with a maximum growth rate for oblique waves. The growth rate of the most amplified Mack mode for $Re_{\delta^*} = 20000$ is about 2.6 times larger than that of the most unstable oblique first mode, which explains why transition is dominated by the second mode at these Mach numbers. However, this is only true for smooth flat plates. We have already shown that when dealing with porous surfaces the growth rate of the second Mack mode decreases by a factor of about 2.5 and that three-dimensional second mode waves are strongly damped in the near wall region. In addition, LST calculations with the model of Fedorov *et al.* (2001) suggest that the oblique first modes are slightly destabilized by the porous surfaces, so that they may play an important role in the transition process. LST indicates that the most unstable first mode ($\alpha = 2\pi/12$ and $k_z = 2\pi/6.2$) grows at a rate of $\omega_i = 0.0136$ over a smooth flat plate, whereas in the presence of a porous surface with $n = 0.25$ and $d_h = 1.0$, the most unstable first mode moves

to a higher streamwise wavenumber ($\alpha = 2\pi/9.5$ and $k_z = 2\pi/6.8$) and grows at a rate $\omega_i = 0.0163$.

Two additional simulations, cases R2S-9×6 and R2P-9×6, were carried out in order to investigate the behavior of the boundary layer during transition in the presence of an oblique first mode. The new computational domain allows the growth of both an unstable first mode ($\alpha = 2\pi/9$ and $k_z = 2\pi/6$) and the most unstable Mack mode ($\alpha = 2\pi/3$ and $k_z = 0$). Figure 5.21 shows the evolution of v'-disturbances in the smooth and porous wall cases.

Case R2S-9×6 in figure 5.21(a) shows all the main features already reported for case R2S. The Mack mode (3,0) dominates the linear stages of transition giving rise to its harmonics, see for example mode (6,0). The amplitude of the Mack mode at saturation is slightly lower than in case R2S due to the presence of

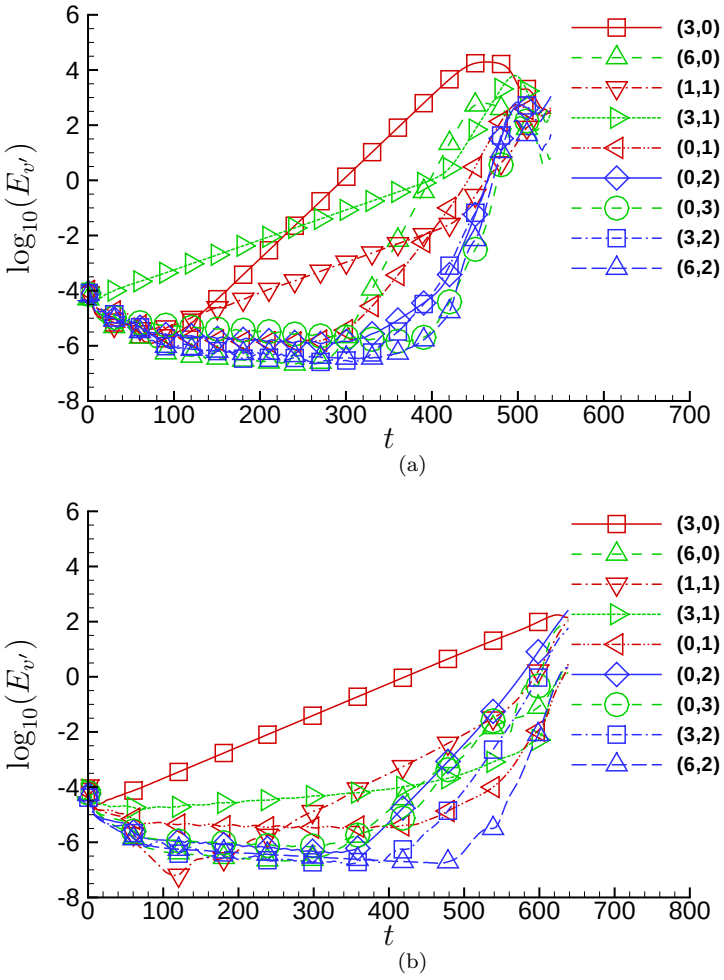

Figure 5.21: Time history of selected v' Fourier modes. (a) case R2S-9×6, (b) case R2P-9×6.

additional finite amplitude waves in the flow-field, which interact with the Mack mode. These waves are modes (1,1) and (3,1) in figure 5.21(a) and represent the first mode, which grows at a rate $\omega_i = 0.0128$, and an oblique second mode. After the Mack mode saturation the secondary instability takes place preceding the final breakdown to turbulence. This configuration does not allow the growth of exactly subharmonic secondary waves, however it was already shown in Section 5.4 that, for the cases analyzed in this work, these waves do not play an active role with the present initialisation.

The results for case R2P-9×6 shown in figure 5.21(b) suggest a completely different transition scenario in the presence of a porous surface. The Mack mode (3,0) grows at the expected rate ($\omega_i = 0.0132$, in agreement with case R2P) but this time its nonlinear self-interaction, leading to mode (6,0) and the higher harmonics, does not lead to a saturation state. The reason for this is that the oblique first mode (1,1) grows at a rate of $\omega_i = 0.0162$, in good agreement with the LST result, and gives rise to a spanwise (0,2) mode by interacting with a (-1,1) wave, which in turn has a temporal growth rate of about $\omega_i = 0.0330$. This fast growing mode drives the flow directly to a turbulent state by nonlinear interactions, without the need for a secondary instability. This transition mechanism is similar to the oblique-transition scenario found in low supersonic Mach numbers (Kosinov *et al.*, 1990; Sandham & Adams, 1993). In the light of this result it seems that the first mode regains importance in the transition process at high Mach numbers when dealing with porous surfaces.

5.6 Validity of the forcing term

The TDNS approach taken in this paper has been widely used, see for example Kleiser & Zang (1991) and Adams & Kleiser (1996). However, when adding forcing terms to the Navier-Stokes equations care is needed in order to correctly interpret the results obtained. As already mentioned the role of the forcing terms in this work is to prevent the growth of the initial laminar boundary layer, which is taken as the basic flow over which disturbances evolve, and to maintain the correct velocity profile. The forcing term is based on the initial laminar boundary layer and is kept constant throughout the simulation. In this framework the forcing term can interact with the disturbances, as in this case the decomposition is not orthogonal, $\int_V (U_b \cdot u')\, dV \neq 0$ where V represents the computational domain

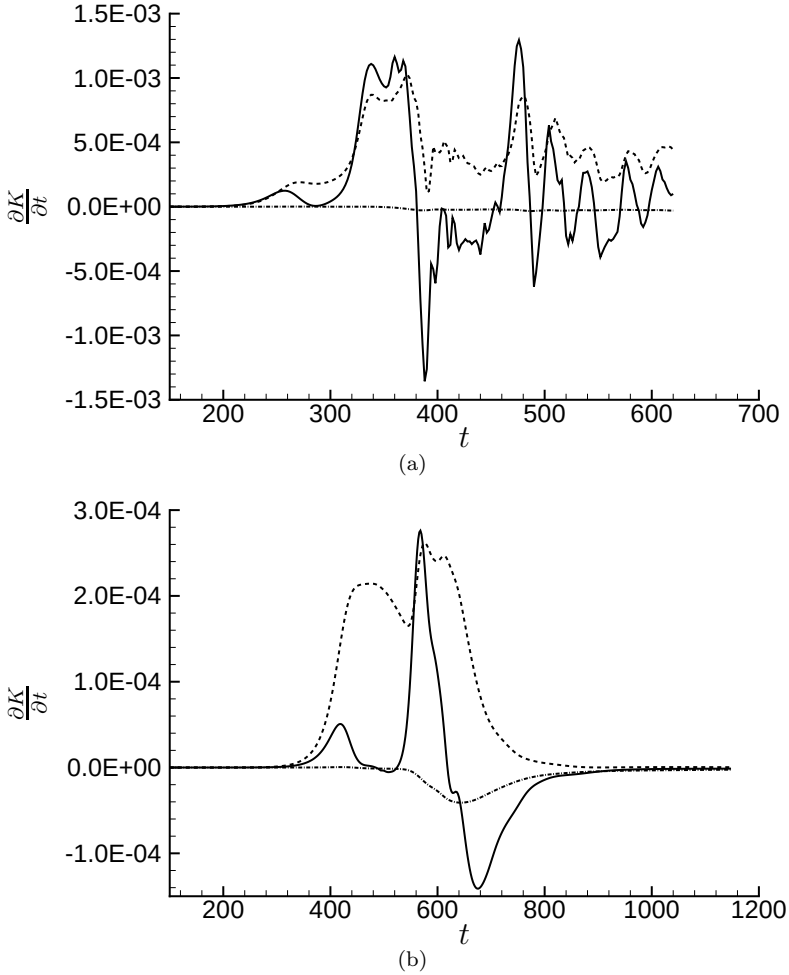

Figure 5.22: The effect of the forcing term on the disturbance kinetic energy, a) case R2S, b) case R6S: — , net production of K; – – – , production term; – · – contribution of the forcing term.

volume, giving a non-zero contribution to the total disturbance energy, or more precisely acting as a dissipative term in the disturbance energy equation.

For the simulations carried out in the present work the forcing term for the u-momentum equation takes the following form

$$F_{M1} = -\frac{d}{dy}\left[\frac{\mu}{Re}\frac{dU_b}{dy}\right], \tag{5.11}$$

whereas the forcing terms for the v-momentum and w-momentum equations are identically zero. The contribution from this term to the total velocity disturbance energy, $K = (u'^2 + v'^2 + w'^2)/2$, is given by $\int_V (u' \cdot F_{M1})\, dV$. By comparing this term with the right hand side of the total kinetic energy equation and with the

integrated production term

$$P = -\int_V u'v'\frac{dU_b}{dy}dV, \tag{5.12}$$

it is possible to quantify the effect of the forcing. We note that the forcing term is inversely proportional to the Reynolds number, hence it is more important at low Re.

Figure 5.22 shows the effect of the forcing term on the kinetic energy of the disturbances for cases R2S and R6S. The forcing term becomes important in the final stages of transition, starting from $t \approx 600$ for the low Reynolds number case, whereas its effect is negligible in the high Reynolds number case throughout the entire simulation. The amount of energy dissipated by the forcing term per unit time is very small when compared with the net disturbance kinetic energy produced in the boundary layer. Therefore in the high Reynolds number cases, although the mean boundary layer profile changes drastically during the simulation, as can be appreciated in figure 5.18, the effect of the forcing term on the evolution of the velocity disturbance energy is negligible.

5.7 Conclusions

Three-dimensional temporal direct numerical simulations of hypersonic boundary layer transition to turbulence over a porous surface have been carried out in the present work. Initially the $M_\infty = 6$ flat plate laminar boundary layer was perturbed with small random v'-disturbances with a maximum amplitude of the order of $10^{-3} \times U_\infty$. Two Reynolds numbers based on laminar displacement thickness were considered, namely $Re_{\delta^*} = 6000$ and $Re_{\delta^*} = 20000$. Smooth and porous wall calculations, all starting from the same laminar similarity profile, were analyzed for comparison. The results show that in all cases there is transient growth of u', ρ' and T' at the beginning of the simulation leading to streamwise streaks. Nonlinear interactions of these modes with the primary wave lead to the excitation of fundamental three-dimensional modes, thereby favoring the K-type transition scenario.

A reduction of primary wave growth rate due to the presence of pores confirmed the stabilizing effect of porous surfaces. The secondary wave growth rate was also found to be reduced, but this is argued to be due mainly to the lower primary wave amplitude at saturation. The direct effect of the pores on the secondary instability

is to almost entirely suppress the secondary wave growth in the near wall region. The analysis of the evolution of total drag during transition revealed that the rise from the laminar to the turbulent value is much more sudden in the presence of a porous surface. This is due to the fact that the three-dimensional secondary waves, which cause the initial increase in skin friction in the smooth wall case, are suppressed by the pores in the near wall region. Therefore the skin friction rises suddenly when the turbulence developing near the edge of the boundary layer reaches the wall. The onset of secondary instability was also found to be responsible for a heat transfer peak in the smooth wall simulations. The effects of transition on the wall heat flux were negligible in the porous wall case. It was found that, even at the high Mach numbers considered in this work, oblique first mode disturbances are the most dangerous waves for laminar boundary layers developing over porous surfaces. In this case an oblique mode transition mechanism drives the flow directly to a turbulent state without going through a secondary instability.

The conclusions drawn in this work are relevant to the classical small disturbance transition scenario, where the linear amplification of boundary layer modes is followed by nonlinear interactions and possibly secondary instabilities before the modes become stable as they convect downstream. The routes to transition are numerous. The effects of non-parallel mean flow, like synchronisation of boundary layer modes which are thought to lead to the excitation of the second mode, can determine the way disturbances enter the boundary layer (receptivity) and how they grow and interact with each other. The way these effects modify the transition scenario in the presence of porous surfaces is still not fully understood. Another problem worth investigating concerns the way the pores interact with the vortical structures entering the near wall region and how they influence the turbulent boundary layer.

Finally, in real applications porous materials are more likely to have a random distribution of pores with different widths and depths. We believe that our conclusions should apply to these cases at least qualitatively. This might not be the case when using fibrous materials, where the layout of the micro-cavities is very complex with intricate interconnections that can lead to non-negligible mean flow effects within the fibers. For these cases appropriate boundary conditions would need to be derived to take into account the effects of porosity.

Chapter 6

Conclusions and future work

The work presented in this dissertation was divided into three parts. Part one (chapter 3) contained a parametric study of the receptivity and subsequent linear growth of small disturbances in the laminar flow around localised sharp-edged roughness elements, which takes into account the effects of Mach number, roughness height, disturbance type and wall temperature. The second part (chapter 4) was focused on the nonlinear stages of transition to turbulence, with particular attention to the mechanisms leading to breakdown to turbulence following the linear growth of small disturbances and to the dominant processes in the evolution of a turbulent wedge downstream of the roughness element after breakdown. In this part of the investigation the effects introduced on the transition process by an oblique shock impingement on the transitional boundary layer were also analysed. The final part of this dissertation (chapter 5) was devoted to the study of a passive method for the control of transition to turbulence in high speed boundary layers based on the use of porous materials to damp the linear growth of boundary layer instability modes.

A synthesis of the principal results obtained in this work and suggestions for further study are provided in the following.

Receptivity due to roughness

Both at $M_\infty = 6.0$ and $M_\infty = 2.5$, isolated roughness elements induce pairs of counter-rotating streamwise vortices which, by lifting up low momentum fluid from the near wall region, lead to the generation of a low velocity streak bounded by regions of high wall-normal and lateral detached shear in the wake of the roughness

element. The strength of these vortices is found to increase with increasing roughness Reynolds number (Re_h) and wall temperature and with decreasing Mach number. As these vortices shape the wake of the roughness element they also determine its stability characteristics.

At the two Mach numbers considered, the effects of small roughness elements on the boundary layer stability are found to be weak. At $M_\infty = 6.0$ a roughness element with height $h/\delta_h^* \approx 0.35$ and $h/\delta_h \approx 0.27$ slightly enhances the receptivity of boundary layer modes, without introducing additional instabilities. The wake of the roughness is found to be stable for all frequencies of the forcing. At $M_\infty = 2.5$ small oscillations appear in the lateral shear layers surrounding the streak for the lowest forcing frequency considered ($F = 0.02$) and grow slowly for increasing streamwise distance. For higher frequencies the boundary layer response is practically undistinguishable from that of the smooth flat plate boundary layer.

Increasing the roughness height by a factor of two leads to a completely different scenario. At $M_\infty = 6.0$ the wake of the roughness sustains the growth of three additional instability modes, characterised by sinuous and varicose deformations of the low velocity streak. Growth of disturbances on the lateral shear layers located at the sides of the roughness-induced streamwise vortices may lead to a sinuous mode (denoted here as mode SL) or to a varicose mode (denoted as mode VL) depending on the nature of the disturbance environment. Disturbances dominated by sound are found here to efficiently excite two-dimensional (zero spanwise wavenumber) boundary layer modes which in turn tend to drive the response of the roughness wake towards a varicose deformation of the streak. Disturbances dominated by streamwise vorticity, on the other hand, lead to a more three-dimensional disturbance field inside the boundary layer and to the excitation of mode SL. The third mode (mode VC) is also associated with a varicose streak deformation and is characterised by the appearance of a near wall maximum near the roughness midplane in the u' and v' disturbance fields. This mode appears to be the roughness wake response to the growth of Mack modes in the laminar boundary layer away from the roughness wake. The most unstable roughness wake modes are mode VL for $F = 0.06$ and mode VC for $F = 0.14$, with $-\alpha_i \approx 0.029$ and $-\alpha_i \approx 0.027$ respectively and are found to be most effectively excited by disturbances dominated by sound.

At $M_\infty = 2.5$ all the forcing frequencies lead to the excitation of instability modes in the roughness wake. Disturbances grow due to the excitation of mode SL, similarly to what was found for the $M_\infty = 6.0$ case, and an additional varicose

mode (mode VT) associated with the Kelvin-Helmholtz instability of the shear layer along the roughness centreline. With a growth rate of $-\alpha_i \approx 0.25$ (about an order of magnitude higher than that of the most unstable wake mode at $M_\infty = 6.0$) mode VT for $F = 0.14$ is the most unstable mode observed. The results show that this mode drives the instability of the wake for $0.08 \leq F \leq 0.14$, while for higher frequencies mode SL is dominant. It appears that any generic boundary layer disturbance can lead to the excitation of mode SL and mode VT, however the results also suggest that in the absence of boundary layer disturbances only the fast acoustic waves are able to penetrate the boundary layer.

A study of the effects of wall temperature on the stability of the flow revealed that at $M_\infty = 6.0$ wall cooling tends to damp the growth of instability modes in the roughness wake and, as it is well known, has a destabilising effect on the Mack modes growing in the boundary layer away from the roughness wake. This result agrees with the damping effect of wall cooling in roughness-induced transition reported in previous studies (Redford *et al.*, 2010; Bernardini *et al.*, 2012). At $M_\infty = 2.5$ a decrease of wall temperature from $T_w = T_{ad}$ to $T_w = T_\infty$ leads to the onset of spontaneous oscillations in the separation bubble induced immediately upstream of the roughness element, suggesting the development of a global mode instability. This result, however, should be verified with further analysis in the future.

Nonlinear transition stages

For both $M_\infty = 6.0$ and $M_\infty = 2.5$ the linear growth of instabilities in the roughness wake eventually leads to breakdown to turbulence leading to the formation of a wedge of turbulence downstream of the roughness element. At $M_\infty = 6.0$, the linear growth of mode SL gives way to an asymmetric disturbance growth in the wake of the roughness element. We speculate that this behaviour is due to non-parallel flow effects leading to algebraic disturbance growth. The onset of nonlinear interactions further downstream leads to a breakdown to turbulence, characterised by the roll-up of the lateral shear layers surrounding the roughness induced streamwise vortices.

At $M_\infty = 2.5$ mode VT grows to finite amplitudes and induces the roll-up of the three-dimensional shear layer induced by the roughness in its wake, forming a series of hairpin-like vortices. The breakdown of these structures precedes the formation of a turbulent wedge.

The rate at which turbulence spreads laterally for increasing streamwise distance after breakdown to turbulence agrees well with experimental (Fischer, 1972) and numerical (Redford *et al.*, 2012) results obtained for the lateral growth of turbulent spots. At $M_\infty = 6.0$ the turbulent wedge has a half spreading angle of $\alpha = 3.0 \pm 0.2°$ while for $M_\infty = 2.5$, $\alpha = 5.5 \pm 0.2°$. Similarly to what was found for turbulent spots, at $M_\infty = 2.5$, the turbulent wedge grows both due to the convection of turbulent structures from the core of the wedge towards the surrounding laminar boundary layer and by an instability of the lateral jets located at the edges of the wedge. At $M_\infty = 6.0$ the growth by destabilisation mechanism is strongly damped and the wedge grows mainly by convection. In this case, the mean lateral flow also appears to play an active role in the generation of new mean flow structures near the edges of the wedge.

An oblique shock impingement on a boundary layer undergoing the final stages of transition was found to lead to an acceleration of the transition process at both $M_\infty = 6.0$ and $M_\infty = 2.5$. A small separation bubble is induced in the laminar boundary layer surrounding the wake of the roughness as a result of SBLI, while the flow in the transitional roughness wake remains mostly attached. This leads to the generation of two regions of high lateral shear near the sides of the roughness wake which sustain the quick growth of disturbances, eventually leading to breakdown to turbulence. The breakdown to turbulence in these lateral regions appears, for both the Mach numbers considered, as vortex shedding at the separation bubble edge with a dominant frequency of $F = 0.02$, which is much lower than the most unstable wake mode frequencies. As a result, the turbulent wedge spreads quickly in the lateral direction immediately downstream of the laminar separation bubble, leading to a wider turbulent in the presence of SBLI. The turbulent wedge recovers the lateral spreading rate of the case without shock further downstream.

Transition control using porous coatings

The effect of pores on the stability of a $M_\infty = 6.0$ boundary layer was studied by performing temporal direct numerical simulations. The stabilising effect of porous surfaces was confirmed by the computed reduction of Mack mode growth rate from $\omega_i = 0.0341$ (in the smooth wall case) to $\omega_i = 0.0132$. The reduced primary wave amplitude at saturation appears to be the main cause of a reduction of secondary instability growth rate in the porous wall case. The secondary wave growth near the wall is almost entirely suppressed by the pores. The increase of total drag during transition, while being delayed, occurs more suddenly in the

presence of pores than in the smooth wall case due to the suppression of the growth of secondary waves near the wall. Secondary instabilities cause the initial skin friction rise in the smooth wall case.

The damping effect of the Mack modes by the pores was found to be accompanied by a slight destabilisation of first mode waves. A combination of the two effects causes oblique first modes to be the most dangerous waves in the presence of pores, despite the high Mack number considered. An oblique mode transition mechanism leads in this case directly to breakdown to turbulence without the need for secondary instabilities.

Suggestions for further work

A continuation of this work could take a number of different paths. A list of suggestions for future work is provided in the following.

- The parametric study on the receptivity of small disturbances in the presence of roughness could be extended to include the effects of different roughness shapes and dimensions. For example, for a constant roughness height, diamond shaped roughness elements have been found experimentally to be more effective at triggering the boundary layer than squared ones. Therefore, it would be interesting to understand the underlying mechanisms responsible for these observations and the consequences these may have on roughness-induced transition criteria based on Re_h.

- The roughness-induced transition criteria proposed by Redford *et al.* (2010) and Bernardini *et al.* (2012) could be improved by performing a study of the effects of Reynolds number and roughness height close to the proposed critical Re_h value. This analysis could also give a better indication of the ability of Re_h to predict transition in the presence of roughness.

- The Roughness-induced transition criteria (see Redford *et al.*, 2010; Bernardini *et al.*, 2012) base their predictions (for a fixed Mach number and wall temperature) solely on the roughness Reynolds number (Re_h or Re_h^*). A significant contribution would be to incorporate the effect of disturbance amplitudes and types into the criteria.

- The receptivity study carried out in this work considered disturbances with different amplitudes of sound, vorticity and temperature fluctuations. For

small perturbations it should in principle be possible to impose disturbances made purely by sound, vorticity and entropy waves, which would help gain a more profound understanding of the process of receptivity. A numerical approach to achieve this is currently missing from the literature.

- The cold-wall $M_\infty = 2.5$ case analysed in section 3.7.3 suggests that an absolute instability developing in the upstream roughness-induced separation bubble drives the flow instability, which occurs in the absence of forced disturbances. It would be interesting to analyse this aspect in more detail by performing linear stability calculations. A full three-dimensional eigenvalue analysis would be challenging. However one could make considerable progress by solving the local and/or bi-global problems together with global stability Navier-Stokes based simulations (i.e. using the temporal DNS approach).

- In section 4.2.2 it was speculated that the asymmetric growth of disturbances in the roughness wake during the linear stages of transition is due to a linear superposition of non-normal modes which occurs as a consequence of non-parallel flow effects. It would be interesting to investigate this behaviour further. A detailed receptivity analysis, as those presented in this work in chapter 3, together with results from the bi-global eigenvalue problem would give considerable insight.

- The lateral growth of turbulent wedges was found in chapter 4 to be governed by similar mechanisms to those observed in turbulent spots studies. A more in depth study of the flow features near the edges of the wedge, perhaps with the use of conditional averages to better quantify the intensity of the lateral jets, would give a clearer picture of the role played by these jets in the spreading of turbulence both in turbulent wedges and spots.

- The study of the effects of SBLI on transitional boundary layers could be extended by considering for example different shock strengths and impingement locations. In addition, it would be of great interest to explore the onset of low-frequency oscillations in this transitional SBLI configuration, for which, however, much longer integration times than those considered in this work would be needed.

- The damping of Mack modes by porous coatings was investigated in chapter 5 in the temporal framework which neglects non-parallel flow effects. An extension of this work would be to consider the full three-dimensional spatial

problem. This would allow an investigation of the effects of pores on the boundary layer receptivity and the effect of non-parallel flow effects on Mack mode damping.

Bibliography

Adams, N. A. & Kleiser, L. 1996 Subharmonic transition to turbulence in a flat-plate boundary layer at Mach number 4.5. *Journal of Fluid Mechanics* **317**, 301–360.

Balakumar, P. 2008 Boundary layer receptivity due to roughness and freestream sound for supersonic flows over axisymmetric cones. *AIAA 2008-4399* .

Balakumar, P. 2009 Receptivity of a supersonic boundary layer to acoustic disturbances. *AIAA Journal* **47** (5), 1069–1078.

Benay, R., Chanetz, B., Mangin, B., Vandomme, L. & Perraud, J. 2006 Shock Wave/Transitional Boundary-Layer Interactions in Hypersonic Flow. *AIAA Journal* **44** (6), 1243–1254.

Bernardini, M., Pirozzoli, S. & Orlandi, P. 2012 Compressibility effects on roughness-induced boundary layer transition. *Int. Journal of Heat and Fluid Flow* **35**, 45–51.

Bountin, D., Shiplyuk, A. & Maslov, A. A. 2008 Evolution of nonlinear processes in a hypersonic boundary layer on a sharp cone. *Journal of Fluid Mechanics* **611**, 427–442.

Brekhovskikh, L. M. & Lysanov, Y. P. 1994 *Fundamentals of Ocean Acoustics*, 2^{nd} edn. Springer.

Brés, G. A., Colonius, T. & Fedorov, A. V. 2008 Interaction of acoustic disturbances with micro-cavities for ultrasonically absorptive coatings. *AIAA 2008-3903* .

Butler, K. M. & Farrel, B. F. 1991 Three-dimensional optimal perturbations in viscous shear flow. *Physics of Fluids A* **3** (9), 2148–2163.

Carpenter, M. H., Nordstrom, J. & Gottlieb, D. 1999 A stable and conservative interface treatment of arbitrary spatial accuracy. *Journal of Computational Physics* **148**, 341–365.

Chang, C. L., Choudhari, M. M. & Li, F. 2010 Numerical computations of hypersonic boundary-layer over surface irregularities. *AIAA 2010-1572* .

Chang, C. L., Choudhari, M. M. & Li, F. 2011 Effects of cavities and protuberances on transition over hypersonic vehicles. *AIAA 2011-3245* .

Chang, C. L. & Malik, M. R. 1994 Oblique-mode breakdown and secondary instability in supersonic boundary layers. *Journal of Fluid Mechanics* **273**, 323–360.

Chokani, N. 1999 Nonlinear spectral dynamics of hypersonic laminar boundary layer flow. *Physics of Fluids* **11** (12), 3846–3851.

Chokani, N. 2005 Nonlinear evolution of Mack modes in a hypersonic boundary layer. *Physics of Fluids* **17** (014102).

Chokani, N., Boutin, D. A., Shiplyuk, A. N. & Maslov, A. A. 2005 Nonlinear aspects of hypersonic boundary-layer stability on a porous surface. *AIAA Journal* **43** (1), 149–155.

Chong, M. S., Perry, A. E. & Cantwell, B. J. 1990 A general classification of three-dimensional flow fields. *Physics of Fluids A* **2** (5), 765–777.

Choudhari, M., Li, F., Chang, C. L. & Norris, A. 2012 Wake instabilities behind discrete roughness elements in high speed boundary layers. *Tech. Rep.* RTO-MP-AVT-200 (28). NATO.

Choudhari, M., Li, F. & Edwards, J. 2009 Stability analysis of roughness array wake in a high-speed boundary layer. *AIAA 2009-0170* .

Choudhari, M., Li, F., Minwei, W., Chang, C. L. & Edwards, J. 2010 Laminar-turbulent transition behind discrete roughness elements in a high-speed boundary layer. *AIAA 2010-1575* .

Choudhari, M. & Street, C. L. 1992 A finite Reynolds-number approach for the prediction of boundary-layer receptivity in localized regions. *Physics of Fluids A* **4** (11), 2495–2514.

Chu, B. T. & Kovasznay, L. S. 1958 Non-linear interactions in a viscous heat-conducting compressible gas. *Journal of Fluid Mechanics* **3** (5), 494–514.

Clark, J. P., Jones, T. V. & LaGraff, J. E. 1994 On the propagation of naturally-occurring turbulent spots. *Journal of Engineering Mathematics* **28**, 1–19.

Clark, J. P., Magari, P. J. & Jones, T. 1993 On the distribution of the heat transfer coefficient in turbulent and transitional wedges. *Int. Journal of Heat and Fluid Flow* **14** (3), 217–222.

Corke, T. C., Bar-Server, A. & Morkovin, M. V. 1986 Experiments on transition enhancement by distributed roughness. *Physics of Fluids* **29** (10), 3199–3213.

Cossu, C. & Brandt, L. 2002 Stabilization of Tollmien-Schlichting waves by finite amplitude optimal streaks in the Blasius boundary layer. *Physics of Fluids* **14** (8), L57.

Crouch, J. D. 1992 Localized receptivity of boundary layers. *Physics of Fluids A* **4** (7), 1408–1414.

De Tullio, N. & Sandham, N. D. 2010 Direct numerical simulation of breakdown to turbulence in a Mach 6 boundary layer over a porous surface. *Physics of Fluids* **22** (094105).

De Tullio, N. & Sandham, N. D. 2012 Direct numerical simulations of roughness receptivity and transitional shock-wave/boundary-layer interactions. *Tech. Rep.* RTO-MP-AVT-200 (22). NATO.

Demetriades, A. 1960 An experiment on the stability of hypersonic laminar boundary layers. *Journal of Fluid Mechanics* **9**, 385–396.

Demetriades, A. 1989 Growth of disturbances in a laminar boundary layer at Mach 3. *Physics of Fluids A* **1** (2), 312–313.

Denissen, N. A. & White, E. B. 2009 Continuous spectrum analysis of roughness-induced transient growth. *Physics of Fluids* **21** (114105).

Dolling, D. S. 2001 Fifty Years of Shock-Wave/Boundary-Layer Interaction Research: What Next?. *AIAA Journal* **39** (8), 1517–1531.

Downs, R. S., White, E. B. & Denissen, N. A. 2008 Transient growth and transition induced by random distributed roughness. *AIAA Journal* **46** (2), 451–462.

Ducros, F., Ferrand, V., Nicoud, F., Weber, C., Darracq, D., Gacherieu, C. & Poinsot, T. 1999 Large-eddy simulation of the shock-/turbulence interaction. *Journal of Computational Physics* **152**, 517–49.

Egorov, I. V., Fedorov, A. V., Novikov, A. V. & Soudakov, V. G. 2007 Direct numerical simulation of supersonic boundary-layer stabilization by porous coatings. *AIAA 2007-948* .

El-Hady, N. 1992 Secondary instability of high-speed flows and the influence of wall cooling and suction. *Physics of Fluids A* **4** (4), 727–743.

Ellingsen, T. & Palm, E. 1975 Stability of linear flow. *Physics of Fluids* **18** (4), 487–488.

Emmons, H. W. 1951 The laminar-turbulent transition in a boundary layer - Part I. *Journal of Aeronautical Sciences* **18** (7), 490–498.

Erlebacher, G. & Hussaini, M. Y. 1990 Numerical experiments in supersonic boundary-layer stability. *Physics of Fluids A* **2** (1), 94–104.

Farrel, B. F. & Ioannou, P. J. 2000 Transient and asymptotic growth of two-dimensional perturbations in viscous compressible shear flow. *Physics of Fluids* **12** (11), 3021–3028.

Fasel, H., Thumm, A. & Bestek, H. 1993 Direct numerical simulation of transition in supersonicboundary layer: oblique breakdown. *In Transitional and Turbulent Compressible Flows (ed. L. D. Kral & T. A. Zang), FED 151* pp. 77–92.

Fedorov, A. 2011 Transition and stability of high-speed boundary layers. *Annual Review of Fluid Mechanics* **43**, 79–95.

Fedorov, A. V. 2003 Receptivity of a high-speed boundary layer to acoustic disturbances. *Journal of Fluid Mechanics* **491**, 101–129.

Fedorov, A. V. 2009 Temporal Stability of Hypersonic Boundary Layer on Porous Wall: Comparison of Theory with DNS. *AIAA 2010-1242* .

Fedorov, A. V. & Khokhlov, A. P. 2001 Prehistory of instability in a hypersonic boundary layer. *Theoret. Comput. Fluid Dynamics* **14**, 359–375.

Fedorov, A. V., Malmuth, N. D., Rasheed, A. & Hornung, H. G. 2001 Stabilisation of hypersonic boundary layers by porous coatings. *AIAA Journal* **39** (4), 605–610.

Fedorov, A. V., Shiplyuk, A., Maslov, A. A., Burov, E. & Malmuth, N. 2003 Stabilization of a hypersonic boundary layer using an ultrasonically absorptive coating. *Journal of Fluid Mechanics* **479**, 99–124.

Fiala, A. & Hillier, R. 2005 Aerothermodynamics of turbulent spots and wedges at hypersonic speeds. *Proceeding of the Fifth European Symposium on Aerothermodynamics for Space Vehicles* pp. 615–620.

Fiala, A., Hillier, R., Mallinson, S. G. & Wijesinghe, H. S. 2006 Heat transfer measurement of turbulent spots in a hypersonic blunt-body boundary layer. *Journal of Fluid Mechanics* **555**, 81–111.

Fischer, M. C. 1972 Spreading of a turbulent disturbance. *AIAA Journal* **10** (7), 957–959.

Forgoston, E. & Tumin, A. 2005 Initial-value problem for three-dimensional disturbances in a compressible boundary layer. *Physics of Fluids* **17** (084106).

Fransson, J. H., Brandt, L., Talamelli, A. & Cossu, C. 2005 Experimental study of the stabilization of Tollmien-Schlichting waves by finite amplitude streaks. *Physics of Fluids* **17** (054110).

Fransson, L., Talamelli, J. H., Brandt, A. & Cossu, C. 2006 Delaying transition to turbulence by a passive mechanism. *Physical Review Letters* **96** (064501).

Fujii, K. 2006 Experiment of the two-dimensional roughness effect on hypersonic boundary-layer transition. *Journal of Spacecraft and Rockets* **43** (4), 731–738.

Gaster, M., Grosch, C. E. & Jackson, T. L. 1994 The velocity field created by a shallow bump in a boundary layer. *Physics of Fluids* **6** (9), 3079–3085.

Goldstein, M. E. 1983 The evolution of Tollmien-Schlichting waves by small streamwise variations in surface geometry. *Journal of Fluid Mechanics* **127**, 59–81.

Goldstein, M. E. 1985 Scattering of acoustic waves into Tollmien-Schlichting waves by small streamwise variations in surface geometry. *Journal of Fluid Mechanics* **154**, 509–529.

Graziosi, P. & Brown, G. L. 2002 Experiments on stability and transition at Mach 3. *Journal of Fluid Mechanics* **472**, 83–124.

Hanifi, A. & Henningson, D. S. 1998 The compressible inviscid algebraic instability for streamwise independent disturbances. *Physics of Fluids* **10** (8), 1784–1786.

Hanifi, A., Schmid, P. J. & Henningson, D. S. 1995 Transient growth in compressible boundary layer flow. *Physics of Fluids* **8** (3), 826–837.

Gad-el Haq, M., Blackwelder, R. F. & Riley, J. J. 1981 On the growth of turbulent regions in laminar boundary layers. *Journal of Fluid Mechanics* **110**, 73–96.

Herbert, T. 1988 Secondary instability of boundary layers. *Annual Review of Fluid Mechanics* **20**, 487–526.

Horvath, T. J., Zalameda, J. N., Wood, A. W. & Berry, S. A. 2012 Global Infrared Observations of Roughness Induced Transition on the Space Shuttle Orbiter. *Tech. Rep.* RTO-MP-AVT-200 (27). NATO.

Jiménez, J. & Moin, P. 1991 The minimal flow unit in near wall turbulence. *Journal of Fluid Mechanics* **225**, 213–240.

Jones, L. E. 2008 Numerical study of the flow around an airfoil at low Reynolds number. PhD thesis, School of Engineering Sciences.

Joslin, R. D. & Grosch, C. E. 1995 Growth characteristics downstream of a shallow bump: Computation and experiment. *Physics of Fluids* **7** (12), 3042–3047.

Kachanov, Y. S. 1994 Physical mechanisms of laminar-boundary-layer transition. *Annual Review of Fluid Mechanics* **26**, 411–482.

Kegerise, M., King, R., Owens, L., Choudhari, M., Li, F., Chang, C. L. & Norris, A. 2012 An experimental and numerical study of roughness-induced instabilities in a Mach 3.5 boundary layer. *Tech. Rep.* RTO-MP-AVT-200 (29). NATO.

Kendall, J. M. 1975 An experiment on the stability of hypersonic laminar boundary layers. *AIAA Journal* **13** (3), 290–299.

Kim, J. & Moser, R. D. 1989 On the secondary instability in plane poiseuille flow. *Physics of Fluids A* **1** (5), 775–777.

Klebanoff, P. S. & Tidstrom, K. D. 1972 Mechanism by which a two-dimensional roughness element induces boundary layer transition. *Physics of Fluids* **15** (7), 1173–1188.

Kleiser, L. & Zang, T. A. 1991 Numerical simulation of transition in wall-bounded shear flows. *Annual Review of Fluid Mechanics* **23**, 495–537.

Kosinov, A. D., Maslov, A. A. & Shevelkov, S. G. 1990 Experiments on the stability of supersonic laminar boundary layers. *Journal of Fluid Mechanics* **219**, 621–633.

Kovasznay, L. S. 1953 Turbulence in supersonic flow. *Journal of Aeronautical Sciences* **20** (10), 657–674,682.

Krishnan, L. & Sandham, N. D. 2006*a* Effect of Mach number on the structure of turbulent spots. *Journal of Fluid Mechanics* **566**, 225–234.

Krishnan, L. & Sandham, N. D. 2006*b* On the merging of turbulent spots in a supersonic boundary-layer flow. *Int. Journal of Heat and Fluid Flow* **27**, 542–550.

Krishnan, L. & Sandham, N. D. 2007 Strong interaction of a turbulent spot with a shock-induced separation bubble. *Physics of Fluids* **19** (016102).

Landahl, M. T. 1975 Wave breakdown and turbulence. *SIAM J. Appl. Math.* **28** (4), 735–756.

Landahl, M. T. 1980 A note on an algebraic instability of inviscid parallel shear flow. *Journal of Fluid Mechanics* **98** (2), 243–251.

Laufer, J. & Vrebalovich, T. 1960 Stability and transition of a supersonic laminar boundary layer on an insulated flat plate. *Journal of Fluid Mechanics* **9**, 257–299.

Lees, L. 1947 The stability of the laminar boundary layer in a compressible fluid. *Tech. Rep.* 1360. NACA.

Lees, L. & Lin, C. C. 1946 Investigation of the stability of the laminar boundary layer in a compressible fluid. *Tech. Rep.* 1115. NACA.

Li, Q. 2003 Numerical study of the Mach number effect in compressible wall-bounded turbulence. PhD thesis, School of Engineering Sciences.

Lysenko, V. I. & Maslov, A. A. 1984 The effect of cooling on supersonic boundary-layer stability. *Journal of Fluid Mechanics* **147**, 39–52.

Ma, Y. & Zhong, X. 2003*a* Receptivity of a supersonic boundary layer over a flat plate. Part 1. Wave structures and interactions. *Journal of Fluid Mechanics* **488**, 31–78.

Ma, Y. & Zhong, X. 2003*b* Receptivity of a supersonic boundary layer over a flat plate. Part 2. Receptivity to free-stream sound. *Journal of Fluid Mechanics* **488**, 79–121.

Mack, L. M. 1984 Boundary layer linear stability theory. *Tech. Rep.* 705. AGARD.

Marxen, O., Iaccarino, G. & Shaqfeh, S. G. 2010 Disturbance evolution in a Mach 4.8 boundary layer with two-dimensional roughness-induced separation and shock. *Journal of Fluid Mechanics* **648**, 435–469.

Masad, J. A. & Nayfeh, H. 1990 Subharmonic instability of compressible boundary layers. *Physics of Fluids A* **2** (8), 1380–1392.

Masad, J. A. & Nayfeh, H. 1991 Effect of heat transfer on the subharmonic instability of compressible boundary layers. *Physics of Fluids A* **3** (9), 2148–2163.

Maslov, A. A. 2003 Experimental and theoretical studies of hypersonic laminar flow control using ultrasonically absorptive coatings (UAC). *Tech. Rep.* 2172-2001. ITSC.

Maslov, A. A., Shiplyuk, A. N., Sidorenko, A. A. & Arnal, D. 2001 Leading-edge receptivity of a hypersonic boundary layer on a flat plate. *Journal of Fluid Mechanics* **426**, 73–94.

Mee, D. J. 2002 Boundary-layer transition measurements in hypervelocity flows in a shock tunnel. *AIAA Journal* **40** (8), 1542–1548.

Morkovin, M. V. 1991 Panoramic view of changes in vorticity distribution in transition instabilities and turbulence. *Boundary Layer Stability and Transition to Turbulence* **114**, 1–12.

Morkovin, M. V., Reshotko, E. & Herbert, T. 1994 Transition in open flow systems — A reassessment. *Bull. Am. Phys. Soc.* **39**.

Muppidi, S. & Mahesh, K. 2012 Direct numerical simulations of roughness-induced transition in supersonic boundary layers. *Journal of Fluid Mechanics* **693**, 28–56.

Murphree, Z. R., Jagodzinski, J., Hood, E. S., Clemens, N. T. & Dolling, D. S. 2006 Experimental Studies of Transitional Boundary Layer Shock Wave Interactions. *AIAA 2006-326* .

Ng, L. L. & Erlebacher, G. 1992 Secondary instabilities in compressible boundary layers. *Physics of Fluids A* **4** (4), 710–726.

Pirozzoli, S., Grasso, F. & Gatsky, T. B. 2004 Direct numerical simulation and analysis of a spatially evolving supersonic turbulent boundary layer at $M = 2.5$. *Physics of Fluids* **16** (3), 530–545.

Rasheed, A., Hornung, H. G., Fedorov, A. V. & Malmuth, N. D. 2002 Experiments on passive hypervelocity boundary-layer control using an ultrasonically absorptive surface. *AIAA Journal* **40** (3), 481–489.

Rayleigh, F. . R. S. 1878 On the stability, or instability, of certain fluid motions. *Proceedings* **10** (4), 57–74.

Rayleigh, F. . R. S. 1880 On the stability of certain fluid motions, II. *Math. Soc. Proc.* **11** (57), 67–75.

Redford, J. A., Sandham, N. D. & Roberts, G. T. 2010 Compressibility effects on boundary-layer transition induced by an isolated roughness element. *AIAA Journal* **48** (12), 2818–1830.

Redford, J. A., Sandham, N. D. & Roberts, G. T. 2012 Numerical simulations of turbulent spots in supersonic boundary layers: Effects of Mach number and wall temperature. *Prog Aerospace Sci* **52**, 67–79.

Reshotko, E. 2001 Transient growth: A factor in bypass transition. *Physics of Fluids* **13** (5), 1067–1075.

Reshotko, E. & A., T. 2004 Role of transient growth on roughness-induced transition. *AIAA Journal* **42** (4), 766–770.

Reynolds, O. 1883 An experimental investigation of the circumstances which determine whether the motion of water shall be direct or sinuous, and of the law of resistance in parallel channels. *Philos. Trans. R. Soc.* **174**, 935–82.

Ricco, P. & Wu, X. 2007 Response of a compressible laminar boundary layer to free-stream vortical disturbances. *Journal of Fluid Mechanics* **587**, 97–138.

Rizzetta, D. P. & Visbal, M. R. 2007 Direct numerical simulations of flow past an array of distributed roughness elements. *AIAA Journal* **45** (8), 1967–1976.

Sandham, N. D. & Adams, N. A. 1993 Numerical simulation of boundary-layer transition at Mach two. *Applied Scientific Research* **51**, 371–375.

Sandham, N. D., Adams, N. A. & Kleiser, L. 1995 Direct simulation of breakdown to turbulence following oblique instability waves in a supersonic boundary layer. *Applied Scientific Research* **54**, 223–234.

Sandham, N. D. & Kleiser, L. 1992 The late stages of transition to turbulence in chanel flow. *Journal of Fluid Mechanics* **245**, 319–348.

Sandham, N. D., Li, Q. & Yee, H. C. 2002 Entropy splitting for high-order numerical simulation of compressible turbulence. *Journal of Computational Physics* **178**, 307–322.

Sandham, N. D. & Lüdeke, H. 2009 A numerical study of Mach 6 boundary layer stabilization by means of a porous surface. *AIAA Journal* **47** (9), 2243–2252.

Saric, W. S., Carpenter, A. & Reed, H. L. 2008 Laminar flow control on a swept wing with distributed roughness. *AIAA 2008-500* .

Saric, W. S., Helen, L. R. & Banks, D. W. 2004 Flight testing of laminar flow control in high-speed boundary layers. *Tech. Rep.* RTO-MP-AVT-111. NATO.

Saric, W. S., Reed, H. L. & Kerschen, E. J. 2002 Boundary-layer receptivity to freestream disturbances. *Annual Review of Fluid Mechanics* **34**, 291–319.

Schlichting, H. & Gersten, K. 2000 *Boundary layer theory*, 8^{th} edn. Springer.

Schneider, S. P. 2008 Effects of roughness on hypersonic boundary-layer transition. *Journal of Spacecraft and Rockets* **45** (2), 193–209.

Schubauer, G. B. & Klebanoff, P. S. 1955 Contributions on the mechanics of boundary layer transition. *Tech. Rep.* TN-3489. NACA.

Schubauer, G. B. & Skramstad, H. K. 1948 Laminar boundary layer oscillations and transition on a flat plate. *Tech. Rep.* 909. NACA.

Stetson, K. F. & Kimmel, R. L. 1992 Example of second-mode instability dominance at a Mach number of 5.2. *AIAA Journal* **30** (12), 2974–2976.

Stuart, J. T. 1965 The production of intense shear layers by vortex stretching and convection. *Tech. Rep.* 514. AGARD.

Tani, I. & Sato, H. 1956 Boundary-layer transition by roughness element. *Journal of the Physical Society of Japan* **11** (12), 1284–1291.

Thomson, K. W. 1987 Time dependent boundary conditions for hyperbolic systems. *Journal of Computational Physics* **68**, 1–24.

Thomson, K. W. 1990 Time dependent boundary conditions for hyperbolic systems, II. *Journal of Computational Physics* **89**, 439–461.

Touber, E. & Sandham, N. D. 2009 Large-eddy simulation of low-frequency unsteadiness in a turbulent shock-induced separation bubble. *Theoret. Comput. Fluid Dynamics* **23**, 79–107.

Touber, E. & Sandham, N. D. 2011 Low-order stochastic modelling of low-frequency motions in reflected shock-wave/boundary-layer interactions. *Journal of Fluid Mechanics* **671**, 417–465.

Tumin, A. & Reshotko, E. 2001 Spatial theory of optimal disturbances in boundary layers. *Physics of Fluids* **13** (7), 2097–2098.

Tumin, A. & Reshotko, E. 2003 Optimal disturbances in compressible boundary layers. *AIAA Journal* **41** (12), 2357–2363.

Tumin, A. & Reshotko, E. 2005 Receptivity of a boundary-layer flow to a three-dimensional hump at finite Reynolds numbers. *Physics of Fluids* **17** (094101).

Visbal, M. R. & Gaitonde, D. V. 2002 On the use of higher-order finite-difference schemes on curvilinear and deforming meshes. *Journal of Computational Physics* **181**, 155–185.

Waleffe, S. 1997 On a self-sustaining process in shear flows. *Physics of Fluids* **9** (4), 883–900.

Wang, X. & Zhong, X. 2008 Receptivity of a hypersonic flat-plate boundary layer to three-dimensional surface roughness. *Journal of Spacecraft and Rockets* **45** (6), 1165–1175.

Wartemann, V., Lüdeke, H. & Sandham, N. D. 2009 Spatial stability analysis of hypersonic boundary layer flow over microporous surfaces. *AIAA 2009-7202* .

White, E. B. 2002 Transient growth of stationary disturbances in a flat plate boundary layer. *Physics of Fluids* **14** (12), 4429–4439.

White, F. M. 1991 *Viscous fluid flow*, 2^{nd} edn., chap. 7, pp. 504–507. McGraw-Hill.

White, E. B. and Rice, J. M and Gökhan Ergin, F. 2005 Receptivity of stationary transient disturbances to surface roughness. *Physics of Fluids* **17** (064109).

Wilkinson, S. P. 1997 A review of hypersonic boundary layer stability experiments in a quiet Mach 6 wind tunnel. *AIAA-97-1819* .

Wray, A. A. 1986 Very low storage time-advancement schemes. *Tech. Rep.*. NASA Ames Research Centre.

Wygnanski, I., Sokolov, M. & Friedman, D. 1982 On a turbulent 'spot' in a laminar boundary layer in the absence of a pressure gradient. *Journal of Fluid Mechanics* **123**, 69–90.

Yao, Y., Krishnan, L., Sandham, N. D. & Roberts, G. T. 2007 The effect of Mach number on unstable disturbances in shock/boundary-layer interactions. *Physics of Fluids* **19** (054104-1).

Yao, Y., Shang, Z. & Castagna, J. 2009 Re-engineering a DNS code for high-performance computation of turbulent flows. *AIAA 2009-566* .

Yee, H. C., Sandham, N. D. & Djomehri, M. J. 1999 Low-dissipative high-order shock-capturing methods using characteristic-based filters. *Journal of Computational Physics* **150**, 199–238.

Zhong, S., Chong, T. P. & Hodson, H. P. 2003 A comparison of spreading angles of turbulent wedges in velocity and thermal boundary layers. *Journal of Fluids Engineering* **125**, 267–274.

Zhong, X. & Ma, Y. 2006 Boundary-layer receptivity of Mach 7.99 flow over a blunt cone to free-stream disturbances. *Journal of Fluid Mechanics* **556**, 55–103.

Zuccher, S., Tumin, A. & Reshotko, E. 2006 Parabolic approach to optimal perturbations in compressible boundary layers. *Journal of Fluid Mechanics* **556**, 189–216.